JOURNAL OF THE AERONAUTICAL SCIENCES

VOLUME 12 APRIL, 1945 NUMBER 2

CONTENTS

Compressible Flows in Aeronautics . . . . . JOHN STACK 127

The Effective Use of Aerodynamic Balance on Control Surfaces . . . L. E. ROOT 149

Coefficient Method for Solving the Flutter Frequency Equation . M. V. BARTON 164

A Specific Chart for Flying Boat Take-Off Performance . . . . . JOHN D. PIERSON AND JOSEPH E. BURGHARDT 169

The Glauert-Prandtl Approximation for Subsonic Flows of a Compressible Fluid . . . . . HSUE-SHEN TSIEN AND LESTER LEES 173

Shock Waves in Aerodynamics . . . . . HOWARD W. EMMONS 188

Measurement of Maneuvering Loads in Flight . . . . . C. J. BUZZETTI AND W. L. HOWLAND 195

Stress Analysis of Nondevelopable Semimonocoque Structures Considered as Beams of Variable Section . . . . . LEON BESKIN 203

Determination of the Axis of Rotation of a Skewed Axis Landing Gear . . . . . J. J. JERGER 217

Equivalent Circuits of Compressible and Incompressible Fluid Flow Fields . . . . . GABRIEL KRON 221

Numerical and Network-Analyzer Tests of an Equivalent Circuit for Compressible Fluid Flow . . . . . G. K. CARTER AND G. KRON 232

Stresses in a Ring Loaded Normal to Its Plane . . . . . E. R. WALTERS 235

The Thermodynamics of the Laminar Boundary Layer of a Heated Body in a High-Speed Gas Flow Field . . . . . ARTHUR N. TIFFORD 241

Letters to the Editor 220, 240, 251

Copyright, 1945, by the

INSTITUTE OF THE AERONAUTICAL SCIENCES, INC.

JOURNAL OF THE AERONAUTICAL SCIENCES

VOL. 12 APRIL, 1945 NO. 2

PUBLISHED QUARTERLY BY THE INSTITUTE OF THE AERONAUTICAL SCIENCES, INC.

Chairman of the Editorial Board: HUGH L. DRYDEN, *Chief of Mechanics and Sound Division, National Bureau of Standards*

Editor: ROBERT R. DEXTER *Manager:* JOSEPH J. MAITAN

The Institute of the Aeronautical Sciences publishes the JOURNAL OF THE AERONAUTICAL SCIENCES quarterly, in January, April, July, and October, and the AERONAUTICAL ENGINEERING REVIEW monthly.

The JOURNAL OF THE AERONAUTICAL SCIENCES prints papers of scientific and technical interest to Institute members and subscribers. In general, it provides an opportunity for specialists to publish articles disclosing new knowledge and new applications in the field of the aeronautical sciences. The JOURNAL restricts itself to the aeronautical aspects of advances in science and engineering, and papers printed have either been submitted directly to the JOURNAL or have been previously presented at a meeting of the Institute.

The AERONAUTICAL ENGINEERING REVIEW keeps members and subscribers informed regarding the contents of new books and current periodicals in the field of aeronautics. It reviews new developments in the aircraft industry and reports on progress from house organs and catalogues published by aircraft and engine manufacturers and other companies engaged in aeronautical activities. It publishes papers on applied engineering and aircraft production. News of Institute activities is published in the REVIEW.

Statements and opinions expressed in the JOURNAL are to be understood as individual expressions of the authors and not those of the Institute.

SUBSCRIPTION RATES

Journal of the Aeronautical Sciences
Published Quarterly

United States and Possessions		Foreign Countries Including Canada (American Currency Rates)	
1 Year	$7.00	1 Year	$9.00
Single Copies	2.00	Single Copies	2.50

Aeronautical Engineering Review
Published Monthly

United States and Possessions		Foreign Countries Including Canada (American Currency Rates)	
1 Year	$3.00	1 Year	$3.50
Single Copies	0.30	Single Copies	0.35

Notices of change of address should be sent to the Institute at least 30 days prior to actual change of address.

Manuscripts for publication, proofs, and all correspondence should be addressed to the Editorial Office of the JOURNAL.

Correspondence regarding subscriptions may be addressed to Publication Office, 20th and Northampton Sts., Easton, Pa., or to the Editorial Office of the JOURNAL OF THE AERONAUTICAL SCIENCES, 1505 RCA Building West, 30 Rockefeller Plaza, New York 20, New York.

Entered as Second-Class Matter at the Post Office, Easton, Pa., May 1, 1937. Acceptance for mailin at a ecial rate of Postage provided for in the Act of August 24, 1912. Authorized April 29, 1937.

I

CHARL

W. A.
LEROY
I. M.
ARTHU

BENNE

P. R. B
REX B
GEORG
WILLIA

WALTE
LAWRE
C. L. B
ALLAN
R. H. B
JACK F
R. T. G
ROBERT
R. M. B
J. C. H

GRIFFITH
LYMAN J.
W. A. M
FRANK O

H. H. AR
D. W. DO
HUGH L.
W. F. DU
SIR RICHA

EDWARD
HART O.
E. L. CO
D. W. DO
SHERMAN
SIR RICHA

JOHN D. A
EDWIN E.
KARL ARN
J. L. ATW
PAUL S. B
RALPH S.
P. R. BAS
WELLWOO
REX B. BE
G. M. BEL
DON R. BI
HENRY A.
B. C. BOU
GEORGE W
LYMAN J.
W. G. BRO
CHARLES
FRANK W.
CHARLES
ALLAN CH
V. B. CLA
CHARLES
KARL T. C
JOHN W. C
RALPH S.
LUIS DE FI
A. V. DE F
SMITH J. D
J. P. DEN
WALTER S.
JAMES H.
C. S. DRAP
IVAN H. D

INSTITUTE of the AERONAUTICAL SCIENCES

President

CHARLES H. COLVIN

Vice-Presidents

W. A. M. BURDEN
LEROY R. GRUMMAN
I. M. LADDON
ARTHUR E. RAYMOND

Executive Vice-President

BENNETT H. HORCHLER

Past-Presidents

J. C. HUNSAKER
CHARLES L. LAWRANCE
D. W. DOUGLAS
GLENN L. MARTIN
CLARK B. MILLIKAN
T. P. WRIGHT
GEORGE W. LEWIS
JAMES H. DOOLITTLE
FRANK W. CALDWELL
HALL L. HIBBARD
HUGH L. DRYDEN
R. H. FLEET

Assistant to the President

GEORGE R. FORMAN

Secretary

ROBERT R. DEXTER

Treasurer

EARL D. OSBORN

Controller

JOSEPH J. MAITAN

COUNCIL

LESTER D. GARDNER, *Chairman*

P. R. BASSETT
REX B. BEISEL
GEORGE W. BRADY
WILLIAM K. EBEL
SHERMAN M. FAIRCHILD
CHARLES FROESCH
R. PAUL HARRINGTON
C. S. JONES
OTTO E. KIRCHNER
JOHN C. LESLIE
ALFRED MARCHEV
ELMER A. SPERRY, JR.

ADVISORY BOARD

WALTER BEECH
LAWRENCE D. BELL
C. L. EGTVEDT
ALLAN D. EMIL
R. H. FLEET
JACK FRYE
R. T. GOODWIN
ROBERT E. GROSS
R. M. HAZEN
J. C. HUNSAKER
TH. VON KÁRMÁN
J. H. KINDELBERGER
P. W. LITCHFIELD
F. W. MAGIN
CHARLES MARCUS
GLENN L. MARTIN
THOMAS A. MORGAN
R. C. MUIR
JOHN K. NORTHROP
W. A. PATTERSON
E. T. PRICE
F. W. REICHELDERFER
FRED H. ROHR
T. CLAUDE RYAN
J. T. TRIPPE
GUY W. VAUGHAN
J. G. VINCENT
EDWARD P. WARNER
E. E. WILSON

HONORARY MEMBERS

GRIFFITH BREWER
LYMAN J. BRIGGS
W. A. M. BURDEN
FRANK O. CARROLL
ARTEMUS L. GATES
HARRY F. GUGGENHEIM
ROBERT A. LOVETT
JOHN S. MCCAIN
CLEMENTS MCMULLEN
GEORGE B. PEGRAM
L. WELCH POGUE
J. LAURENCE PRITCHARD
D. C. RAMSEY
F. W. REICHELDERFER
EUGEN G. REINARTZ
C.-G. A. ROSSBY
T. P. WRIGHT

HONORARY FELLOWS

H. H. ARNOLD
D. W. DOUGLAS
HUGH L. DRYDEN
W. F. DURAND
SIR RICHARD FAIREY
SIR ROY FEDDEN
J. C. HUNSAKER
SIR MELVILL JONES
TH. VON KÁRMÁN
GEORGE W. LEWIS
GLENN L. MARTIN
GEORGE J. MEAD
SIR FREDERICK HANDLEY PAGE
D. R. PYE
IGOR I. SIKORSKY
G. I. TAYLOR
EDWARD P. WARNER
ORVILLE WRIGHT

BENEFACTOR MEMBERS

EDWARD E. ALDRIN
HART O. BERG (Deceased)
E. L. CORD
D. W. DOUGLAS
SHERMAN M. FAIRCHILD
SIR RICHARD FAIREY
R. H. FLEET
FLORENCE GUGGENHEIM (Deceased)
C. D. HANSCOM
JOHN P. V. HEINMULLER
ALEXANDER KLEMIN
PAUL KOLLSMAN
BELLA C. LANDAUER
WILLIAM LANDAUER
GROVER LOENING
EDMUND C. LYNCH (Deceased)
F. W. MAGIN
GLENN L. MARTIN
GEORGE J. MEAD
S. A. REED (Deceased)
L. S. ROCKEFELLER
EDWARD P. WARNER

AMERICAN FELLOWS

JOHN D. AKERMAN
EDWIN E. ALDRIN
KARL ARNSTEIN
J. L. ATWOOD
PAUL S. BAKER
RALPH S. BARNABY
P. R. BASSETT
WELLWOOD E. BEALL
REX B. BEISEL
G. M. BELLANCA
DON R. BERLIN
HENRY A. BERLINER
B. C. BOULTON
GEORGE W. BRADY
LYMAN J. BRIGGS
W. G. BROMBACHER
CHARLES P. BURGESS
FRANK W. CALDWELL
CHARLES H. CHATFIELD
ALLAN CHILTON
V. E. CLARK
CHARLES H. COLVIN
KARL T. COMPTON
JOHN W. CROWLEY, JR.
RALPH S. DAMON
LUIS DE FLOREZ
A. V. DE FOREST
SMITH J. DE FRANCE
J. P. DEN HARTOG
WALTER S. DIEHL
JAMES H. DOOLITTLE
C. S. DRAPER
IVAN H. DRIGGS
WILLIAM K. EBEL
C. L. EGTVEDT
FREDERIC FLADER
CHARLES FROESCH
JACK FRYE
GARLAND FULTON
LESTER D. GARDNER
RICHARD C. GAZLEY
MICHAEL E. GLUHAREFF
MELVIN N. GOUGH
LEROY R. GRUMMAN
R. M. HAZEN
ALBERT F. HEGENBERGER
EDWARD H. HEINEMANN
S. D. HERON
HALL L. HIBBARD
L. S. HOBBS
PAUL E. HOVGAARD
WILLIAM HOVGAARD
ROBERT INSLEY
EASTMAN N. JACOBS
CLARENCE L. JOHNSON
ALEXANDER KARTVELI
PAUL H. KEMMER
J. H. KINDELBERGER
OTTO E. KIRCHNER
ARTHUR L. KLEIN
ALEXANDER KLEMIN
W. B. KLEMPERER
PAUL KOLLSMAN
OTTO C. KOPPEN
B. V. KORVIN-KROUKOVSKY
S. M. KRAUS
I. M. LADDON
E. S. LAND
CHARLES L. LAWRANCE
JOHN G. LEE
CHARLES A. LINDBERGH
WILLIAM LITTLEWOOD
GROVER LOENING
W. RANDOLPH LOVELACE, II
EUGENE E. LUNDQUIST
R. D. MACCART
ERLE MARTIN
WM. H. MCAVOY
C. J. MCCARTHY
RICHARD VON MISES
CLARK B. MILLIKAN
ROBERT J. MINSHALL
JOSEPH S. NEWELL
ALFRED S. NILES
JOHN K. NORTHROP
ARTHUR NUTT
SHATSWELL OBER
ROBERT R. OSBORN
W. BAILEY OSWALD
GEORGE A. PAGE, JR.
F. W. PAWLOWSKI
F. W. PENNOYER, JR.
A. A. PRIESTER
ARTHUR E. RAYMOND
F. W. REICHELDERFER
ELLIOTT G. REID
H. J. E. REID
H. C. RICHARDSON
LEONARD E. ROOT
C. E. ROSENDAHL
WILLIAM T. SCHWENDLER
JAMES M. SHOEMAKER
MAC SHORT
IGOR ALEXIS SIKORSKY
SELDEN B. SPANGLER
ELMER A. SPERRY, JR.
JOHN STACK
WILLIAM B. STOUT
HARRY A. SUTTON
C. FAYETTE TAYLOR
EDWARD S. TAYLOR
PHILIP B. TAYLOR
TH. THEODORSEN
T. E. TILLINGHAST
S. TIMOSHENKO
STARR TRUSCOTT
L. B. TUCKERMAN
RALPH H. UPSON
J. G. VINCENT
P. V. H. WEEMS
FRED E. WEICK
R. D. WEYERBACHER
JOHN B. WHEATLEY
ANDREW V. WILLGOOS
DONALD H. WOOD
ROBERT J. WOODS
T. P. WRIGHT
JOHN E. YOUNGER
ALBERT F. ZAHM
STEPHEN J. ZAND

An Appreciation

TO CORPORATE MEMBERS OF THE

INSTITUTE OF THE AERONAUTICAL SCIENCES

Listed below are the leading aeronautical and industrial companies that make possible the publication of the *Journal of the Aeronautical Sciences*.

They enable the Institute to publish scientific and technical papers in the *Journal* and to devote its pages exclusively to editorial material.

Dues from individual members which would normally be used to publish this scientific and engineering quarterly are thus released for additional services to the profession and industry.

Advertising defrays the cost of publishing the *Aeronautical Engineering Review* and the *Aeronautical Engineering Catalog*.

These publications provide a comprehensive technical information service for the benefit of the aircraft and related industries.

ACADEMY OF AERONAUTICS
ADEL PRECISION PRODUCTS CORPORATION
AERO INSURANCE UNDERWRITERS
AEROJET ENGINEERING CORPORATION
AERONAUTICAL PRODUCTS, INC.
AEROQUIP CORPORATION
AGAWAM AIRCRAFT PRODUCTS, INC.
AIRCHOX COMPANY DIVISION, JOYCE AVIATION, INC.
AIRCRAFT RADIO CORPORATION
AIREON MANUFACTURING CORPORATION
AIRESEARCH MANUFACTURING COMPANY
AIRESEARCH MANUFACTURING COMPANY OF ARIZONA, INC.
AIREX MANUFACTURING COMPANY, INC.
ALLIS-CHALMERS MANUFACTURING COMPANY
ALLISON DIVISION, GENERAL MOTORS CORPORATION
ALUMINUM COMPANY OF AMERICA
AMERICAN AIRLINES, INC.
AMERICAN BOSCH CORPORATION
AMERICAN CENTRAL MANUFACTURING CORPORATION
AMERICAN EXPORT AIRLINES, INC.
AMERICAN PHENOLIC CORPORATION
THE AMERICAN ROLLING MILL COMPANY
AMERICAN TUBE BENDING COMPANY, INC.
ASSOCIATED AVIATION UNDERWRITERS
ASSOCIATED FOUNDRIES & MANUFACTURERS, INC.
BAKER STEEL & TUBE COMPANY
BAUSCH & LOMB OPTICAL COMPANY
BEECH AIRCRAFT CORPORATION
THE BG CORPORATION
BELL AIRCRAFT CORPORATION
BENDIX AVIATION CORPORATION
BENDIX PRODUCTS DIVISION
BENDIX RADIO CORPORATION
ECLIPSE-PIONEER DIVISION
EXPORT DIVISION
JULIEN P. FRIEZ & SONS DIVISION
PACIFIC DIVISION
SCINTILLA MAGNETO COMPANY
BOEING AIRCRAFT COMPANY
BOEING SCHOOL OF AERONAUTICS
BOLTON MANUFACTURING CORPORATION
BOOTS AIRCRAFT NUT CORPORATION
BREEZE CORPORATIONS, INC.
ESSEX TOOL & DIE COMPANY
FEDERAL LABORATORIES, INC.
EDWARD G. BUDD MANUFACTURING COMPANY
CARRIER CORPORATION
CESSNA AIRCRAFT COMPANY
CHANDLER-EVANS CORPORATION
CHASE NATIONAL BANK OF THE CITY OF NEW YORK
THE CLEVELAND GRAPHITE BRONZE COMPANY
THE CLEVELAND PNEUMATIC TOOL COMPANY
AUTOMOTIVE-AIRCRAFT DIVISION
CLIFFORD MANUFACTURING COMPANY
CONSOLIDATED VULTEE AIRCRAFT CORPORATION
NASHVILLE DIVISION
STINSON AIRCRAFT DIVISION
CONTINENTAL MOTORS CORPORATION
CULVER AIRCRAFT CORPORATION
CURTISS-WRIGHT CORPORATION
AIRPLANE DIVISION
PROPELLER DIVISION
WRIGHT AERONAUTICAL CORPORATION
DOAK AIRCRAFT COMPANY, INC.
DOUGLAS AIRCRAFT COMPANY, INC.
EL SEGUNDO PLANT
LONG BEACH PLANT
THE DOW CHEMICAL COMPANY
DZUS FASTENER COMPANY, INC.
EASTERN AIR LINES, INC.
EATON MANUFACTURING COMPANY
THOMAS A. EDISON COMPANY, INC., INSTRUMENT DIVISION
EDO AIRCRAFT CORPORATION
ELASTIC STOP NUT CORPORATION OF AMERICA
THE ELECTRIC AUTO-LITE COMPANY
ELECTROL INCORPORATED
EMBRY-RIDDLE COMPANY
ENGINEERING AND RESEARCH CORPORATION
ETHYL CORPORATION
THE FAFNIR BEARING COMPANY
FAIRCHILD CAMERA & INSTRUMENT CORPORATION
FAIRCHILD AERIAL SURVEYS, INC.
FAIRCHILD ENGINE AND AIRPLANE CORPORATION
DURAMOLD AIRCRAFT CORPORATION
FAIRCHILD AIRCRAFT DIVISION
RANGER AIRCRAFT ENGINES DIVISION
FEDERAL TELEPHONE AND RADIO CORPORATION
FIRESTONE AIRCRAFT COMPANY
FLEETWINGS DIVISION, KAISER CARGO, INC.
FLETCHER AVIATION CORPORATION
G & A AIRCRAFT, INC.
GENERAL AIRCRAFT EQUIPMENT, INC.
GENERAL AVIATION EQUIPMENT COMPANY, INC.
GENERAL ELECTRIC COMPANY
GENERAL INSTRUMENT CORPORATION
GENERAL MOTORS CORPORATION
AC SPARK PLUG DIVISION
AEROPRODUCTS DIVISION
BUICK MOTOR DIVISION
CADILLAC MOTOR CAR DIVISION
CHEVROLET MOTOR DIVISION
DELCO PRODUCTS DIVISION
DELCO-REMY DIVISION
EASTERN AIRCRAFT DIVISION
FISHER BODY DIVISION
FRIGIDAIRE DIVISION
HARRISON RADIATOR DIVISION
RESEARCH LABORATORIES DIVISION
ROCHESTER PRODUCTS DIVISION
GENERAL TIRE & RUBBER COMPANY
THE B. F. GOODRICH COMPANY
THE GOODYEAR TIRE & RUBBER COMPANY
GRAND CENTRAL AIRPORT COMPANY
THE GRAY MANUFACTURING COMPANY
GRUMMAN AIRCRAFT ENGINEERING CORPORATION
GUIBERSON DIESEL ENGINE COMPANY
W. & L. E. GURLEY
HANNA ENGINEERING WORKS
HASKELITE MANUFACTURING CORPORATION
HAYES INDUSTRIES, INC.
HIGGINS AIRCRAFT, INC.
THE INTERNATIONAL NICKEL COMPANY
IRVING AIR CHUTE COMPANY, INC.
JACK & HEINTZ, INC.
JACOBS AIRCRAFT ENGINE COMPANY
CASEY JONES SCHOOL OF AERONAUTICS, INC.
KELLETT AIRCRAFT CORPORATION
KENYON INSTRUMENT COMPANY, INC.
WALTER KIDDE & COMPANY, INC.
KOLLSMAN INSTRUMENT DIVISION, SQUARE D COMPANY
LAISTER-KAUFFMANN AIRCRAFT CORPORATION
LANGLEY CORPORATION
LAVELLE AIRCRAFT CORPORATION
LEAR INCORPORATED
LIBERTY AIRCRAFT PRODUCTS CORPORATION
LIGHTS, INCORPORATED
LINK AVIATION DEVICES, INC.
THE LIQUIDOMETER CORPORATION
LOCKHEED AIRCRAFT CORPORATION
LONGINES-WITTNAUER WATCH COMPANY, INC.
MAGNAFLUX CORPORATION
THE MARQUETTE METAL PRODUCTS COMPANY
THE GLENN L. MARTIN COMPANY
WARREN McARTHUR CORPORATION
McDONNELL AIRCRAFT CORPORATION
MENASCO MANUFACTURING COMPANY
MICROMATIC HONE CORPORATION
MINNEAPOLIS-HONEYWELL REGULATOR COMPANY
MOORE DROP FORGING COMPANY
NASH-KELVINATOR CORPORATION
NATIONAL CITY BANK OF NEW YORK
NATIONAL CREDIT OFFICE, INC.
THE NATIONAL SCREW & MANUFACTURING COMPANY
THE NEW YORK AIR BRAKE COMPANY
NOORDUYN AVIATION LIMITED
NORMA-HOFFMANN BEARINGS CORPORATION
NORTH AMERICAN AVIATION, INC.
NORTH AMERICAN AVIATION, INC., OF TEXAS
NORTHROP AIRCRAFT, INC.
NORTHWEST AIRLINES, INC.
OTTO AVIATION CORPORATION
OWENS-CORNING FIBERGLAS CORPORATION
PACKARD MOTOR CAR COMPANY
PAN AMERICAN AIRWAYS SYSTEM
THE PARKER APPLIANCE COMPANY
PENNSYLVANIA-CENTRAL AIRLINES CORPORATION
PHILLIPS PETROLEUM COMPANY
PIONEER PARACHUTE COMPANY, INC.
PESCO PRODUCTS COMPANY DIVISION, BORG-WARNER CORPORATION
THE PURE OIL COMPANY
REPUBLIC AVIATION CORPORATION
RIDGEFIELD MANUFACTURING CORPORATION, AIRCRAFT DIVISION
JOHN A. ROEBLING'S SONS COMPANY
ROHR AIRCRAFT CORPORATION
ROMEC PUMP COMPANY
ROOSEVELT FIELD, INC.
THE RYAN AERONAUTICAL COMPANY
SCIAKY BROTHERS
SCOTT AVIATION CORPORATION
SHAKESPEARE PRODUCTS COMPANY
SHELL OIL COMPANY, INC.
SIMMONDS AEROCESSORIES, INC.
SKYDYNE, INC.
SOCONY-VACUUM OIL COMPANY
SOLAR AIRCRAFT COMPANY
SOUTHERN AVIATION SCHOOL
SPERRY GYROSCOPE COMPANY, INC.
SQUARE D COMPANY
STANDARD OIL COMPANY OF CALIFORNIA
STANDARD OIL COMPANY (INDIANA)
STANDARD OIL COMPANY OF NEW JERSEY
STEEL IMPROVEMENT & FORGE COMPANY
SUMMERILL TUBING COMPANY
SWEDLOW AEROPLASTICS CORPORATION
TELEFLEX LIMITED
THE TEXAS COMPANY
THOMPSON PRODUCTS, INC.
TINNERMAN PRODUCTS, INC.
TITEFLEX, INC.
TRANSCONTINENTAL & WESTERN AIR, INC.
TRIPLETT & BARTON, INC.
UNION CARBIDE AND CARBON CORPORATION
BAKELITE CORPORATION
HAYNES STELLITE COMPANY
LINDE AIR PRODUCTS COMPANY
NATIONAL CARBON COMPANY
UNITED AIRCRAFT CORPORATION
CHANCE VOUGHT AIRCRAFT DIVISION
HAMILTON STANDARD PROPELLERS DIVISION
PRATT & WHITNEY AIRCRAFT DIVISION
PRATT & WHITNEY AIRCRAFT CORPORATION OF MISSOURI
SIKORSKY AIRCRAFT DIVISION
UNITED AIR LINES TRANSPORT CORPORATION
UNITED STATES AVIATION UNDERWRITERS, INC.
UNITED STATES RUBBER COMPANY
DOMINION RUBBER COMPANY, LTD.
UNIVERSAL MOULDED PRODUCTS CORPORATION
THE VARIETY AIRCRAFT CORPORATION
VICKERS, INC.
VICTOR ADDING MACHINE COMPANY
VIDAL RESEARCH CORPORATION
THE WACO AIRCRAFT COMPANY
WARNER AIRCRAFT CORPORATION
THE WEATHERHEAD COMPANY
WESTERN AIRLINES, INC.
WESTINGHOUSE ELECTRIC & MANUFACTURING COMPANY
WESTON ELECTRICAL INSTRUMENT CORPORATION
WYMAN-GORDON COMPANY
YOUNG RADIATOR COMPANY

JOURNAL OF THE AERONAUTICAL SCIENCES

VOLUME 12 APRIL, 1945 NUMBER 2

Compressible Flows in Aeronautics

The Eighth Wright Brothers Lecture*

JOHN STACK†

National Advisory Committee for Aeronautics

Introduction

FORTY-ONE YEARS AGO the Wright Brothers performed the first flights by man in a heavier-than-air machine. Their success in achieving man's oldest aspiration inaugurated an epoch in civilization. Like the few truly great achievements, it was but little regarded at the time; yet since that day, only 41 years ago, the work of the Wright Brothers has produced most revolutionary effects. Clearly, the world was not prepared for this event and, had it not been for the sound engineering basis upon which the Wright Brothers had erected their achievement, it is indeed likely that the developments that have followed would have been much slower in coming. Not only did the Wright Brothers show us how to fly but they also showed us the methods through which flight by man has been developed and expanded; for it has been by their methods, the careful and thorough laboratory investigations establishing the basic principles and then the application to flight, that the aircraft of today have come to span continents and oceans overnight.

In the development of the science and industry founded on their achievement serious problems have been encountered, but we who followed have not had to have their courage and conviction for they had shown us in their flights of 41 years ago that all these problems have a solution. Hence, it is only in retrospect that we can appraise the magnitude of their achievement and the appraisal, as we all know, has required a steady upward revision with each difficulty we, the followers, have overcome.

It is indeed fitting, therefore, that we should commemorate this event, and it is most appropriate that the Institute of the Aeronautical Sciences has established as the form of this commemoration that we, the followers, should annually, on this occasion, take stock of our efforts and with our minds toward the future face the problems ahead, taking courage and conviction from the achievements of the Wright Brothers.

In accepting the invitation of the Committee of the Wright Brothers Lecture, I am deeply grateful for the opportunity to honor the efforts and the achievements of the Wright Brothers. I am cognizant of the responsibility assigned me as well as appreciative of the honor conferred. It is with the utmost concern that I have proceeded to execute this responsibility, not only because of the occasion but also because of the high standards

* Presented before the Institute of the Aeronautical Sciences in the U.S. Chamber of Commerce Auditorium, Washington, D.C., December 17, 1944.

† Chief, Compressibility Research Division, Langley Memorial Aeronautical Laboratory.

set by my predecessors and because of the duty to present properly the work of my colleagues whose contributions, even in such few parts of the research to be discussed as is my own, have been of inestimable value.

The subject of the Lecture "Compressible Flows in Aeronautics" is perhaps most appropriate to the occasion for we have in the years past rather well exploited flight possibilities in the lower speed regions wherein air may be treated as an incompressible fluid. We are now entering a new phase of flight into which our accumulated aerodynamic experience cannot be extrapolated. For this reason some of us have been all too ready to regard the phenomena encountered as wholly new and, as a consequence, have lost sight of applicable knowledge only a few years old. It is well, therefore, that we pause to consider the position of aerodynamics in the general aero-thermo-hydrodynamic field and to review briefly some of the earlier work.

Historical

The classic aerodynamic theory assumes a frictionless, continuous medium. Potential energy and kinetic energy within the medium are assumed to be freely convertible, one type to the other, without loss of energy to vorticity or heat. The process assumed in the theory is therefore a special case of thermodynamics and actually the simplest of all thermodynamic processes. It is described by a single vertical line on the temperature-entropy diagram. Moreover, the great body of the classic theory is even further simplified by the assumption of constant density or, in other words, the fluid is assumed incompressible. These assumptions are, of course, in disagreement with the actual physical nature of air and have, as a consequence, been the cause of extensive investigation in special laboratory facilities. Compressibility phenomena and the manner in which they modify the flows described by the theory have come of great concern to aeronautical engineers only recently but they have been under investigation for a long period in anticipation of the coming needs. Ballistic engineers have, of course, been familiar with certain phases of the compressibility phenomena for a long time but, as their efforts have been largely in the supersonic velocity region, practically none of this work is yet of value to the aeronautical engineer. Some work in the study of flow through nozzles by Prandtl and others in the essentially pre-aeronautical period and the work of Hugoniot on compression shocks near the end of the last century have been of great importance. Work of direct aeronautical interest, however, commenced about 25 years ago. Rayleigh,[1] Bryan,[2] and Prandtl[3] appear to have been among the first to conceive of the compressible flow field as a distorted incompressible flow field. Prandtl is reported in N.A.C.A. Miscellaneous Paper No. 19 as stating that the compressible flow field about an airfoil is similar to the incompressible flow field for a thicker airfoil. This concept is, of course, a physical representation of all of the theoretic work since. Important as this concept is, it does not have any bearing on flows above the critical Mach Number and is applicable only when the speeds everywhere in the flow field are less than the speed of sound. When the speed of sound is first attained in a flow field, a change to a new type of flow occurs and no adequate theoretic basis is yet available which describes this flow. The problem is essentially an experimental problem, one of determining what forces are encountered and what happens in the flow to produce the changes found, in order to provide a basis for the establishment of a theory. The first significant effort in this field related directly to aeronautics appears to have been the work done by Caldwell and Fales[4] at McCook Field, reported in 1920. Unfortunately, the air speeds attainable in this investigation of airfoils were limited to approximately 450 m.p.h. so that much of the significant compressibility phenomena could not be found. Nevertheless, important compressibility effects on the maximum lift coefficient were found at rather low speeds. The importance of the work and its implications were realized as evidenced by the further researches[5, 6, 7] instituted by the N.A.C.A. in 1922 and reported by Briggs, Dryden, and Hull in 1925, 1927, and 1929. The results obtained from this work showed that a large drag rise and a lift loss occurred at high speeds and that the Mach Number at which these aerodynamic characteristics changed is a function of both lift and thickness. The magnitude of the changes was alarming, but the speeds at which they occurred were so far beyond the range of any speeds then contemplated that the work did not attract the attention it so well deserved, except among the few propeller designers who were then becoming cognizant of tip-speed limitations and a few foresighted aeronautical scientists.

At about the same time the latter phases of this work were being performed, the N.A.C.A. had under active investigation at the Langley Memorial Aeronautical Laboratory certain types of thrust augmentors for jet propulsion which were reported a few years later by Jacobs and Shoemaker.[8] In reviewing these results in 1927, Dr. George W. Lewis, N.A.C.A. Director of Research, who with great foresight actively sponsored this early research at high Mach Numbers, saw the possibility of what was then considered to be a large high-speed wind tunnel using the waste air of the variable-density wind tunnel as the motive power in an induction-jet arrangement. Experiments were immediately started with a 1-in. throat high-speed wind tunnel, and early in 1928 this work was finished with the construction of the old 12-in. throat high-speed wind tunnel which was driven by a compressed air jet, utilizing the waste air of the variable-density wind tunnel.

Numerous experiments were conducted in this tunnel which, as originally constructed, was an open-throat tunnel. Violent flow disturbances were encountered at

high speeds with the open-throat tunnel, so that for certain speeds observations were impossible. These disturbances appear to have been similar to those later encountered by Ferri in Italy.[9] The disturbances existed to some degree over the entire speed range but became particularly violent when what we now know as the critical speed was reached. In order to eliminate these disturbances so that observations could be made at and just above the critical speed, this tunnel was finally converted to a closed-throat type and late in 1928 and through 1929 pressure-distribution studies of airfoils were made in the closed-throat arrangement. The characteristic change of shape of the pressure diagram which occurs with the onset of compression shock was found. These results and the earlier results of Briggs and Dryden were in qualitative agreement as regards the changes in the forces and moments on airfoils but large quantitative disagreements occurred. It was considered that the quantitative disagreements were due to the differences in the test arrangements, as the earlier results were obtained on 1-in. chord models spanning a 2-in. jet discharging directly into the atmosphere (except for the first experiments of the series which were made with 3-in. chord airfoils spanning a 12-in. jet discharging directly into the atmosphere), whereas the experiments of 1928 and 1929 were made with 3-in. chord airfoils in a 12-in. closed throat. All of the results were difficult to explain as existing theory did not admit of the possibility of such pressure distributions as were found. A part of these results was discussed with Prof. G. I. Taylor on his visit to the Langley Memorial Aeronautical Laboratory in 1929. Professor Taylor had just finished his experiments with the electrical analogy to compressible flow[10] and these experiments did not admit of the kind of phenomena being found. It was, of course, appreciated that the existing theories should fail but the flow differences found as the local velocities over the airfoils exceeded the local speed of sound were so great that question as to the validity of the experiments arose, particularly because of the possibility of large air-stream boundary effects. Decision was then made to improve the experimental apparatus, eliminating certain known difficulties, and to check the results before publication of any of the data. In retrospect, most of the phenomena as originally found now appear reasonable and, to a certain extent, logical. While we had come to the point of discarding the usual theory as having any bearing on the flows being found, we placed too great significance on the electrical analogy results which were at first thought to give indication of the impossibility of such flows as were being found. It is easily recognized today that the electrical analogy results are exactly the same as the theory which we had come to the point of discarding, for the electrical analogy is essentially a computing machine for potential flows.

The decision to improve the facilities for investigating the high-speed flows proved to be satisfactory, however, as the need for such information was not acute at the time and data much more consistent and more nearly of direct applicability were obtained well in advance of any real need in aeronautical engineering. During this period of experimentation, the open-throat tunnel was again investigated because some of the earlier experiments indicated that higher speeds could be obtained with this arrangement than with the closed-throat tunnel. Practically all the objectionable unsteadiness of the flow was eliminated by shortening the distance between the entrance cone and the exit cone, and by increasing the ratio of the exit cone area to the entrance cone area. As a consequence of these modifications, the resulting open-throat tunnel was quite unconventional as compared to those found satisfactory for low speeds. Three significant difficulties remained, however, and these were the presence of some disturbances at supercritical speeds which made observations difficult and at times impossible with some airfoils, a large stream boundary effect which was evidenced by extremely low lift-curve slopes, and pronounced effects on the stream by the presence of objects unsymmetrically placed around the jet even when far outside the air-stream boundary. The latter effect was similar to that produced by air-stream misalignment. As a balance in which to mount the airfoils for test was, of course, vitally necessary, the possibility of unsymmetric shielding was present and, in fact, did occur with the balance used which had been previously constructed. To modify the balance so as to provide symmetric shielding around the jet was, of course, possible but the tunnel would then approach a closed throat. Because of this and the other two objections, it was finally determined to adopt the closed-throat type. The N.A.C.A. 11-in. high-speed wind tunnel, Fig. 1, evolved from this work. Airfoil experiments were continued in this tunnel and some of the first work, as well as a description of the tunnel, was presented in 1933.[11] While this work was going on, tests of full-scale propellers at high tip speeds were conducted in the N.A.C.A. propeller-research tunnel.[12] Thus, it was possible to effect a comparison between calculated propeller characteristics based on airfoil section data obtained in the high-speed wind tunnel and actual measured characteristics of full-scale propellers working at supercritical tip speeds.[11] Through the low-speed range and up to propeller tip Mach Numbers of 0.75, surprisingly close agreement was found. The adverse effects on propeller efficiency at the high tip speeds was shown and in approximately the same degree in the calculations based on the high-speed wind-tunnel airfoil characteristics as in the full-scale propeller results. There was, however, a discrepancy in the Mach Number at which the adverse effects first appeared, the airfoil data indicating earlier compressibility effects. Two causes for the difference were recognized at the time, a constriction effect in the high-speed wind tunnel due to the reduction of free-stream cross-sectional area by the model and scale effects be-

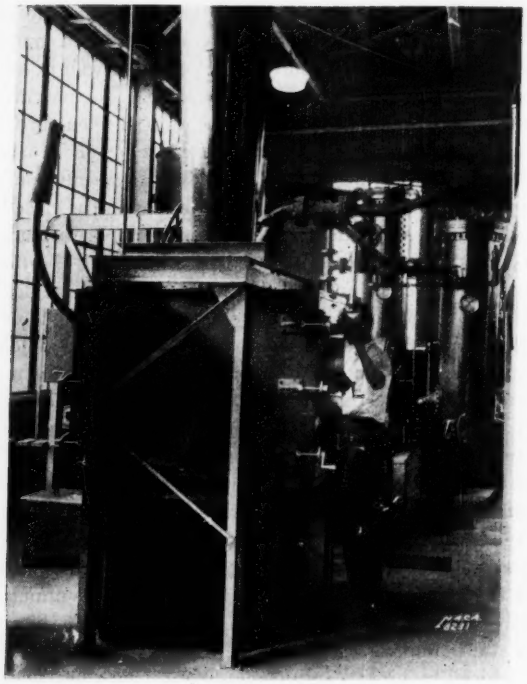

FIG 1a. The N.A.C.A. 11-in. high-speed wind tunnel.

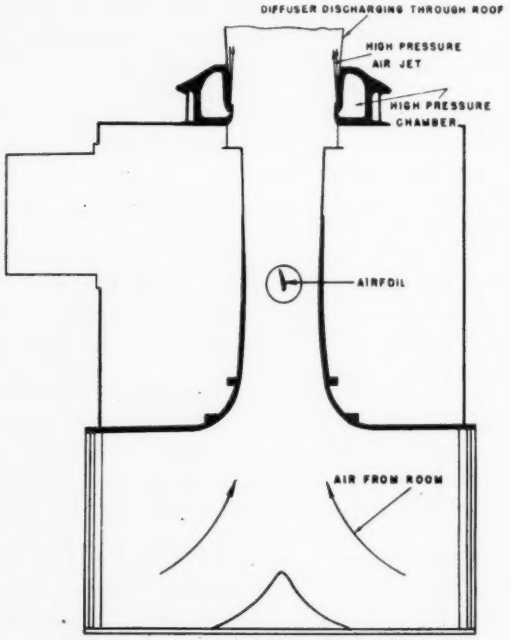

FIG. 1b. Schematic diagram of the 11-in. high-speed wind tunnel.

cause of the lower Reynolds Number of the airfoil data. Lending credence to the latter cause were some earlier British model propeller tests[13] which showed earlier compressibility losses than the full-scale tests. Later work seems to have eliminated the Reynolds Number as a large contributing factor to the discrepancy and it appears now that the constriction effect and the three-dimensional flow at the tip account for the differences found. All of these studies, had, however, validated in large measure the high-speed wind-tunnel results we had been obtaining and we proceeded with the further research with some degree of confidence. Throughout this whole period, the first experiments were continuously studied and comparison with the nozzle phenomena found by Prandtl and others had given considerable credence to the results. It was during this period that potential flow considerations were disregarded insofar as supercritical flows were concerned. These studies taken with the other experiments[6, 7, 11] led to the conclusion that some improvements in airfoil shapes were possible. Accordingly, experiments were undertaken which led to the introduction of shapes having the maximum ordinate moved to the rear of the conventional location. Not only were important gains made through delay of the adverse compressibility effects but reduced drag over the whole speed range was found.[14] The better airfoils of the family were known as the NACA 0000-34 and 0000-64 series. These shapes seem not to have been accepted here but they were used abroad, as evidenced by the propeller-blade sections found on Messerschmitt airplanes shot down in England in 1940. The British also seem to have made some use of these results.

To those few of us then associated with the work, it was strikingly apparent that something more detailed than force measurements or even pressure-distribution measurements was necessary if we were to understand the flow phenomena. Further, as we had in the airfoil experiments[14] temporarily exhausted our intuition as regards methods for improving aerodynamic shapes, necessity as well as curiosity turned our attention to a more fundamental approach. Accordingly, a schlieren apparatus was set up early in 1933 to observe the flow. This apparatus, though extremely crude, showed surprisingly new phenomena as the density variations in supercritical flows for airfoils and cylinders were observed for the first time. These flows, which we shall review later in the Lecture, left us, figuratively speaking, in the same state of mind as in 1928 and 1929. Simultaneous recording of pressure distribution and schlieren photographs and later wake surveys was undertaken. The latter parts of this work were performed on an NACA 4412 airfoil in the N.A.C.A. 24-in. high-speed tunnel, Fig. 2, which had been erected and placed in operation in 1934. A part of this work was reported later[15] and a part was presented at the Volta Congress in Rome in 1935.[16] The major portion of the work was not reported until 1938.[17]

The long delay between the experiments and the research report was occasioned in part by the inspiration given by the experiments which led immediately to a new approach to the problem of developing better shapes to permit higher aircraft speeds and our efforts

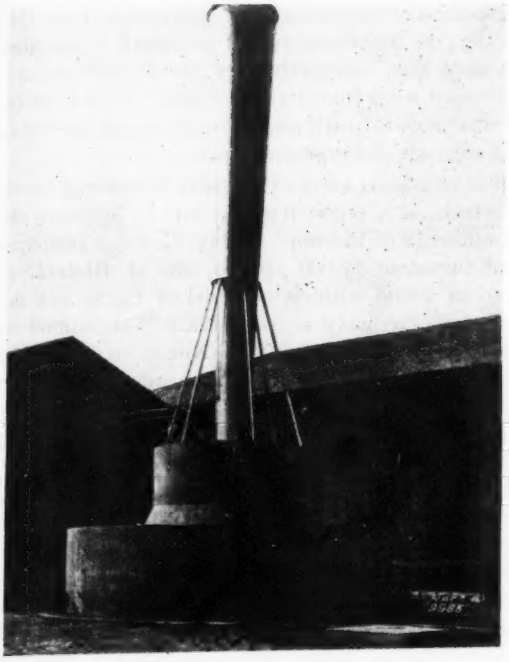

FIG. 2a. The N.A.C.A. 24-in. high-speed wind tunnel.

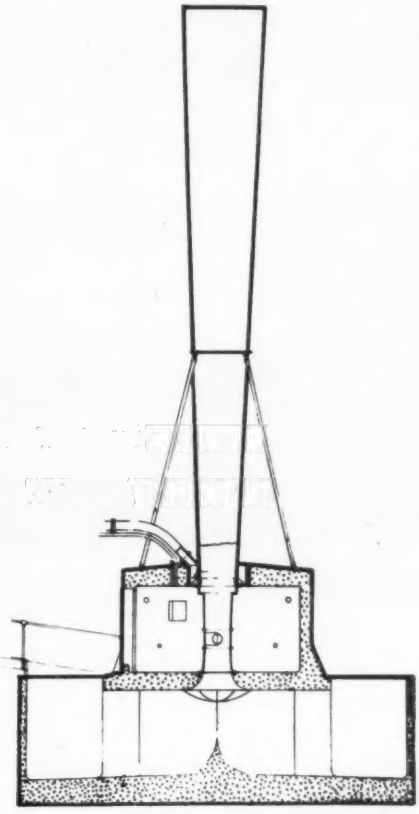

FIG. 2b. Schematic diagram of the 24-in. high-speed wind tunnel.

were occupied accordingly. Much of this latter effort has had a pronounced influence on aeronautical engineering for war.

Throughout this period, aircraft were attaining ever increasing speeds. With characteristic foresight, Dr. Lewis saw the forthcoming need for more intensive research and initiated the construction of the N.A.C.A. 8-ft. high-speed tunnel, Fig. 3, which was placed in operation early in 1936. This wind tunnel was a distinct advance over any previously constructed aeronautical laboratory facilities. It combines high speed, low turbulence,[18] and reasonably high Reynolds Number. This tunnel, based in part on experience with the smaller equipment, operated satisfactorily and with excellent success right from the beginning. Taken with the two smaller tunnels that preceded it, these facilities have had a most profound effect on American aeronautical development. Applications of the research from these tunnels and other laboratory facilities have produced such marked effects on aircraft development that even larger and faster tunnels have been necessary. The later equipment, the N.A.C.A. 16-ft. high-speed wind tunnels at Ames Aeronautical Laboratory and at Langley Memorial Aeronautical Laboratory, illustrated by Fig. 4, has proved equally successful.

While we in this country were conducting this work, other nations, notably Germany, England, and, somewhat later, Italy, were also active. With the inauguration of the Kaiser Wilhelm Institute for Flow Research in 1925, the Germans under the direction of Prandtl instituted the construction of a high-speed wind tunnel.[19] This tunnel, however, was small, 2.36-

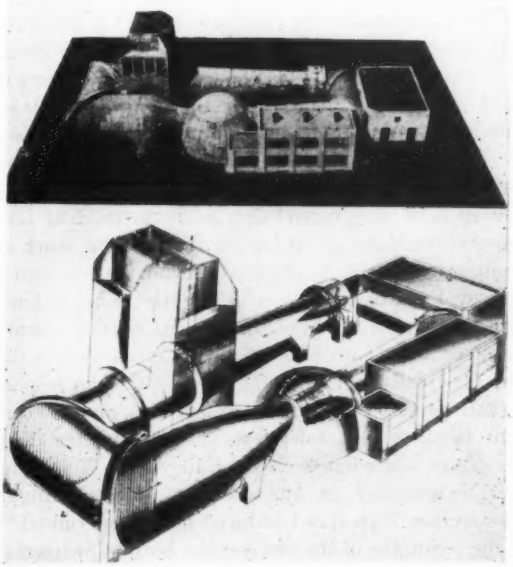

FIG. 3a (*top*). The 8-ft. high-speed wind tunnel.
FIG. 3b (*bottom*). Schematic diagram of the 8-ft. high-speed wind tunnel.

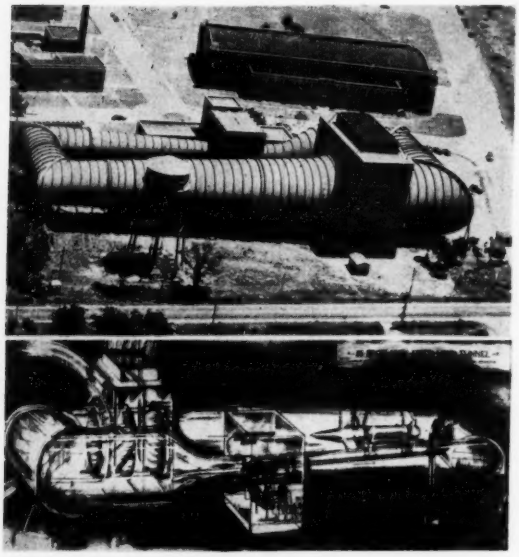

FIG. 4a (*top*). The N.A.C.A. 16-ft. high-speed wind tunnel at the Langley Memorial Aeronautical Laboratory. FIG. 4b (*bottom*). Schematic diagram of the 16-ft. high-speed wind tunnel.

by 2.36-in. throat, and its operating time was short, 10 sec. The air stream was provided by means of an evacuated tank of 353.1 cu.ft. to which the discharge end of the tunnel was attached. Atmospheric air flowed through the tunnel proper to the evacuated tank. The tunnel appears to have been made ready for operation in 1928.[20] Much of the work known to us which was performed in this wind tunnel was in the supersonic flow régime, hence its influence is yet to be felt in aeronautical engineering. At about this same time, the late Sir Thomas Stanton[21] had erected at the National Physical Laboratory in England a 3-in. diameter closed-throat wind tunnel capable of speeds up to 1.7 times the speed of sound. Some few investigations of airfoils and cylinders were made in this equipment but the apparatus appears not to have been extensively used. Stanton later inaugurated the development of a high-speed induced-flow wind tunnel similar to the original 12-in. tunnel of the N.A.C.A. at Langley Field. This work was prompted by Prof. G. I. Taylor who, on his visit to Langley Field in 1929, was sufficiently impressed with our earliest effort to urge the construction of a similar tunnel on his return to England. Certain design data were provided the British by the N.A.C.A. in response to their request in 1930. Stanton's work on this equipment began with model tests. Following his death, this phase was carried on by Bailey and Wood[22] and later culminated in the erection of a rectangular cross-section high-speed induced-flow wind tunnel.[23,24] At the beginning of the last decade, both in Switzerland and in Italy, research at high air speeds was initiated. At Zurich plans for a high-speed wind tunnel driven by an axial-flow compressor were announced in 1930.[25] These plans culminated in the construction of the $15^3/_4$- by $15^3/_4$-in. supersonic tunnel in Zurich.[26] At about this same time, or shortly after, the Italians erected a high-speed wind tunnel at Guidonia.[9] This wind tunnel was provided with arrangements to permit tests at both subsonic and supersonic speeds.

It is, of course, known that there has been a tremendous increase in research in this field in Germany since the outbreak of the war. A 9-ft. diameter high-speed wind tunnel of 17,000 hp., capable of attaining the speed of sound without a model in place, has been erected in Germany at the DVL. This tunnel was placed in operation in 1940. Numerous small high-speed wind tunnels have also been constructed by several of the German aircraft manufacturers. It is indeed likely that the Germans, whose principal efforts a few years ago seem to have been directed at wholly supersonic flows, have, since the outbreak of the war, changed emphasis in a large degree to research in the transsonic region. In fact, until recently, most of the experimental research in other nations on compressibility phenomena was directed toward the wholly supersonic field, except for some work in Britain and the work at Guidonia which started so auspiciously but has since been interrupted by destruction of the laboratory at Guidonia and confiscation of much of its equipment by the Germans. Most of the American effort, however, has been directed from the beginning to the problem of transsonic flow. This was not accidental but was the result of a deliberated decision after consideration of, first, the fact that no adequate theory of mixed flow existed and still is lacking, whereas good theoretic basis existed for the wholly supersonic flow; second, the limited facilities and support that could be mustered for airflow research near the speed of sound for aeronautics 16 to 20 years ago and, finally, any flight at supersonic velocity required passage through the transsonic region. The necessity for supersonic research was not ignored, however, for in the planning of the N.A.C.A. 11-in. high-speed wind tunnel two throat arrangements were designed, one for subsonic studies and one for supersonic studies. This equipment was replaced in 1940 by a new type of tunnel using the same motive equipment, the N.A.C.A. 4- by 18-in. high-speed wind tunnel, Fig. 5, better suited to the conduct of experiments near sound speed. The work conducted in these facilities has disclosed virtually a whole new research field in aerodynamics and in proceeding to the discussion of this field it is well to consider the elements of the theory in relation to the phenomena to be expected.

SYMBOLS •

x	= distance along axis parallel to undisturbed stream
y	= distance along axis normal to undisturbed stream
u	= velocity along x-axis
v	= velocity along y-axis
V	= stream velocity
a	= rate of pressure propagation (speed of sound)

M = Mach Number, $M = V/a$
ρ = mass density
p = absolute static pressure
p_T = absolute total pressure
P = pressure coefficient $P = (p_l - p_0)/(\rho_0 V_0^2/2)$
q = dynamic pressure $q = \rho V^2/2$
Δp_T = total pressure loss in wake
$C_{m_{c/4}}$ = pitching-moment coefficient about quarter-chord axis
$C_{m_{c.g.}}$ = pitching-moment coefficient about center-of-gravity axis

Subscripts

0 = stream conditions
1 = conditions in front of shock
2 = conditions behind shock
cr = critical
l = local

Theoretic Considerations

In an incompressible fluid, the influence of an applied change in pressure must be felt in all parts of the mass of fluid instantaneously. In a compressible fluid, however, a similar change in pressure produces, first, a distortion surrounding the origin of the applied pressure change. Equilibrium within the body of fluid is thus locally disturbed and is re-established as the locally disturbed region extends its influence to adjacent regions progressively through the whole body of fluid. Thus, the influence of a pressure change in a compressible fluid is transmitted in a finite time interval as distinguished from instantaneous transmission in an incompressible fluid. It is also apparent that after equilibrium is established in the compressible fluid the mass of the fluid occupies a volume different from that initially occupied; hence its density is changed. In the simple case, a compressible fluid is elastic if, in the absence of heat conduction or the conversion of mechanical energy to heat, it returns to its original volume upon restoration of the pressure to its original value. The resultant forces experienced on a body moving in such a fluid are therefore determined by the elastic forces as well as the mass forces, whereas in the incompressible fluid the resultant forces are determined by the mass forces alone. Thus, an additional variable is introduced, the ratio of the mass forces to the elastic forces. The square root of this ratio is well known as the Mach Number, the ratio of the speed of flow to the speed of pressure propagation. The Mach Number is, then, a similarity criterion for compressible flows in the same sense that the Reynolds Number is a similarity criterion for flows involving viscosity.

The elastic forces, the rate of pressure propagation, and the change of density with pressure are a function of the density-pressure relation. It is important, therefore, that this relation correspond to the principal characteristics of the air flows encountered. The relation ordinarily employed, $p = C\rho^\gamma$—where p is the pressure; ρ, the density; γ, the specific heat ratio; and C, a constant—follows the adiabatic law. It is assumed, thus, that the flows occur without the addition or subtraction of heat from an external source, without heat conduc-

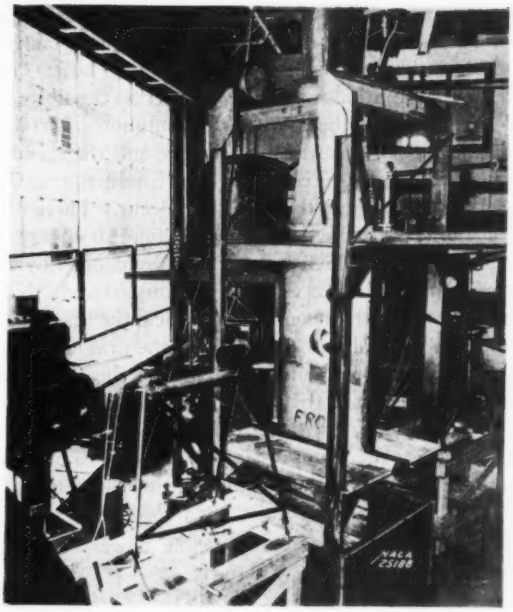

Fig. 5a. The N.A.C.A. 4- by 18-in. high-speed wind tunnel.

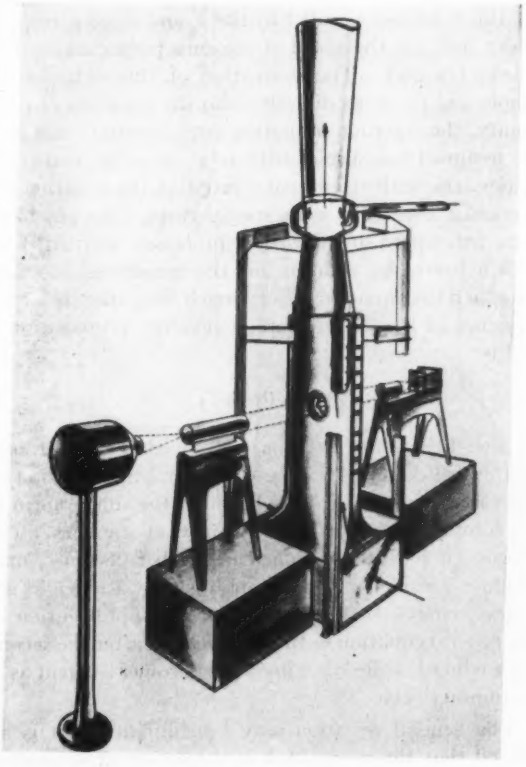

Fig. 5b. Schematic diagram of the 4- by 18-in. high-speed wind tunnel.

tion as between elements of the fluid, and that the process is reversible; that is to say, that there is no conversion of mechanical energy to vorticity or heat. The first two assumptions are quite in order as the flows occur in the atmosphere without communication with bodies of higher or lower temperature and the speed of flow is generally so great that heat conduction as between elements of the fluid does not occur. There does occur, however, conversion of mechanical energy to vorticity or heat which is, of course, evidenced by the presence of drag. Hence, we are led immediately to the conclusion that the accuracy to which the theory describes the general flow decreases as the drag increases. Thus, with the occurrence of high drag the theory becomes invalid. It is with these considerations in mind that we should examine the theory to determine characteristics of the compressible flow and to indicate where possible the limitations of the theoretic relations.

For two-dimensional compressible flows the fundamental equation in the x, y plane is

$$\frac{\partial u}{\partial x}\left[1-\left(\frac{u}{a}\right)^2\right]+\frac{\partial v}{\partial y}\left[1-\left(\frac{v}{a}\right)^2\right]-\frac{uv}{a^2}\left[\frac{\partial u}{\partial y}+\frac{\partial v}{\partial x}\right]=0 \quad (1)$$

where x and y are the abscissa and ordinate, u and v are the velocities parallel to the x and y axes, respectively, and a is the speed of pressure propagation—the speed of sound. The derivation of this equation is simple and proceeds directly from the equation of continuity, the equation of motion after Newton's law and the assumed pressure-density relation. The real difficulties arise with attempted solution of the equation for particular flows. In some special cases, solutions have been attempted by iteration processes starting first with a particular solution for the incompressible flow for which the equation is very much simplified as a consequence of the infinite rate of pressure propagation a and is

$$(\partial u/\partial x) + (\partial v/\partial y) = 0 \quad (2)$$

In a slightly different form this equation is recognized as the well-known Laplace equation. Substitution of the values obtained from solution of the simple form in the complete equation leads to a new set of values. The process, if repeated a sufficient number of times, may produce a sufficiently accurate answer. Rayleigh[1] appears to have been the first to attempt solution of the general equation in this manner but after the second approximation the labor involved becomes so great as to be impracticable.

The general equation may be simplified if it is assumed that the normal velocity component is small in relation to the velocity of sound a and the horizontal velocity u and that u differs from the stream speed by only a small amount. These assumptions are equivalent to those of the thin airfoil theory. The simplified form of the general equation is then

$$(\partial u/\partial x)\,(1 - M^2) + (\partial v/\partial y) = 0 \quad (3)$$

where M is the Mach Number.

The physical character of subcritical, subsonic compressible flows as compared to incompressible flows can be deduced directly from this equation. Where components of velocity normal to the direction of motion exist, as must be the case for finite thickness or lift, these components vary with distance away from the body. The variation of the normal component of velocity $\partial v/\partial y$ is by Eq. (3) a function of both $\partial u/\partial x$ and M and decreases in value with increase of M. In an incompressible flow field, the variation of the normal component of velocity is uninfluenced by M for M is always zero as a consequence of the infinite rate of pressure propagation. Hence, any normal component of velocity at points distant from the body exists in greater magnitude when the flow is compressible. A principal effect of compressibility is, therefore, exhibited in the increasing intensity of the disturbances at points in the flow field with increase of Mach Number. This effect leads directly to the conclusion that the total force experienced by a body at a given attitude in the air stream—for example, the lift of an airfoil—increases at a rate greater than the square of the speed. Ackeret[27] and Glauert[28] have shown that this increase is proportional to $1/\sqrt{1 - M^2}$. When $M = 1.0$, the value of $\partial v/\partial y$, by Eq. (3), is zero. Thus, any normal component of velocity existing at the surface of a body exists through the whole flow field to infinity. This gives rise to the conclusion that infinite forces occur for the speed $M = 1.0$.

Proceeding from Eq. (3) Prandtl[29] has shown that the compressible flow about a body is similar to the incompressible flow about a thicker body. Thus, if we assume a given disturbance v occurring at a common point out from a body in compressible and incompressible flow fields, it is necessary because of smaller decay of normal velocity $\partial v/\partial y$ in the compressible flow field that the normal velocity v at the surface of the body in the compressible flow be greater than the corresponding normal velocity at the body in an incompressible flow. A greater normal velocity at the surface implies directly a greater effective slope of the surface. Thus, for a given thickness of body, the length is effectively shorter in the compressible flow than in the incompressible flow; hence, the physical concept of the compressible flow for an airfoil or body being similar to the incompressible flow for the same body with its chord foreshortened. The shortening of the chord is approximately as the factor $\sqrt{1 - M^2}$.

The physical concept is illustrated by Fig. 6 where the solid lines represent the incompressible flow and the dotted lines the compressible flow. This physical concept is, of course, an approximation and is applicable to points in the flow field at a distance from the body. In the actual flow the body does not change shape but the streamlines do. This is illustrated by Fig. 7. The streamlines in the compressible flow, shown dotted,

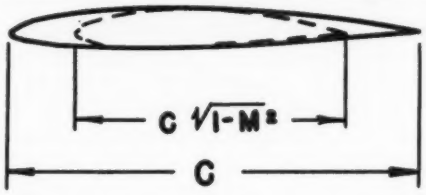

FIG. 6. Simulation of effect of compressibility.

FIG. 7. Streamlines in incompressible and compressible flows.

have greater curvature and correspondingly affect the pressures and forces experienced by the body.

It was noted in the first examination of the fundamental flow equation that infinite forces were indicated when the Mach Number attained a value of 1.0. As infinite force cannot be presumed to exist it is well to examine again the physical basis for the flow relations. In the derivation of these relations it was assumed that the motion was steady, that the forces were balanced by change of momentum, and that the pressure-density relation was given by the thermodynamically reversible relation $p = C\rho^{\gamma}$. Thermodynamically stated, the process is a constant entropy process. As the entropy is the sole remaining term considered invariable in the theoretic relations, the result indicating infinite forces can be presumed an error and that, actually, change of entropy occurs. A decrease of entropy is precluded by the second law of thermodynamics and thus the sole possible change is an increase of entropy. In the absence of an external energy source, the increase of entropy can occur only at the expense of the mechanical energy available at any point in the flow. Thus, it can be presumed that the indication of infinite force is in error and that a different type of flow, probably with discontinuities, occurs which involves the conversion of mechanical energy of the flow to heat and, hence, involves losses. Such losses would be evidenced by drag rise.

FLOWS AT SUPERCRITICAL MACH NUMBERS

A consequence of the finite rate-of-pressure propagation is that discontinuities can exist. Small disturbances originating at a point in the field are propagated upstream and downstream at the normal velocity of sound. If the velocity of the stream is equal to the local velocity of sound, the disturbance moving upstream becomes stationary. As related to an actual flow over an airfoil, disturbances originating downstream in a subsonic region will be propagated forward until they reach a station in the flow field where the local velocity of sound occurs. The disturbances would then be expected to be additive at this point producing a stationary front involving rapid change of pressure. Any flow changes occurring downstream of the stationary front would be expected to have no influence on the flow ahead of the front.

This phenomenon is actually found and is illustrated by Fig. 8. The flow photograph shown in this figure was made by a schlieren method in the N.A.C.A. 4- by 18-in. rectangular high-speed wind tunnel. The model is a $1^1/_2$-in. chord NACA 0012 airfoil from which the rear 25 per cent has been cut off, leaving the tail blunt. The bulge shown in the photograph is not in the air stream. This bulge is the shadow cast by the trunnions in the glass plates which form the side walls of the tunnel and support the model. The stream Mach Number is approximately 0.7 and was chosen to correspond to the attainment of the local velocity of sound at one point on the airfoil surface at approximately the maximum thickness position. Disturbances are precipitated at the rear corners of the airfoil by alternating partial closure and separation of the flow at each corner. It is apparent from the alternate spacing of the disturbances on opposite sides of the airfoil that they are precipitated alternately at each of the back corners. Over the rear portion of the airfoil the disturbances join the airfoil surfaces approximately normal to the surface. As the successive disturbances move forward into the region of local sonic velocity on the airfoil surface their shapes change. There is a reversal of curvature close to the surface of the airfoil. In regions close to the surface of the airfoil no disturbances move ahead of the region of local velocity of sound and, hence, disturbances occurring downstream can have no influence on the flow over the forward portion of the airfoil. In regions outward from the airfoil surface in a direction normal to the chord the local velocities decrease and the dis-

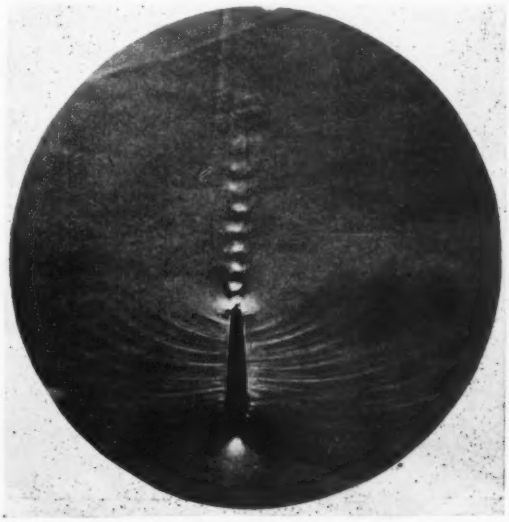

$M = 0.704$

FIG. 8. Schlieren photographs of NACA 0012 airfoil with tail cut off, illustrating propagation of disturbances. N.A.C.A. rectangular high-speed wind tunnel.

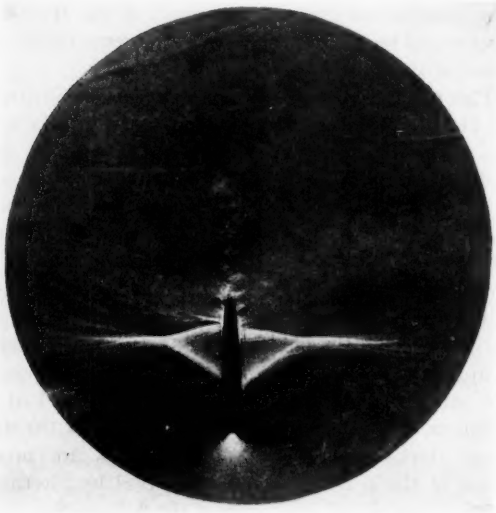

$M = 0.833$

FIG. 9. Schlieren photographs of NACA 0012 airfoil with tail cut off, illustrating propagation of disturbances. N.A.C.A. rectangular high-speed wind tunnel.

turbances can move forward in these outer regions. This is shown by the upstream slope of the wave fronts at the surface of the airfoil near the region of maximum thickness and by the disturbances ahead of the airfoil at a distance out from the chord extended.

With increase of speed the stationary disturbance is swept back on the airfoil as shown by Fig. 9. The stationary disturbance becomes more intense and extends further outward into the stream from the airfoil. The disturbances originating downstream do not progress ahead of the stationary front except in regions far out from the airfoil surface. These downstream disturbances, hence, have no effect on the flow over the forward portion of the airfoil. Great consequences are apparent. For example, a deflected aileron normally obtains its effectiveness through changing the pressures acting over the whole airfoil surface. At these speeds, deflection of the aileron can have no effect on the flow over the forward portion of the airfoil. Its effectiveness may therefore be markedly reduced.

The general flow for an airfoil as the speed is increased is shown in Figs. 10 and 11. At the higher speeds stationary shocks appear in the flow, first as small disturbances and then as marked fronts when the speed is further increased. Ahead of the sharp front is a lesser disturbance starting at the airfoil surface and inclined downstream. Pronounced separation of the flow is likewise shown. The separation phenomena are likely analogous to that which occurs at low speeds. The pressure behind the shock is much greater than that ahead of the shock. This high pressure acting on the reduced energy air of the boundary layer causes thickening of the boundary layer and finally arrests the downstream velocity component of the inner layers of the boundary layer and forces the air in the inner layers forward, producing actual reversal and the separation of the flow shown by the dark line issuing from the airfoil surface approximately parallel to, or inclined outward slightly from, the airfoil chord direction. This dark line which bounds the outer limit of the separation region at the base of, and immediately ahead of, the

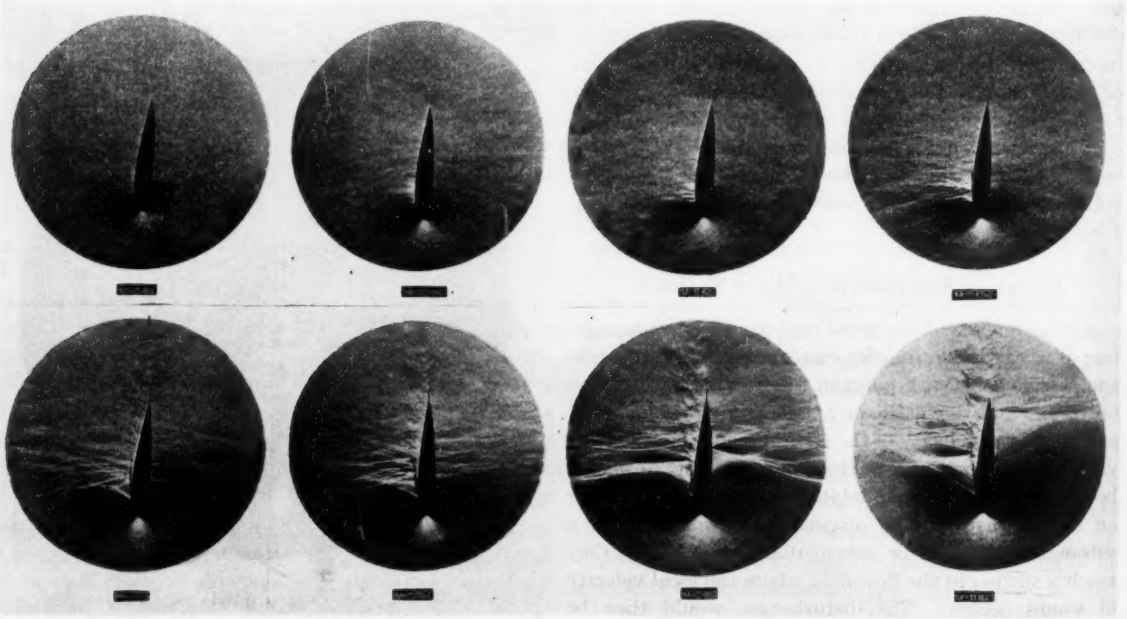

FIG. 10. Schlieren photographs of flow. NACA 23015 airfoil. Rectangular high-speed wind tunnel. Airfoil chord, 2 in. Angle of attack, 3°.

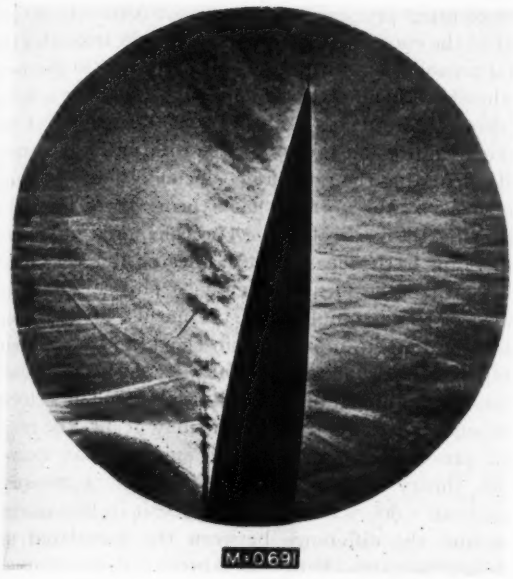

FIG. 11. Schlieren photograph of separated flow for rear portion of NACA 23015 airfoil. N.A.C.A. rectangular high-speed wind tunnel. Airfoil chord, 5 in. Angle of attack, 6°.

shock forms a boundary of the high-velocity flow outside the boundary layer. As this line is inclined outward from the airfoil it forms a contracting boundary for the outside flow which is supersonic. In accordance with well-known principles of supersonic flows the contracting boundary leads to compression in the outer flow which must occur along a Mach line. The inclined lesser disturbance ahead of the normal shock may be such a Mach line.

The airfoil chordwise pressure distribution over the upper surface as it changes over the speed range is illustrated by Fig. 12. For the lowest Mach Number the diagram is of the familiar form and is in close agreement with theoretic calculations for incompressible flow. With increase of speed to a Mach Number of 0.634, the pressure coefficients increase numerically. This increase is predicted by the theory when the effect of compressibility is included and is an evidence of the previously discussed spreading of the flow field. At this value of the air-stream Mach Number the maximum local velocity over the surface of the airfoil corresponding to the peak negative pressure coefficient is approximately equal to the speed of sound. The theory fails to give any solution above this speed. When the speed is further increased the shape of the diagram changes. The peak negative pressure moves to the rear and an abrupt change in the pressure-distribution curve appears. Correlation of these data with schlieren photographs shows that the abrupt change of pressure occurs at the shock. The shock is thus a severe adverse pressure gradient which, as previously discussed, separates the flow from the airfoil surface.

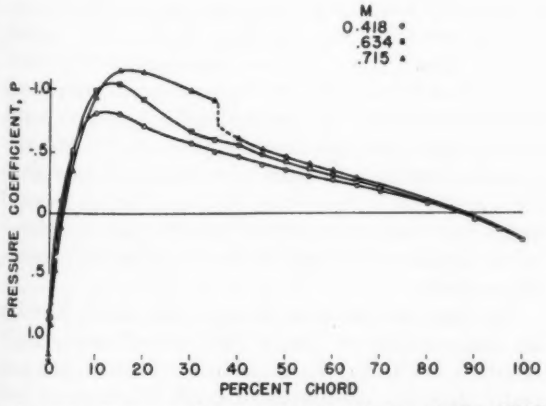

FIG. 12. Upper surface pressure distribution NACA 23015 airfoil, $\alpha = 0°$. Rectangular high-speed wind tunnel.

The existence of the two phenomena, shock and separation, suggests the examination of the relative effect of each with regard to the losses in the flow which appear as drag rise. These are indicated by Fig. 13 which presents the total-head loss across the wake of an NACA 0012 airfoil at a position two chord lengths behind the trailing edge for two Mach Numbers. Intense shock has not occurred at the lower Mach Number. The shape of the diagram is familiar. The maximum total-head loss in the wake is not very great and the wake is narrow. At the higher Mach Number intense shock has occurred and precipitated the flow separation shown in the photographs. The maximum total-head loss in the wake becomes large and the wake width has increased from a fraction of a chord length to practically five chord lengths. The shape of the wake loss diagram has changed. In addition to the reg'on of large loss at the center, which is usual at low speeds, regions of lesser total-head defect spread outward. The center region corresponds to the region of separated flow and the outer regions to the unseparated flow outside the turbulent wake but behind the shock. It is shown that a very large part of the loss is due to the separated flow. The direct shock loss is much smaller than the total loss, the maximum value being indicated by the more or less flat portions of the curve extending outward on either side from the central core. The large contribution of

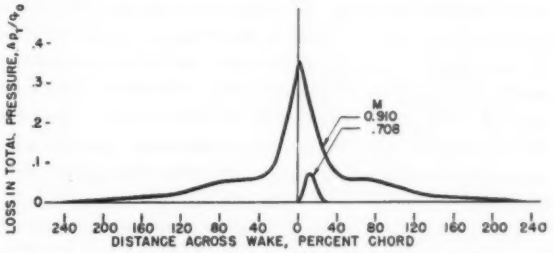

FIG. 13. Wake shape and total pressure defect as influenced by Mach Number. NACA 0012 airfoil, $\alpha = 0°$. N.A.C.A. rectangular high-speed wind tunnel.

the separated flow to the total losses suggests, of course, the application of boundary-layer control in much the same form as it has been applied at low speeds but with considerably increased difficulty because of the presence of shocks.

The increasing intensity of the wake and its spread have consequences in airplane design beyond the drag rise problem. Tail buffeting at high speed can and does occur. It is, of course, obvious that the spread of the turbulent wake region can envelop the horizontal tail. Hence, the vertical distance between the horizontal tail and the wing must increase. It cannot be supposed, however, that the buffeting can be entirely eliminated by simply moving the tail a distance sufficient to clear the turbulent wake region. The outer boundaries of this turbulent region form a boundary of the flow outside and, as the turbulent wake boundary is wavelike rather than straight and the wavelike contour changes with time as a result of nonuniformity in the shedding of the eddies rolled up in the separated region on the airfoil surface, the air immediately outside the wake probably oscillates in direction in correspondence with the wake boundary. These directional oscillations occurring as they do in a high-speed flow may tend to persist in accordance with the theoretic spreading of the flow field to fairly large distances. To insure absolute steadiness of the airflow into the tail may therefore require an impracticably large movement of the tail above the center of the wake. Hence, we seem to be faced with the problem of designing the tail to work in a somewhat oscillating airflow. Such design is, of course, far more critical than that heretofore encountered. Increase of tail weight may be required and more precise considerations will have to be given to the vibration problem.

The occurrence of large losses other than the direct shock loss was illustrated several years ago.[17] This same work illustrates another interesting phenomenon. Typical results from this earlier investigation are illustrated in Fig. 14. The curve on the left of the figure shows the pressure distribution over the upper surface of an NACA 4412 airfoil. The shock occurs in the region of rapid pressure change at approximately 80 per cent of the chord. The curve on the right indicates the total pressure loss in the wake at a station 20 per cent of the chord behind the trailing edge. Taking a value of the total-head loss outside of the deep part of the wake along the flat portion of the total-head loss curve and calculating the pressure coefficient change through the shock by the normal shock theory gives the value shown by the vertical line. The calculated value corresponding to the measured total-head loss is very much greater than the measured value. This might be ascribed to the assumptions of the normal shock theory which assume an infinitely thin shock and no velocity components parallel to the front. As the actual shocks cannot be presumed to be infinitely thin and as velocity components parallel to the front may occur, the measured pressure change could be smaller than normal shock theory shows. Because, however, a measured total-head value was taken as the basis in this calculation and the difference between the calculated and measured pressure changes is so great it does not appear that the discrepancy can be wholly accounted for by the simplifying assumptions of the normal shock theory. A possibility is that the pressures measured on the surface of the airfoil which are those occurring in the boundary layer may differ from those outside the boundary layer. It is recognized that this possibility is contrary to all experience obtained at lower speeds where the pressures occurring outside the boundary layer are transmitted through the boundary layer without change, but lending some support to this supposition are the schlieren photographs of Figs. 10 and 11. The schlieren method shows regions of sharp density change. The normal and inclined shocks are such regions and it is known that sharp pressure changes occur in these regions. The dark lines that are shown in these photographs issuing from the airfoil surface approximately parallel to or slightly inclined to the chord direction must be regions of sharp density change and hence there might be a pressure jump across this line. In regard to this possibility it must also be noted that the velocities in the inner layers of the boundary layer are considerably less than the local supersonic velocities occurring over the forward portion of the airfoil outside the boundary layer. The usual conception of the velocity gradient in the boundary layer requires that Mach Numbers less than 1.0 occur within the boundary layer. Hence, while the high pressures occurring on the rear portion of the airfoil cannot be transmitted forward in the general flow they may be transmitted forward within the boundary layer and thus the dark line shown on the schlieren photographs may be an actual pressure discontinuity.

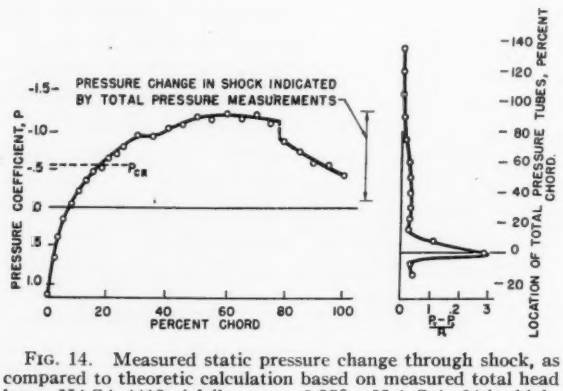

FIG. 14. Measured static pressure change through shock, as compared to theoretic calculation based on measured total head loss. NACA 4412 airfoil, $\alpha = -0.25°$. N.A.C.A. 24-in. high-speed wind tunnel. M = 0.770.

The force and moment changes with Mach Number are illustrated for an NACA 23015 airfoil for one angle of attack in Fig. 15. As the schlieren photographs generally show the occurrence of small disturbances first when the local speed of sound is reached in the flow lo-

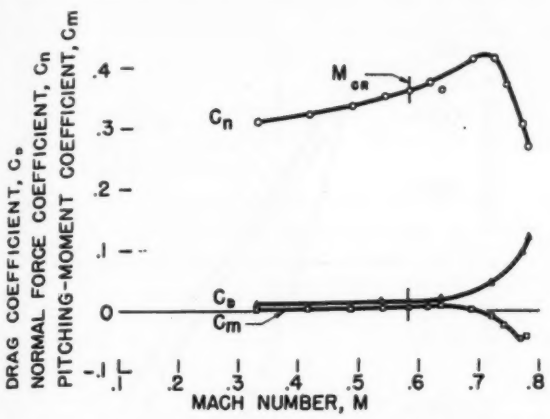

FIG. 15. Force and moment coefficient variation with Mach Number. NACA 23015 airfoil, $\alpha = 0°$. N.A.C.A. rectangular high-speed wind tunnel.

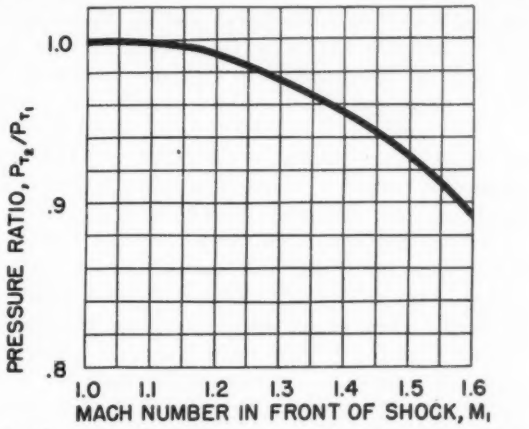

FIG. 16. Ratio of total pressure behind shock to total pressure in front of shock as a function of the Mach Number in front of shock.

cally over the airfoil the stream Mach Number corresponding to this condition is marked as M_{cr} in the figure. This definition of critical Mach Number is, of course, the standard that has been used throughout aeronautical engineering for the last several years and is based on the mass of experimental data previously discussed as well as the indication from the theory of flow change at Mach Number 1.0. It is shown by the figure that force changes do not occur at the speed marked M_{cr} but rather at some speed above this value. Numerous attempts have been made at theoretic determination of the speed at which the force changes occur. In the main, these have been based on empiric modifications of the potential flow theory. Such empiric modifications as have been developed are found to fit in perhaps one or two cases but are not general and general use of such relations not founded on assumptions in agreement with the actual physical phenomena including the entropy change in the flow can be expected to lead to serious difficulties.

The basic reason for the difference in Mach Number between the defined critical and the Mach Number at which the large changes in the force and moment coefficients occur is shown by the schlieren photographs. With the first attainment of the critical Mach Number numerous small shocks of insignificant intensity occur. No extensive flow separation is shown. It is not until sufficiently high speeds are attained so that the smaller shocks combine to form a steep front that pronounced separation and the consequent flow changes occur. This is further illustrated by Fig. 16, which shows the theoretic total pressure loss through a normal shock. The abscissa is the Mach Number in front of shock and the ordinate is the total pressure loss expressed as the ratio of the total pressure behind the shock to the total pressure in front of the shock. When the Mach Number in front of shock is 1.0, no losses occur. With increase of Mach Number in front of shock, losses occur which, as shown by the curve, are insignificant until Mach Numbers in front of shock considerably greater than 1.0 occur. Because pronounced separation requires a rather definite and moderate loss, it cannot be expected to occur until the Mach Number in front of the shock has reached values sufficiently high to cause a significantly large loss of total head in the shock. As the loss of total head required to produce separation is dependent upon the boundary-layer thickness, the total-head loss required to produce separation in any given case may depend upon the shape of the airfoil, the surface condition ahead of shock, the pressure gradients ahead of shock and the Reynolds Number, all of which affect the boundary-layer thickness. Hence, the difference in Mach Number between the defined critical and the Mach Number for force discontinuities may be expected to differ with all of these factors.

AERONAUTICAL ENGINEERING PROBLEMS AND DEVELOPMENTS

As adverse force changes are precipitated with the attainment of the local speed of sound over the surfaces of bodies, improvements can be made by the development of forms having favorable pressure distributions to reduce the local surface velocities. This approach has been employed most effectively. For airfoils, the problem was considered to be composed of two parts: first, the development of a basic shape having minimum induced velocity for a given thickness and, second, the derivation of a camber line which produced a given lift, with minimum induced velocity. The basic shape and the camber line could then be combined to give the optimum airfoil for a given thickness and lift coefficient as related to critical speed. The selection of the camber line is quite easy. The condition that the lift be uniformly distributed chordwise is the necessary criterion. The camber line is then directly calculated from the thin airfoil theory of Glauert, Munk, Prandtl, and others. The determination of the optimum basic

shape was not quite so simple. Starting with the experimental work[14] on basic shapes and the theory of airfoils of arbitrary shapes by Theodorsen,[30] a wide variety of forms was investigated theoretically until an optimum shape was found. Oddly enough, it was found that this basic shape fitted within the structure of the family of shapes studied in the N.A.C.A. 11-in. high-speed wind tunnel.[14] In the designation system of this family the shape derived is, closely, an NACA 0009-45. Airfoils of this new family known as the NACA 16-series[31] have found wide use over the last several years in applications to propellers where high tip speeds are attained. These airfoil shapes were later developed in Britain[32] and Japan[33] also and it is not too surprising as the basic concept had been available from the earlier fundamental studies of compressibility phenomena.[15] The basic camber line corresponding to a lift coefficient of 1.0, the basic airfoil thickness form, and several airfoils designed for various lift coefficients which have been investigated over the last 8 years are shown in Fig. 17.

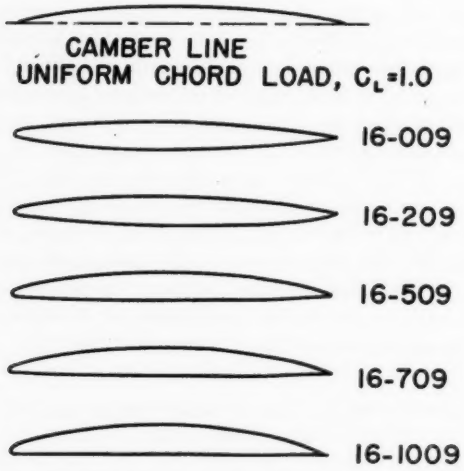

FIG. 17. N.A.C.A. 16-series high critical speed airfoils.

Using the same approach, members of the compressibility research group at the Langley Memorial Aeronautical Laboratory have developed a wide variety of aircraft components to give high critical speeds. The original N.A.C.A. cowling first tested in flight by the N.A.C.A. at Langley Field in 1928 had a critical Mach Number in the range of 0.45 to 0.5. New forms developed several years ago and given general publication recently[34] raised the critical Mach Number to 0.64, nearly 500 m.p.h. at sea level. This particular form of cowling, known as the NACA C cowl, has found nearly universal application on all modern aircraft having radial air-cooled engines. Fundamental research on the general problem of air-inlet openings in the nose of streamline bodies has led to further increase of the critical Mach Number so that now cowling forms for radial air-cooled engine installations having critical Mach Numbers over 0.8 have been obtained. Similarly, other airplane components, as windshields and canopies, have been developed having critical Mach Numbers of 0.8 or slightly better.

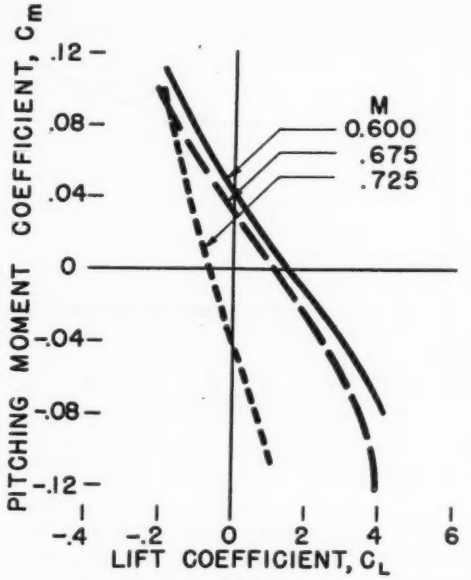

FIG. 18. Static-longitudinal-stability curves as affected by increase of Mach Number through the critical range.

These developments are directly related to the improvement of performance through delaying the onset of shock. The improvement of performance, however, is but one aspect of the problems encountered in airplane design and operation. Regardless of how high the critical Mach Number may be raised, flight at supercritical speeds must eventually be solved. Stability and control problems will require considerable attention. Some fighter aircraft are now capable of attaining supercritical speeds in dives and dive recovery from such speeds has required solution.

The stability change that can be expected is illustrated by the pitching-moment coefficient-lift coefficient plot of Fig. 18, which is taken from tests of a model made in the N.A.C.A. 8-ft. high-speed tunnel. This curve is the usual criterion for static-longitudinal stability. The slope of the curve must, of course, be negative and the magnitude of the slope is a measure of the stick force required. The curve should cross the moment-coefficient axis once, and only once, as this is the trim condition. At subcritical Mach Numbers, this curve, for an approximately satisfactory condition, is shown by the solid line. For the same configuration at critical and at a supercritical Mach Number, the static-longitudinal-stability curves are shown by the other two curves. There is a large decrease in the trim-lift coefficient and thus a diving tendency is exhibited. There is also a very large increase in the slope of the

curve; that is, the stability of the airplane is increased enormously. Hence, the response of the airplane to a given elevator deflection is reduced greatly and a given normal acceleration requires an exceedingly large deflection of the control. The stick force required thus increases greatly and with normally designed controls may be, and is in some instances, beyond the physical capacity of the pilot.

The origin of the stability problem is in the change of lift-curve slope and angle of zero lift which has been found for airfoils at supercritical speeds. This is illustrated by Fig. 19, taken from earlier work,[14] which has, of course, been verified by the later work. With increase of speed above the critical, the lift-curve slope decreases and, finally, the angle of zero lift shifts to the right. Consider an airplane flying at a given attitude at a low lift coefficient as, for example, in a dive with increasing speed. As the critical Mach Number is exceeded, there is a rapid drop in the lift coefficient as the lift curves shown in the figure change from the subcritical type at the lower speed to the supercritical type. The drop in lift coefficient occurs in a very narrow speed range and is far greater than the dynamic-pressure increase corresponding to the gain in speed. The lift decreases and the airplane thus tends to increase its rate of descent, except as modified by the drag-coefficient increase that occurs, but, as a consequence of the loss of lift, the nose of the airplane drops and thus the airplane exhibits a diving tendency. The down-wash angle at the tail likewise decreases with the loss of lift, giving a change of real angle of attack of the stabilizer in the positive direction. The consequent change of load on the tail produces a diving moment.

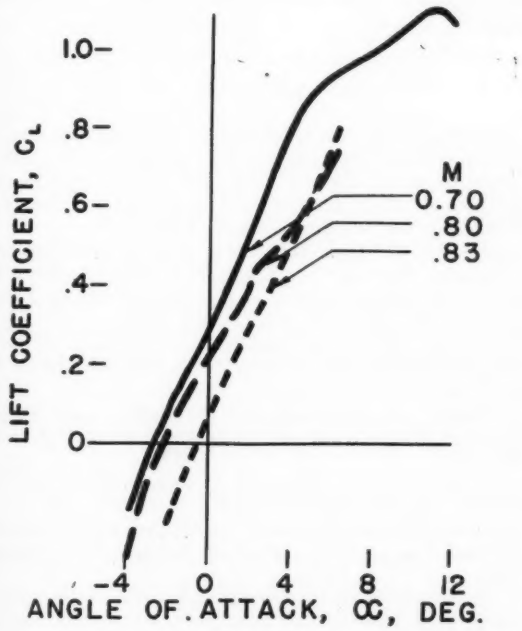

FIG. 19. Lift curve variation with increase of Mach Number through the critical range. NACA 2409-34 airfoil from N.A.C.A. Report No. 492.

Restoration of the attitude of the airplane requires, as shown by the sidewise displacement of the lift curves and the decrease of lift-curve slope, a large increase of angle of attack of the airplane. The angle of attack of the stabilizer is likewise increased. The angle of down-wash, however, is not correspondingly increased as, for a given lift coefficient, the down-wash angle remains sensibly constant. The increased angle of attack of the stabilizer gives a corresponding up load which can be offset only by up deflection of the elevator. Thus, very large control-surface deflections are required to restore the airplane attitude and, of course, very large stick forces. The increment elevator angle required over that for subcritical flows is the amount required to offset an increase of stabilizer angle equal to the sum of the change of wing angle of zero lift plus the change in angle of attack required to obtain the desired lift coefficient with the lower lift-curve slope. The larger elevator angle, of course, leads to very large stick forces. The change of angle of zero lift and the decreased slope of the lift curve thus cause the greatly increased stability. Contributing to this difficulty is the increased wing moment that accompanies this change of lift characteristics, but this effect is definitely secondary.

An airplane at such speeds, when excessive stick forces are encountered, may be flown on the tab which can produce the necessary boost. Use of the tab in dive pull-outs, however; must be done with great care. At the supercritical speed the airplane is very much less responsive to a given movement of the tab and, hence, large tab deflection is required. In the dive condition, however, the airplane is losing altitude rapidly and with lower altitude the combination of increased density and increased velocity of sound reduces the Mach Number attainable—the terminal Mach Number does, in fact, decrease with altitude. It is then not only possible, but indeed quite likely, that the reduction in Mach Number will be sufficiently great so that return to subcritical values occurs. The airplane thus becomes normally responsive to the control movement and, if prior to this stage the tab is deflected a large amount, the airplane will recover with excessive acceleration, sufficient to produce major structural failure.

Control can, of course, be effected by having an adjustable stabilizer. A decrease of the size of the stabilizer relative to the elevator will also help but this has certain disadvantages at subcritical speeds. The decrease of relative size of stabilizer to the point of having special arrangements of all-moving tails is also a possibility that may bear considerable research.

Another solution that was first proposed and investigated at the N.A.C.A. 8-ft. high-speed tunnel is the use of the wing flap. If the lift coefficient of the wing at any given angle at supercritical speed can be restored to its subcritical value, the principal aeromechanics of the airplane are then the same as at low speeds. As flap

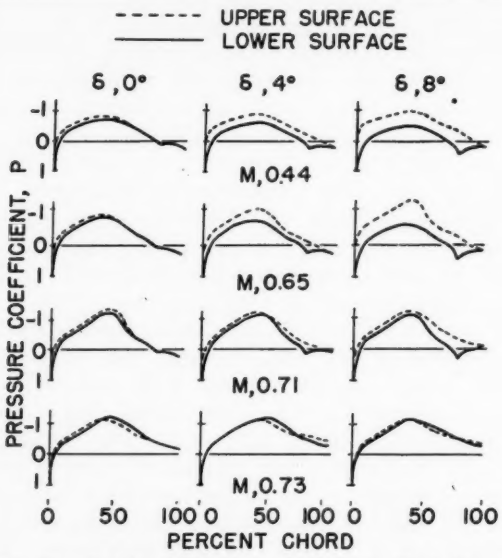

FIG. 20. Variation of aileron action with Mach Number. Two-dimensional pressure-distribution results. Symmetric airfoil, 19 per cent thick, $\alpha = 0°$. N.A.C.A. rectangular high-speed wind tunnel.

deflection produces the desired increase of lift coefficient, it was viewed as a possible solution. The original investigation with an airplane model was based first on tests made on a wing alone with a simulated split trailing-edge flap in the N.A.C.A. 24-in. high-speed tunnel and these results were then applied to the complete airplane model in the N.A.C.A. 8-ft. high-speed tunnel. The results were as expected, the necessary increase in wing lift being produced. A disadvantage was, as could be expected, some increase of tail load. The investigation was then pursued at Ames Laboratory and flaps forward on the lower surface of the wing were developed which produce the desired lift increase without as large an increase in tail load as is obtained with trailing-edge flaps. The Army Air Forces carried this work to flight tests in high-speed dives at Wright Field and from all of this work the so-called dive-recovery flaps found their way to very practical use.

The control problem is perhaps even greater and more difficult than the stability problem. All the usual problems, balance, hinge-moment characteristics, load distribution, and others, are made more complicated because of the speed squared effect on the forces, the possible change of load distribution, the effect of protruding edges, and the effects of sudden changes of surface curvature on peak pressures and shock stalling. It is even in full recognition of these problems that another and more fundamental problem must be noted. It was shown earlier, both by deduction from basic physical considerations and by illustration with schlieren photographs, that at supercritical speed when supersonic velocity extends over the forward portion of an airfoil, disturbances originating downstream cannot influence the flow over the forward portion of an airfoil. Hence, it can be expected that aileron or flap deflection at these speeds will not act as at lower speeds and will, because any pressure field set up by their deflection cannot influence the flow over the forward portion of the airfoil, lose much of their effectiveness. This is illustrated by Fig. 20. The airfoil is a thick symmetric airfoil and was set at 0° angle of attack. With 0° aileron angle, the flow is symmetric and the pressure distribution over both surfaces is the same, as shown by the diagrams. With aileron deflection at low speeds, the flow over the whole airfoil is altered so that the upper and lower surface pressure distributions change, producing a lift over the whole airfoil. This is normal aileron action. With increase of speed, this condition maintains until supercritical speeds are reached, when, as is apparent from the diagrams, the flow over the forward portion of the airfoil ahead of the shock location becomes identical over both upper and lower surfaces and deflection of the aileron produces no lift increment over the main portion of the airfoil. The only lift increment that can be produced is that acting directly on the aileron. The great reduction in effectiveness is apparent. This is a wholly new control problem.

It is, of course, not possible to review in a single lecture all of the many interesting, important, complicated and new phenomena that the aeronautical engineer must understand and the problems he must solve. Thus, only in brief, has this been the history, the flows, and some of the problems introduced in aeronautics by compressibility phenomena. Much remains ahead as the problem of increasing speed is solved to the achievement of clock-stopping speeds in east-to-west flight.

REFERENCES

[1] Rayleigh, Lord, *On the Flow of Compressible Fluid Past an Obstacle*, Philosophical Magazine, Vol. 32, pp. 1–6, July, 1916.

[2] Bryan, G. H., *The Effect of Compressibility on Stream Line Motions. Part I*, R. & M. No. 555, British A.C.A., 1918; *Part II*, R. & M. No. 640, British A.C.A., 1919.

[3] Fales, E. N., *Apparatus for High Speed Research Applicable to Propeller Tip Effect and Comments of Mr. Ackeret and Dr. Prandtl on Certain Features of the Göttingen Wind Tunnel*, N.A.C.A. Misc. Paper No. 19, January, 1926.

[4] Caldwell, F. W., and Fales, E. N., *Wind-Tunnel Studies in Aerodynamic Phenomena at High Speed*, N.A.C.A. Report No. 83, 1920.

[5] Briggs, L. J., Hull, G. F., and Dryden, H. L., *Aerodynamic Characteristics of Airfoils at High Speeds*, N.A.C.A. Report No. 207, 1925.

[6] Briggs, L. J., and Dryden, H. L., *Pressure Distribution Over Airfoils at High Speeds*, N.A.C.A. Report No. 255, 1927.

[7] Briggs, L. J., and Dryden, H. L., *Aerodynamic Characteristics of Twenty-Four Airfoils at High Speeds*, N.A.C.A. Report No. 319, 1929.

[8] Jacobs, Eastman N., and Shoemaker, James M., *Tests on Thrust Augmentors for Jet Propulsion*, N.A.C.A. T.N. No. 431, 1932.

[9] Ferri, Antonio, *Investigations and Experiments in the Guidonia Supersonic Wind Tunnel*, N.A.C.A. T.M. No. 901, 1939.

[10] Taylor, G. I., and Sharman, C. F., *A Mechanical Method for Solving Problems of Flow in Compressible Fluids*, R. & M. 1195, British A.R.C., 1928.

[11] Stack, John, *The N.A.C.A. High-Speed Wind Tunnel and Tests of Six Propeller Sections*, N.A.C.A. Report No. 463, 1933.

[12] Wood, Donald H., *Full-Scale Tests of Metal Propellers at High Tip Speeds*, N.A.C.A. Report No. 375, 1931.

[13] Douglas, G. P., and Wood, R. McKinnon, *The Effects of Tip Speed on Airscrew Performances*, R. & M. No. 884, British A.R.C., 1923.

[14] Stack, John, and von Doenhoff, Albert E., *Tests of 16 Related Airfoils at High Speeds*, N.A.C.A. Report No. 492, 1934.

[15] Stack, John, *The Compressibility Burble*, N.A.C.A. T.N. No. 543, October, 1935.

[16] Jacobs, Eastman N., *Methods Employed in America for Experimental Investigation of Aerodynamic Phenomena at High Speeds* (paper read at Volta Meeting in Italy September 30 to October 6, 1935), N.A.C.A. Misc. Paper No. 42, March, 1936.

[17] Stack, John, Lindsey, W. F., and Littell, Robert E., *The Compressibility Burble and the Effect of Compressibility on Pressures and Forces Acting on an Airfoil*, N.A.C.A. Report No. 646, 1938.

[18] Robinson, Russell G., *Sphere Tests in NACA 8-Foot High-Speed Tunnel* (paper read before Fifth Annual Meeting of the Institute of the Aeronautical Sciences, January 27–29, 1937).

[19] Prandtl, L., *Tasks of Air Flow Research*, N.A.C.A. T.M. No. 365, 1926.

[20] Busemann, A., *Profilmessungen bei Geschwindigkeiten nahe der Schallgeschwindigkeit (im Hinblick auf Luftschrauben)*, Wissenschaftlichen Gesellschaft für Luftfahrt, Jahrbuch, 1928.

[21] Stanton, T. E., *High-Speed Wind Channel for Tests on Airfoils*, R. & M. No. 1130, British A.R.C., 1928.

[22] Bailey, A., and Wood, S. A., *Development of High-Speed Induced Wind Tunnel*, R. & M. No. 1468, British A.R.C., 1932.

[23] Bailey, A., and Wood, S. A., *The Development of a High-Speed Induced Wind Tunnel of Rectangular Cross-Section*, R. & M. No. 1791, British A.R.C., 1937.

[24] Bailey, A., and Wood, S. A., *Further Development of a High-Speed Wind Tunnel of Rectangular Cross-Section*, R. & M. No. 1853, British A.R.C., 1938.

[25] Karner, L., and Ackeret, J., *Aeronautical Education and Research at the Swiss Institute of Technology in Zurich*, N.A.C.A. T.M. No. 616, 1931.

[26] Ackeret, J., *High-Speed Wind Tunnels*, N.A.C.A. T.M. No. 808, November, 1936.

[27] Ackeret, J., *Über Luftkräfte bei sehr grossen Geschwindigkeiten insbesondere bei ebenen Strömungen*, Helvetica Physica Acta, Vol. I, Fasciculus Quintus, 1928.

[28] Glauert, H., *The Effect of Compressibility on the Lift of an Aerofoil*, R. & M. No. 1135, British A.R.C., 1927.

[29] Prandtl, L., *General Considerations on the Flow of Compressible Fluids*, N.A.C.A. T.M. No. 805, 1936.

[30] Theodorsen, Theodore, *Theory of Wing Sections of Arbitrary Shape*, N.A.C.A. Report No. 411, 1931.

[31] Stack, John, *Tests of Airfoils Designed to Delay the Compressibility Burble*, N.A.C.A. Report No. 976, December, 1944.

[32] Taylor, J. Lockwood, *Constant-Velocity Aerofoils*, Aircraft Engineering, December, 1939.

[33] Tani, Itiro, M.A.R.I., and Mituisi, Satosi, *Contributions to the Design of Aerofoils Suitable for High Speeds*, Aeronautical Research Institute, Tokyo Imperial University Report No. 198, Vol. 15, pp. 399–415, 1940.

[34] Robinson, Russell G., and Becker, John V., *High-Speed Tests of Conventional Radial Engine Cowlings*, N.A.C.A. Report No. 745, 1942.

Discussion of the Lecture

Edward P. Warner, Vice-Chairman of the Civil Aeronautics Board, presided as Chairman for the presentation of the Lecture. In a brief introduction, Mr. Warner recalled some of the contributions of early pioneers and paid tribute to the work of the Wright Brothers.

At the conclusion of the Lecture the following prepared comments on the subject were given.

Neil P. Bailey, Head, Department of Mechanical Engineering, Rensselaer Polytechnic Institute; formerly of the General Electric Research Laboratory: "Mr. Stack has done a fine thing in focusing attention on the flow separation energy losses that can result from superacoustic compression shocks. In general, mechanical engineers have been prone to look only at the compression shock losses and to ignore the jet separation losses that may be induced by the shock.

"A good example of the significance of the induced losses is shown by Curve No. 1. This shows the efficiency of a high-flow supercharger impeller plotted against the maximum inlet Mach Number. Since the Mach Number was calculated by using the maximum relative air velocity at the periphery of the inlet, the sudden serious loss in impeller efficiency shown can hardly be explained by the small fraction of the inlet airfoil subjected to compression shock. This is especially true when it is remembered that only a portion of the total impeller work is done by the inlet airfoils, the major portion being done in the impeller passages. This would appear to be clearly a case where the jet separation and turbulence produced in the impeller by minor compression shocks in a portion of the inlet resulted in a serious efficiency loss.

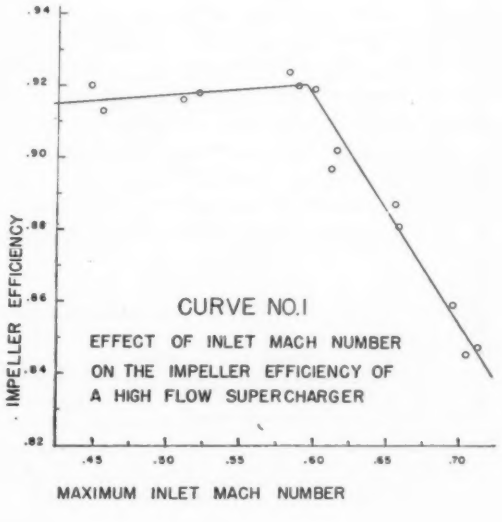

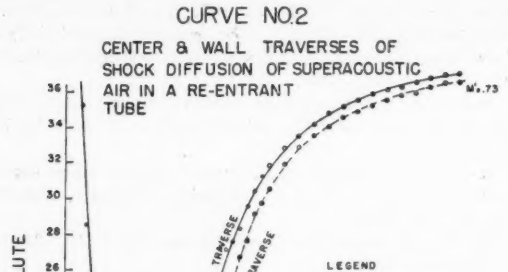

"Mr. Stack has suggested the possibility that in a region of compression shock pressures measured inside the boundary layer may not be the same as those outside. Curve No. 2 shows centerline and wall pressure traverses through a compression shock in a straight walled tube.

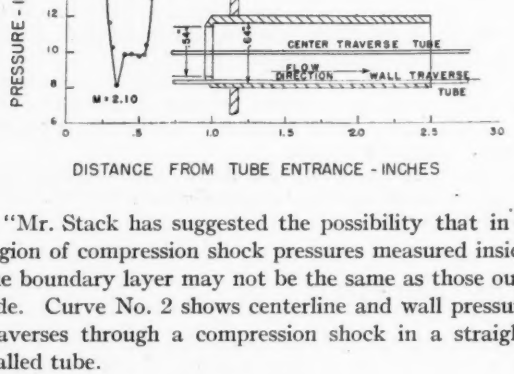

"After the angle shocks that resulted from the use of a re-entrant tube had culminated in a plane shock, the average Mach Number was 1.46. While the centerline pressure and the wall pressure check within an inch of mercury, this is in reality no answer to Mr. Stack's question. Both traverses were made using an 0.0125-in. static hole in a 0.10-in. traversing tube, so both readings were inside a boundary layer. The important point is that either the wall or centerline pressures yield results that check well with classic theory.

"The straight walled tube has no area diffusion to correspond to the flow over an airfoil, and, when a compression shock is induced in a diverging passageway, the results do not check classic theory at all.

"Curve No. 3 shows normal diffusion and combined shock and diffusion in a conical passageway. When normal diffusion started at a Mach Number of unity and continued to a Mach Number of 0.50, the pressure rise was 0.70 as great as that corresponding to a reversible compression.

"However, when the first 0.40 in. of the diffuser acted as a nozzle to raise the Mach Number to 1.56, a combined shock and diffusing action changed the Mach Number to 0.67. The pressure rise realized was only 0.60 of that of a corresponding reversible compression. A plane compression shock would have resulted in a final Mach Number of 0.68 and a pressure rise of 0.86 that of a reversible change.

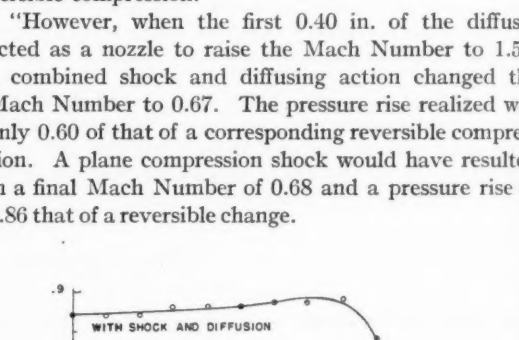

"Since the compression shock of Curve No. 2 in a straight walled tube gave a pressure rise 0.86 times a reversible compression, Mr. Stack's conclusion that a compression shock in a diffusing region is a wasteful process would appear to be borne out.

"Curve No. 4, which shows discharge traverses of the conical diffuser of Curve No. 3, reveals that in the case of shock and diffusion the losses are concentrated at the walls. For example, using only the Mach Number in the central portion, a diffusion from $M = 1.56$ to $M = 0.88$ would result in an ideal pressure ratio of 2.43. Since the actual pressure ratio is 2.18, the central portion gives a pressure rise ratio of $1.18/1.43 = 0.825$, which is a far cry from the average value of 0.60.

"The turbulence that follows a compression shock in a diffusing region has not been given due consideration by mechanical engineers, and Mr. Stack deserves much credit for focusing attention on this phase of high velocity flow phenomena."

Dr. Hugh L. Dryden, Chief, Mechanics and Sound Division, National Bureau of Standards: "The confidence placed by the Institute in the Eighth Wright Brothers Lecturer has been fully justified by the timeliness of the subject selected and the fundamental manner in which it has been treated. Progress in those aspects of aeronautics for which a rational theory has not yet been developed proceeds by the recognition of the common features of complex flow patterns. Mr. Stack has indicated how the field of flow around airfoils at high speeds is built up of shock waves, boundary layers, and regions of flow separation, concepts that in themselves have come to be familiar when encountered in more familiar circumstances.

"The lecturer's review of the early exploratory measurements of Briggs, Hull, and myself brings recollections of our early attempts to observe and understand the forces on airfoils at high speeds. That aspect ratio and constriction effects were so large as to make the results of little quantitative value was recognized at the time. That the qualitative results have been so completely substantiated by the lecturer's careful quantitative measurements with more adequate equipment is surprising. Pressure distribution measurements and observations of the behavior of oil films on the surface of the airfoils established at the time that 'large changes in the force coefficients were associated with a breaking away of the air flow from the upper surface, similar to that which occurs at the burble point at ordinary wind-tunnel speeds.'

"The following quotations summarize the conclusions of interest in connection with the present discussion.

"'A careful inspection of the pressure distribution curves, Figs. 4 to 9, shows the existence of regions characteristic of flow of the type described in which there is a separation from the surface. For example, in Fig. 6 for airfoil 3 the distribution over the upper surface for a speed of $0.5c$ at 24° shows a sharply defined peak followed by a region of nearly constant decrease in pressure such as is found in the case of a cylinder or sphere where the flow breaks away from the surface. A similar distribution may be observed at $0.65c$ at 20° and 24°; $0.8c$ at 16°, 20°, and 24°; $0.95c$ at 4°, 8°, 12°, 16°, 20°, and 24°; and $1.08c$ at all positive angles. In fact, it is possible to trace a rough locus of speeds and angles at which the change takes place. The steps in speed and in angles are unfortunately so far apart that the exact position cannot be plotted, but it may be seen that for thick airfoils at a given speed the break occurs at lower angles and at a given angle at lower speeds than for the thin airfoils. The location of the change in flow is facilitated by the fact that for the burbling type of flow the pressure at the trailing edge is lower than the static pressure, whereas for the smooth high lift type it is higher than the static pressure.'

"'It should be emphasized that the flow at high speeds is of the same general appearance as burbling flow at low speeds and, just as no theory has been worked out for burbling flow, so no theory is available for the high-speed type of flow. Corrections for aspect ratio cannot be computed, and the estimation of interference between blade elements of propellers cannot be based on the theory of induced drag.'

"We did not understand these results at the time. The lecturer and his associates have now given a complete interpretation. Shock waves appear at high speeds, constituting severe adverse pressure gradients. These gradients produce separation of the boundary layer, acting through that part of the boundary layer nearest the wall for which the flow is subsonic and, hence, in which pressure disturbances propagate upstream. The direct shock loss is much smaller than that due to the flow separation. Many of the effects that we commonly regard as due to shock waves are in reality associated with the flow separation—i.e., large loss of lift, unsteadiness of flow, etc. The term 'compressibility burble' applied to this phenomenon by the lecturer in an earlier report is truly descriptive. The main effects are due to a separation analogous to that occurring at the stall at low speeds. Control problems at high speeds are analogous to the control of stalled airplanes. The theoretic approach needed is not one primarily concerned with compressibility effects per se but with flow separation. I believe the lecturer has done a great service in so clearly outlining the fundamental aspects of transsonic flow."

Dr. Norton B. Moore, Southern California Cooperative Wind Tunnel: "The subject, 'Compressible Flows in Aeronautics,' is most appropriate and timely. It is without doubt the highest priority basic problem in the engineering and experimental flight test departments of manufacturers of high-speed and/or high-altitude airplanes and in those research laboratories

whose primary interest is better and faster airplanes; these groups look to the National Advisory Committee for Aeronautics for the basic experimental work such as has been reviewed by Mr. Stack today.

"I recall that it was my privilege also to discuss the Sixth Wright Brothers Lecture, at which time I said '. . . . it will not be very long before we will all be much more closely acquainted with compressibility effects . . . .' We are certainly getting acquainted, but more complete understanding is still much needed. The lecture today will help fill that need.

"In the Historical Section, reference might well be made to the work of Molenbroek, and particularly Tchapliguine, in connection with distorted incompressible flow fields. Also, the statement: 'This concept is, of course, a physical representation of *all* the theoretic work since' (referring to the concept of similarity between the compressible flow field about a given airfoil, and the incompressible flow field for a thicker airfoil), is subject to question—in the Rayleigh-Janzen approximation method one deals always with the original profile (there is no distortion).

"There might be some question directed also to the statement: 'When the speed of sound is first attained in a flow field, a change to a new type of flow occurs and *no adequate* theoretic basis is yet available which describes this flow.' The questioning depends on the severity of the word 'adequate'—several exact solutions involving local supersonic flows are known. A familiar example is the compressible analogue of incompressible flow through a parabolic channel.

"Again, it is appreciated that this lecture is delivered from the experimental point of view, but the statement that ' . . . . no theory of mixed flow existed and still is lacking . . . .' might be questioned—there *are* theories of mixed flows.

"In the Theoretic Considerations Section, it may be in order to remember that the equation of continuity, Eq. (2), becomes Laplace's equation *only* if irrotational flow is postulated.

"I am afraid that the lecturer has taken some liberties with Eq. (3), the equation for small perturbations, in putting $M = 1$ and drawing physical interpretations of infinite forces at $M = 1$, where the equation is definitely not valid. As $M \to 1$, $\partial v/\partial y$ may approach zero, *unless* $\partial u/\partial x$ approaches infinity. Small perturbations cannot be assumed at or near $M = 1$. A true physical explanation for entropy increase cannot then be merely that Eq. (3), illegally extended to $M = 1$, shows infinite forces.

"In connection with the section on Flows at Super-Critical Mach Numbers, it is wondered whether, in the explanation of formation of shock waves leading up to Fig. 8, it is really intended to give one the impression that shock waves are *always* to be expected in mixed flows.

"There is a basic difficulty with schlieren photographs. They show *all* irregularities in the flow, from wall to wall. Accordingly, they *may* give misleading pictures. For example, some of the photographs here show shock waves extending *through* the separated regions, to or very close to the airfoil. I wonder if this is actually the case? A careful check of spanwise wake and pressure distributions would seem to be in order before general conclusions are drawn from these photographs. Also, the presence of pressure discontinuities within the boundary layer may be similarly questioned.

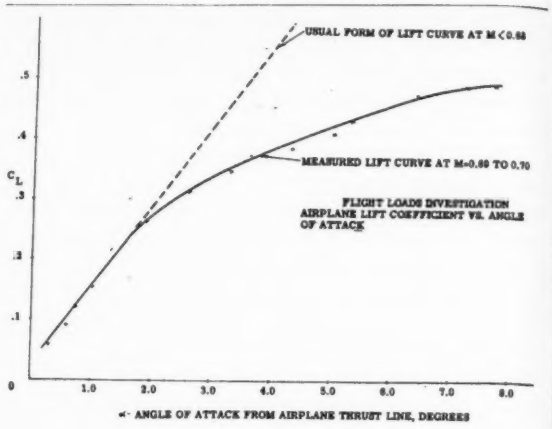

"In connection with the section on Aeronautical Engineering Problems and Developments, it is obvious that we are in a most interesting and challenging period of aerodynamic development. Much high-speed work is yet to be done on paper, in wind tunnels, and in flight, on wing sections and other airplane components, and on performance, stability and control for the airplane as a whole.

An example of the serious problem now being faced by designers is illustrated in Fig. 19, which shows decrease in lift with increasing Mach Number. The problem is actually more serious than Fig. 19 indicates. The accompanying figure, showing flight test points of lift coefficient vs. angle of attack for a modern airplane at Mach Numbers between 0.69 and 0.70, illustrates the great loss in both lift and lift-curve slope, which leads to obvious difficulties in stability and control.

"In closing, I wish to acknowledge the assistance of Messrs. Fred W. Geiger and Henry T. Nagamatsu in reviewing this comprehensive lecture in the short time that was available.

"Our congratulations to the Institute of the Aeronautical Sciences and to Mr. Stack, on this day of tribute to the Wright Brothers!"

L. E. Root, Chief, Aerodynamics Section, El Segundo Plant, Douglas Aircraft Company, Inc.; Member N.A.C.A. Committee on Aerodynamics: "John Stack is to be congratulated not only for his admirable presentation of the Eighth Wright Broth-

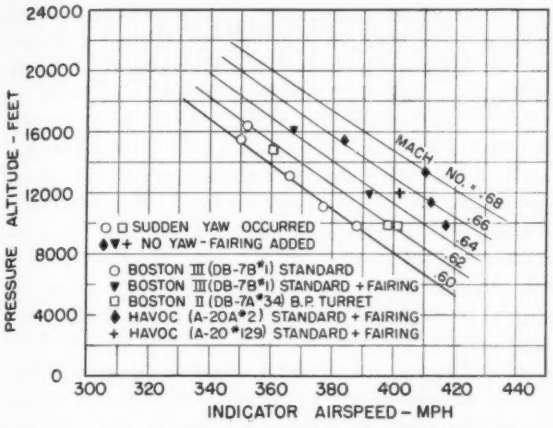

FIG. 1. Relationship between wing-nacelle flow breakdown and Mach Number on Boston and Havoc light bombers showing effect of adding oil cooler scoop fairings.

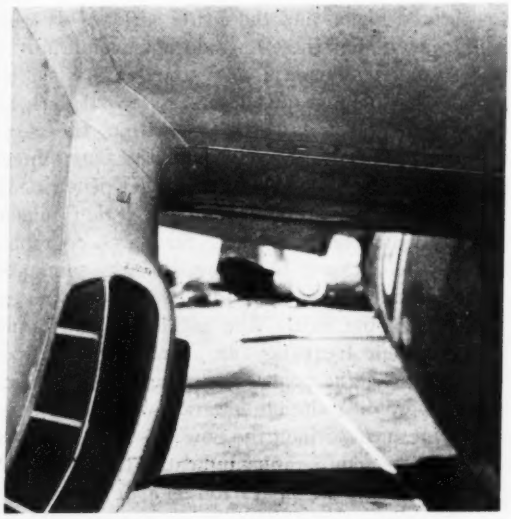

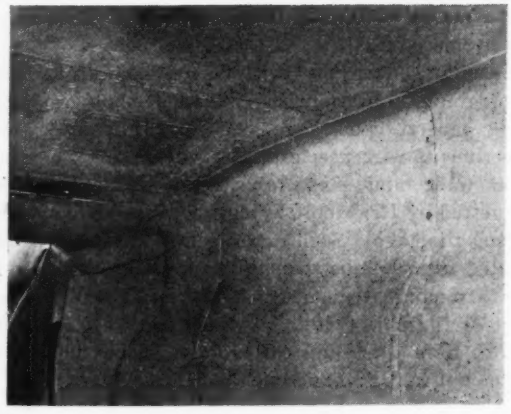

FIGS. 2a (*top*) and 2b (*bottom*). Original lines at inner wing-nacelle junction.

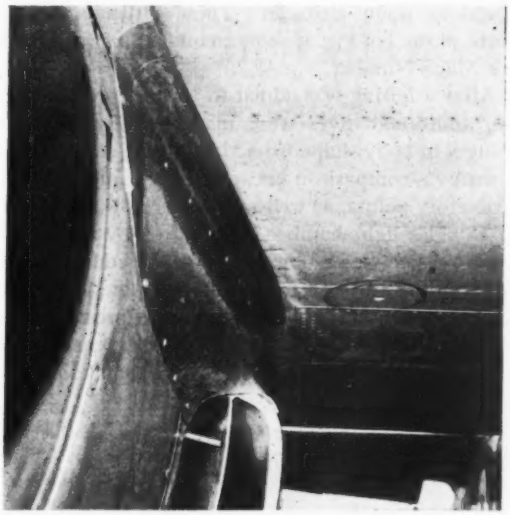

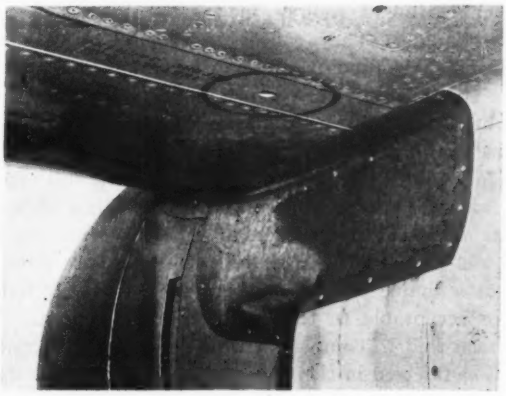

FIGS. 3a (*top*) and 3b (*bottom*). Revised lines at inner wing-nacelle junction with fairing added.

ers Lecture but for his courage in choosing what is generally accepted as a difficult subject. From the standpoint of a design aerodynamicist, his treatment of the subject of Compressible Flows from a fundamental or physical point of view is appreciated. Mr. Stack has pointed out that aerodynamic improvements can be made through the development of shapes having favorable pressure distributions to reduce local surface velocities. In this respect it may be of interest to present a Douglas experience wherein this approach gave a satisfactory solution to a flow problem associated with Mach Number.

"Early in 1941, while attempting to demonstrate Boston Models II and III to an indicator air speed of 400 m.p.h., test pilots reported a sudden change in heading without previous warning through either buffeting or control surface movement. This yaw occurred either to the left or right and could be quickly eliminated by reduction in speed. When allowed to develop fully, the motion was oscillatory in character through approximate angles of $\pm 15°$. After several dives had been made, it became apparent that the sudden yaw was occurring at different values of indicator air speed

dependent upon altitude. These altitude air-speed points, plotted in Fig. 1, show an interesting relationship with Mach Number.

"After a fairing was added to the wing-nacelle junction, additional dives were made without difficulty. Changes in body shape from the original conditions are shown by a comparison between Figs. 2 and 3. These satisfactory points, as well as those for other models of the Douglas light bomber series, are shown on Fig. 1. It is a reasonable assumption that the addition of the fairing in the critical nacelle-wing junction lowered the numerical value of the peak negative pressure below its critical value, which previously was exceeded without the fairing, thus resulting in flow breakdown at a given free-stream Mach Number."

Mr. John Stack: I quite agree with Dr. Moore that "reference might well be made" to Molenbroek and Tchapliguine. They concerned themselves with the solution of the fundamental flow equations at an earlier date than others referred to in the Lecture, and their work has been taken up and extended by mathematicians to the end of obtaining rigorous solutions of the fundamental equations. Rigorous solution still eludes us, however, and existing solutions still remain approximations even in the mathematical view. More emphasis was placed upon Prandtl's work because from it stems a simple physical concept that is usually found more acceptable to the engineer and physicist. No claim is laid to completeness in the historical section, and, as inferred in the text, this section concerns itself principally with the work undertaken from an aeronautical point of view rather than from a general physics or mathematics point of view.

As to the existence of theories of mixed flows as questioned and stated by Dr. Moore, it is recognized that certain cases have been solved mathematically. However, search for the existence of these mathematically described flows in nature has so far proved unfruitful. One recent mathematical solution of a mixed flow involving adiabatic recompression from extremely large supersonic velocities has aroused the curiosity of many. Kantrowitz, of the Langley Memorial Aeronautical Laboratory, has pointed out that such flows are unstable and, hence, will likely fail, because disturbances are always present. On this whole question, it seems to me that Dr. Dryden has made the clearest statement in his comment: "The theoretic approach needed is not one primarily concerned with compressibility effects per se but with flow separation."

Dr. Moore's meaning when he states that schlieren photographs "show *all* irregularities in the flow" is not wholly clear. It is generally recognized that the schlieren photographs can be expected to show all the *density* variations in the flow. This does not mean, however, that the photographs may give misleading pictures but rather that incautious interpretation of the photographs may prove misleading. The question of whether or not shock extends through the boundary layer is an interesting one. A careful examination of the photographs indicates that the shock does not extend through the boundary layer or separated region contrary to the inference drawn in Dr. Moore's comment. There is but one photograph in the group which might be considered to indicate penetration of the boundary layer by the shock; that is Fig. 10 for a Mach Number of 0.821. In this instance, for the flow over the upper surface two thin lines appear to extend into the region between the heavy dark line indicating the separated region and the airfoil surface. It seems clear, however, that these lines do not extend into the airfoil surface. There is also apparent, when one examines this photograph closely, a second dark line issuing from the airfoil surface within the region bounded by the airfoil surface and the outer intense dark line. The two thin shock lines that penetrate the outer line appear to terminate in the region bounded by the inner dark line extended. Such a photograph as this might be obtained by exposure of the same plate at two different times. Actually, this is not the case here, however, but as the flow oscillates violently and with very high frequency as shown by high-speed motion pictures, the probable explanation is that the spark that provides the illumination was discharged in the interval during which the flow was changing. The great mass of photographs indicates that the shock does not penetrate the separated region or the boundary layer. In this respect, the results are in agreement with the phenomena found in the divergent passages of supersonic nozzles.

General conclusions have been drawn from these photographs and from much earlier photographs, as have general conclusions been drawn from similar experiments with nozzles. The careful check of spanwise wake and pressure-distribution measurements suggested by Dr. Moore as in order were, in fact, made a long time ago. Such experiments are more directly related to technique than to phenomena of concern to the aeronautical engineer and, hence, form no real part of the object at hand. The general conclusions drawn from these and earlier photographs have been borne out in flight experiments on aircraft.

The Effective Use of Aerodynamic Balance on Control Surfaces

L. E. ROOT*

Douglas Aircraft Company, Inc.

SUMMARY

This paper is concerned with (a) an analysis of wind-tunnel data obtained from a 2-ft. constant chord control surface model constructed so that the separate effects of variation in aerodynamic balance overhang and movable surface nose shape could be obtained, and (b) the presentation of design methods leading toward the effective use of aerodynamic balance on control surfaces. The basic airfoil section used is an NACA 0012 modified to 10.7 per cent maximum thickness by 12 per cent chord extension and straight-sided afterbody. These modifications were made in accordance with 1935 results from DC-2 flight tests which specifically indicated that flat-sided rudders or elevators were less subject to flow conditions causing undesirable oscillations, particularly when control forces had been substantially reduced through the use of aerodynamic balance. The nature of the overhanging balance effectiveness in reducing hinge moments is illustrated by presenting representative pressure distributions over a surface with and without balance at various angles.

Using theoretic control surface parameters for simply hinged flaps as a basis, hinge-moment data from the model were analyzed to obtain empiric factors that correct for variations in aerodynamic balance and nose shape. Parameters are obtained for use in estimating three-dimensional control surface effectiveness and hinge moments with a degree of accuracy corresponding to the similarity of airfoil sections taken along the span of any specific control surface to the section tested, particularly with respect to movable surface shape. This method of calculating hinge moments has been checked by measurements on scale airplane models and was found to be reasonably accurate considering differences in hinge-line locations. Upon the basis of hinge-moment tests on sharp (A), medium (B), and blunt (C) noses, an intermediate shape, (B + C)/2, was chosen for design use. Comparison of control surface factors for this nose shape obtained from scale airplane model tests and from the basic model show good agreement.

With particular respect to air-transport operation, an important factor affecting the design of the movable control surface section is the degree to which the balance nose is subject to critical icing when the surface is held at a trim angle, such as in the case of a rudder after engine failure. From 1937 tests in the Goodrich ice tunnel using the 2-ft. chord model, an approximate relationship between balance nose shape and critical ice formation was suggested. Application of this limit to the (B + C)/2 nose-shaped rudders on present multiengined transports at best rate of climb with full asymmetric power indicates that the required rudder angles are not critical to dangerous icing conditions.

Additional factors affecting the choice of aerodynamic balance are discussed, and practical design limits applicable to elevators are given. From the basic wind-tunnel data, relationships of maximum up-travel, horizontal surface stalling, and free-control longitudinal stability to variation in aerodynamic balance and nose shape are determined. Application of these limits to typical airplane designs, in relation to the amount of hinge-moment reduction desired and the amount of balance recommended, shows the basic difficulty of reducing elevator control forces to acceptable magnitude and at the same time of providing enough elevator control for landing without exceeding the design limits.

To illustrate the use of aerodynamic balance on control surfaces, representative horizontal and vertical mean airfoil sections for eight Douglas airplanes are presented. Both the shape and amount of balance are clearly shown, as well as hinge location, maximum travel, control surface gap, and modifications to the basic airfoil. It is emphasized that proportionality of plan form and section will contribute to the more effective use of aerodynamic balance. To obtain maximum hinge-moment reduction for a given degree of unporting, it is necessary to avoid plan-form irregularities and movable control surface area aft of the hinge line which cannot be effectively balanced.

Presented at the Summer Annual Meeting, I.A.S., Los Angeles, July 27–28, 1944.

* Chief, Aerodynamics Section, El Segundo Plant.

INTRODUCTION

THE SATISFACTORY DESIGN of control surfaces on an airplane has always presented a fundamentally difficult aerodynamic problem, particularly with respect to control force reduction. Although symmetric overhang-type aerodynamic balance has been used on many movable surface designs, this use has been all too frequently associated with undesirable cut-and-try processes during experimental flight tests leading toward an acceptable arrangement. Such was the experience of the Douglas Aircraft Company, Inc., during the final development of the Model DC-2 transport control surfaces in the first half of 1935. Upon the basis of flight-test results obtained with a number of variations in elevator and rudder plan form and section on the DC-2 airplane, a few basic principles of control surface design were indicated. As a step toward further clarification of these principles, extensive wind-tunnel tests were conducted in the 10-ft. circular wind tunnel at GALCIT in the early part of 1936 on a large-scale control surface model so constructed that the separate effects of variation in overhang and balance nose shape could be obtained. The results from these wind-tunnel tests, used in combination with the DC-2 flight experience, have effectively contributed to the successful design of control surfaces on Douglas airplanes.

This material is offered with the full realization that there are many ways to design control surfaces which are entirely satisfactory but do not necessarily incorporate the features presented. With variation in airplane size, it is possible that optimum aerodynamic balancing of control surfaces is not always necessary, although its consistent use will undoubtedly result in the most efficient arrangement for a large airplane, particularly with respect to weight reduction. In the case

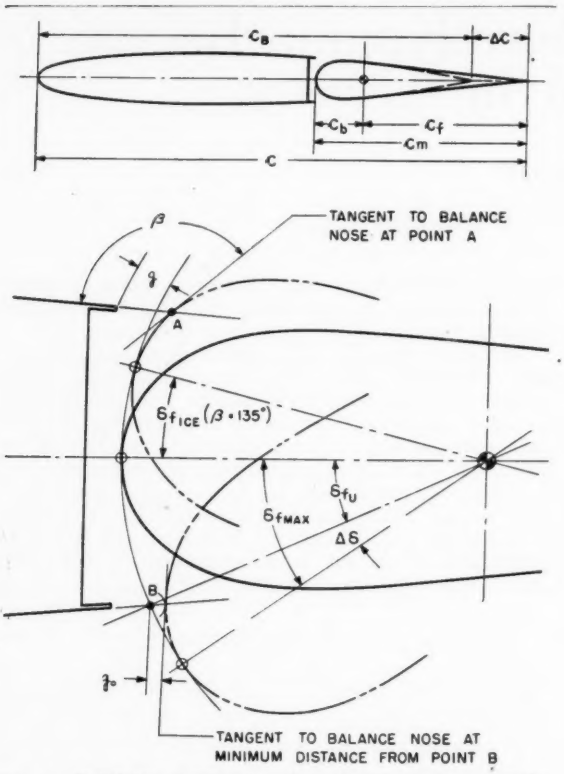

FIG. 1. Definition of control surface chords, gaps, and angles associated with the use of aerodynamic balance.

of smaller airplanes, particularly those restricted in dimensions, free-control stability considerations may predominate, thus limiting the use of proportional aerodynamic balance to partial control surface span. Bearing in mind the compromising nature of control surface design and the many associated difficulties, this paper is presented with the thought that Douglas design practice may be of general interest.

SYMBOLS

Chords, Gaps, and Angles (See Fig. 1)

- c = chord of control surface airfoil section
- $\bar{c}$ = mean geometric chord
- c_f = chord of movable control surface section aft of hinge line
- c_B = chord of basic control surface airfoil section before chord extension
- Δ_c = chord of extension to give modified airfoil section with straight-sided afterbody
- c_b = chord of movable control surface airfoil section ahead of hinge line
- c_m = chord of movable control surface airfoil section including balance ($c_b + c_f$)
- c_b/c_f = aerodynamic balance or overhang of movable control surface section
- c_b/c_m = hinge-line location of movable control surface section from balance nose leading edge
- g = minimum clearance gap between fixed and movable control surface sections
- g_0 = overtravel gap for movable control surface section
- x = chordwise station of airfoil section
- δ_f = movable control surface angle in degrees with respect to fixed surface
- δ_{f_u} = movable control surface angle in degrees where balance nose leading edge starts to project or unport beyond airfoil contour
- $\delta_{f\,max.}$ = angle in degrees at which movable control surface hits mechanical stop
- $\Delta\delta$ = angular overtravel in degrees, ($\delta_{f\,max.} - \delta_{f_u}$)
- β = angle in degrees between airfoil contour and line tangent to balance nose at point of intersection with airfoil
- $\delta_{f\,ice}$ = movable control surface angle in degrees beyond which disturbing ice formations are likely to occur ($\delta_{f\,ice}$ is taken when $\beta = 135°$)
- α = control surface angle of attack for finite span in degrees
- α_0 = control surface angle of attack for infinite aspect ratio in degrees
- a_0 = slope of control surface lift curve for infinite aspect ratio, $2\pi\eta$, radian measure (in text, $\eta = 0.875$)
- ψ = angle of yaw in degrees

Coefficients and Parameters

- C_L = control surface lift coefficient, (L/qS)
- c_l = airfoil section lift coefficient, (l/qc)
- C_H = movable control surface hinge-moment coefficient, ($H/q\bar{c}_f S_f$)
- c_h = movable control surface section hinge-moment coefficient, (h/qc_f^2)
- $C_{L\alpha} = \partial C_L/\partial\alpha$
- $c_{l\alpha} = \partial c_l/\partial\alpha$
- $C_{L\delta} = \partial C_L/\partial\delta$
- $C_{H\alpha} = \partial C_H/\partial\alpha$
- $c_{h\alpha} = \partial c_h/\partial\alpha$
- $C_{H\delta} = \partial C_H/\partial\delta$
- $c_{h\delta} = \partial c_h/\partial\delta$
- $\eta_\alpha, \eta_\beta, \eta_\lambda$ = empiric control surface hinge moment and effectiveness factors used to correct for variations in balance nose shape and overhang
- AR = geometric aspect ratio, (b^2/S)
- AR_e = effective aspect ratio
- p = lift curve slope reduction factor without end plates
- r = lift curve slope correction factor with end plates

Subscripts

- C_L, c_l, δ = variables held constant during differentiation
- f = movable control surface aft hinge line
- m = movable control surface including overhang
- b = balance or overhang
- r = rudder, chord aft hinge line
- e = elevator, chord aft hinge line
- W = wing
- H = horizontal control surfaces
- V = vertical control surfaces

Capital letters used in designating forces, moments, and their coefficients and derivatives indicate finite aspect ratio characteristics, while lower case letters indicate section characteristics.

CHOICE OF CONTROL SURFACE AIRFOIL SECTION

In view of optimum lifting characteristics shown for the NACA 0012 section[1] this airfoil was chosen as basic for control surface use and modified by a 12 per cent chord extension and straight-sided afterbody as shown in Fig. 2. Ordinates for this modified airfoil section are given in Table I. Although the maximum thickness was thus reduced to 10.7 per cent based on the extended chord, it was considered that the desirable aero-

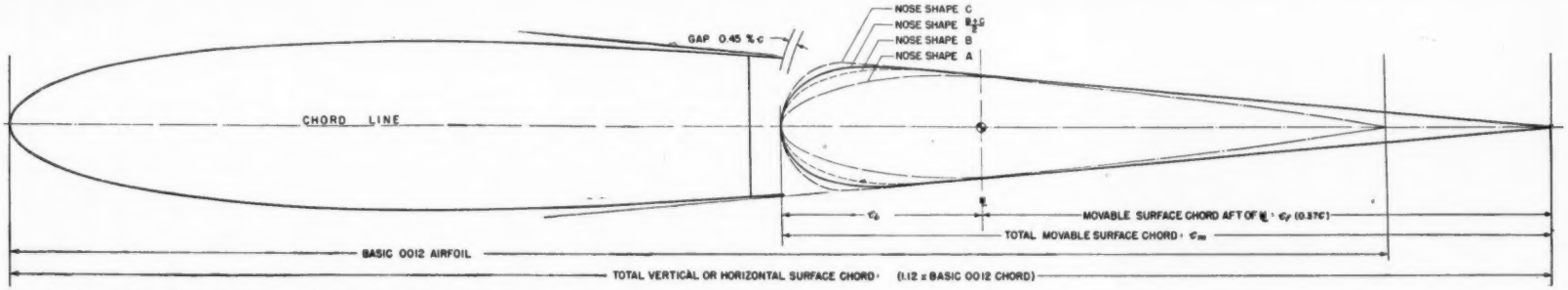
NOSE SHAPE C
NOSE SHAPE B
NOSE SHAPE A
GAP 0.45 %c
CHORD LINE
MOVABLE SURFACE CHORD AFT OF
TOTAL MOVABLE SURFACE CHORD
BASIC 0012 AIRFOIL
TOTAL VERTICAL OR HORIZONTAL SURFACE CHORD (1.12 x BASIC 0012 CHORD)

FIG. 2 · THE DEVELOPMENT OF A SUITABLE CONTROL SURFACE AIRFOIL SECTION

METHOD OF AIRFOIL CONSTRUCTION: THE NACA 0012 AIRFOIL SECTION IS MODIFIED BY EXTENDING THE CHORD 12% AND DRAWING STRAIGHT LINES FROM THIS EXTENDED POINT TANGENT TO THE BASIC AIRFOIL AT THE 60% CHORD POINT THICKNESS BASED ON THE NEW CHORD IS 10.7%. FOR CONVENTIONAL RATIOS OF MOVABLE TO FIXED SURFACES, THE ELEVATOR OR RUDDER WILL HAVE STRAIGHT SIDES AFT OF THE

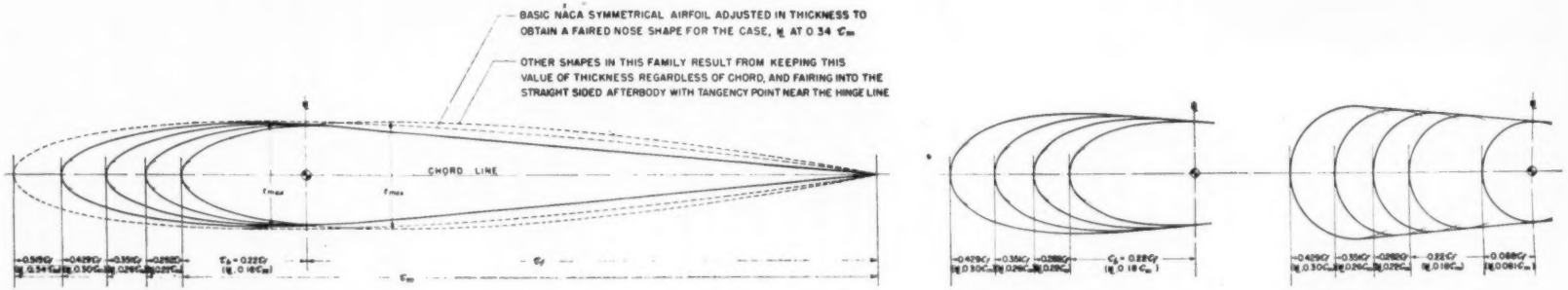
BASIC NACA SYMMETRICAL AIRFOIL ADJUSTED IN THICKNESS TO OBTAIN A FAIRED NOSE SHAPE FOR THE CASE, AT 0.34
OTHER SHAPES IN THIS FAMILY RESULT FROM KEEPING THIS VALUE OF THICKNESS REGARDLESS OF CHORD, AND FAIRING INTO THE STRAIGHT SIDED AFTERBODY WITH TANGENCY POINT NEAR THE HINGE LINE
CHORD LINE

(a) MOVABLE CONTROL SURFACES WITH NOSE SHAPE A

(b) NOSE SHAPE B

(c) NOSE SHAPE C

FIG. 3 SYSTEMATIC VARIATION OF AERODYNAMIC BALANCE AND NOSE SHAPE

METHOD OF BALANCE NOSE CONSTRUCTION

NOSE SHAPE A USING THE FUNDAMENTAL NACA SYMMETRICAL AIRFOIL THICKNESS DISTRIBUTION WITH MAXIMUM THICKNESS AT 30% CHORD, BASIC NOSE SHAPE A IS OBTAINED WITH TOTAL MOVABLE SURFACE CHORD AS A BASIS ONLY THE ORDINATES FORWARD OF 30% CHORD ARE REQUIRED TO FAIR INTO THE STRAIGHT SIDED AFTERBODY MAXIMUM THICKNESS IS ADJUSTED FOR THE VARIOUS NOSES TO OBTAIN A POINT OF TANGENCY WITH THE STRAIGHT SIDES AS CLOSE TO THE HINGE LINE AS POSSIBLE FOR EXAMPLE, IN THE CASE WITH THE AT 0.26 THE TANGENCY POINT IS AT 0.28 FOR THE SHORTER NOSES, SOME FAIRING ADJUSTMENT IS NECESSARY NEAR THE HINGE LINE

NOSE SHAPE C CONSTRUCTION OF THIS SHAPE IS OBTAINED BY FORWARD EXTENSION OF THE STRAIGHT SIDES TANGENT TO A LEADING EDGE CIRCLE OF MAXIMUM RADIUS

NOSE SHAPE B AN INTERMEDIATE NOSE BALANCE SHAPE IS OBTAINED BY USING ORDINATES HALF WAY BETWEEN THOSE FOR NOSES A AND C SOME FAIRING ADJUSTMENT IS REQUIRED NEAR THE TANGENCY POINT AS CAN BE SEEN ABOVE IN FIG 3b TANGENCY POINT WITH THE STRAIGHT SIDES FOR THIS NOSE IS MIDWAY BETWEEN THOSE FOR NOSE A AND NOSE C

NOSE SHAPE USED IN DESIGN AERODYNAMIC BALANCE NOSE SHAPE USUALLY EMPLOYED IN DOUGLAS DESIGNS IS ONE TERMED OR INTERMEDIATE BETWEEN THE SHAPES B AND C, DESCRIBED ABOVE

ORDINATES IN PERCENT OF AIRFOIL CHORD	
STATION	ORDINATES
000	000
1 116	1 691
2 232	2 335
4 460	3 174
6 700	3 750
8 930	4 181
13 390	4 772
17 860	5 183
22 320	5 504
26 780	5 559
35 710	5 181
44 640	4 726
53 570	4 074
62 500	3 271
100 000	000
L E R	1 41

STRAIGHT TAPER FROM APPROXIMATELY 60% CHORD TO TE

TABLE I : ORDINATES FOR NACA 0012 AIRFOIL MODIFIED TO 10.7% THICKNESS

ORDINATES IN PERCENT OF TOTAL MOVABLE SURFACE CHORD	
STATION	ORDINATES
1.25	3 633
2 50	4 951
5 00	6 371
7 50	7 132
10 00	7 454
15 00	7 420
20 00	7 048
100 00	000
L E R	8 3

TABLE II : ORDINATES FOR NOSE SHAPE

dynamic characteristics of the 0012 airfoil were maintained for the most part.

The afterbody modification to straight sides was a result of DC-2 flight-test experience with a number of control surface modifications. With flat sides, for example, the DC-2 rudder exhibited a marked reduction in the magnitude of oscillations, particularly in disturbed air. As a verification of this effect, a "bulged" rudder with convexity purposely overemphasized gave an extreme increase in surface oscillations. Since this same phenomenon occurred in the case of an elevator on the DC-2, it was definitely indicated that movable control surface sections should be modified to have straight-sided afterbodies for design use if the possibility of peculiar characteristics were to be minimized. The 12 per cent chord extension was therefore chosen so that the amount of afterbody usually employed for a movable control surface would have flat sides aft of the hinge line.

Basic Wind-Tunnel Tests

GALCIT Model and Tests

Using the symmetric airfoil section described above, a 2-ft. chord, 6-ft. span model with end plates was constructed so that the movable surface balance nose shape and amount of overhang could be systematically varied with one hinge-line position of 63 per cent c. The range of adjustments is illustrated in Fig. 3 where the method of construction for the different nose shapes is described. Balance noses are designated as sharp (nose shape A), medium (nose shape B), and blunt (nose shape C). Details of the model are shown in Fig. 4. Removable cover plates made it possible to maintain a constant gap of 0.45 per cent c with changes in balance overhang.

The model was rigged in the GALCIT 10-ft. wind tunnel as shown in Fig. 5 so that lift and drag could be measured in the normal manner and hinge moments could be obtained directly from the pitching moment balance. For each run the fixed surface was set at a given angle of attack and the flap rotated through a series of positions.

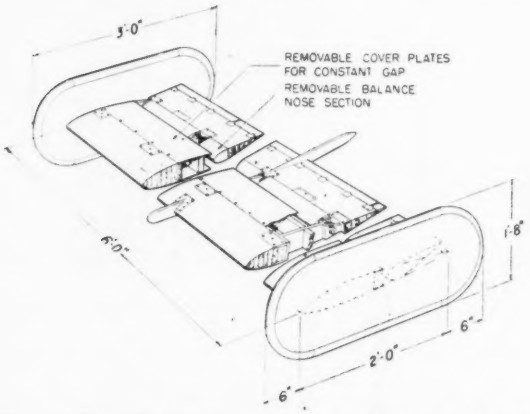

Fig. 4. Basic 2-ft. chord model used to obtain the effects of variation in movable control surface nose shape and aerodynamic balance. Test Reynolds Number 2.2×10^6.

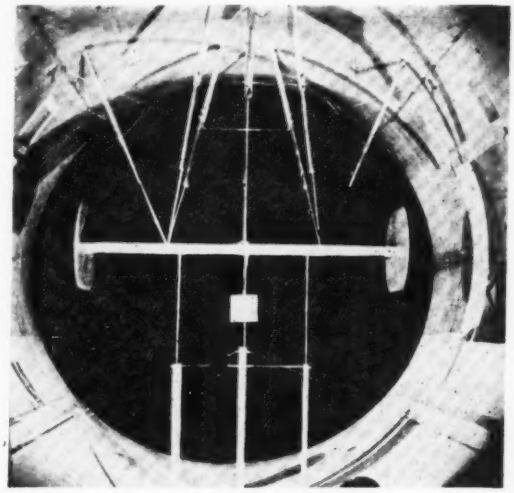

Fig. 5. Basic 2-ft. chord control surface model rigged in GALCIT 10-ft. wind tunnel.

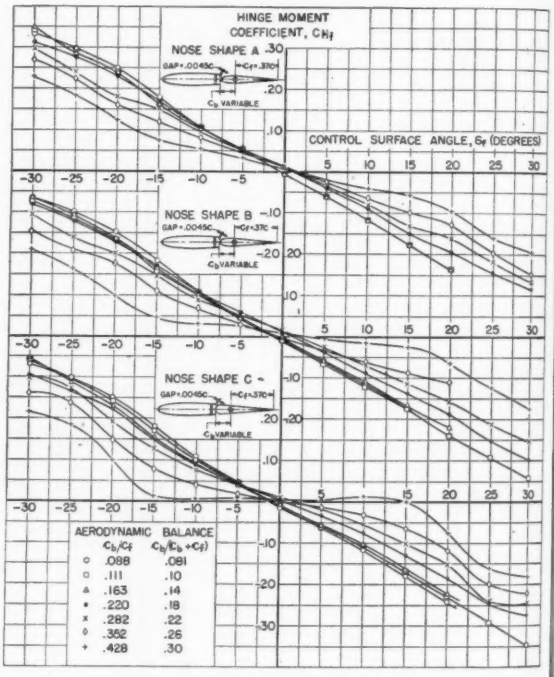

Fig. 6. Basic hinge moment curves at $\alpha = 0°$ for model of Fig. 4 with changes in aerodynamic balance and nose shape.

No attempt was made to correct data for tunnel-wall interference in view of the use of end plates, since interference corrections for a wing with end plates were not known. Corrections were made, however, for tare moment. Tests were conducted at a wind speed of 132 m.p.h. corresponding to a Reynolds Number based on total chord of 2,200,000. Hinge-moment data ob-

tained from the several balance nose shapes and amounts of overhang were plotted in the form shown in Fig. 6 ($\alpha = 0°$) for angles of attack of 0°, 5°, 10°, 15°, and 20°.

Control Surface Icing Tests

Through the courtesy of The B. F. Goodrich Company, refrigerated wind-tunnel tests were made in June, 1937, on the 2-ft. chord control surface model of Fig. 4 using various balance nose shapes and amounts of overhang. Since the object of these tests was to determine where and how ice would form on the various movable surface noses, wax impressions were taken where ice became of appreciable thickness and plaster casts were made. By starting each run at the same temperature and keeping the duration constant, comparisons between various nose ice formations could be made.

Photostats of the plaster casts have been reduced in size and are represented in Fig. 7 for $\alpha = 0°$. Although it was originally intended to duplicate ice formations obtained on the several nose shapes and to measure hinge moments in the wind tunnel, this was never done. The results from the ice tunnel, therefore, must necessarily remain qualitative in nature.

Control Surface Pressure Distribution

In connection with the structural design of one particular airplane, it was necessary to obtain representative pressure distributions over the vertical surface with and without rudder aerodynamic balance. Wind-tunnel tests were conducted at GALCIT on a complete scale model equipped to measure pressures on fin and rudder at various angles of rudder deflection and yaw. Pressure distributions for the mean vertical surface airfoil section are shown in Fig. 8 for a test Reynolds Number of 870,000 based on the above chord. These data are presented as a matter of interest in showing the effect of aerodynamic nose balance upon the pressure distribution over a representative control surface section.

Analysis of Data

Theory

The equations for the lift and hinge-moment characteristics of a control surface with finite aspect ratio under the assumptions of the lifting-line theory and for an elliptic span loading may be written in the following differential form:

$$dC_L = C_{L_\alpha}\, d\alpha + C_{L_\delta}\, d\delta \qquad (1)$$

$$dC_H = C_{H_\alpha}\, d\alpha + C_{H_\delta}\, d\delta \qquad (2)$$

From Eqs. (1) and (2)

$$C_{H_\alpha} = \left(\frac{dC_H}{dC_L}\right)_\delta C_{L_\alpha} = \left(\frac{dc_h}{dc_l}\right)_\delta C_{L_\alpha} \qquad (3)$$

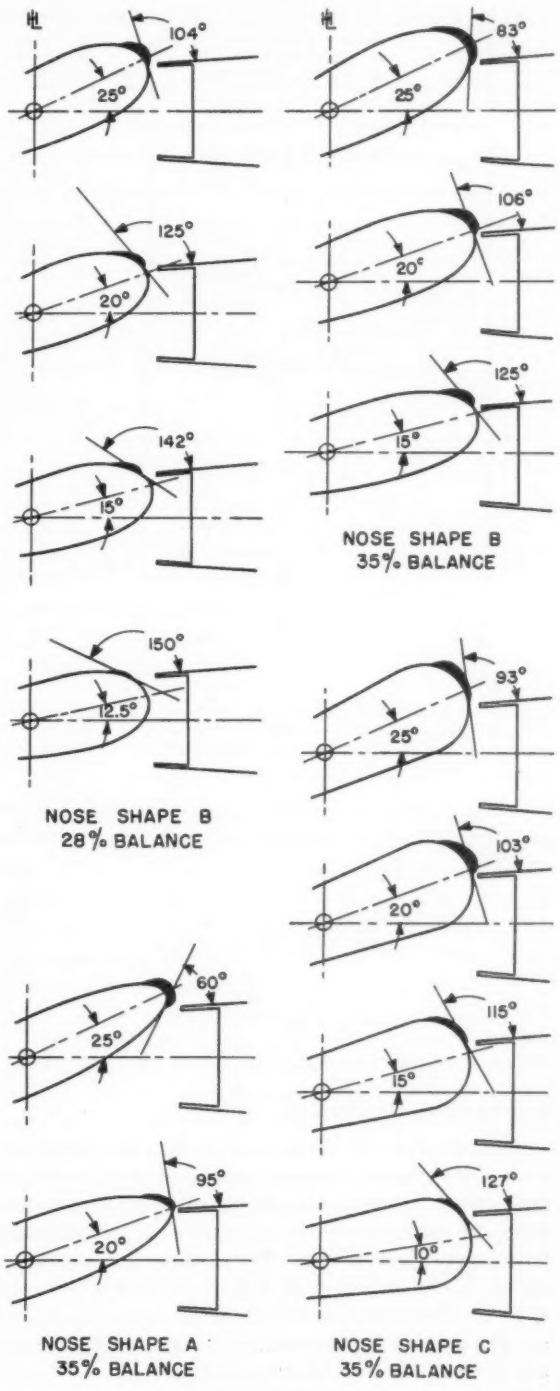

FIG. 7. Ice formations on a movable control surface with variations in aerodynamic balance and nose shape. Tests were made in the Goodrich ice tunnel using model of Fig. 4 at zero angle of attack.

From Eq. (2)

$$C_{H_\delta} = (dC_H/d\delta) - C_{H_\alpha}(d\alpha/d\delta) \qquad (4)$$

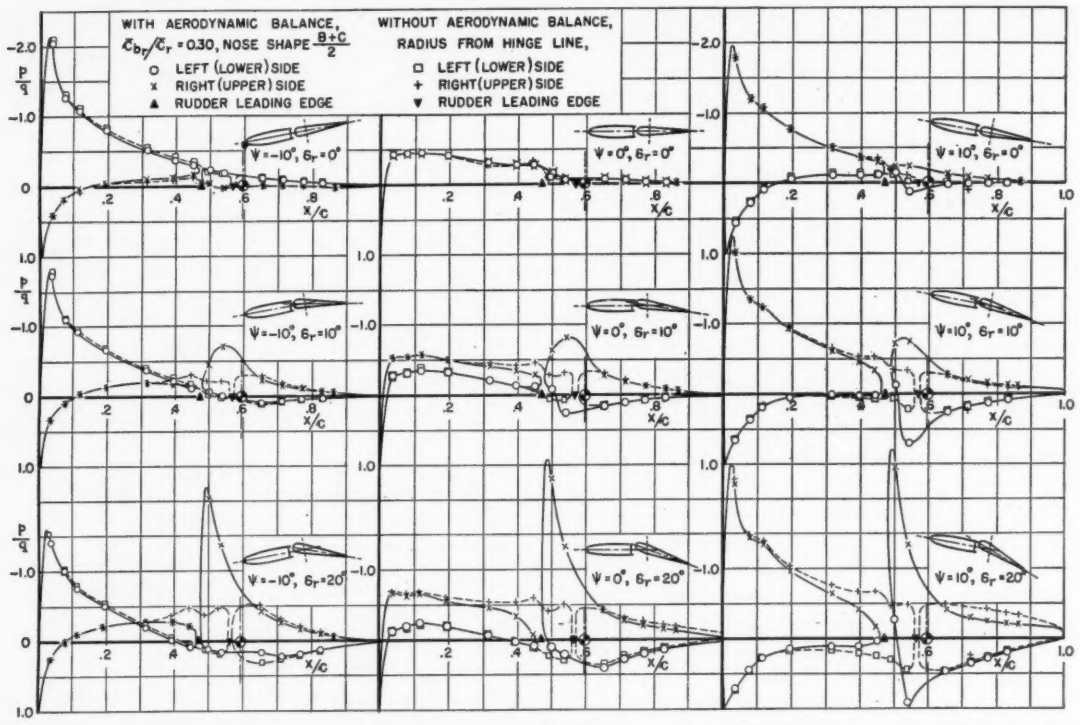
WITH AERODYNAMIC BALANCE, $\bar{c}_{b_r}/\bar{c}_r$ = 0.30, NOSE SHAPE $\frac{B+C}{2}$
LEFT (LOWER) SIDE
RIGHT (UPPER) SIDE
RUDDER LEADING EDGE
WITHOUT AERODYNAMIC BALANCE, RADIUS FROM HINGE LINE,
LEFT (LOWER) SIDE
RIGHT (UPPER) SIDE
RUDDER LEADING EDGE
$\frac{P}{q}$
x/c
ψ = −10°, δr = 0°
ψ = 0°, δr = 0°
ψ = 10°, δr = 0°
ψ = −10°, δr = 10°
ψ = 0°, δr = 10°
ψ = 10°, δr = 10°
ψ = −10°, δr = 20°
ψ = 0°, δr = 20°
ψ = 10°, δr = 20°

FIG. 8. Representative pressure distributions obtained from the GALCIT 10-ft. wind tunnel on the mean airfoil section of a vertical surface at various angles of yaw and rudder deflection with and without aerodynamic balance. Airfoil section and hinge locations shown in Fig. 18, Airplane No. 2. Test Reynolds Number 870,000. Gap = 0.0023C.

Substituting Eq. (3) in Eq. (4) and fixing $d\alpha/d\delta$ by the condition that C_L be constant during the variation in α and δ, Eq. (4) becomes,

$$C_{H_\delta} = \left(\frac{dc_h}{d\delta}\right)_{cl} - \left(\frac{dc_h}{dc_l}\right)_\delta \left(\frac{d\alpha}{d\delta}\right)_{cl} C_{L_\alpha} \tag{5}$$

where

$$(dC_H/d\delta)_{C_L} = (dc_h/d\delta)_{cl} \tag{6}$$

under the above assumptions.

Empiric Correction Factors

Using the lift and hinge-moment data from the basic wind-tunnel model, necessary cross plots were made and slopes were measured so that empiric correction factors could be determined for variations in aerodynamic balance and nose shape. These slopes were read between the limits $-10° < \delta < +10°$ and $0° < \alpha < +10°$. The correction factors, designated as η_α, η_δ, and η_λ, are applied to the section coefficients from thin-airfoil theory in the following manner:

$$(d\alpha/d\delta)_{C_L} = \eta_\lambda (d\alpha/d\delta)_{cl} \tag{7}$$

$$C_{H_\alpha} = \eta_\alpha (dc_h/dc_l)_\delta C_{L_\alpha} \tag{8}$$

$$C_{H_\delta} = \eta_\delta \left(\frac{dc_h}{d\delta}\right)_{cl} - \eta_\lambda \left(\frac{d\alpha}{d\delta}\right)_{cl} \left[\eta_\alpha \left(\frac{dc_h}{dc_l}\right)_\delta C_{L_\alpha}\right] \tag{9}$$

The section parameters, $(d\alpha/d\delta)_{cl}$, $(dc_h/dc_l)_\delta$, and $(dc_h/d\delta)_{cl}$ are obtained from Fig. 10. Correction factors are given in Fig. 9 for various nose shapes and amounts of overhang. Since these factors are independent of aspect ratio only under the assumptions of the lifting-line theory and for an elliptic span loading, their use can be considered to give strictly accurate results only for the control surface configuration tested. Design experience, however, has indicated that η_α, η_δ, and η_λ may be used with reasonable accuracy over the normal range of aspect ratios for control surfaces having the airfoil section of Fig. 2 and proportional plan form.

As an indication of the accuracy that can be expected, comparisons were made between calculations and scale airplane model tests where movable control surface hinge moments were measured. Agreement is shown in Fig. 11 where calculated values of C_{H_α} and C_{H_δ} are compared with those obtained from complete model empennages with control surface aspect ratios ranging from 1.5 to 5.0. It is indicated that a reasonable approximation of hinge-moment parameters may be expected using the factors of Fig. 9. C_{L_α} for the finite-span model surfaces was obtained from the relation

$$C_{L_\alpha} = p\left[\frac{a_0}{1 + (ra_0/\pi AR_e)}\right]\frac{\pi}{180} \tag{10}$$

AR_e, p, and r depend upon the type of control surface design as follows:

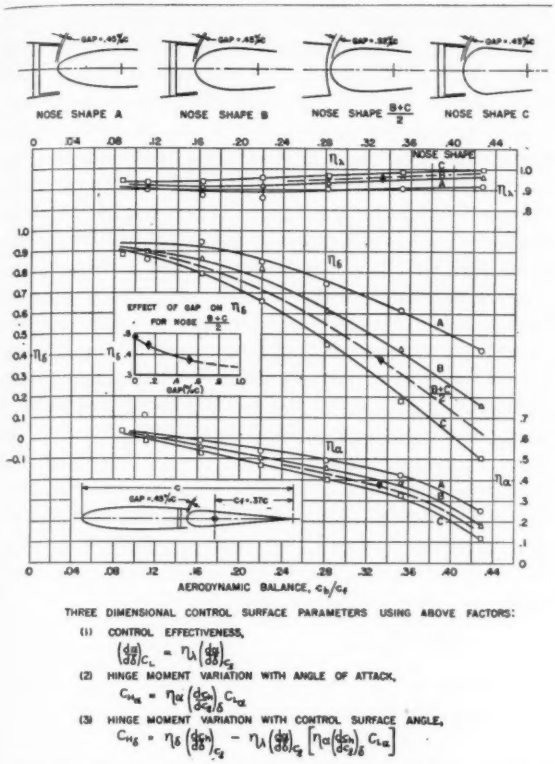
NOSE SHAPE A
NOSE SHAPE B
NOSE SHAPE (B+C)/2
NOSE SHAPE C
AERODYNAMIC BALANCE, c_b/c_f
THREE DIMENSIONAL CONTROL SURFACE PARAMETERS USING ABOVE FACTORS:
(1) CONTROL EFFECTIVENESS,
$\left(\frac{d\alpha}{d\delta}\right)_{C_L} = \eta_\lambda \left(\frac{d\alpha}{d\delta}\right)_{c_l}$
(2) HINGE MOMENT VARIATION WITH ANGLE OF ATTACK,
$C_{H_\alpha} = \eta_\alpha \left(\frac{dc_h}{dc_l}\right)_\delta C_{l_\alpha}$
(3) HINGE MOMENT VARIATION WITH CONTROL SURFACE ANGLE,
$C_{H_\delta} = \eta_\delta \left(\frac{dc_h}{d\delta}\right)_{c_l} - \eta_\lambda \left(\frac{d\alpha}{d\delta}\right)_{c_l} \left[\eta_\alpha \left(\frac{dc_h}{dc_l}\right)_\delta C_{l_\alpha}\right]$

FIG. 9. Factors η_α, η_δ, and η_λ used for obtaining control surface hinge moment and effectiveness parameters when aerodynamic balance and nose shape are varied.

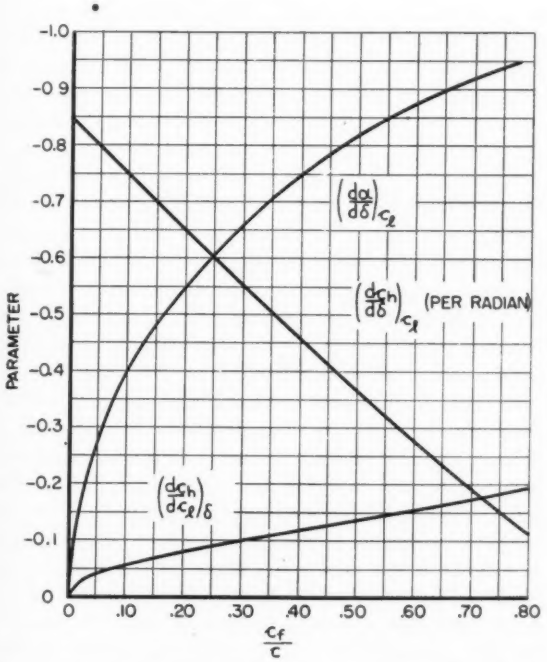

FIG. 10. Theoretic control surface parameters for simply hinged flaps. Multiplicative factors η_α, η_δ, and η_λ give corrected parameters for the aerodynamic balance variations shown in Fig. 3 using the airfoil section of Fig. 2.

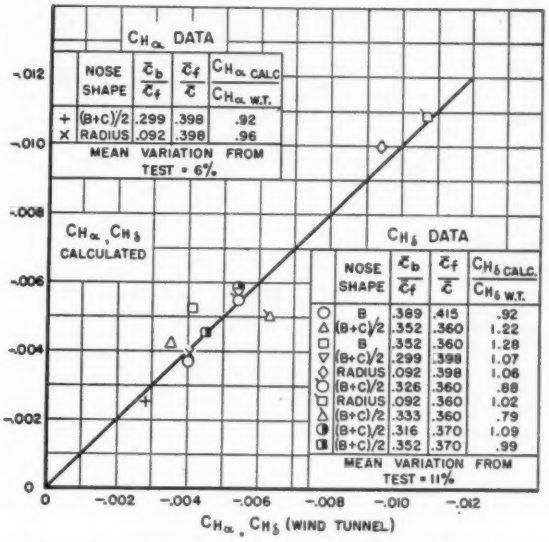
C_{H_α} DATA
NOSE SHAPE
$\frac{\bar{c}_b}{\bar{c}_f}$
$\frac{\bar{c}_f}{\bar{c}}$
C_{H_α} CALC / C_{H_α} W.T.
+ (B+C)/2 .299 .398 .92
× RADIUS .092 .398 .96
MEAN VARIATION FROM TEST = 6%
C_{H_α}, C_{H_δ} CALCULATED
C_{H_δ} DATA
NOSE SHAPE
C_{H_δ} CALC / C_{H_δ} W.T.
○ B .389 .415 .92
△ (B+C)/2 .352 .360 1.22
□ B .352 .360 1.28
▽ (B+C)/2 .299 .398 1.07
◇ RADIUS .092 .398 1.06
⬡ (B+C)/2 .326 .360 .88
□ RADIUS .092 .360 1.02
△ (B+C)/2 .333 .360 .79
◑ (B+C)/2 .316 .370 1.09
◨ (B+C)/2 .352 .370 .99
MEAN VARIATION FROM TEST = 11%
C_{H_α}, C_{H_δ} (WIND TUNNEL)

FIG. 11. Comparison of hinge moment parameters $C_{H\alpha}$ and $C_{H\delta}$ obtained from calculations and wind-tunnel tests showing the accuracy that may be expected using the factors η_α, η_δ, and η_λ.

$AR_{H_\delta} = AR_H$, p variable with single vertical surfaces
$AR_{H_\delta} = AR_H$, r variable, $p = 1.0$ with double vertical surfaces
$AR_{V_\delta} = 1.55\, AR_V$, $p = 1.0$ with single vertical surfaces
$AR_{V_\delta} = AR_V$, $p = 1.0$ with double vertical surfaces

Parameters p and r are found in Fig. 4 of reference 2.

The nose shape adopted for design and used in most cases on the various model control surfaces was intermediate between shapes B and C, designated as (B + C)/2. This shape is shown in Fig. 2 with ordinates given in Table II. Tests on the basic model (Fig. 4) were made with this nose shape and one value of aerodynamic balance, $\bar{c}_b/\bar{c}_f = 0.33$.

Correction factors for other values of overhang are taken intermediate between those for shapes B and C as shown in Fig. 9. Agreement between this interpolated curve and actual test points on complete models with control surfaces having nose shape (B + C)/2 is shown in Fig. 12. Considering variations in hinge-line location, the comparison is reasonably good. In determining η_α and η_δ from wind-tunnel tests on the complete models, it was assumed that the dynamic pressure at the tail equaled that in the free stream.

Design Factors Affecting the Choice of Aerodynamic Balance

Control Forces

Obviously, the primary purpose for using aerodynamic balance on movable control surfaces is to reduce control forces. Through choice of nose shape and amount of balance overhang, a considerable range of hinge moment adjustment is available, although defi-

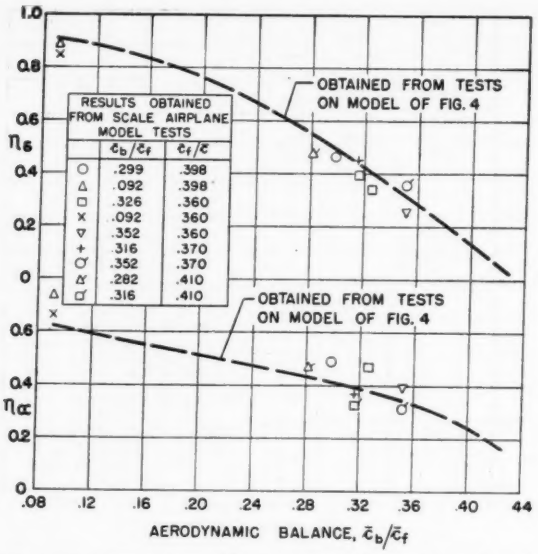

FIG. 12. Comparison of hinge moment factors η_α and η_δ obtained from tests on the model of Fig. 4 and tests on scale airplane models having control surfaces with balance nose shape (B+C)/2.

nitely restricted by other control surface design requirements. In the case of modern airplanes characterized by relatively wide speed ranges, it will undoubtedly be impossible to solve all the control-force problems satisfactorily through the use of aerodynamic balance alone. Some hinge-moment reduction can be effected, however, thus resulting in a more efficient control system by virtue of lighter design loads. In the case of an extremely large aircraft, hinge-moment reduction will add to flight safety in the event of power boost failure, since the pilot can more easily control the airplane directly through his own strength.

As a means of presenting what can be accomplished, three representative airplane designs with gross weights varying from 15,000 to 60,000 lbs. have been studied with respect to elevator stick force per unit normal acceleration in pull-outs. For each design the horizontal surfaces were chosen to satisfy the longitudinal stability and control requirements of the particular case, using the modified airfoil section of Fig. 2 and proportional horizontal surface plan form. Elevator aerodynamic balance overhang and nose shape were then varied, giving the force changes shown in Fig. 14. These changes were computed using the empiric correction factors of Fig. 9, a common c.g. location of 25 per cent M.A.C. (mean aerodynamic chord), and sea-level altitude. Based upon recent control-force requirements, values of stick force per unit acceleration should be 10, 30, and 45 for the one-, two-, and four-engined cases, respectively. Although inspection of each example presented in Fig. 14 shows that the above-required values of stick force per unit acceleration could be obtained with some combination of elevator nose shape and balance overhang, certain design limitations exist and will be discussed below.

The aerodynamic balance designs recommended for the various cases incorporate the intermediate nose shape (B + C)/2, with values of $\bar{c}_b/\bar{c}_f = 0.33$, 0.33, and 0.37. From Fig. 14 these balance combinations give stick forces under acceleration of 20, 30, and 110 lbs. per g, thus indicating that elevator control forces are in excess of requirements in the first and third cases. Since a common c.g. position of 25 per cent M.A.C. may not represent final comparative normal loading conditions for one-, two-, and four-engined airplanes, the relative magnitude of these forces may change. It may be concluded from Fig. 14, however, that difficulty can be expected in meeting elevator control-force requirements for all cases through the use of balance overhang alone. Nevertheless, the effectiveness of the subject method in reducing forces can be clearly shown for the three examples through a comparison of elevator control forces per unit acceleration with and without aerodynamic balance. The values are 50, 80, and 600 with a radius balance nose in comparison with values of 20, 30, and 110 which can be obtained with reasonable values of aerodynamic balance.

Control Effectiveness

In order to provide adequate control effectiveness, particularly at low air speeds, without an excess of movable surface area, it is considered best to use the highest allowable movable control surface angle consistent with a continuous increase in lift. This design consideration materially affects the choice of aerodynamic balance, since it is evident from the basic wind-tunnel data that for a given hinge-moment reduction the blunt-nose-shaped balance causes premature stall, while the sharp-nose-shaped balance gives hinge-moment reversal at high angles. The tendency to stall off the control surface nose at high angles is greatly affected by the surface angle of attack. At $\alpha = 0°$, for example, as in the case of a rudder on a twin-engined airplane after engine failure when trimmed for zero sideslip, the stall occurs much earlier than when the angle of attack of the surface is opposed to the flap deflection as in the case of an elevator during landing or the rudder in a sideslip. This difference usually limits the amount of aerodynamic balance which can be used on a rudder in comparison with that on an elevator.

In order to illustrate further the effects of this consideration on the choice of aerodynamic balance, curves of hinge moment and lift characteristics vs. control surface angle were analyzed from the basic data. The point at which the movable surface stalled was taken as that where either an abrupt increase in hinge moment or a break in lift occurred. Results of this study are given in Figs. 13a and 13b in the form of stall boundaries, limiting the values of elevator aerodynamic balance for the particular case of a horizontal surface in the landing attitude, $\alpha = 10°$. A comparison of these figures indicates a required reduction in aerodynamic balance as the maximum up-travel of the elevator is in-

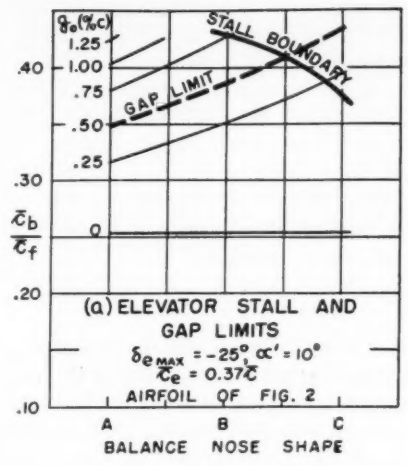

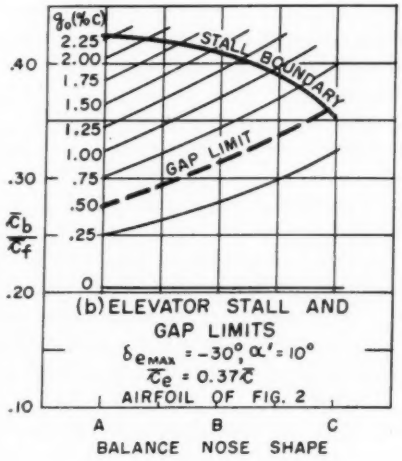

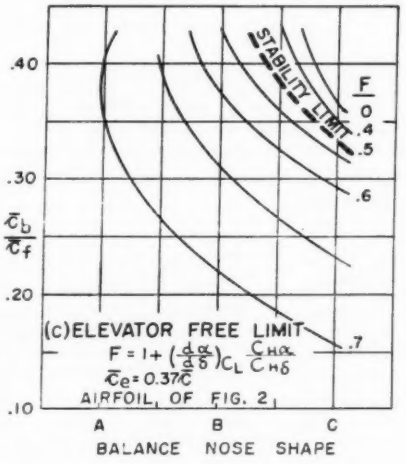

FIG. 13. Practical design limits applicable to elevator aerodynamic balance and nose shape.

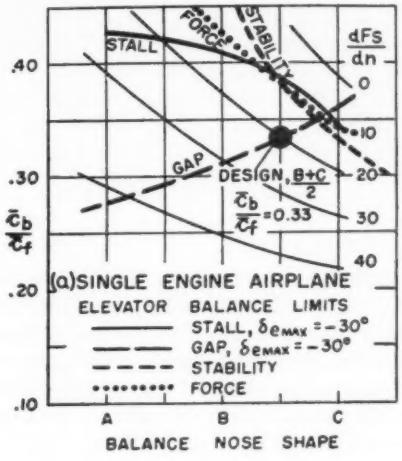

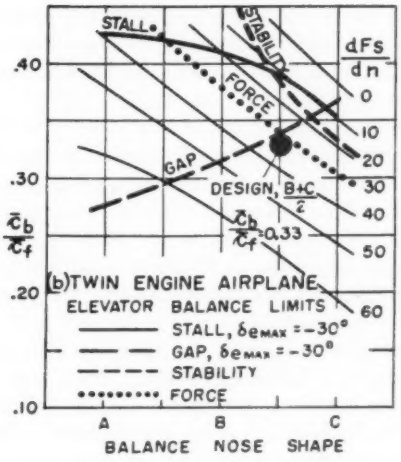

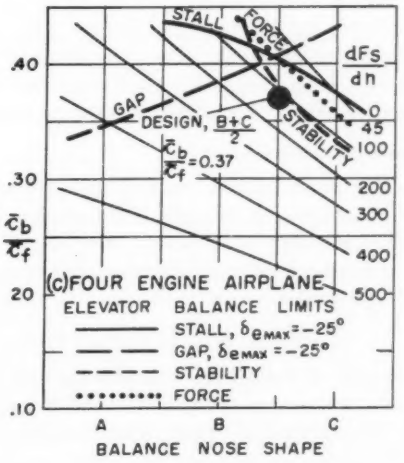

FIG. 14. Application of aerodynamic balance limits to representative airplanes showing relationship to elevator stick force per unit normal acceleration and recommended aerodynamic balance.

creased ($\delta_{emax.}$ from $-25°$ to $-30°$). Although advantage may sometimes be taken of less maximum elevator travel to effect a stick-force reduction through resulting increase in mechanical advantage as well as through increased aerodynamic balance, other design considerations usually demand that all available control surface effectiveness from angular throw be obtained.

Overtravel Gap

If a control surface is deflected beyond a certain angle, unporting of the nose leading edge outside the airfoil contour will be sufficient to cause a sudden hinge-moment reversal, particularly when the angle of attack on the surface opposes that of the control. This brings another consideration into the picture, the amount of allowable overtravel gap (g_0). Whereas with a sharp-nose shape and high balance overhang, maximum throw will be severely limited by this consideration, a blunt-nose shape with less overhang will permit more angular travel. Although no quantitative data are available to establish a gap limit, design experience indicates that the value of g_0 should be taken as $\leqq 0.50$ per cent c for satisfactory hinge-moment characteristics at full movable surface throw. The relationship of this limit to variation in balance overhang and nose shape is shown for the case of an elevator in Figs. 13a and 13b for limiting travels of $\delta_{emax.} = -25°$ and $-30°$. It is apparent from these figures that a fixed value of overtravel gap limits particularly the amount of overhang which can be used as balance nose shape is sharpened.

It is possible to increase the allowable overtravel gap by the use of a fabric seal between fixed and movable surfaces in cases where maximum control effectiveness has not been obtained. Here the difficulty of designing and manufacturing a satisfactory seal must be compared with the aerodynamic advantages gained. These will be discussed later in the paper. In order to prevent exceeding the limiting angular travel of a control surface once the allowable value of overtravel gap has been chosen, it is imperative that stops be furnished at the control surface rather than in the cockpit.

Free-Control Stability

A further consideration bearing directly upon the choice of aerodynamic balance is the degree to which control-free stability is adversely affected. The ratio of free- to fixed-control stability due to tail surfaces only may be expressed as

$$F = 1 + (d\alpha/d\delta)c_L(C_{H_\alpha}/C_{H_\delta}) \qquad (11)$$

The variation of F with aerodynamic balance is shown in Fig. 13c, where a pronounced decrease in free-control stability is evident with hinge-moment reduction. The factor, F, decreases both as the balance nose shape is changed from sharp to blunt and as the amount of balance overhang is increased. This loss in free-control stability with proportional balance overhang must be considered during the initial stages of control surface design in relation to the advantages of control-force reduction. For the study of balance limits applicable to an elevator (Fig. 14) a value of $F = 0.5$ was chosen to represent the maximum loss in free-control longitudinal stability which could be exchanged for desirable control force reduction on a large airplane. This limit is closely approached in the case of the four-engined airplane (Fig. 14c) where a high degree of hinge-moment reduction is required to bring control forces within the fixed limit of pilot strength.

Icing

Another factor entering into the design of a movable control surface is the degree to which the balance nose is subject to critical ice formation. The results of the Goodrich icing tests shown in Fig. 7 indicate that formations of a critical nature can form on the various balance noses, particularly at high control surface angles. For example, with $\delta_f = 20°$ the ice formations on all nose shapes with 35 per cent balance are such that the control surface probably could not be returned to neutral. In order to evaluate the degree to which the various noses are subject to icing, the angle, β, was measured for all cases. A purely qualitative inspection indicates that when this angle is greater than 135° a critical condition will probably result. Upon this basis the limiting control surface angles shown in Fig. 15 for balance overhang and nose-shape variations were obtained.

The primary instance where icing possibilities must be avoided is in the case of the rudder of a multiengined airplane. After failure of an engine, the asymmetric thrust must be trimmed out for a considerable length of time well within the limits for critical ice formation to occur. In designing the rudder for such a case it is necessary that the effectiveness be adequate to trim for the most critical engine failure condition with a rudder angle such that $\beta \leqq 135°$. Using representative two- and four-engined airplane designs with rudders having the (B + C)/2 nose-shape and balance overhang values of 0.28 and 0.33, respectively, the rudder angles

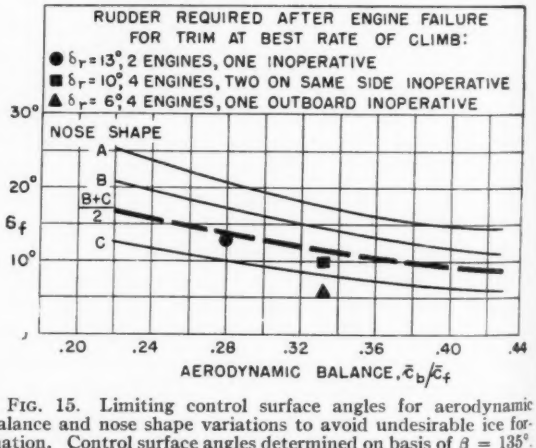

FIG. 15. Limiting control surface angles for aerodynamic balance and nose shape variations to avoid undesirable ice formation. Control surface angles determined on basis of $\beta = 135°$. [Examples are with (B + C)/2 nose shape.]

for various conditions of engine failure are shown in Fig. 15. Although the twin-engined case after failure of one engine is the most critical, the rudder effectiveness has been chosen such that δ_r does not exceed the icing limit. Because the rudder in the case of the four-engined airplane was necessarily designed for the critical condition of two engines inoperative on the same side, ample margin exists for the more usual case of only one outboard engine inoperative ($\delta_r = 6°$).

Effect of Modifications

Although the factors given in Fig. 9 specifically apply only to control surfaces having the NACA 0012 section modified to 10.7 per cent c thickness by 12 per cent c extension with flat-sided afterbody and with hinge line at 63 per cent c, design applications have indicated that the data presented may be used with reasonable approximation for cases varying from the above airfoil section. Since application of these data to other cases must be accompanied by good judgment and the full realization of possible errors, a brief discussion is included treating the effects of various modifications and their relative merits based principally upon Douglas testing and design experience.

Airfoil Section

Reasons for selecting the NACA 0012 airfoil as the basic section have already been discussed. Other than leading edge radius, which exerts a powerful influence upon the stalling characteristics, the most important airfoil section properties that may be altered are the maximum thickness and chordwise location of maximum thickness. For a control surface without aerodynamic balance, increasing the thickness or moving the maximum ordinate aft will generally reduce the factors η_α, η_δ, and η_λ. The principal effect of these changes is to increase the included angle at the trailing edge with resulting decrease in circulation and alteration in pressure distribution, particularly over the movable control surface afterbody. From DC-2 flight tests and later model tests, changes in airfoil contour forward of the movable surface appear to have minor effects on control surface parameters. It is reasonable to expect, however, that the effects of viscosity will become more pronounced as airfoil thickness is increased, making it necessary to interpret carefully wind-tunnel results on thicker surfaces.

For an aerodynamically balanced surface the above reductions in factors η_α, η_δ, and η_λ are partially offset by a decrease in balance effectiveness. Increasing the thickness of the balance nose section, whether by moving the maximum ordinate aft or by increasing airfoil thickness, reduces the amount of balance which will project outside the airfoil contour for a given δ_f, with the inevitable result that the balancing pressures are reduced. Thus, Fig. 9 cannot be used to calculate accurately the effects of change in balance overhang or nose shape for airfoil sections of different thickness ratio or distribution. Since, however, the loss in balance effectiveness is offset by a corresponding reduction in the factors for an unbalanced surface, it is considered that the use of Fig. 9 for estimating hinge moments on other airfoils can be used for a rough first approximation in the absence of more specific data on the correct airfoil section.

In general, the use of airfoil sections of maximum thickness greater than 12 per cent c is not recommended for control surface design, primarily because the thicker sections indicate a greater tendency to develop "flat spots" in the hinge moment vs. angle curve near neutral, particularly when the control surface is subject to the seemingly inevitable manufacturing irregularities that move the transition point forward. For a limited range of angle of attack and control surface deflection, C_{H_α} may become positive and C_{H_δ} extremely small. With control system friction, the floating tendency of a control surface having this combination of parameters may give rise to objectionable oscillations.

Afterbody Shape

Considerable variation in the hinge-moment parameters of a control surface may be obtained through

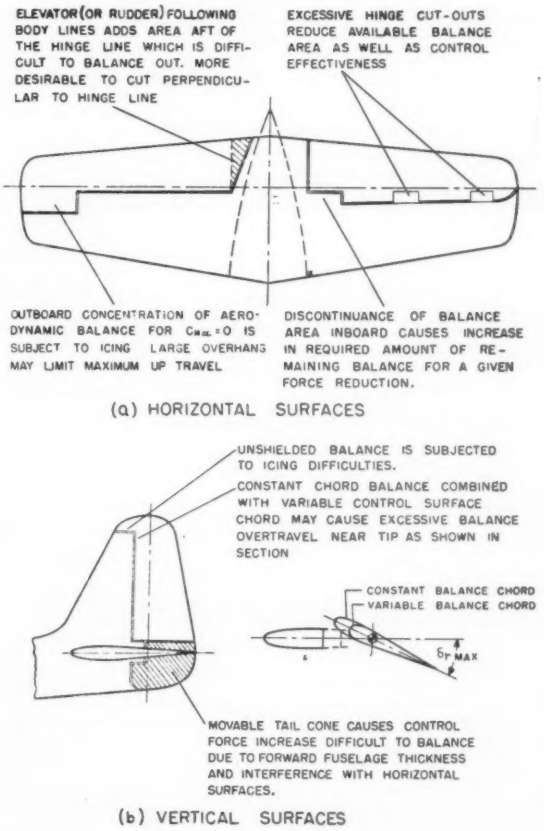
ELEVATOR (OR RUDDER) FOLLOWING BODY LINES ADDS AREA AFT OF THE HINGE LINE WHICH IS DIFFICULT TO BALANCE OUT. MORE DESIRABLE TO CUT PERPENDICULAR TO HINGE LINE
EXCESSIVE HINGE CUT-OUTS REDUCE AVAILABLE BALANCE AREA AS WELL AS CONTROL EFFECTIVENESS
OUTBOARD CONCENTRATION OF AERODYNAMIC BALANCE FOR $C_{H_\alpha}=0$ IS SUBJECT TO ICING LARGE OVERHANG MAY LIMIT MAXIMUM UP TRAVEL
DISCONTINUANCE OF BALANCE AREA INBOARD CAUSES INCREASE IN REQUIRED AMOUNT OF REMAINING BALANCE FOR A GIVEN FORCE REDUCTION.
(a) HORIZONTAL SURFACES
UNSHIELDED BALANCE IS SUBJECTED TO ICING DIFFICULTIES.
CONSTANT CHORD BALANCE COMBINED WITH VARIABLE CONTROL SURFACE CHORD MAY CAUSE EXCESSIVE BALANCE OVERTRAVEL NEAR TIP AS SHOWN IN SECTION
CONSTANT BALANCE CHORD
VARIABLE BALANCE CHORD
$\delta_{r\,MAX}$
MOVABLE TAIL CONE CAUSES CONTROL FORCE INCREASE DIFFICULT TO BALANCE DUE TO FORWARD FUSELAGE THICKNESS AND INTERFERENCE WITH HORIZONTAL SURFACES.
(b) VERTICAL SURFACES

FIG. 16. Design features to be avoided for maximum aerodynamic balance efficiency.

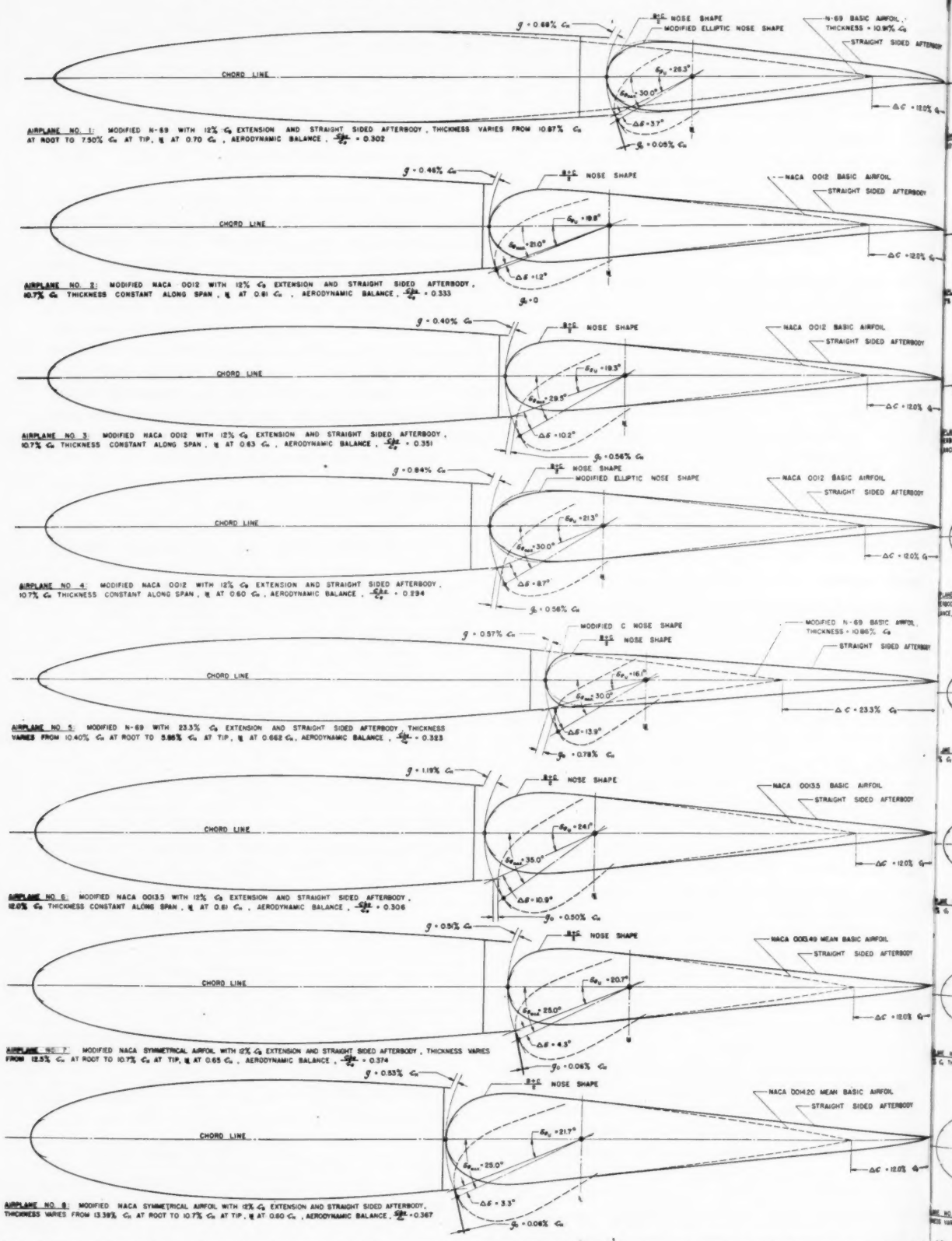
g = 0.68% c_a
NOSE SHAPE
MODIFIED ELLIPTIC NOSE SHAPE
N-69 BASIC AIRFOIL, THICKNESS = 10.9% c_a
STRAIGHT SIDED AFTERBODY
CHORD LINE
δ_{e_u} = 28.3°
$\delta_{e_{max}}$ = 30.0°
$\Delta\delta$ = 3.7°
Δc = 12.0% c_a
g_0 = 0.05% c_a
AIRPLANE NO. 1: MODIFIED N-69 WITH 12% c_a EXTENSION AND STRAIGHT SIDED AFTERBODY, THICKNESS VARIES FROM 10.87% c_a AT ROOT TO 7.50% c_a AT TIP, $\frac{y}{b/2}$ AT 0.70 c_a, AERODYNAMIC BALANCE, $\frac{c_b z}{c_a}$ = 0.302
g = 0.48% c_a
NOSE SHAPE
NACA 0012 BASIC AIRFOIL
STRAIGHT SIDED AFTERBODY
CHORD LINE
δ_{e_u} = 19.8°
$\delta_{e_{max}}$ = 21.0°
$\Delta\delta$ = 1.2°
g_0 = 0
AIRPLANE NO. 2: MODIFIED NACA 0012 WITH 12% c_a EXTENSION AND STRAIGHT SIDED AFTERBODY, 10.7% c_a THICKNESS CONSTANT ALONG SPAN, $\frac{y}{b/2}$ AT 0.81 c_a, AERODYNAMIC BALANCE, $\frac{c_b z}{c_a}$ = 0.333
g = 0.40% c_a
NOSE SHAPE
NACA 0012 BASIC AIRFOIL
STRAIGHT SIDED AFTERBODY
CHORD LINE
δ_{e_u} = 19.3°
$\delta_{e_{max}}$ = 29.5°
$\Delta\delta$ = 10.2°
g_0 = 0.56% c_a
AIRPLANE NO. 3: MODIFIED NACA 0012 WITH 12% c_a EXTENSION AND STRAIGHT SIDED AFTERBODY, 10.7% c_a THICKNESS CONSTANT ALONG SPAN, $\frac{y}{b/2}$ AT 0.63 c_a, AERODYNAMIC BALANCE, $\frac{c_b z}{c_a}$ = 0.351
g = 0.84% c_a
NOSE SHAPE
MODIFIED ELLIPTIC NOSE SHAPE
NACA 0012 BASIC AIRFOIL
STRAIGHT SIDED AFTERBODY
CHORD LINE
δ_{e_u} = 21.3°
$\delta_{e_{max}}$ = 30.0°
$\Delta\delta$ = 8.7°
g_0 = 0.56% c_a
AIRPLANE NO. 4: MODIFIED NACA 0012 WITH 12% c_a EXTENSION AND STRAIGHT SIDED AFTERBODY, 10.7% c_a THICKNESS CONSTANT ALONG SPAN, $\frac{y}{b/2}$ AT 0.60 c_a, AERODYNAMIC BALANCE, $\frac{c_b z}{c_a}$ = 0.294
g = 0.57% c_a
MODIFIED C NOSE SHAPE
NOSE SHAPE
MODIFIED N-69 BASIC AIRFOIL, THICKNESS = 10.86% c_a
STRAIGHT SIDED AFTERBODY
CHORD LINE
δ_{e_u} = 16.1°
$\delta_{e_{max}}$ = 30.0°
$\Delta\delta$ = 13.9°
Δc = 23.3% c_a
g_0 = 0.78% c_a
AIRPLANE NO. 5: MODIFIED N-69 WITH 23.3% c_a EXTENSION AND STRAIGHT SIDED AFTERBODY, THICKNESS VARIES FROM 10.40% c_a AT ROOT TO 5.86% c_a AT TIP, $\frac{y}{b/2}$ AT 0.662 c_a, AERODYNAMIC BALANCE, $\frac{c_b z}{c_a}$ = 0.323
g = 1.19% c_a
NOSE SHAPE
NACA 0013.5 BASIC AIRFOIL
STRAIGHT SIDED AFTERBODY
CHORD LINE
δ_{e_u} = 24.1°
$\delta_{e_{max}}$ = 35.0°
$\Delta\delta$ = 10.9°
g_0 = 0.50% c_a
AIRPLANE NO. 6: MODIFIED NACA 0013.5 WITH 12% c_a EXTENSION AND STRAIGHT SIDED AFTERBODY, 12.0% c_a THICKNESS CONSTANT ALONG SPAN, $\frac{y}{b/2}$ AT 0.81 c_a, AERODYNAMIC BALANCE, $\frac{c_b z}{c_a}$ = 0.306
g = 0.91% c_a
NOSE SHAPE
NACA 0013.49 MEAN BASIC AIRFOIL
STRAIGHT SIDED AFTERBODY
CHORD LINE
δ_{e_u} = 20.7°
$\delta_{e_{max}}$ = 25.0°
$\Delta\delta$ = 4.3°
g_0 = 0.06% c_a
AIRPLANE NO. 7: MODIFIED NACA SYMMETRICAL AIRFOIL WITH 12% c_a EXTENSION AND STRAIGHT SIDED AFTERBODY, THICKNESS VARIES FROM 12.5% c_a AT ROOT TO 10.7% c_a AT TIP, $\frac{y}{b/2}$ AT 0.65 c_a, AERODYNAMIC BALANCE, $\frac{c_b z}{c_a}$ = 0.374
g = 0.83% c_a
NOSE SHAPE
NACA 0014.20 MEAN BASIC AIRFOIL
STRAIGHT SIDED AFTERBODY
CHORD LINE
δ_{e_u} = 21.7°
$\delta_{e_{max}}$ = 25.0°
$\Delta\delta$ = 3.3°
g_0 = 0.06% c_a
AIRPLANE NO. 8: MODIFIED NACA SYMMETRICAL AIRFOIL WITH 12% c_a EXTENSION AND STRAIGHT SIDED AFTERBODY, THICKNESS VARIES FROM 13.39% c_a AT ROOT TO 10.7% c_a AT TIP, $\frac{y}{b/2}$ AT 0.60 c_a, AERODYNAMIC BALANCE, $\frac{c_b z}{c_a}$ = 0.367

FIG. 17. Representative horizontal surface mean airfoil sections from a number of full-scale airplanes upon which elevator aerodynamic ba[lan]cing has been successfully employed.

18. Repre

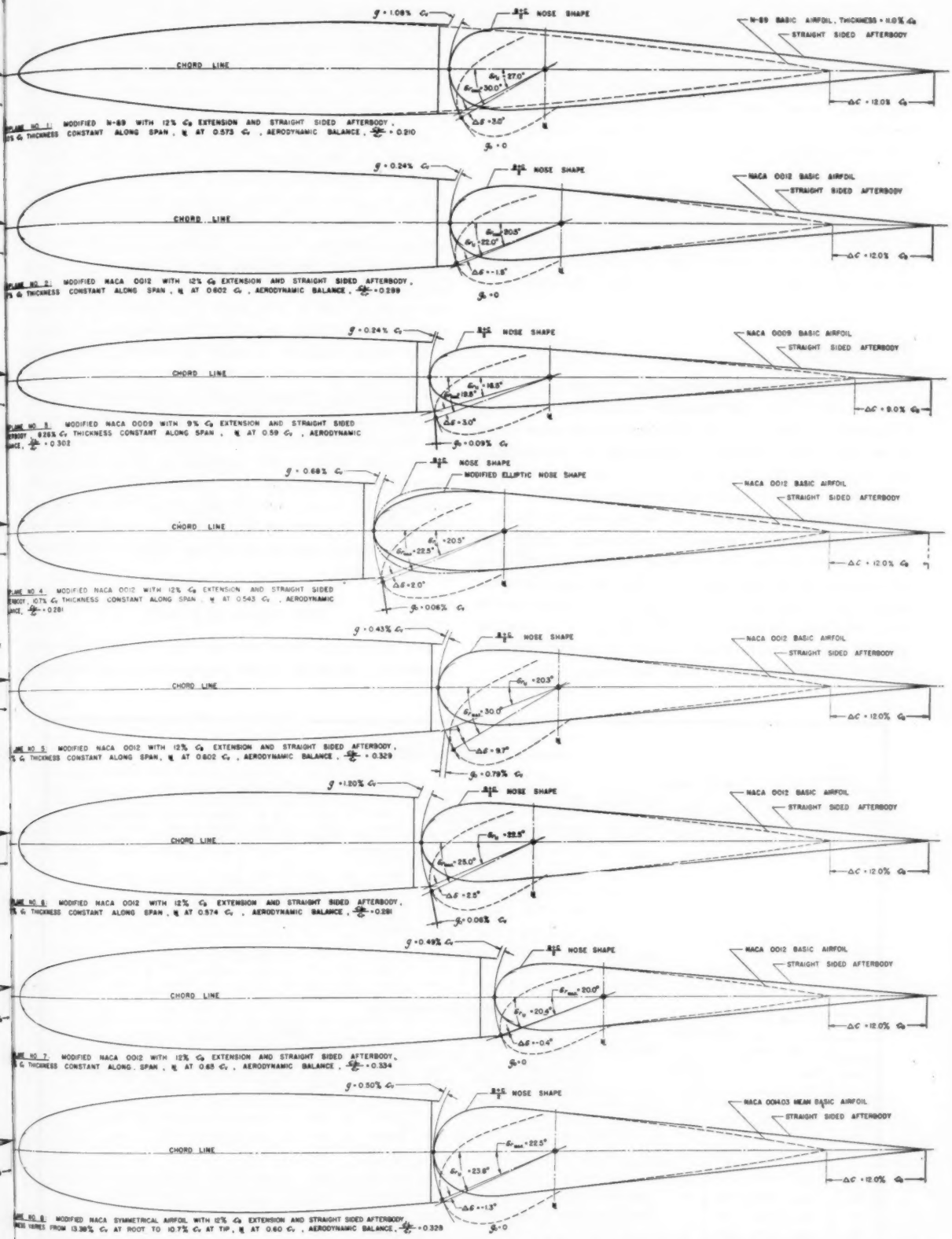

Fig. 18. Representative vertical surface mean airfoil sections from a number of full-scale airplanes upon which rudder aerodynamic balancing has been successfully employed.

alteration of afterbody shape. Data in Fig. 9 are specifically applicable to flat-sided control surfaces having a trailing edge angle of 10° and therefore cannot be applied with any degree of accuracy to control surfaces with afterbodies convexed, concaved, thickened, bevelled, or stripped. In general, any modification that increases the trailing edge angle will decrease η_α, η_δ, and η_λ as in the case of an increase in thickness. Although a convex-sided afterbody may be effectively used to change hinge-moment parameters, particularly to reduce C_{H_α}, a movable control surface with this shape is considered more susceptible to undesirable oscillations and to a loss in control "feel" through neutral.

Hinge Location

The empiric correction factors, η_α, η_δ, and η_λ, are used in conjunction with the theoretic parameters of Fig. 10 to permit a variation in movable surface per cent chord to be taken into account in obtaining the parameters, $(dc_h/dc_l)_\delta$, $(dc_h/d\delta)_{cl}$, and $(d\alpha/d\delta)_{cl}$. As c_f/c is varied, a change in aerodynamic balance effectiveness is to be expected, since the thickness in the region of the balance nose is altered with hinge-line relocation. Since test points shown in Fig. 12 for scale models do not show any consistent trend within the range of hinge locations tested, it is believed that the present method can be used without appreciable error for $\Delta c_f/c = \pm 0.04$. Rudder and elevator hinge lines used on conventional designs will probably lie within this range.

Gaps and Seals

In addition to permitting an acceptable increase in rudder or elevator angular travel, sealing the gap between a fixed and movable control surface offers a method of increasing the fixed-control stability through an increase in C_{L_α}. This increase, however, is usually obtained at the expense of a corresponding hinge-moment increase as illustrated in the auxiliary graph of Fig. 9. Here the effect of reducing control surface gap (g) is shown for (B + C)/2 nose shape and 33 per cent aerodynamic balance. Factors η_α and η_λ are not affected by gap size within the accuracy of the basic test data. The empiric factor, η_δ, however, was increased from 0.39 to 0.49 with gap change from 0.5 per cent c to a complete seal. For the horizontal surface of the single-engined example previously used, these changes amount to increases in elevator stick force per unit acceleration from 20 to 30 in exchange for an approximate 2 per cent M.A.C. rearward movement of the fixed-control longitudinal stability neutral point. Presumably some of this increase in stick force could be overcome through use of a smaller tail surface in the initial design stage. Loss in lift curve slope, C_{L_α}, would be expected to increase with larger gaps and with forward chordwise movement of gap location into a lower pressure region.

Influence on Design

For maximum aerodynamic balance efficiency it is considered advisable to use proportional control surface

TABLE III

HORIZONTAL SURFACE SECTION CHARACTERISTICS

Airplane Number	AIRFOIL SECTION: BASIC AIRFOIL Type	Root	Tip	Chord Extension (% c_R)	THICKNESS (%c) Root	Tip	TRAILING EDGE Included Angle (deg.)	Radius (% c)	ELEVATOR: Hinge Location $\bar{z}_e/\bar{z}_H$	Aerodynamic Balance $\bar{z}_{b_e}/\bar{z}_e$	Nose Shape	ANGLES (Degrees): Design Stops $\delta_{e\ max.}$°	L.E. Unporting δ_{e_u}°	Over Travel $\Delta\delta_e$°	Icing Limit $\delta_{e\ ice}$°	GAPS (% c): Minimum Clearance g	Over Travel δ_g
1	N-69	12.17	8.40	12	10.87	7.50	13.7	0.12	0.300	0.302	Modified Elliptic	-30 + 20	26.3	3.7	16.0	0.68	0.05
2	NACA	0012	0012	12	10.7	10.7	10.1	0.06	0.390	0.333	B+C/2	-21 + 18	19.8	1.2	11.7	0.46	0
3	NACA	0012	0012	12	10.7	10.7	10.1	0.12	0.370	0.351	B+C/2	-29.5 + 11.75	19.3	10.2	10.7	0.40	0.56
4	NACA	0012	0012	12	10.7	10.7	10.1	0.10	0.400	0.294	Modified Elliptic	-30 + 20	21.3	8.7	14.8	0.84	0.56
5	N-69	11.10	9.32	23.3	10.40	5.85	9.2	0.08	0.338	0.323	Modified C	-30 + 20	16.1	13.9	4.5	0.57	0.78
6	NACA	0013.5	0013.5	12	12.0	12.0	11.3	0.07	0.390	0.306	B+C/2	-35 + 20	24.1	10.9	14.7	1.19	0.50
7	NACA	0014	0012	12	12.5	10.7	11.3	0.15	0.350	0.374	B+C/2	-25 + 15	20.7	4.3	10.7	0.51	0.06
8	NACA	0015	0012	12	13.39	10.7	11.8	0.10	0.400	0.367	B+C/2	-25 + 20	21.7	3.3	11.3	0.53	0.06

TABLE IV

VERTICAL SURFACE SECTION CHARACTERISTICS

Airplane Number	AIRFOIL SECTION: BASIC AIRFOIL Type	Root	Tip	Chord Extension (% c_R)	THICKNESS (%c) Root	Tip	TRAILING EDGE Included Angle (deg.)	Radius (% c)	RUDDER: Hinge Location $\bar{z}_r/\bar{z}_v$	Aerodynamic Balance $\bar{z}_{b_r}/\bar{z}_r$	Nose Shape	ANGLES (Degrees): Design Stops $\delta_{r\ max.}$°	L.E. Unporting δ_{r_u}°	Over Travel $\Delta\delta_r$°	Icing Limit $\delta_{r\ ice}$°	GAPS (% c): Minimum Clearance g	Over Travel δ_g
1	N-69	11.20	11.20	12	10.0	10.0	11.7	0.12	0.427	0.210	B+C/2	±30	27.0	3.0	16.0	1.08	0
2	NACA	0012	0012	12	10.7	10.7	10.1	0.06	0.398	0.299	B+C/2	±20.5	22.0	-1.5	13.7	0.24	0
3	NACA	0009	0009	9	8.26	8.26	8.2	0.17	0.410	0.302	B+C/2	±19.5	16.5	3.0	10.0	0.24	0.09
4	NACA	0012	0012	12	10.7	10.7	10.1	0.07	0.457	0.281	Modified Elliptic	±22.5	20.5	2.0	15.7	0.68	0.06
5	NACA	0012	0012	12	10.7	10.7	10.1	0.14	0.398	0.329	B+C/2	±30	20.3	9.7	11.9	0.43	0.79
6	NACA	0012	0012	12	10.7	10.7	10.1	0.06	0.426	0.281	B+C/2	±25	22.5	2.5	13.7	1.20	0.06
7	NACA	0012	0012	12	10.7	10.7	10.1	0.13	0.350	0.334	B+C/2	±20	20.4	-0.4	11.0	0.49	0
8	NACA	0015	0012	12	13.39	10.7	11.8	0.08	0.400	0.328	B+C/2	±22.5	23.8	-1.3	12.9	0.50	0

plan form and section. Since balance overhang can then be chosen as a constant ratio along the span, both the amount of balance required for a given hinge-moment reduction and the overtravel gap can be minimized, thus increasing control effectiveness. To obtain completely uniform angular projection of the balance nose section outside the control surface airfoil contour all along the span, airfoil sections must necessarily be similar. In cases, however, where the root thickness has been increased for structural reasons, balance overhang or nose shape will have to be altered along the span to provide equivalent hinge-moment reduction. Proportionality of both plan form and section not only permits a closer approximation of control surface characteristics to be made from section test data but also provides a major simplification in design layout and lofting processes.

Several horizontal and vertical control surface planform variations to be avoided for maximum balance efficiency are shown in Fig. 16. It is necessary to point out that, although certain of these features have been successfully employed in control surface design, their use will not result in the best solution with respect to satisfying the aerodynamic balance design requirements previously outlined. The degree to which it is necessary to meet these requirements remains directly dependent upon the amount of hinge moment reduction desired without resorting to other means. In this respect an airplane with conventional empennage proportions and a wing area of 1,400 sq.ft. is considered representative of a conservative upper limit beyond which a satisfactory solution to the control force problem using aerodynamic balance alone cannot be expected. For designs above this arbitrary limit, however, conservative aerodynamic balance values can still be used to design advantage as follows: by reducing hinge moments that must be handled by power boost or other means; by providing means for sectional balance weight attachment, thus giving movable surface dynamic as well as static mass balance; by reducing control system loads; and by increasing the control effectiveness of a tab.

As an aid toward the application of the design principles discussed in this paper, the airfoil section characteristics for the horizontal and vertical surfaces of eight Douglas airplanes are presented in Figs. 17 and 18. Quantitative data are listed in Tables III and IV, from which representative variations may be obtained with respect to airfoil section, hinge location, balance over-hang, nose shape, limiting angular travels, and gaps.

References

[1] Jacobs, E. N., Ward, K. E., and Pinkerton, R. M., *The Characteristics of 78 Related Airfoil Sections from Tests in the Variable-Density Wind Tunnel*, N.A.C.A. T.R. No. 460, 1933.

[2] Ames, M. B., Jr., and Sears, R. I., *Determination of Control-Surface Characteristics from NACA Plain-Flap and Tab Data*, N.A.C.A. T.R. No. 721, 1941.

Erratum

In the article "Stress Analysis of Open Cylindrical Membranes" by Leon Beskin (JOURNAL OF THE AERONAUTICAL SCIENCES, Vol. 11, No. 4, p. 343, October, 1944) a mistake occured on page 350, right column, under Eq. (48). The sentence should read: "The coordinates of that point being (x_1, y_1) in respect to the shear center."

Coefficient Method for Solving the Flutter Frequency Equation*

M. V. BARTON†

The University of Texas

ABSTRACT

The flutter frequency equation for a three-degree-of-freedom system is a cubic equation with complex coefficients. The usual methods of solving this equation involve the solution of a cubic equation for every assumed value of the "reduced velocity." The coefficient method makes it possible to determine the stability of the motion from the relations of the coefficients of the frequency equation and eliminates the necessity of solving any cubic equation to determine the critical conditions. The method also makes it possible to obtain a "bracket" of the critical conditions, thereby reducing the number of trial values of the reduced velocity. The intersection of the curves indicating the critical conditions is, in general, more definitely established by the coefficient method than by other methods. The method may be easily extended to systems with more than three degrees of freedom.

INTRODUCTION

THERE HAVE BEEN many methods[1–4] devised for solving the stability determinant or the frequency equation that arises in determining the flutter speed of a portion of the aircraft structure. The equation representing the critical conditions for a three-degree-of-freedom system—for example, wing-bending, wing-torsion, and aileron-rotation—is a cubic equation with complex coefficients. The coefficients of the equation are functions of a large number of structural and frequency parameters. The nature of the problem is such that the unknowns cannot be separated, thus making it impossible to solve the cubic frequency equation for the critical conditions directly. A trial-and-error solution is therefore indicated. The straightforward procedure of solution consists of assuming one of the unknown parameters, usually the "reduced velocity," and determining the corresponding cubic frequency equation. The equation is then divided into its real and imaginary parts and the roots of these two equations are determined in the usual way. The roots from the real and the imaginary equations are plotted and the intersection of their graphs indicate the values of the parameters for the critical conditions. For each assumed value of the reduced velocity there must be solved at least one cubic equation in order to determine the roots for plotting. The method proposed here would obviate the necessity for solving any cubic equations. It will be shown that an examination of the coefficients of the frequency equation is sufficient for determining the critical stability conditions.

Received June 12, 1944.

* The author has recently learned that Dr. S. Sherman, of Curtiss-Wright Corporation, has had considerable success in solving this problem by means of a generalization of the Routh Discriminant.

† Professor of Aeronautical Engineering.

FREQUENCY EQUATION FOR TWO DEGREES OF FREEDOM

Although the coefficient method is more valuable when applied to a three-degree-of-freedom system, a binary system will first be discussed in order to indicate the nature of the problem.

Consider a vibrating system involving only two flexibilities, such as wing-bending and wing-torsion. A mechanical model of such a system might be represented as shown in Fig. 1, in which the restraint to the bending and the twisting of the wing section is provided by springs. The other quantities to be considered are:

m_w = mass of wing per unit ft. (slugs per ft.)
$r_\alpha b$ = radius of gyration of wing about elastic axis (ft.)
$x_\alpha b$ = distance from elastic axis to center of gravity (ft.)
k_y = bending stiffness of wing (lb. per ft.)
k_α = torsional stiffness of wing about elastic axis (lb.ft. per rad.)
$2b$ = chord of wing (ft.)
α = angle of attack measured from a nonoscillating equilibrium position (rad.)
y = deflection of elastic axis (ft.)

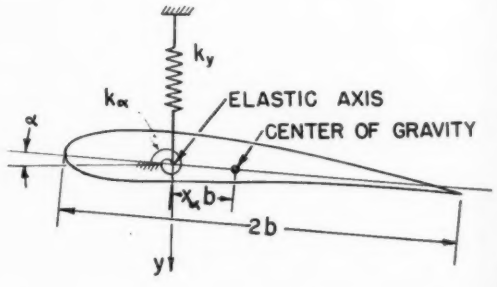

FIG. 1. Mechanical system for wing-bending wing-torsion.

The dynamic forces acting on a vibrating typical section of an airfoil consist of (1) elastic forces, (2) inertia forces, (3) damping forces, and (4) aerodynamic forces.

Elastic Forces

The elastic force and moment will be the product of the spring constant and the displacement, respectively. Force = $k_y y$. Moment = $k_\alpha \alpha$.

Inertia Forces

The inertia force and moment will be the product of the mass and acceleration and the mass moment of inertia and angular acceleration, respectively. Force = $m_w\ddot{y} + m_w x_\alpha b\ddot{\alpha}$. Moment = $m_w r_\alpha{}^2 b^2\ddot{\alpha} + m_w x_\alpha b\ddot{y}$. Where $\dot{y} = dy/dt$ and $\ddot{y} = d^2y/dt^2$.

Damping Forces

Numerous investigators[2] have shown that the structural damping force is almost directly proportional to the amplitude of displacement and independent of the frequency. If all the factors contributing to damping are combined for each degree of freedom, then the damping force can be expressed in terms of a coefficient g, which is defined as the ratio between the damping force and the elastic force. This damping force is in phase with the velocity and therefore leads the displacement by 90°. This can be taken into account by multiplying the displacement vector by $i = \sqrt{-1}$. Damping force = $ig_y k_y y$; damping moment = $ig_\alpha k_\alpha \alpha$.

Aerodynamic Forces

Theordorsen[1] and others have determined the additional aerodynamic forces and moments acting on an airfoil due to its vibration at constant amplitude. Such vibration would correspond to the motion between the stable and unstable regions. The force and moment for the binary system considered are:

$$L = \rho b^2\pi(v\dot{\alpha} + \ddot{y} - ba\ddot{\alpha}) + 2\pi\rho v b\overline{P} \times [v\alpha + y + b(1/2 - a)\dot{\alpha}]$$

$$M = -\rho b^2\pi[(1/2 - a)vb\dot{\alpha} + b^2(1/8 + a^2)\ddot{\alpha} - ab\ddot{y}] + 2\rho v b^2\pi(a + 1/2)\overline{P}[v\alpha + \dot{y} + b(1/2 - a)\dot{\alpha}]$$

where L = lift force (+ upward) (lb.)
M = moment of air forces about elastic center (lb.ft.)
ab = distance from mid-chord to elastic center (ft.)
v = relative air velocity (ft. per sec.)
ρ = density of air (slugs per cu.ft.)
$\overline{P} = F - iG$, a complex constant depending on the ratio $v/\omega b$ where ω is the circular frequency of vibration. (For values of F and G see reference 1.)

From a consideration of the equilibrium of the forces and moments acting on the airfoil, two equations can be obtained in terms of y and α and their derivatives. Since the motion is assumed at the borderline of instability, the vibratory motion can be assumed to be taking place at constant amplitude and simplification of the equations is obtained if the forms of y and α are taken as

$$y = y_0 e^{i\omega t}$$
$$\alpha = \alpha_0 e^{i(\omega t + \phi_1)}$$

then $\dot{y} = i\omega y$, $\ddot{y} = -\omega^2 y$, etc.

The equations of equilibrium thus may be written

$$\left.\begin{aligned} \overline{A}\,(y/b) + \overline{B}\alpha = 0;\ \text{from}\ \Sigma F_y = 0 \\ \overline{C}\,(y/b) + \overline{D}\alpha = 0;\ \text{from}\ \Sigma M = 0 \end{aligned}\right\} \quad (1)$$

where $\overline{A} = \mu\left[-1 + \frac{\omega_y{}^2}{\omega^2}(1 + ig_y)\right] - 1 + 2i\left(\frac{v}{\omega b}\right)\overline{P}$

$$\overline{B} = -\mu x_\alpha + i\left(\frac{v}{\omega b}\right) + a + \left[2\left(\frac{v}{\omega b}\right) + i(1 - 2a)\right]\left(\frac{v}{\omega b}\right)\overline{P}$$

$$\overline{C} = -\mu x_\alpha + a - 2i\left(\frac{v}{\omega b}\right)(a + 1/2)\overline{P}$$

$$\overline{D} = -2(a + 1/2)\left(\frac{v}{\omega b}\right)\left[\frac{v}{\omega b} + i(1/2 - a)\right]\overline{P} - \mu r_\alpha{}^2\left[1 - \frac{\omega_\alpha{}^2}{\omega^2}(1 + ig_\alpha)\right] + i\left(\frac{v}{\omega b}\right)(1/2 - a) - 1/8 - a^2$$

$\mu = m_w/\pi\rho b^2$
ω_y = uncoupled natural circular frequency of wing in bending = $\sqrt{k_y/m_w}$
ω_α = uncoupled natural circular frequency of wing in torsion = $\sqrt{k_\alpha/I_\alpha}$

The solution of Eqs. (1) requires the determinant of the coefficients be zero or

$$\Delta = \begin{vmatrix} \overline{A} & \overline{B} \\ \overline{C} & \overline{D} \end{vmatrix} = \overline{A}\overline{D} - \overline{B}\overline{C} = 0 \quad (2)$$

This is known as the "frequency equation." It should be noticed that only the term $\overline{A}$ and $\overline{D}$ contain both ω^2 and $v/\omega b$. For assumed values of $v/\omega b$, Δ becomes a quadratic in ω^2.

Solution of the Frequency Equation

The straightforward solution of the frequency equation used by Theodorsen[1] can be illustrated as follows:

If it is assumed that the damping coefficients are equal, $g_y = g_\alpha = g$, then a new variable can be introduced.

$$\Omega = X(1 + ig) \quad \text{where } X = \omega_\alpha{}^2/\omega^2$$

and for each value of $v/\omega b$ the equation for $\Delta = 0$ can be written

$$\Omega^2 + (a_1 + ib_1)\Omega + a_2 + ib_2 = 0 \quad (3)$$

If it is desirable to determine the flutter velocity for zero damping (side of safety), Eq. 3 can be written

$$X^2 + (a_1 + ib_1)X + a_2 + ib_2 = 0$$

Dividing this equation into real and imaginary parts, then two simultaneous equations result:

$$\text{Real: } X^2 + a_1X + a_2 = 0$$
$$\text{Imaginary: } b_1X + b_2 = 0$$

Three values of X can therefore be determined for each $v/\omega b$ that satisfies the frequency equation. The root of interest is the one satisfying both of the above equations simultaneously. This root may be found by determining the intersection of the real and imaginary equations as shown in Fig. 2. Having the values of X and $v/\omega b$ that satisfy $\Delta = 0$, the flutter speed can be determined from

$$v = (v/\omega b)(\omega/\omega_\alpha)\omega_\alpha b = (v/\omega b)(\omega_\alpha b/\sqrt{X})$$

where $v/\omega b$ and X are determined from the intersection of the curves.

In order to plot the curves and determine the intersection of the real and imaginary parts, it is necessary to solve the quadratic real equation for each value of $v/\omega b$ assumed. For a ternary system, the corresponding equation is a cubic and therefore more difficult to solve.

FIG. 2. Solution of frequency equation for binary system.

COEFFICIENT METHOD FOR BINARY SYSTEM

Starting with the frequency equation for a given value of $v/\omega b$ in the form

$$\Omega^2 + (a_1 + ib_1)\Omega + a_2 + ib_2 = 0$$

let a root be $\Omega_1 = X_1(1 + ig)$.

If the equation is now considered one with the damping coefficient g and the frequency ratio X as the variables,[6] then from the roots of the equation for various assumed values of $v/\omega b$ the variation of v and g can be obtained and plotted. See Fig. 3. From the conditions of the problem, each point on the curve represents the relation between the velocity v and the damping coefficient g which satisfies the frequency equation.

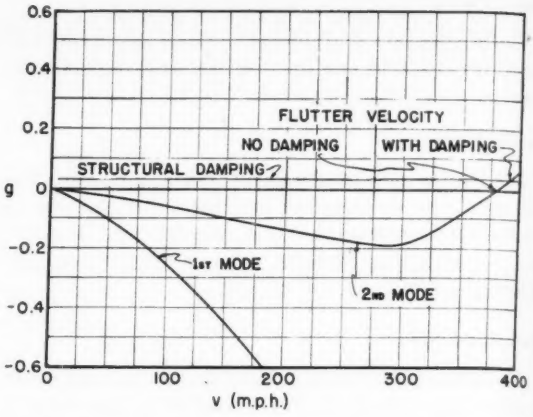

FIG. 3. Relations of velocity and damping for binary system.

Positive values of g greater than the amount of structural damping indicate an unstable motion, since more damping is required for stability than can be developed by the structure. If the structural damping available is assumed zero, then the critical condition is indicated when the damping coefficient passes through zero from a negative to a positive value. The root for this critical condition can be assumed

$$\Omega_1 = X_1$$

Substituting this in the frequency equation and separating the real and imaginary parts, gives

$$\text{Real: } X_1^2 + a_1X_1 + a_2 = 0$$
$$\text{Imaginary: } b_1X_1 + b_2 = 0$$

From the second, $X_1 = -b_2/b_1$. This value substituted into the first gives

$$(b_2/b_1)^2 = a_1(b_2/b_1) - a_2 \qquad (4)$$

It can be shown by substitution into a case with a known solution, that if

$$(b_2/b_1)^2 < (a_1b_2/b_1) - a_2$$

the motion is stable and if

$$(b_2/b_1)^2 > (a_1b_2/b_1) - a_2$$

the motion is unstable.

Examination of the coefficients of the frequency equation, therefore, will indicate whether the assumed value of $v/\omega b$ gives a stable or unstable motion. The value of $v/\omega b$ that corresponds to the borderline between these motions is easily obtained by plotting the values $(b_2/b_1)^2$ versus $v/\omega b$ and $(a_1b_2/b_1) - a_2$ versus $v/\omega b$. Their intersection satisfies Eq. 4.

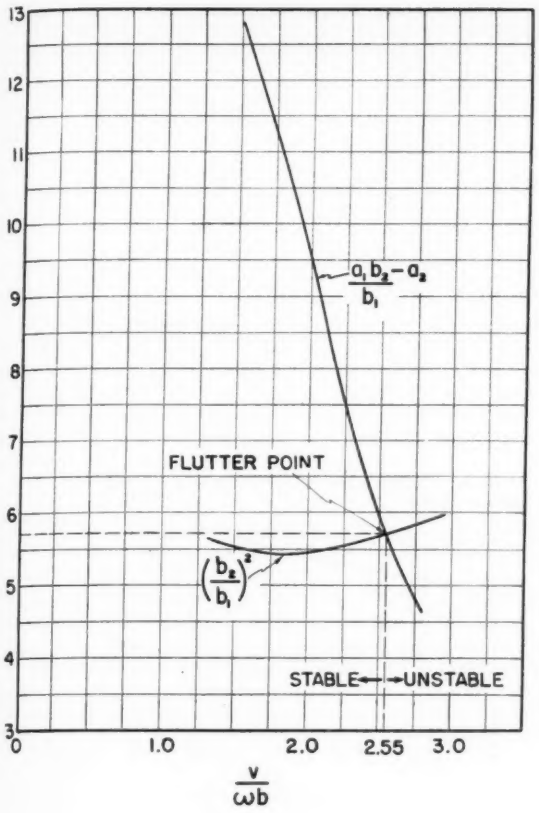

FIG. 4. Determination of stable and unstable regions by coefficient method for a binary system.

Since $X = \omega_\alpha^2/\omega^2 = -b_2/b_1$ then $-b_2/b_1$ must be positive and the value of the flutter speed is determined from $v = (v/\omega b)(\omega_\alpha b/\sqrt{X})$ as before.

Fig. 4 shows the plot of the coefficient relations for the same case previously evaluated. The intersection indicating the critical condition is more definitely established than previously.

COEFFICIENT METHOD FOR TERNARY SYSTEM

The coefficient method does not have much to commend it over other methods for the case of two degrees of freedom. It does have the advantage that the coefficients of the frequency equation can be used as an indication of state of stability of the motion for a given $v/\omega b$. This helps in selecting a new $v/\omega b$ so that the intersection can be "bracketed."

The main use of this method for a three-degree system is to overcome the necessity for solving a cubic equation.

The frequency equation for three degrees of freedom can always be written in the form

$$\Omega^3 + (a_1 + ib_1)\Omega^2 + (a_2 + ib_2)\Omega + a_3 + ib_3 = 0$$

For any root with the damping zero

$$\Omega_1 = X_1$$

Then

$$X_1^3 + (a_1 + ib_1)X_1^2 + (a_2 + ib_2)X_1 + a_3 + ib_3 = 0$$

Separating into real and imaginary parts,

$$\begin{aligned} &\text{Real:} \quad X_1^3 + a_1X_1^2 + a_2X_1 + a_3 = 0 \\ &\text{Imaginary:} \quad b_1X_1^2 + b_2X_1 + b_3 = 0 \end{aligned}$$

The solution of the quadratic is

$$X_1 = (-b_2 \pm \sqrt{b_2^2 - 4b_1b_3})/2b_1 = k_1, \; k_2$$

Calling these roots k_1 and k_2 and substituting into the cubic, then

$$\left.\begin{aligned} k_1^3 &= -a_1k_1^2 - a_2k_1 - a_3 \\ k_2^3 &= -a_1k_2^2 - a_2k_2 - a_3 \end{aligned}\right\} \tag{5}$$

If either of these equations is satisfied, the system is on the borderline between stable and unstable motion.

The determination of the stability conditions for the ternary system is somewhat more complicated than for the binary system. In order to establish the conditions, a root of the frequency equation will be assumed in which the damping coefficient is not zero. A consideration of the equations will be made when g is assumed to be extremely small and varying between plus and minus values.

Assuming a root

$$\Omega_1 = X_1(1 + ig)$$

Substituting this root into the frequency equation and separating into the real and imaginary parts gives

$$\begin{aligned} \text{Real:} \quad & (1 - 3g^2)X_1^3 + (a_1 - a_1g^2 - 2b_1g)X_1^2 + \\ & (a_2 - b_2g)X_1 + a_3 = 0 \\ \text{Imaginary:} \quad & (3g - g^2)X_1^3 + (2a_1g + b_1 - b_1g^2)X_1^2 + \\ & (b_2 + a_2g)X_1 + b_3 = 0 \end{aligned}$$

Since g can be made as small as desired, solve the imaginary equation with $g = 0$ to determine the roots k_1 and k_2. These roots have the same meaning as before. Substituting one of these values, say k_1, into the real equation and neglecting higher powers of g

$$k_1^3 + a_1k_1^2 + a_2k_1 + a_3 \approx (2b_1k_1 + b_2)k_1g$$

Since $k_1 > 0$ then if $g < 0$ the motion is stable and

$$k_1^3 + a_1k_1^2 + a_2k_1 + a_3 < 0$$

if $2b_1k_1 + b_2 > 0$. Hence, the motion is *stable* if

$$k_n^3 < -a_1k_n^2 - a_2k_n - a_3$$

when $2b_1k_n + b_2 > 0$

$$k_n^3 > -a_1k_n^2 - a_2k_n - a_3$$

when $2b_1k_n + b_2 < 0$; *unstable* if

$$k_n^3 > -a_1k_n^2 - a_2k_n - a_3$$

when $2b_1k_n + b_2 > 0$

$$k_n^3 < -a_1k_n^2 - a_2k_n - a_3$$

when $2b_1k_n + b_2 < 0$; for $n = 1$ *or* 2.

Since k_1 or $k_2 = X = \omega_\alpha^2/\omega^2$, both must be positive to have real physical meaning.

The values of k_n^3 and $(-a_1k_n^2 - a_2k_n - a_3)$ are plotted versus $v/\omega b$, and the intersection determines the critical condition. Since there is a possibility of intersections between the curves for $k_n = k_1$ and also intersections between the curves for $k_n = k_2$, the intersection giving the lowest flutter speed is the critical one.

Fig. 5 shows the plot of the roots of the real and imaginary parts of the frequency equation for a ternary system. In this particular case, no definite intersection could be obtained. Fig. 6 shows the curves for the same system determined by the coefficient method. These curves show that the motion is unstable for only a short range between points A and B. The curves for k_2 were not plotted, since they give no intersection for this particular system.

Point A on the curves in Fig. 6 corresponds to the lowest flutter speed. The values to be used from these curves in calculating the flutter speed are $v/\omega b = 1.2$ and $k_1^3 = (\omega_\alpha/\omega)^6 = 1.63$. Then $v = (v/\omega b)(\omega/\omega_\alpha) \times b\omega_\alpha = [1.2/(1.63)^{1/6}]b\omega_\alpha$.

Extention of Method to Systems of More Than Three Degrees of Freedom

For systems with more than three degrees of freedom, the frequency equation can be divided into its real and imaginary parts having one equation of odd degree and one of even degree. The values of k_n can then be determined from the simplest equation and the relations of the coefficients similarly established.

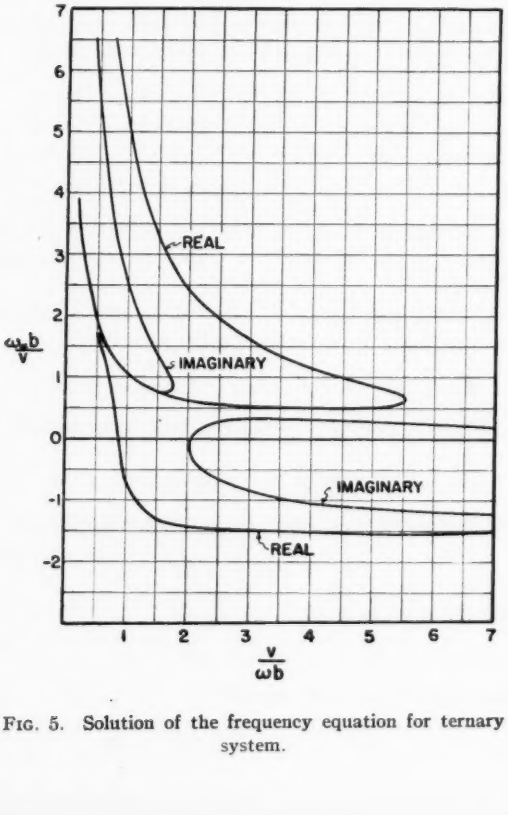

FIG. 5. Solution of the frequency equation for ternary system.

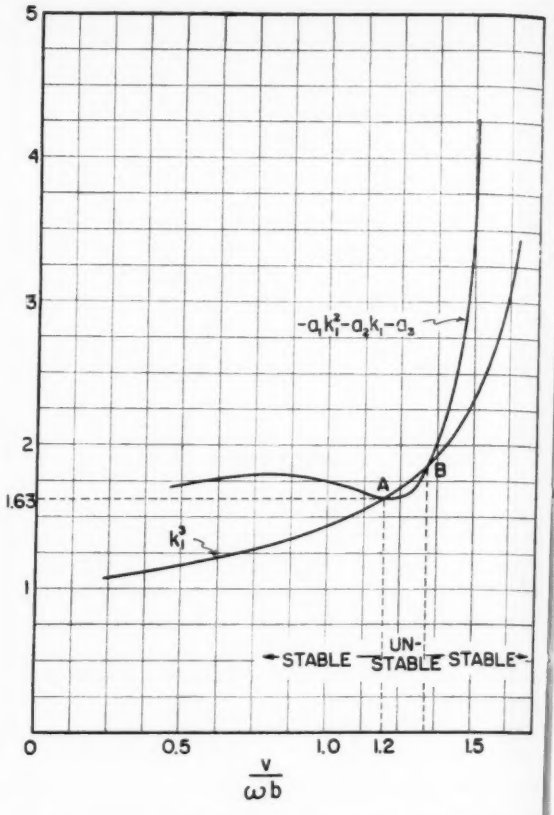

FIG. 6. Determination of stable and unstable regions by the coefficient method for a ternary system.

REFERENCES

[1] Theodorsen, Theodore, *General Theory of Aerodynamic Instability and the Mechanism of Flutter*, N.A.C.A. Report No. 496, 1934.

[2] Theodorsen, Theodore, and Garrick, I. E., *Mechanism of Flutter, A Theoretical and Experimental Investigation of the Flutter Problem*, N.A.C.A. Report No. 685, 1940 (Restricted).

[3] Bergen, W. B., and Arnold, Lee, *Graphical Solution of the Bending-Aileron Case of Flutter*, Journal of the Aeronautical Sciences, Vol. 17, No. 12, page 495, October, 1940.

[4] Bleakney, William M., *Three-Dimensional Flutter Analysis*, Journal of the Aeronautical Sciences, Vol. 9, No. 2, page 56, December, 1941.

[5] Loring, Samuel J., *Use of Generalized Coordinates in Flutter Analysis*, SAE Journal, page 113, April, 1944.

[6] Lombard, Albert E., Jr., *An Investigation of the Conditions for the Occurrence of Flutter in Aircraft and the Development of Criteria for the Prediction and Elimination of Such Flutter*, Thesis, California Institute of Technology, 1939.

[7] Bergen, William B., *Experimental Investigations in Aircraft Dynamics*, Journal of the Aeronautical Sciences, Vol. 10, No. 8, page 233, October, 1943.

A Specific Chart for Flying Boat Take-Off Performance

JOHN D. PIERSON* AND JOSEPH E. BURGHARDT†
The Glenn L. Martin Company

ABSTRACT

The take-off performance of a flying boat is complicated in practice by the variety of possible combinations of the basic operating variables—weight, power, wind, and getaway speed. The desirability of a simple method of evaluating and presenting the required information is evident in view of the labor involved in computing performance for all the possible combinations of conditions involved.

From early studies of Diehl and others and from later correlations of take-off data (both calculated and flight test), it has become clear that there exists an approximately linear relationship between the reciprocal of the take-off time and the four operating parameters listed above. It is empirically shown in this paper that, in addition, the take-off distance is directly proportional to the product of take-off time and getaway speed.

These relationships form the basis for a new type of chart for the prediction of the take-off time and distance for a specific flying boat under any reasonable combination of the operating variables or for the reduction of flight-test data to a standard of comparison.

INTRODUCTION

FOR SOME TIME the determination of take-off time and distance for flying boats has been a vexing problem. Calculations or estimates of this important design characteristic are generally made for certain "normal" conditions that are but rarely duplicated simultaneously in the actual operation of the ship.

In a specific design (that is, one having given hydrodynamic and aerodynamic characteristics), take-off time and distance are dependent upon the following basic operating variables: (1) gross weight, (2) brake horsepower applied, (3) wind velocity and direction, and (4) getaway speed. There is also a dependence upon pilot technique, but this is too uncertain a factor for quantitative correlation.

When model-test data and thrust curves are available, it would be possible to compute take-off time and distance for every conceivable combination of the above variables. However, this would be a tedious process. The standard step-by-step graphic integration process[1] that is necessary involves fairly lengthy thrust and resistance computations for accurate results. It is evident that the repetition of such calculations for a comprehensive coverage of the possible variations would be impractical. Because of the complex variation of water resistance and air drag with speed, an analytic solution is apparently not possible.

Received September 9, 1944.

*† Hydrodynamic Development Engineers.

The problem is to reduce the required calculations to a minimum, correlating the results in such a way as to enable interpolation for any reasonable combination of the variables. The solution should be applicable not only to prediction of take-off time and distance for any given set of operating conditions but to the inverse problem of reduction of flight-test data to standard conditions as well. This is accomplished in the take-off chart (Fig. 1), the development and construction of which are traced below.

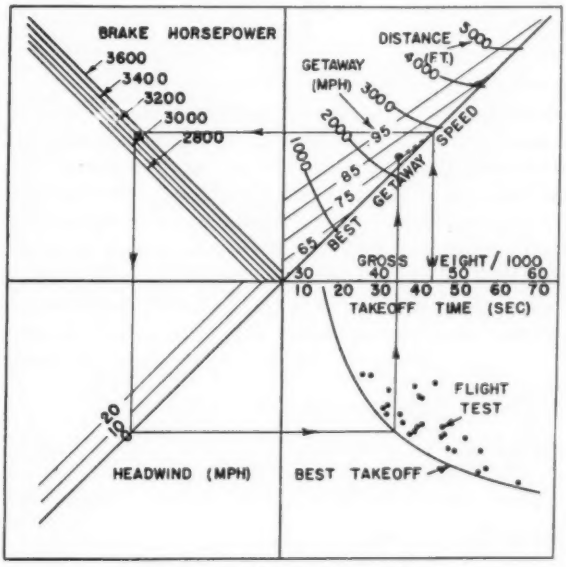

FIG. 1. Take-off performance chart.

EVOLUTION OF THE CHART

Take-Off Time Correlation

From time to time there have been advances made in the correlation of flying boat take-off time data to obtain simple charts or formulas for the handling of changes in some of the basic operating variables, but these have not been followed through to a complete solution of the problem.

Diehl[2, 3] evolved the following equation for maximum load capacity for take-off:

$$W_{max.} = W + (140 \text{ b.hp.}/t) \qquad (1)$$

or, for relating different cases,

$$(W_1/\text{b.hp.}_1) + (140/t_1) = (W_2/\text{b.hp.}_2) + (140/t_2) \quad (1a)$$

where W = gross weight, lbs.; b.hp. = total brake horsepower; and t = take-off time, sec. This relationship was established from flight-test data[2] for various gross weights at constant power. Experience indicates that it does not accurately account for changes of power at constant weight, although it is often misused for that purpose.

Analysis of flight-test take-off data and calculations for a number of modern flying boats has shown that, although the slope (140) is a rough average value for all of the ships, the individual values vary from 110 to 170 and are about in inverse proportion to the brake horsepower. This led to the suggestion that the power be eliminated from Eq. (1) by writing:

$$W_{max.} = W + (k_W/t) \quad (2)$$

where k_W is a function of virtual hull efficiency. The success of this form of equation suggested an analogous form to express the power relationship at constant weight:

$$\text{b.hp.}_{min.} = \text{b.hp.} - (k_p/t) \quad (3)$$

where, it was found, k_p is a function of propulsive efficiency only. Note that $W_{max.}$ and $\text{b.hp.}_{min.}$ are, respectively, the greatest weight for constant power and the least power for given weight that will allow take-off (infinite take-off time). However, there is a practical limit corresponding to a large finite time, such as 2 or 3 min.

For convenience in use, Eqs. (2) and (3) may be converted to incremental form:

$$W_1 + (k_W/t_1) = W_{max.} = W_2 + (k_W/t_2)$$
$$k_W[(1/t_1) - (1/t_2)] = W_2 - W_1$$

Therefore:

$$\Delta(1/t)_W = -K_W(\Delta W) \quad (2a)$$

where $K_W = 1/k_W$.

Similarly,

$$\Delta(1/t)_p = K_p(\Delta \text{ b.hp.}) \quad (3a)$$

where $K_p = 1/k_p$.

Similar investigations of wind and getaway speed variations have indicated substantially straight-line relationships over the practical range, so that equations for these may be written in the same form as above (the effect of moderate seaway, being small, may be included with the corresponding wind condition):

$$\Delta(1/t)_{V_w} = K_{V_w}(V_w) \quad (4)$$

and

$$\Delta(1/t)_{V_G} = -K_{V_G}(\Delta V_G) \quad (5)$$

where V_w = wind velocity, m.p.h., and V_G = getaway air speed, m.p.h.

In accordance with the accepted practice of taking off into the wind whenever possible, the term V_w in Eq. (4) is considered as a head wind. The effects of cross winds on take-off may be roughly approximated by using only the wind component in the direction of the take-off run. In connection with Eq. (5), it should be emphasized that ΔV_G represents a deviation from the *best* estimated getaway speed for the particular gross weight under consideration. The effect of the normal variation of best getaway speed with gross weight is included in the K_W of Eq. (2a).

The above relationships are sufficiently independent to permit combining the incremental variations into a single equation:

$$\frac{1}{t} = \frac{1}{t_0} - K_w(\Delta W) + K_p(\Delta \text{b.hp.}) + K_{V_w}(V_w) - K_{VG}(\Delta VG) \quad (6)$$

where t_0 = normal take-off time at design weight and power, zero wind, and best getaway speed.

Correlation of the various slopes for the above equations has been hampered by the limited number of modern flying boats for which accurate take-off data are available and, even more seriously, by the lack of suitable criteria to represent such factors as hull form and propeller efficiency through the take-off range. Values of the slopes for a number of large modern flying boats have been found to fall within the following limits (average values for the ships investigated are given in parentheses):

K_W	from 0.0000005	to 0.0000020	(0.0000016)
K_p	from 0.000005	to 0.000025	(0.000013)
K_{V_w}	from 0.00020	to 0.00060	(0.00035)
K_{V_G}	from 0.00030	to 0.00060	(0.00047)

These values are in dimensional units corresponding to the equations already given—pounds, horsepower, miles per hour, and seconds.

These four slopes form the basis for the construction of the take-off chart. For a specific case they may be

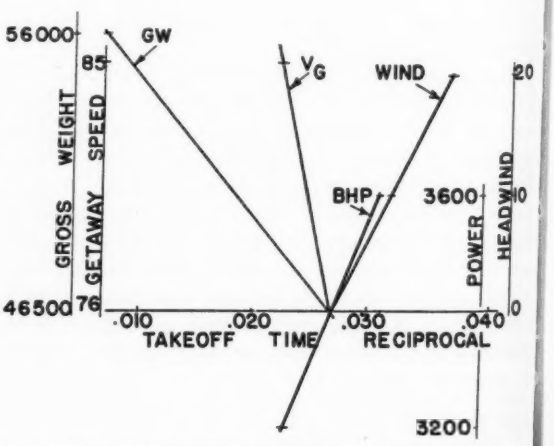

FIG. 2. Effect of independent changes in the variables on (1/t).

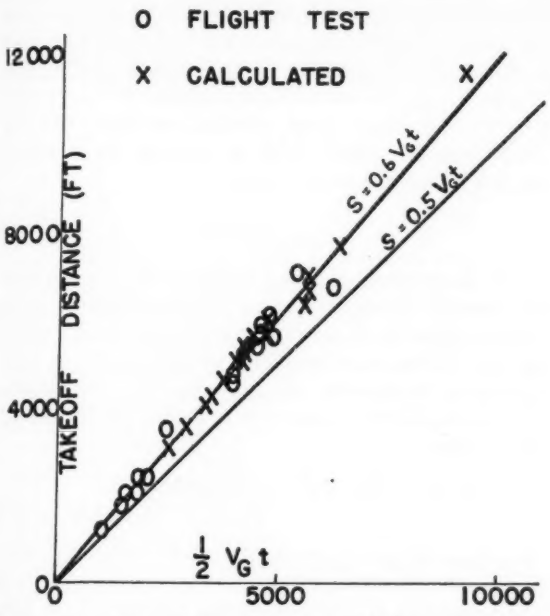

FIG. 3. Correlation of take-off distance with time and getaway speed.

obtained by calculating a limited number of take-offs from model or flight-test data when a wide range of test conditions has been covered. When model data are used, calculations need cover only radiating changes from normal condition take-off. These calculated data, plotted as in Fig. 2, will yield the required slopes. To obtain the slopes from flight-test data may be somewhat more complicated because of the probable random combinations of weight, power, etc. However, a reiterated solution of Eq. (6) with successively approximated constant slopes will generally be rapidly convergent within the limits of accuracy of the tests.

Take-Off Distance Correlation

The other hydrodynamic performance criterion, take-off distance, is not so generally used as is take-off time but often becomes of considerable importance. It can be calculated by the graphic integration process[1] or by integration of the basic expression:

$$S = \int^t V\,dt = \int_0^t (V/a)dV \qquad (7)$$

where

S = take-off distance, ft.

a = horizontal acceleration = $\dfrac{[T - (R + D)]}{(W/g)}$

T = propeller thrust, lbs.

R = hydrodynamic resistance, lbs.

D = aerodynamic drag, lbs.

If, arbitrarily, the acceleration is assumed to have a constant mean value, $\bar{a}$, then

$$\bar{a} = V_G/t$$

and Eq. (7) may be integrated to give the relation

$$S = (1/\bar{a})(V_G^2/2) = V_G t/2 \qquad (7a)$$

It will be observed that the presence of the term t in this equation automatically accounts for effects on take-off distance of changes in the basic variables, weight, power, etc.

Calculated and flight-test data for flying boats under various conditions have been found to correlate very well against the product $(V_G t/2)$, as shown in Fig. 3. The deviation of the line from unit slope (the slope is greater than 45°) indicates the relative error introduced by assumption of the mean acceleration, $\bar{a}$. It is apparent from Fig. 3 that this discrepancy may be all but eliminated by the application of an empiric constant, thus:

$$S = 1.2(V_G t/2) = 0.6 V_G t \qquad (8)$$

or, with V_G expressed in m.p.h.,

$$S = 0.88\ V_G t \qquad (8a)$$

PREPARATION OF THE CHART

The following information is required for the preparation of the chart: normal take-off time (t_0) at standard conditions (W_0, b.hp.$_0$, V_{G_0} and no wind); a plot of best estimated V_G against W; the four slopes (K_W, K_p, K_{V_W}, K_{V_G}) of Eq. (6); and, finally, Eq. (8). With these data at hand, the chart is prepared as follows:

(1) Lay off desired gross weight scale at bottom of Quadrant I (see Fig. 4). This automatically fixes a corresponding reciprocal time ($1/t$) scale, by the relation (derived from Eq. (2a))

$$1/t = (1/t_0) - K_W(W - W_0) \qquad (9)$$

(2) Draw 45° lines in Quadrants I, II, and III to represent normal conditions of V_G, b.hp., and V_w, respectively. Under these normal conditions, there is

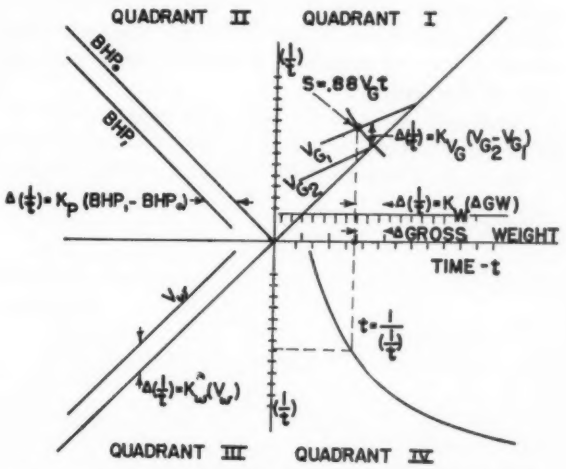

FIG. 4. Construction details for take-off performance chart.

no change in the take-off time as determined by Eq. (9), so that the same $(1/t)$ scale may be used as ordinate and abscissa in each quadrant, as shown in Fig. 4.

(3) Using the plot of V_G versus W, spot points for desired values of V_G at corresponding W's on the 45° line of Quadrant I. Using Eq. (5), lay off vertically the corresponding $(1/t)$ increments at these points, as shown in Fig. 4. Fair through like points to get constant V_G lines. (Theoretically, these V_G curves cannot be equally spaced and still intersect the 45° line at the unequally spaced points given by the nonlinear $V_G - W$ relationship, but this discrepancy is generally too slight in the normal V_G range to be noticeable on the chart.)

(4) In Quadrant II, lay off parallel 45° lines for desired values of b.hp., spaced according to Eq. (3a).

(5) Perform a similar operation in Quadrant III for values of V_w, using Eq. (4).

(6) Lay off any desired take-off time (t) scale at top of Quadrant IV, and plot master conversion curve from $(1/t)$ scale at left to (t) scale through points where the reciprocals correspond.

(7) This (t) scale may be considered the base scale for a "fifth quadrant" superposed on Quadrant I. Then, any point along the constant V_G lines corresponds to a unique pair of values for t and V_G—hence, by Eq. (8), to a certain take-off distance S. Contours of take-off distance may then be drawn across the V_G lines at desirable intervals.

Use of the Chart

Use of the take-off chart is illustrated by the arrows on Fig. 1. Entering at the given gross weight, project vertically upward to the given getaway speed; if minimum getaway is specified, to the 45° line. Then proceed horizontally across to the appropriate brake horsepower curve, downward to the wind velocity line, across to the master transformation curve of Quadrant IV, and upward to read take-off time. Finally, continue vertically upward on the time line to intersect again the same given V_G line as before—the point thus obtained may be interpolated between the curves for take-off distance.

Conversely, flight-test data may be used to check the chart by traversing as above for the given conditions, as far as Quadrant IV. There, instead of intersecting the transformation curve, proceed across to the abscissa corresponding to observed take-off time and plot the point. Flight-test points will generally be found to fall slightly to the right of the master curve because of minor imperfections in the intangible pilot technique. The transformation curve, denoting minimum time for ideal technique, should form an envelope below and to the left of such flight-test points.

Conclusions

(1) Four main variables affecting the take-off time of a specific flying boat have been considered: gross weight, brake horsepower, wind velocity, and getaway speed. Within practical limits, changes in any of these operating conditions produce directly proportional increments in the value of the reciprocal of take-off time; thus:

$$1/t = (1/t_0) - K_W(\Delta W) + K_p(\Delta \text{b.hp.}) + K_{Vw}(V_w) - K_{VG}(\Delta V_G) \quad (6)$$

The proportionality constants for this equation have not yet been correlated against specific dimensions or characteristics of the flying boat, but they have been bracketed within certain limits, as listed on page 170, and may be determined for individual ships from limited test data.

(2) The take-off distance of any flying boat under almost any conditions may be determined with reasonable accuracy from the empiric equation

$$S = 0.6\ V_G t \quad (8)$$

(3) These equations have been used to construct a single chart (Fig. 1), which may be traversed to obtain the take-off performance of a specific flying boat under any reasonable combination of the basic variables.

(4) Flight tests will usually show slightly inferior performance because of imperfections of pilot technique.

References

[1] Herrmann, H., *Seaplane Floats and Hulls—Part I*, N.A.C.A. T.M. No. 426, August, 1927.

[2] Diehl, Walter S., *The Estimation of Maximum Load Capacity of Seaplanes and Flying Boats*, N.A.C.A. T.R. No. 453, 1932.

[3] Diehl, Walter S., *Engineering Aerodynamics*, Revised Edition, Chap. XVII; The Ronald Press Company, Inc., New York City, 1936.

The Glauert-Prandtl Approximation for Subsonic Flows of a Compressible Fluid

HSUE-SHEN TSIEN* AND LESTER LEES†

California Institute of Technology

RECENT INTEREST in the compressibility effects has encouraged various investigations in the field of hydrodynamics of compressible fluids, or gas dynamics. Because of the inherent complexity of the problem, the main effort up until now seems to be concentrated in finding a satisfactory approximate solution. One of these approximations is the Glauert-Prandtl method. The only conditions required for its validity are the vanishing of vorticity and that the deviation from the undisturbed parallel flow must be small. It is realized, of course, that these conditions are not always satisfied. For instance, near the nose of a thin airfoil, the deviation from the undisturbed parallel flow is not small. Furthermore, the flow behind a detached shock wave is subsonic but not irrotational. However, there are many problems in airplane design and its related fields which can be treated by the Glauert-Prandtl method, at least in first approximation. The method itself is simple and is applicable to three-dimensional flows as well as two-dimensional flows. These features are not present in other more refined approximations, such as the hodograph method.

The authors therefore believe that such a powerful method should have a wider recognition of its potentiality beyond its present restricted application to thin airfoil theory. The first part of the present paper gives a general formulation of the three-dimensional flow problem with application to the calculation of wall interference in wind-tunnel testing at high speeds. This part of the work is prompted by a paper of the late Wieselsberger,[1] which seems to be erroneous.

Prandtl[2] himself has formulated the general problem and applied the method to the three-dimensional wing theory. Küssner[3] in his general wing theory has also touched upon this question. However, both treatments are brief and use the concept of acceleration potential, which is, perhaps, not so well known as the concept of trailing vortices. Hence, it seems desirable to re-examine the wing theory from the usual point of view. This, of course, involves the derivation of the Biot-Savart law for the compressible flow by the Glauert-Prandtl approximation. This investigation constitutes the second part of the present paper where the mistake in Husk's treatment of the down-wash problem[4] will be pointed out. The first order effect of compressibility on the down-wash at an airplane tail surface will be calculated for the simple case of a uniform wing lift distribution as an illustration. Three-dimensional wind-tunnel wall corrections for subsonic free-stream velocities will also be treated briefly. The induced velocity field of the helical vortex, which represents approximately the trailing vortex shed from a propeller blade, will then be investigated and its effect on the aerodynamic characteristics of propellers discussed.

Received July 20, 1944.

* Assistant Professor in Aeronautics.

† Research Fellow in Aeronautics.

THE GENERAL PROBLEM

By denoting the Cartesian coordinates by x_1, x_2, x_3 and the corresponding velocity components by v_1, v_2, and v_3, the continuity equation for the steady flow is

$$\sum_{i=1}^{3} (\partial/\partial x_i)(\rho v_i) = 0 \tag{1}$$

where ρ is the density. The conditions of irrotational flow are

$$\left.\begin{aligned} (\partial v_3/\partial x_2) - (\partial v_2/\partial x_3) &= 0 \\ (\partial v_1/\partial x_3) - (\partial v_3/\partial x_1) &= 0 \\ (\partial v_2/\partial x_1) - (\partial v_1/\partial x_2) &= 0 \end{aligned}\right\} \tag{2}$$

With Eq. (2), the Euler equations of motion can be written as

$$(\rho/2)(\partial v^2/\partial x_i) = -\partial p/\partial x_i \tag{3}$$

where $v^2 = v_1^2 + v_2^2 + v_3^2$ and p is the pressure. However, in the case of irrotational adiabatic flow, the pressure is a function of density only. Thus Eq. (3) can be expressed in the form

$$(\rho/2)(\partial v^2/\partial x_i) = -(dp/d\rho)(\partial\rho/\partial x_i) \tag{4}$$

But $dp/d\rho = a^2$, where a is the velocity of sound or velocity of the propagation of infinitesimal disturbances. Then Eq. (4) gives

$$\partial\rho/\partial x_i = -(\rho/2a^2)(\partial v^2/\partial x_i) \tag{5}$$

With this equation, the continuity equation can be written as

$$\sum_{i=1}^{3} (\partial v_i/\partial x_i) = (1/a^2) \sum_{i=1}^{3} \sum_{j=1}^{3} v_i v_j (\partial v_i/\partial x_j) \tag{6}$$

Now let $x_1 = x$, $x_2 = y$, $x_3 = z$, and consider only the case where the velocity is only slightly different from the velocity U of the parallel flow. Then if u, v, w

are the components of the disturbance velocity defined by

$$\left.\begin{aligned} v_1 &= U + u \\ v_2 &= v \\ v_3 &= w \end{aligned}\right\} \tag{7}$$

Eq. (6) is approximated by

$$(1 - M^2)(\partial u/\partial x) + (\partial v/\partial y) + (\partial w/\partial z) = 0 \tag{8}$$

where M is the Mach Number of the free stream or the ratio of U and velocity of sound corresponding to U. Eq. (8) is the modified equation of continuity in the Glauert-Prandtl approximation of irrotational adiabatic flow of compressible fluids. When the Mach Number is extremely small, this equation reduces to the familiar form for incompressible flow.

In investigating the flow over slender bodies placed in an otherwise parallel flow, it is convenient to use the potential function defined by

$$u = \partial\varphi/\partial x,\ v = \partial\varphi/\partial y,\ w = \partial\varphi/\partial z \tag{9}$$

Then the conditions of irrotational flow as expressed by Eq. (2) are identically satisfied and the continuity equation takes the form

$$(1 - M^2)(\partial^2\varphi/\partial x^2) + (\partial^2\varphi/\partial y^2) + (\partial^2\varphi/\partial z^2) = 0 \tag{10}$$

This is the partial differential equation for the potential function φ. This equation has to be solved together with the following boundary conditions:

(1) At the surface of a solid boundary, the resultant velocity, obtained by adding the velocity due to φ and the parallel velocity U, must be tangential to the surface.

(2) At distances far away from the solid body, the disturbance velocities due to φ must vanish so that the parallel flow is not disturbed, as required by the problem.

To solve this problem, Glauert and Prandtl introduce the new Cartesian coordinates ξ, η, ζ. These new variables are related to x, y, z by

$$\left.\begin{aligned} \xi &= x \\ \eta &= \sqrt{1 - M^2}\, y \\ \zeta &= \sqrt{1 - M^2}\, z \end{aligned}\right\} \tag{11}$$

Then Eq. (10) is reduced to the Laplace equation

$$(\partial^2\varphi/\partial\xi^2) + (\partial^2\varphi/\partial\eta^2) + (\partial^2\varphi/\partial\zeta^2) = 0 \tag{12}$$

The solutions of the Laplace equation are well known and easily found. Now, if a solution of this equation is found and for a particular point ξ_1, η_1, ζ_1 in the ξ, η, ζ space the value of φ is given to be φ_1, then at the point x_1, y_1, z_1 in the original x, y, z space determined by the relations

$$\left.\begin{aligned} \xi_1 &= x_1 \\ \eta_1 &= \sqrt{1 - M^2}\, y_1 \\ \zeta_1 &= \sqrt{1 - M^2}\, z_1 \end{aligned}\right\} \tag{13}$$

the value of the function φ satisfying Eq. (10) will be the same φ_1. In other words, points in ξ, η, ζ space and x, y, z space related by Eq. (11) have the same value of φ.

Since the boundary conditions are given in terms of the velocity components, the relation between the derivatives of φ in the two spaces has to be found. This is easily done by using Eq. (11). Thus, if

$$\left.\begin{aligned} u' &= \partial\varphi/\partial\xi \\ v' &= \partial\varphi/\partial\eta \\ w' &= \partial\varphi/\partial\zeta \end{aligned}\right\} \tag{14}$$

then

$$\left.\begin{aligned} u &= \frac{\partial\varphi}{\partial x} = \frac{\partial\varphi}{\partial\xi}\frac{d\xi}{dx} = \frac{\partial\varphi}{\partial\xi} = u' \\ v &= \frac{\partial\varphi}{\partial y} = \frac{\partial\varphi}{\partial\eta}\frac{d\eta}{dy} = \sqrt{1 - M^2}\,v' \\ w &= \frac{\partial\varphi}{\partial z} = \frac{\partial\varphi}{\partial\zeta}\frac{d\zeta}{dz} = \sqrt{1 - M^2}\,w' \end{aligned}\right\} \tag{15}$$

u', v', and w' can be considered as the disturbance velocities in the ξ, η, ζ space. Therefore, Eq. (15) gives the relation between the disturbance velocities in the two spaces at points related by Eq. (11).

Because of the assumption that the disturbance velocities are small compared with U, the velocity components of the resultant flow are $U + u \sim U$, v, and w. Given the shape of the boundary, the condition that the resultant velocity must be tangential to the boundary then gives the value of velocity components v_s and w_s at any point x_s, y_s, z_s of the surface. This condition and the requirement of vanishing disturbance at points far from the solid body are the boundary conditions in the x, y, z space. These conditions can be formulated in the ξ, η, ζ space by means of Eqs. (11) and (15):

(1) At the point $\xi_s = x_s$, $\eta_s = \sqrt{1 - M^2}\,y_s$, $\zeta_s = \sqrt{1 - M^2}\,t_s$, the values of v_s' and w_s' are $v_s/\sqrt{1 - M^2}$ and $w_s/\sqrt{1 - M^2}$.

(2) u', v', and w' vanish at points far from the body.

The essential characteristic to be remembered is that in the ξ, η, ζ space, where the determination of φ is first carried out, the coordinates of the boundary surface are *contracted* in comparison with those in the physical x, y, z space, but the lateral velocity components v', w' are *magnified* in comparison with those in the physical space.

In the case of a single slender body in a parallel flow, the coordinate contraction does not actually appear in the calculation. This simplification is the result of the fact that because of the small lateral dimensions the velocity components v_s' and w_s' can be evaluated at the axis or chord of the body, which is often taken as the x or ξ axis, instead of at the boundary of the body. However, in the case of an airfoil lattice or a body placed in a wind-tunnel, the requirement of lateral contraction in the ξ, η, ζ space must be taken into account. Then the problem is not so simple as that of a single body.

Axially Symmetric Body in a Wind Tunnel

The potential φ in ξ, η, ζ space for an axially symmetric body with its axis parallel to the undisturbed velocity U can be obtained as a distribution of sources and sinks on its axis, which can be taken as the ξ-axis. The lateral velocity components v_s' and w_s' can be evaluated at the ξ-axis and are directly proportional to the strength of the sources and the sinks. For "closed" bodies, the sum of the strength of the sources must be equal to that of the sinks. Therefore, for points not too close to the ξ-axis or, more precisely, for points where the distance from the body is large compared with the length of the body, the potential φ is approximated by that of a doublet placed at the middle point of the body, say the origin of the ξ, η, ζ space. The strength of this doublet is, of course, directly proportional to the average values of v_s' and w_s' at the surface of the body.

If the body is enclosed in a wind tunnel of height a and width b (Fig. 1), then at the "walls" $a\sqrt{1-M^2}/2$ and $b\sqrt{1-M^2}/2$ from the ξ-axis in the ξ, η, ζ space (Fig. 2), the v' and the w' velocity component must vanish, respectively. These requirements can be satisfied by an appropriate distribution of "images" of the source and sinks in the ξ, η, ζ space in addition to those on the ξ-axis. In case a and b are not small in comparison with the length of the body, then at the "walls" the potential φ due to the sources and sinks on the ξ-axis can be considered as that of a doublet at the origin. Therefore, the image system is composed of doublets of equal strength as shown in Fig. 2. Let S be the strength of the doublets. Then $\Delta u'$, or the induced ξ-component of the velocity at the origin due to the images, is given as[1]

$$\left.\begin{aligned}\Delta u' = \frac{S}{4\pi}\sum_{n=-\infty}^{\infty}\sum_{m=-\infty}^{\infty} \times \\ \frac{1}{[(na\sqrt{1-M^2})^2 + (mb\sqrt{1-M^2})^2]^{3/2}} = \\ \frac{S}{4\pi}\frac{1}{(1-M^2)^{3/2}}\sum_{n=-\infty}^{\infty}\sum_{m=-\infty}^{\infty}\frac{1}{(n^2a^2+m^2b^2)^{3/2}}\end{aligned}\right\} \quad (16)$$

But, by means of Eq. (15), $\Delta u' = \Delta u$. The induced x-component velocity in the physical space Δu can be considered as the increase in the velocity over the surface of the body due to the presence of wind-tunnel walls or the interference velocity. From Eq. (16) it seems that the interference velocity is proportional to $(1-M^2)^{-3/2}$. However, one must remember that for a given body the strength S of the doublets is determined by the conditions on v_s' and w_s'. The values of v_s' and w_s', being equal to $v_s/\sqrt{1-M^2}$ and $w_s \div \sqrt{1-M^2}$ as shown before, increase with M as $U \div \sqrt{1-M^2}$. Then Eq. (16) shows that for given wind-tunnel proportions the interference velocity can be calculated from

$$(\Delta u/U)_M/(\Delta u/U)_0 = 1/(1-M^2)^2 \quad (17)$$

where the subscripts M and 0 denote values at Mach Number M and 0, respectively.

Eq. (17) shows that the effect of the wall interference increases rapidly with Mach Number (Table 1). To keep the interference effect to a small value, one has to use a much larger wind tunnel for a given model dimension as the speed of testing is increased.

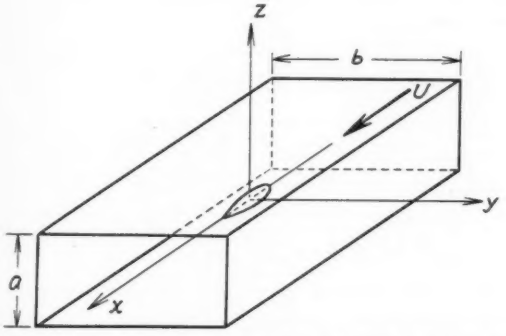

Fig. 1. Axially symmetric body in a wind tunnel of rectangular cross section.

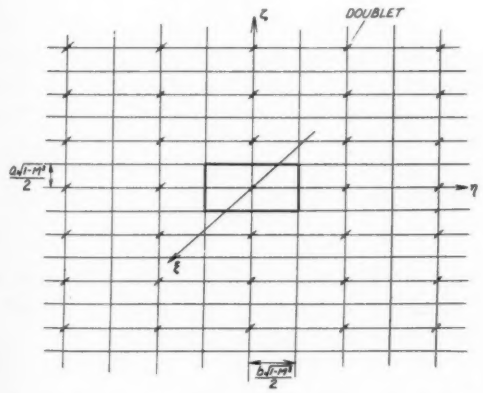

Fig. 2. Doublet-image system for axially symmetric body in ξ-, η-, ζ-space.

Table 1

M	$(\Delta u/U)_M/(\Delta u/U)_0$
0.3	1.204
0.4	1.412
0.5	1.778
0.6	2.44
0.7	3.84
0.75	5.21

Interference Effect on Thin Airfoils in a Two-Dimensional Wind Tunnel

In the calculation explained in the previous section, the source and sink distribution is replaced by a doublet for the determination of the image system. Strictly speaking, this is allowed only if the spacing of the images

in the ξ, η, ζ space is not too small compared with the length of the body concerned. The spacing of the image, however, decreases with increase in Mach Number M as $\sqrt{1 - M^2}$. Therefore, for high Mach Numbers, the result obtained can only be considered as approximate even with large values of a and b. To get more satisfactory results the exact image of the source and sink distribution has to be used.

Consider a symmetric airfoil of small thickness-chord ratio at zero angle of attack located at the center of a two-dimensional wind tunnel of height b. If the slope of the biconvex surfaces of the airfoil is tan β, the boundary condition for the airfoil can be approximately expressed as

$$v_0 = U \tan \beta \tag{18}$$

where v_0 is the value of v at the chord of the airfoil, here taken as the x-axis (Fig. 3). The condition at the wall is that

$$v = 0 \quad \text{at} \quad y = \pm b/2 \tag{19}$$

The conditions for determining φ in the ξ, η plane can be formulated according to rules previously stated. These conditions are

$$(\partial\varphi/\partial\eta)_0 = v_0' = U \tan \beta/\sqrt{1 - M^2} \tag{20}$$

at that part of the ξ-axis representing the chord of the airfoil, or for $-c/2 < \xi < c/2$ as shown in Fig. 3, and

$$\partial\varphi/\partial\eta = v' = 0 \quad \text{at} \quad \eta = \pm(b/2)\sqrt{1 - M^2} \tag{21}$$

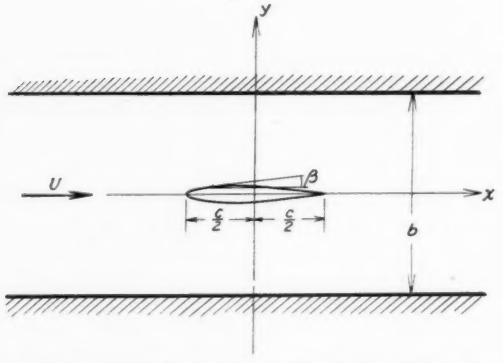

FIG. 3. Thin symmetric airfoil in two-dimensional wind tunnel.

To satisfy the condition given by Eq. (20), a distribution of sources on the ξ-axis in the interval $-c/2 < \xi < c/2$ is necessary. To satisfy the condition given by Eq. (21), an image system of the source distributions $b\sqrt{1 - M^2}$ apart is introduced in addition to the distribution on the ξ-axis as shown by Fig. 4. Along any line parallel to the η-axis, the sources are of equal strength and sign. It is then evident that the image system contributes nothing to v_0' at the ξ-axis. Then Eq. (20) gives the strength of the source distribution simply as $2U(\tan \beta/\sqrt{1 - M^2})$. Let $g = b\sqrt{1 - M^2}$.

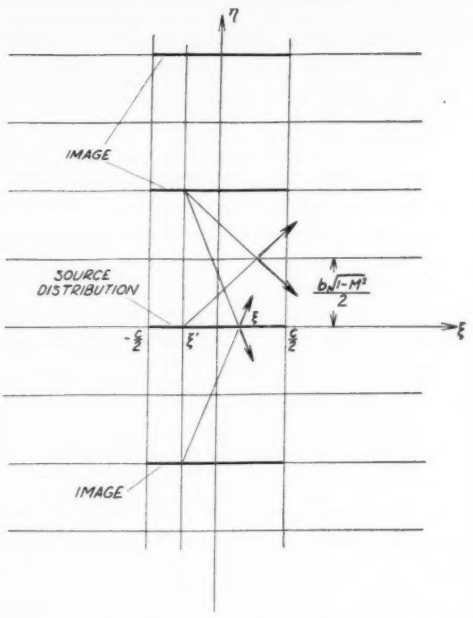

FIG. 4. Source-image system for symmetric airfoil in two-dimensional wind tunnel.

Then the velocity u_0' or u_0 at the chord of the airfoil is easily calculated as

$$\frac{u}{U} = \frac{1}{\pi\sqrt{1 - M^2}} \int_{c/2}^{c/2} \tan \beta(\xi')d\xi' \times \left[\frac{1}{\xi - \xi'} + \sum_{n=1}^{\infty} \frac{2(\xi - \xi')}{(\xi - \xi')^2 + (ng)^2}\right] = \frac{1}{g\sqrt{1 - M^2}} \int_{-c/2}^{c/2} \tan \beta(\xi') \coth \frac{\pi(\xi - \xi')}{g} d\xi' \tag{22}$$

This is the general expression for the x-component of the disturbance velocity over the surface of the airfoil for any given airfoil. The pressure p over the airfoil can be calculated by the approximate expression

$$p - p_0 = -2Uu\rho \tag{23}$$

where p_0 is the free-stream static pressure and ρ is the free-stream density. Thus the problem of an airfoil in a two-dimensional wind tunnel is completely solved.

As an example, take the half thickness function y_s of the airfoil to be

$$y_s = (c\epsilon/2)\{1 - [x^2/(c/2)^2]\} \tag{24}$$

In other words, the profile is given by a parabolic arc with maximum ordinate at the center of the airfoil. Then

$$\tan \beta = -2\epsilon[x/(c/2)] = -2\epsilon[\xi/(c/2)] \tag{25}$$

By substituting into Eq. (22), the x-component of the disturbance velocity at the point x on the chord is

$$\frac{u}{U}(x) = -\frac{4\epsilon}{gc\sqrt{1-M^2}}\int_{-c/2}^{c/2}\xi' \coth\frac{\pi(x-\xi')}{g}d\xi' \quad (26)$$

The maximum value of u/U occurs evidently at $x = 0$, or the origin. Denote this value by $u_{max.}$. Then Eq. (26) gives

$$\frac{u_{max.}}{U} = \frac{8\epsilon}{gc\sqrt{1-M^2}}\int_0^{c/2}\xi' \coth\frac{\pi\xi'}{g}\,d\xi' =$$

$$\frac{2\epsilon c}{g\sqrt{1-M^2}}\int_0^1 t\coth\frac{\pi c}{2g}t\,dt \quad (27)$$

The integral can be evaluated by expanding the hyperbolic cotangent in a power series of t and integrating term by term. The result is

$$\frac{u_{max.}}{U} = \frac{4\epsilon}{\pi\sqrt{1-M^2}}\times$$

$$\left[1+\sum^{\infty}\frac{(-1)^{n-1}2^{2n}B_{2n-1}}{(2n+1)(2n)!}\left(\frac{\pi c}{2g}\right)^{2n}\right] \quad (28)$$

where B_{2n-1} is the Bernoulli Number. This series is convergent for $\pi c/2g < 1$. For larger values of this parameter, the hyperbolic cotangent should be expanded into a series of exponential functions and the series integrated term by term. Therefore

$$\frac{u_{max.}}{U} = \frac{2\epsilon c}{g\sqrt{1-M^2}}\int_0^1 t\left[1+2\sum_1^{\infty}e^{-(n\pi c/g)t}\right]dt =$$

$$\frac{4\epsilon}{\pi\sqrt{1-M^2}}\left[\frac{1}{4}\left(\frac{\pi c}{g}\right)+\frac{\pi^2}{6}\left(\frac{g}{\pi c}\right)-\right.$$

$$\left.\sum_1^{\infty}\left(1+\frac{g}{n\pi c}\right)\frac{1}{n}e^{-n\pi c/g}\right] \quad (29)$$

This series is rapidly convergent for large values of $\pi c/g$. Calculations were made for the cases $\epsilon = 0.10$ and $\pi c/b = 1.0$ and $\pi c/b = 3.0$. Thus, for one case the ratio between the width of the wind tunnel and the chord is π, while for the second case this ratio is $\pi/3$. The results are shown in Figs. 5 and 6, where the curves obtained by the ordinary correction factor $1/\sqrt{1-M^2}$ are also shown. It is seen that the ordinary correction factor is unconservative, especially for narrow wind tunnels.

When $b \to \infty$, or $g \to \infty$, i.e., for the airfoil alone, Eq. (28) shows that

$$u_{max.}/U = 4\epsilon/\pi\sqrt{1-M^2}, \quad b \to \infty$$

Therefore the interference velocity Δu at the center of the airfoil is obtained as

$$\Delta u/U = (u_{max.}/U) - (4\epsilon/\pi\sqrt{1-M^2}) \quad (30)$$

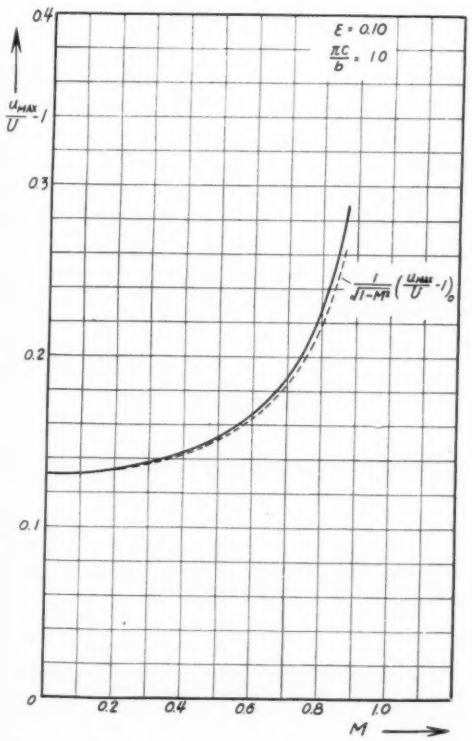

FIG. 5. Maximum velocity $u_{max.}$ on airfoil vs. Mach Number for symmetric airfoil of thickness ratio $\epsilon = 0.10$, with tunnel width—chord ratio $b/c = \pi$.

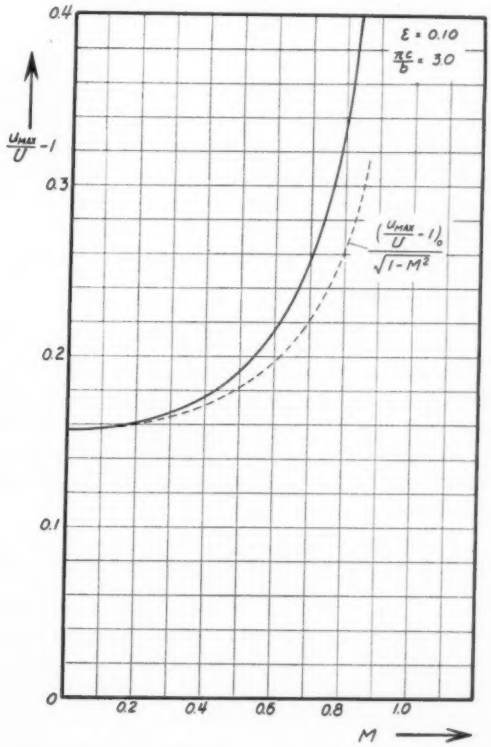

FIG. 6. Maximum velocity $u_{max.}$ on airfoil vs. Mach Number for symmetric airfoil of thickness ratio $\epsilon = 0.10$, with tunnel width—chord ratio $b/c = \pi/3$.

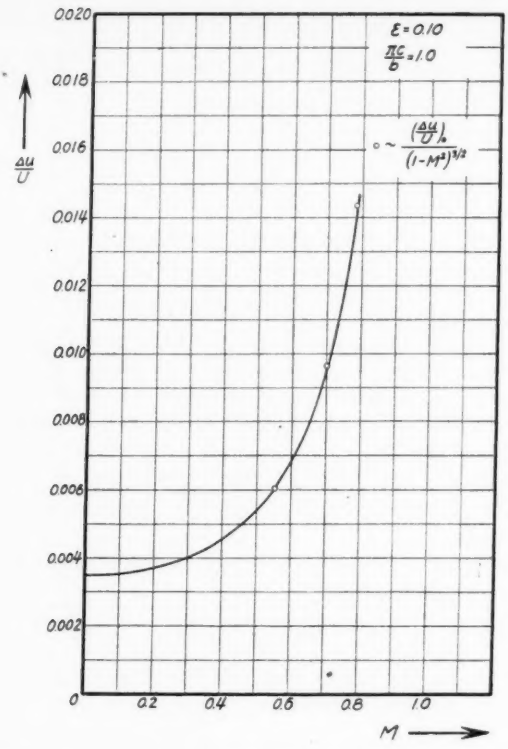

FIG. 7. Maximum interference velocity $\Delta u_{m\,x}$ on airfoil vs. Mach Number for symmetric airfoil of thickness ratio $\epsilon = 0.10$, with tunnel width—chord ratio $b/c = \pi$.

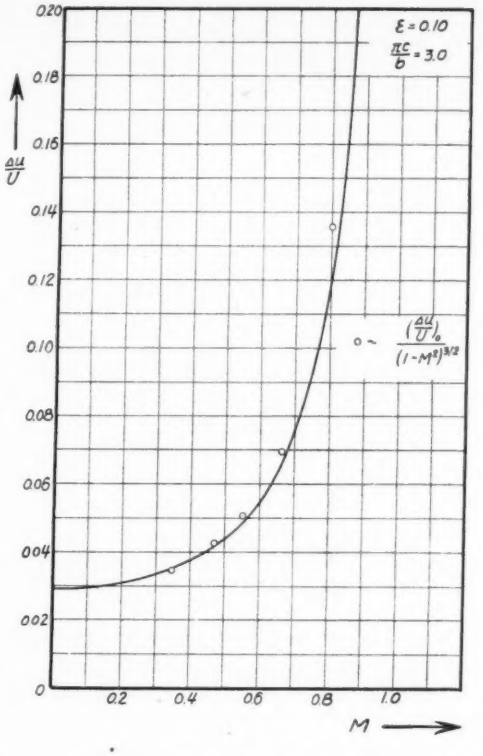

FIG. 8. Maximum interference velocity Δu_{max} on airfoil vs. Mach Number for symmetric airfoil of thickness ratio $\epsilon = 0.10$, with tunnel width—chord ratio $b/c = \pi/3$.

This quantity is plotted against the free-stream Mach Number M for the two cases investigated in Figs. 7 and 8, where the rapid rise of the interference velocity is obvious. By an argument similar to that used in treating approximately the problem of three-dimensional wall interference, it can be shown that if the images of the airfoil are considered as two-dimensional doublets,

$$(\Delta u/U)_M/(\Delta u/U)_0 = 1/(1 - M^2)^{3/2} \qquad (31)$$

The values so calculated are also included in Figs. 7 and 8. For $\pi c/b = 1.0$ this approximation is quite satisfactory. But for the case of a narrower wind tunnel, $\pi c/b = 3.0$, Eq. (31) gives values that are generally a little too high. This result is, of course, expected as the doublet approximation breaks down for small width-chord ratios.

Thin Airfoils at Small Angles of Attack in a Two-Dimensional Wind Tunnel

In the first-order calculation of the present investigation, the effect of thickness and camber can be separated. In this section, only the effect of camber and angle of attack will be considered. The result of this section can be combined with that of the previous section to obtain the total interference effect of any thin airfoil.

Consider the case of a cambered airfoil of zero thickness at an angle of attack in a wind tunnel of width b, Fig. 9. In the ξ, η plane, the boundary conditions can be satisfied by a vortex distribution in the interval $-c/2 < \xi < c/2$ on the ξ-axis and its images spaced $g = b\sqrt{1 - M^2}$ apart in the η-direction. To satisfy the condition that $v' = 0$ at $\eta = (b/2)\sqrt{1 - M^2}$, the images must be of alternate signs as shown in Fig. 10. Then by a similar calculation, as shown in previous

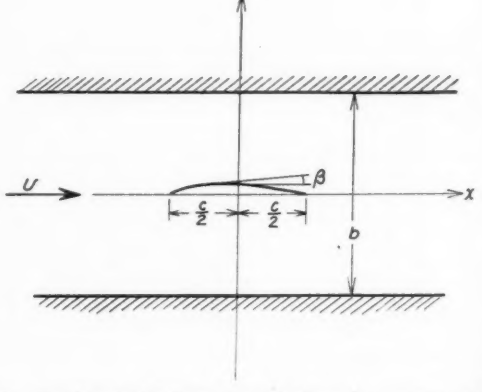

FIG. 9. Cambered airfoil of zero thickness in two-dimensional wind tunnel.

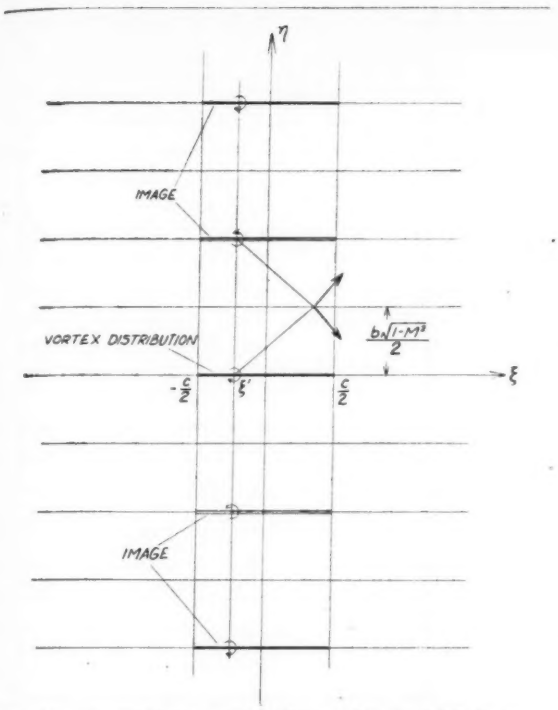

FIG. 10. Vortex-image system for cambered airfoil in two-dimensional wind tunnel.

sections, the value of v' at a point ξ on the ξ-axis is given by

$$v'(\xi) = -\frac{1}{4g}\int_{-c/2}^{c/2}\gamma(\xi')\times\left[\coth\frac{\pi(\xi-\xi')}{2g}-\tanh\frac{\pi(\xi-\xi')}{2g}\right]d\xi' = -\frac{1}{2g}\int_{-c/2}^{c/2}\frac{\gamma(\xi')d\xi'}{\sinh[\pi(\xi-\xi')/g]} \quad (32)$$

where $\gamma(\xi)$ is the strength of the vortex distribution at the point ξ. The value of $\gamma(\xi)$ has to be so determined as to make $v(x) = \sqrt{1-M^2}v'(\xi)$ equal to $U\tan\beta$, β being the angle of inclination of the airfoil surface at the point x. Thus the integral equation for $\gamma(\xi)$ is

$$\frac{U\tan\beta(\xi)}{\sqrt{1-M^2}} = -\frac{1}{2g}\int_{-c/2}^{c/2}\frac{\gamma(\xi')d\xi'}{\sinh[\pi(\xi-\xi')/g]} \quad (33)$$

By the substitution

$$\tanh\frac{\pi\xi}{g} = t, \quad \tanh\frac{\pi\xi'}{g} = t', \quad \tanh\frac{\pi c}{2g} = \lambda \quad (34)$$

Eq. (33) becomes

$$\frac{U\tan\beta}{\sqrt{1-M^2}} = -\frac{1}{2\pi}\int_{-\lambda}^{\lambda}\sqrt{\frac{1-t^2}{1-t'^2}}\frac{\gamma(t')\,dt'}{t-t'} \quad (35)$$

Now let

$$t/\lambda = -\cos\theta, \quad t'/\lambda = -\cos\theta' \quad (36)$$

Then Eq. (35) is transformed into

$$\frac{U\tan\beta}{\sqrt{1-M^2}} = -\frac{\sqrt{1-\lambda^2\cos^2\theta}}{2\pi}\int_0^{\pi}\frac{\gamma(\theta')\sin\theta'\,d\theta'}{\sqrt{1-\lambda^2\cos^2\theta'}(\cos\theta'-\cos\theta)} \quad (37)$$

This integral equation is similar to that of Glauert's thin airfoil theory[5] and therefore can be solved by similar methods. Thus $\gamma(\theta)$ is put into the form of a series

$$\gamma(\theta) = U\sqrt{1-\lambda^2\cos^2\theta}[a_0\cot(\theta/2) - \sum_1^{\infty}a_n\sin n\theta] \quad (38)$$

Then the integral in Eq. (37) can be evaluated.[5] The result is

$$\frac{\tan\beta}{\sqrt{1-M^2}} = -\tfrac{1}{2}\sqrt{1-\lambda^2\cos^2\theta}\sum_0^{\infty}a_n\cos n\theta \quad (39)$$

If the shape of the camber line is given, then $\tan\beta$ is known as a function of x. But $x = \xi$, according to Eq. (11); therefore, $\tan\beta$ can be expressed as a function of θ by using Eqs. (34) and (36). Then Eq. (39) requires that

$$-2\frac{\tan\beta(\theta)}{\sqrt{1-M^2}}\frac{1}{\sqrt{1-\lambda^2\cos^2\theta}} = \sum_0^{\infty}a_n\cos n\theta \quad (40)$$

In other words, the a_n's are simply the Fourier coefficients of the function on the left of Eq. (40). Their values can be easily calculated by using the well-known rule. Then the vortex distribution is known by using Eq. (38) and therefore the problem is completely solved.

As an example, consider a straight lamina at an angle of attack α to the velocity U. Then $\tan\beta = -\tan\alpha$; therefore

$$2(\tan\alpha/\sqrt{1-M^2}\sqrt{1-\lambda^2\cos^2\theta}) = \sum_0^{\infty}a_n\cos n\theta \quad (41)$$

Hence

$$a_0 = 2\frac{\tan\alpha}{\pi\sqrt{1-M^2}}\int_0^{\pi}\frac{d\theta}{\sqrt{1-\lambda^2\cos^2\theta}} \quad (42)$$

$$a_n = 4\frac{\tan\alpha}{\pi\sqrt{1-M^2}}\int_0^{\pi}\frac{\cos n\theta\,d\theta}{\sqrt{1-\lambda^2\cos^2\theta}} \quad (43)$$

Because of the fact that

$$\sqrt{1-\lambda^2\cos^2\theta} = \sqrt{1-\lambda^2\cos^2(\pi-\theta)}$$

the coefficient a_n is different from zero only for even n's.

The total circulation Γ around the airfoil is

$$\Gamma = \int_{-c/2}^{c/2}\gamma(x)\,dx \quad (44)$$

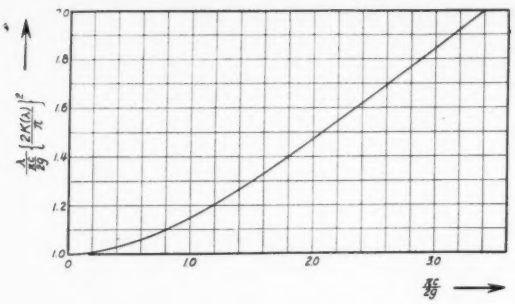

FIG. 11. Lift coefficient factor $[\lambda/(\pi c/2g)]\ [2K(\lambda)/\pi]^2$ vs. chord-tunnel width parameter $\pi c/2g$.

By substituting Eqs. (34), (36), and (38) into Eq. (44), the circulation is given as

$$\Gamma = \frac{g\lambda}{\pi}\int_0^\pi \frac{\gamma(\theta)\sin\theta\,d\theta}{1-\lambda^2\cos^2\theta} =$$

$$\frac{g\lambda U}{\pi}\int_0^\pi \frac{\sin\theta\,d\theta}{\sqrt{1-\lambda^2\cos^2\theta}}\left\{a_0\cot\frac{\theta}{2}-\sum_1^\infty a_n\sin n\theta\right\} \quad (45)$$

However, for the problem concerned, n is even in the series of the above equation. Therefore, the series contributes nothing to the total circulation, and

$$\Gamma = \frac{g\lambda U}{\pi}\,a_0\int_0^\pi \frac{(1+\cos\theta)\,d\theta}{\sqrt{1-\lambda^2\cos^2\theta}} =$$

$$\frac{g\lambda U}{\pi}\,a_0\int_0^\pi \frac{d\theta}{\sqrt{1-\lambda^2\cos^2\theta}} \quad (46)$$

The lift acting on the airfoil is equal to $\rho U\Gamma$. Therefore, the lift coefficient C_L is given by

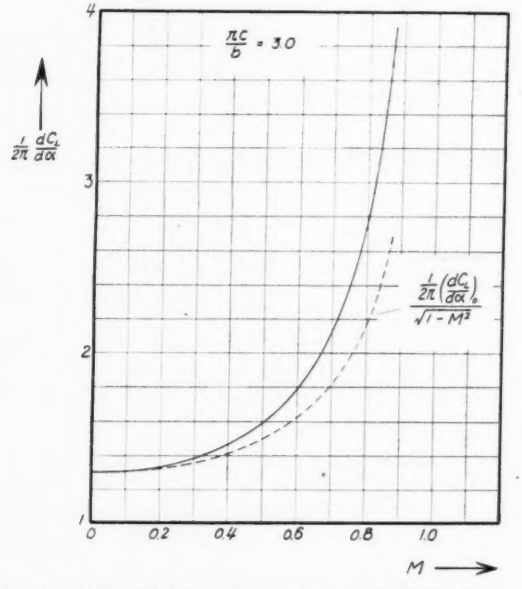

FIG. 12. Lift coefficient slope $dC_L/d\alpha$ vs. Mach Number for flat-plate airfoil in two-dimensional wind tunnel, with tunnel width-chord ratio $b/c = \pi/3$.

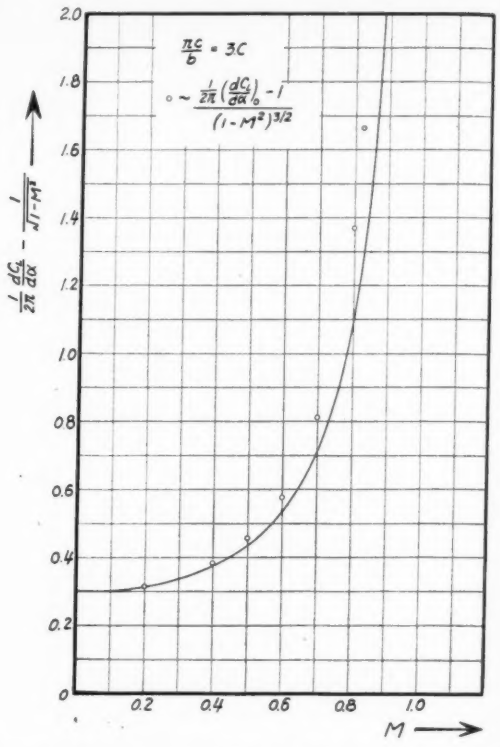

FIG. 13. Wall interference on lift coefficient slope $dC_L/d\alpha$ of a flat-plate airfoil in two-dimensional wind tunnel, with tunnel width—chord ratio $b/c = \pi/3$.

$$C_L = \frac{\rho U\Gamma}{(\rho/2)U^2c} =$$

$$\frac{2\pi\tan\alpha}{\sqrt{1-M^2}}\,\frac{\lambda}{(\pi c/2g)}\left(\frac{1}{\pi}\int_0^\pi \frac{d\theta}{\sqrt{1-\lambda^2\cos^2\theta}}\right)^2 =$$

$$\frac{2\pi\tan\alpha}{\sqrt{1-M^2}}\,\frac{\lambda}{(\pi c/2g)}\left[\frac{2K(\lambda)}{\pi}\right]^2 \quad (47)$$

where $K(\lambda)$ is the complete elliptic integral of the first kind and modulus λ. The slope of the lift curve is then

$$\frac{dC_L}{d\alpha} \cong \frac{2\pi}{\sqrt{1-M^2}}\,\frac{\lambda}{(\pi c/2g)}\left[\frac{2K(\lambda)}{\pi}\right]^2 \quad (48)$$

For the airfoil alone, $b \to \infty$, $g \to \infty$, and $\lambda \to 0$. So $2K(\lambda)/\pi = 1$, $\lambda/(\pi c/2g) = 1$, and $dC_L/d\alpha$ takes the familiar value $2\pi/\sqrt{1-M^2}$. The factor $[\lambda/(\pi c/2g)] \times [2K(\lambda)/\pi]^2$ is plotted against $\pi c/2g$ in Fig. 11. The result of applying Eq. (48) to the case $\pi c/b = 3.0$ is shown in Fig. 12, which again shows that the ordinary multiplying factor $(1-M^2)^{-1/2}$ is too small to give the correct result. The increment $\Delta(dC_L/d\alpha)$ due to wall interference is plotted against the Mach Number M in Fig. 13. The factor $(1-M^2)^{-3/2}$ derived from a rough approximation similar to that used in the three-dimensional case is again too high for the case concerned.

The Biot-Savart Law for Subsonic Compressible Flow

The problem of the three-dimensional flow around a wing of finite span will now be considered. To carry out this investigation, the generalized Biot-Savart law for subsonic compressible flow must first be derived. Since a compressible fluid problem in the real x, y, z space is reduced to an incompressible fluid problem in the ξ, η, ζ space, the velocity components induced by a vortex filament in the ξ, η, ζ space must be given by the classic Biot-Savart law. The induced velocity components in the real x, y, z space can then be obtained from the transformation relations between the two coordinate systems given by Eq. (15). It can be shown that the circulation around a curve enclosing the vortex filament is not changed in the transformation. Thus, the Glauert-Prandtl method furnishes the first approximation to the Biot-Savart law giving the induced velocity field of a vortex filament for subsonic compressible flow. Because of the assumption that the induced velocities or the deviations from the uniform parallel velocity field are small, this approximation is not valid for points close to the vortex filament or if the strength of the vortex is large. However, this difficulty is not encountered in many practical applications where the strength of a vortex filament is infinitesimal and the induced velocities are everywhere small compared with the velocity U of the undisturbed flow.

The Glauert-Prandtl transformation converts the approximate differential equation satisfied by the induced velocity components u, v, w in the real x, y, z space to the continuity equation for an incompressible fluid

$$(\partial u/\partial \xi) + (\partial v/\partial \eta) + (\partial w/\partial \zeta) = 0 \qquad (49)$$

satisfied by the induced velocity components u', v', w' in the ξ, η, ζ space. Helmholtz has shown that if the vorticity distribution is specified the induced velocity field is completely determined by the additional condition

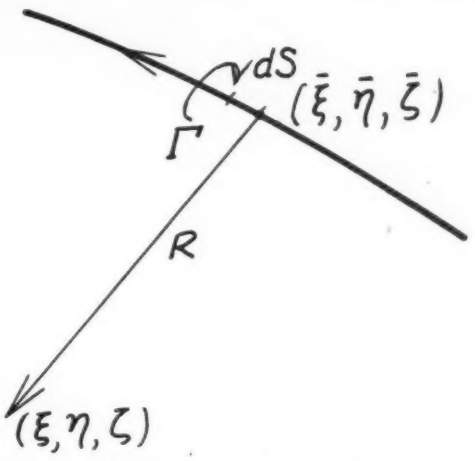

FIG. 14. Equivalent vortex filament in ξ-, η-, ζ-space.

given by Eq. (49).[6] In the case of a vortex filament, Helmholtz's result leads to the classic Biot-Savart law for the induced velocity field. If ds (Fig. 14) is the vector differential of length along the vortex filament, Γ is the circulation around a curve that encloses the filament (taken in a clockwise direction looking along dS), R is the vector distance between an arbitrary point ξ, η, ζ and a point of the filament $\bar{\xi}, \bar{\eta}, \bar{\zeta}$, and r is the magnitude of this distance; then the induced velocity vector V'' at the point ξ, η, ζ is given by the line integral along the vortex filament

$$V''(\xi, \eta, \zeta) = 1/4\pi \int \Gamma \, dSR/r^3 \qquad (50)$$

Here,

$$dS = id\bar{\xi} + jd\bar{\eta} + kd\bar{\zeta}, \; R = i(\xi - \bar{\xi}) + j(\eta - \bar{\eta}) + k(\zeta - \bar{\zeta}) \qquad (51)$$

where i, j, k are the unit vectors along the ξ, η, ζ axes, respectively. From the transformation relations between the induced velocity components and the coordinates in the x, y, z and ξ, η, ζ spaces,

$$u(x, y, z) = u'(\xi, \eta, \zeta) = \frac{1}{4\pi} \int \frac{\Gamma[(\zeta - \bar{\zeta})\, d\bar{\eta} - (\eta - \bar{\eta})\, d\bar{\zeta}]}{r^3} \qquad (52)$$

or

$$u(x, y, z) = \frac{1 - M^2}{4\pi} \int \frac{\Gamma[(z - \bar{z})\, d\bar{y} - (y - \bar{y})\, d\bar{z}]}{\{(x - \bar{x})^2 + (1 - M^2)[(y - \bar{y})^2 + (z - \bar{z})^2]\}^{3/2}} \qquad (53)$$

$$v(x, y, z) = v'(\xi, \eta, \zeta)\sqrt{1 - M^2} = \frac{\sqrt{1 - M^2}}{4\pi} \int \frac{\Gamma[(\xi - \bar{\xi})\, d\bar{\zeta} - (\zeta - \bar{\zeta})\, d\bar{\xi}]}{r^3} \qquad (54)$$

or

$$v(x, y, z) = \frac{1 - M^2}{4\pi} \int \frac{\Gamma[(x - \bar{x})\, d\bar{z} - (z - \bar{z})\, d\bar{x}]}{\{(x - \bar{x})^2 + (1 - M^2)[(y - \bar{y})^2 + (z - \bar{z})^2]\}^{3/2}} \qquad (55)$$

Similarly,

$$w(x, y, z) = \frac{1 - M^2}{4\pi} \int \frac{\Gamma[(y - \bar{y})\, d\bar{x} - (x - \bar{x})\, d\bar{y}]}{\{(x - \bar{x})^2 + (1 - M^2)[(y - \bar{y})^2 + (z - \bar{z})^2]\}^{3/2}} \tag{56}$$

Eqs. (53), (55), and (56) represent a first approximation to the Biot-Savart law giving the induced velocity field of a weak vortex filament for subsonic compressible flow.

Application to Vortex Lines and the Horseshoe Vortex

Since the horseshoe vortex will be useful later in re-examining the Prandtl three-dimensional wing theory, the approximate Biot-Savart law will be applied first to the calculation of the velocity components induced by this vortex in subsonic compressible flow at several points of interest. To a first approximation, because of the assumption of small induced velocity, the plane of the horseshoe vortex is parallel to the direction of the undisturbed air stream. Locate the origin of a right-handed system of coordinates at the center of the base of the horseshoe, with the x-axis in the direction of the main flow velocity and the z-axis downward (Fig. 15).

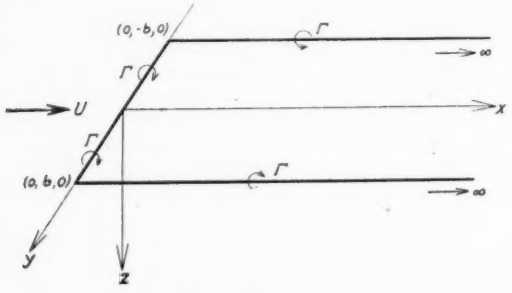

Fig. 15. Horseshoe vortex.

The horseshoe vortex then consists of semi-infinite vortex lines parallel to the x-axis starting at the points $\bar{x} = 0$, $\bar{y} = \pm b$, $\bar{z} = 0$, joined by the "bound" vortex of length $2b$ along the y-axis. Before proceeding with the calculations, the first-order effects of compressibility on the induced velocity field will be estimated qualitatively with the aid of the transformation relations between the real x, y, z space and the ξ, η, ζ space.

For incompressible flow, the velocity components induced at an arbitrary point x, y, z, by a vortex line of given strength depend only upon the perpendicular distance from the point to the line and the angle subtended by the line at the point. In transforming the real x, y, z space to the ξ, η, ζ space, the perpendicular distance from the point (x, y, z) to the semi-infinite vortex line defined by $\bar{x} \geqq 0$ $\bar{y} = +b$, $\bar{z} = 0$ will be reduced in the ratio $\sqrt{1 - M^2}$:1. On the other hand, the angle subtended by this vortex line at the point (x, y, z) will increase if $x > 0$ and will decrease if $x < 0$.

The velocity components v' and w' at the corresponding point ξ, η, ζ will therefore be increased by a ratio more than $1:\sqrt{1 - M^2}$ if $x > 0$ and by a ratio less than $1:\sqrt{1 - M^2}$ if $x < 0$ ($u = u' = 0$, for this vortex line). From Eq. (15) it can be seen that the velocity components v and w at (x, y, z) induced by the semi-infinite vortex line will be increased by compressibility if $x > 0$ and decreased by compressibility if $x < 0$. The lines of constant velocity in a plane perpendicular to the vortex line remain circles. At a point in the $0yz$ plane, or far behind the bound vortex, the angle subtended by the semi-infinite vortex line is not changed by the transformation to the ξ, η, ζ space, and the lateral induced velocity components will be unaltered by compressibility. This conclusion is important in the Prandtl wing theory to be discussed in the next section.

The perpendicular distance from a point in the $0xy$ plane to the bound vortex along the y-axis is not changed in the transformation from the compressible flow problem to the incompressible flow problem, but the length of the bound vortex is reduced in the ratio $\sqrt{1 - M^2}$:1. The only velocity component, w', at the point $(\xi, \eta, 0)$ will also be reduced, and the velocity component w at the point $(x, y, 0)$ will therefore be reduced by more than the ratio $\sqrt{1 - M^2}$:1. At a point in the $0yz$ plane, on the other hand, the perpendicular distance from the point $(0, \eta, \zeta)$ to the bound vortex line is reduced in the ratio $\sqrt{1 - M^2}$:1, but the angle subtended by the vortex line at this point is not changed. The induced velocity component u' at the point $(0, \eta, \zeta)$ is increased in the ratio $1:\sqrt{1 - M^2}$, and therefore $u(0, y, z)$ is also increased in this ratio. The lines of constant velocity in a plane perpendicular to the bound vortex line are thus elongated in the z-direction and compressed in the x-direction.

Quantitatively, at an arbitrary point x, y, z, the contributions to the induced velocity components from the semi-infinite vortex line defined by $\bar{x} \geqq 0$, $\bar{y} = +b$, $\bar{z} = 0$ can be readily obtained from Eqs. (53), (55), and (56). The results are

$$u(x, y, z) = 0 \tag{57}$$

$$v(x, y, z) = \frac{\Gamma}{4\pi} \frac{z}{(b - y)^2 + z^2} \times \left\{1 + \frac{x}{\sqrt{x^2 + (1 - M^2)[(b - y)^2 + z^2]}}\right\} \tag{58}$$

$$w(x, y, z) = \frac{\Gamma}{4\pi}\left[\frac{b - y}{(b - y)^2 + z^2}\right]\times \left\{1 + \frac{x}{\sqrt{x^2 + (1 - M^2)[(b-y)^2 + z^2]}}\right\} \quad (59)$$

The contributions to the induced velocity components at the point $(\bar{y}, y, \bar{z})$ from the semi-infinite vortex line defined by $x \geq 0$, $\bar{y} = -b$, $\bar{z} = 0$ are given by expressions similar to those of Eqs. (58) and (59).

$$u(x, y, z) = 0 \quad (60)$$

$$v(x, y, z) = -\frac{\Gamma}{4\pi}\left[\frac{z}{(b + y)^2 + z^2}\right]\times \left\{1 + \frac{x}{\sqrt{x^2 + (1 - M^2)[(b + y)^2 + z^2]}}\right\} \quad (61)$$

$$w(x, y, z) = \frac{\Gamma}{4\pi}\left[\frac{b + y}{(b + y)^2 + z^2}\right]\times \left\{1 + \frac{x}{\sqrt{x^2 + (1 - M^2)[(b + y)^2 + z^2]}}\right\} \quad (62)$$

The contributions from the bound vortex along the y-axis are

$$u(x, y, z) = -(1 - M^2)\frac{\Gamma}{4\pi}\left[\frac{z}{x^2 + (1 - M^2)z^2}\right]\left\{\frac{b - y}{\sqrt{x^2 + (1 - M^2)[(b - y)^2 + z^2]}} + \frac{b + y}{\sqrt{x^2 + (1 - M^2)[(b + y)^2 + z^2]}}\right\} \quad (63)$$

$$v(x, y, z) = 0 \quad (64)$$

$$w(x, y, z) = (1 - M^2)\frac{\Gamma}{4\pi}\left[\frac{x}{x^2 + (1 - M^2)z^2}\right]\left\{\frac{b - y}{\sqrt{x^2 + (1 - M^2)[(b - y)^2 + z^2]}} + \frac{b + y}{\sqrt{x^2 + (1 - M^2)[(b + y)^2 + z^2]}}\right\} \quad (65)$$

It is not difficult to see that these equations agree with the qualitative discussion at the beginning of the present section.

Prandtl Wing Theory for Subsonic Compressible Flow

In the Prandtl wing theory for incompressible flow, the wing of finite span is replaced by the bound vortex, or lifting line along the y-axis, and the trailing vortex system is replaced by a plane trailing vortex sheet shed from the lifting line in a direction parallel to the main flow. This simplification is based upon the assumption that the induced velocities are small, which implies that the vortexes in the fluid are weak and the wing is lightly loaded.* These are exactly the conditions for the validity of results obtained by the Glauert-Prandtl method. Therefore, the results obtained in the previous section can be used to calculate the induced velocity field of the trailing vortexes. To a first approximation, it has been shown that the induced velocity field around a semi-infinite vortex line lying in the direction of the main flow is unaffected by compressibility in a plane perpendicular to the vortex line through the point from which the line originates. The semi-infinite trailing vortex of strength $-(d\Gamma/d\bar{y})\,d\bar{y}$ shed from the point $y = \bar{y}$ generates an induced velocity dw at a point y on the lifting line given by

$$dw(0, y, 0) = -(d\Gamma/d\bar{y})\,d\bar{y}/4\pi(\bar{y} - y) \quad (66)$$

The total down-wash velocity at the point y on the lifting line is then expressed by the well-known integral

$$w(0, y, 0) = (1/4\pi)\int_{-b}^{b}(d\Gamma/d\bar{y})\,d\bar{y}/(y - \bar{y}) \quad (67)$$

Hence, the down-wash velocity along the lifting line depends only upon the circulation distribution explicitly and is not directly dependent of Mach Number.

Under the assumptions of the Prandtl wing theory, the flow around each airfoil section can be computed as in the case of two-dimensional flow, except that the local angle of attack is reduced by the down-wash angle $\epsilon = w/U$ at any section. The circulation around any section is

$$\Gamma = (c/2)U(dc_l/d\alpha)[\alpha - (w/U)] \quad (68)$$

where α is the airfoil section angle of attack measured from the zero lift line, c is the section chord length, and $dc_l/d\alpha$ is the slope of the section lift coefficient curve. Thus, the spanwise lift distribution for subsonic compressible flow can be calculated by the methods utilized for incompressible flow, except that the airfoil section properties must be taken at the Mach Number of the undisturbed flow.

* It seems to the authors that the assumption of small induced velocities also requires that the spanwise variation of lift be small. Therefore, the Prandtl wing theory breaks down at points where $d\Gamma/dy$ is not small. Physically, this means that the values of lift distribution near the wing tip or a discontinuity in geometric angle of attack cannot be accurate even if they are the results of an exact calculation using the Prandtl theory.

Since the spanwise distribution of induced velocity depends only upon the spanwise lift distribution to a first approximation, the induced drag on the wing for a given spanwise lift distribution is the same in both subsonic compressible and incompressible flow. This fact was first observed by Prandtl, using the concept of the acceleration potential.[2] However, except in the special case for which the wing twist is zero and the down-wash is constant along the span (elliptic lift distribution), the spanwise lift distribution for a given total wing lift will be altered by compressibility.

If it were required to maintain the circulation constant at every section for a given wing lift, then

$$\Gamma = \frac{c}{2}U\left(\frac{dc_l}{d\alpha}\right)_c\left[\alpha_c - \left(\frac{w}{U}\right)_c\right] = \frac{c}{2}U\left(\frac{dc_l}{d\alpha}\right)_i\left[\alpha_i - \left(\frac{w}{U}\right)_i\right] \tag{69}$$

where the subscript c denotes the compressible flow, and the subscript i denotes the incompressible flow. Since

$$(dc_l/d\alpha)_c = (dc_l/d\alpha)_i/\sqrt{1 - M^2}$$

and

$$(w/U)_c = (w/U)_i$$

if the spanwise lift distribution is assumed to be unchanged,

$$\alpha_c - (w/U) = \sqrt{1 - M^2}[\alpha_i - (w/U)] \tag{70}$$

or

$$\alpha_i - \alpha_c = (1 - \sqrt{1 - M^2})[\alpha_i - (w/U)] \tag{71}$$

If the wing twist is zero and the down-wash velocity is uniform along the span, the wing angle of attack measured from the zero lift angle will be reduced in accordance with Eq. (71) to maintain an elliptic load distribution at a given wing lift. In the general case, where the effective two-dimensional section angle of attack $[\alpha_i - (w/U)]$ is not uniform along the span, the change in section angle of attack required to maintain the same lift distribution at a given wing lift will also vary along the span. It is apparent, therefore, that the same spanwise lift distribution cannot be maintained for a given wing lift at all Mach Numbers.

From Eq. (70) it can also be seen that the slope of the lift coefficient curve for the whole wing is not increased in the ratio $1:\sqrt{1 - M^2}$, as Husk[4] has assumed. For the simple case of the elliptic lift distribution, $w/U = C_L/\pi$A.R., if A.R. is the aspect ratio. Therefore,

$$\left(\frac{d\alpha}{dC_L}\right)_c = \left(\frac{d\alpha}{dC_L}\right)_i\sqrt{1 - M^2} + \frac{1}{\pi\text{A.R.}}(1 - \sqrt{1 - M^2}) \tag{72}$$

or

$$\left(\frac{dC_L}{d\alpha}\right)_c = \left(\frac{dC_L}{d\alpha}\right)_i \Big/ \left[\sqrt{1 - M^2} + \frac{1}{\pi\text{A.R.}}\left(\frac{dC_L}{d\alpha}\right)_i(1 - \sqrt{1 - M^2})\right] \tag{73}$$

Down-Wash at the Horizontal Tail Surface and Tail Effectiveness for Subsonic Compressible Flow

Silverstein, Katzoff, and Bullivant[7] have shown that for incompressible flow the down-wash behind a monoplane wing can be computed with sufficient accuracy from the Prandtl wing theory. The spanwise lift distribution on the wing is replaced by an equivalent stepwise distribution (Fig. 16), and a trailing vortex of

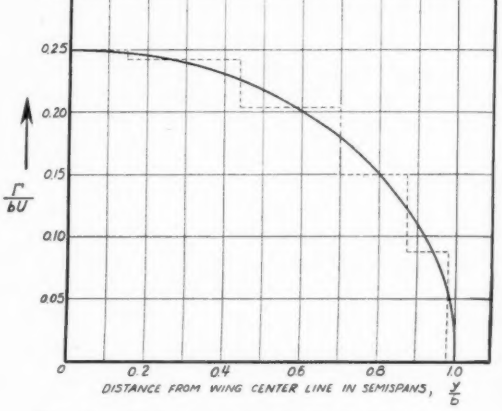

FIG. 16. Equivalent spanwise lift distribution.

strength equal to the "jump" ($\Delta\Gamma$) is shed from each point on the lifting line ($y = \bar{y}$) at which a step occurs. From Eqs. (57) to (65), a first approximation to the down-wash angle induced in the plane ($x0z$) by such a system of horseshoe vortexes will be given by the sum of expressions of the type

$$\epsilon(x, 0, z) = \frac{w(x, 0, z)}{U} = \frac{\bar{y}\Delta\Gamma}{2\pi U}\left\{\frac{1}{\bar{y}^2 + z^2} + \frac{x}{\sqrt{x^2 + (1 - M^2)(\bar{y}^2 + z^2)}}\left[\frac{1}{\bar{y}^2 + z^2} + \frac{1 - M^2}{x^2 + (1 - M^2)z^2}\right]\right\} \tag{74}$$

which reduces, of course, to Eq. (1) of reference 7, for $M = 0$, $\bar{y} = b = s$. Therefore the down-wash at a point not on the lifting line is a function of Mach Number. This is in contradiction with the result of Husk.[4]

Because of the downward displacement of the plane trailing vortex sheet behind the wing, Eq. (74) actually gives the down-wash at a point having a vertical distance z from the displaced vortex sheet. As a second approximation, it is assumed by Silverstein[7] that the

downward displacement of the entire trailing vortex sheet at any point x is equal to the downward displacement of the centerline of the vortex sheet at that point. This displacement h is given by the integral expression

$$h = \int_{x_0}^{x} \tan \epsilon \, dx = \int_{x_0}^{x} \epsilon(x, 0, 0) \, dx \qquad (75)$$

where x_0 is the x-coordinate of the trailing edge of the wing, measured from a line parallel to the y-axis through the quarter-chord point of the wing root section, and $\epsilon(x, 0, 0)$ is the down-wash angle along the centerline, calculated from Eq. (74). The down-wash angle for a given spanwise lift distribution will be reduced by compressibility (Eq. (74)), but the downward displacement of the trailing vortex sheet will also be reduced (Eq. (75)). Since the tail surface is higher than the trailing edge of the wing in modern airplanes, these two effects will partly counterbalance each other. To investigate the relative magnitude of these two effects, a calculation of the down-wash angle distribution in the plane ($x0z$) at $x = {}^3/_4 b$ has been made at several Mach Numbers for the simple case of a uniform wing loading, a wing lift coefficient of 1.0, and a wing aspect ratio of 7.0. The results of this calculation are shown in Fig. 17. At the approximate location of the horizontal tail surface, the reduction in down-wash angle is 4 per cent at $M = 0.5$ and 9 per cent at $M = 0.70$. However, this apparent small reduction has a strong effect on the slope of the pitching moment curve for the complete airplane. This fact will be shown presently.

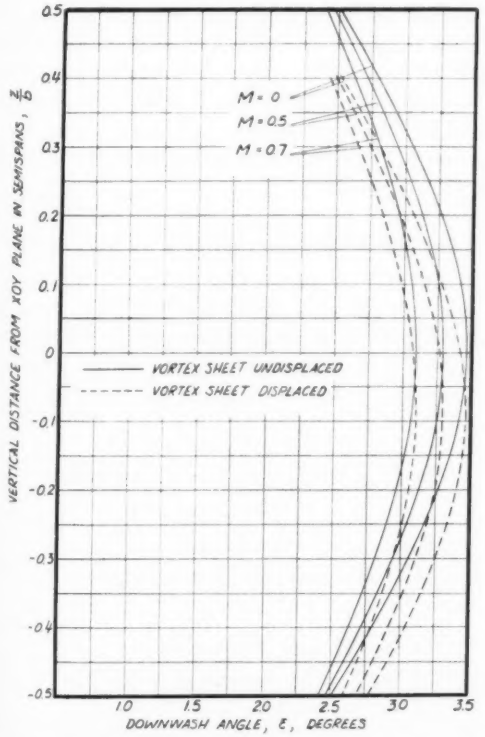

FIG. 17. Downwash angle in plane $x0z$ at $x = {}^3/_4 b$ for uniform wing loading, with $C_L = 1.00$, A.R. = 7.0.

By utilizing the results of the previous section, an approximate calculation of the tail effectiveness for subsonic compressible flow can be made. The angle of attack of the tail is obtained from the relation

$$\alpha_t = \alpha_w + i_t - \epsilon_t + \nu \qquad (76)$$

where α_w is the wing angle of attack measured from the zero lift line, i_t is the angle of incidence of the horizontal stabilizer, measured from the zero lift line of the wing, ϵ_t is the down-wash angle at the tail and ν is the contribution to α_t from the tab and elevator. For the particular case of an elliptic spanwise lift distribution, the wing angle of attack at a given wing lift coefficient is reduced by compressibility in accordance with Eq. (70). However, the slope of the tail lift coefficient curve, $dc_t/d\alpha_t$, is increased by compressibility in accordance with an expression similar to Eq. (73). The tail lift coefficient for compressible flow becomes

$$C_{L_t} = \frac{(dC_t/d\alpha_t)_i}{\sqrt{1 - M^2} + (1 - \sqrt{1 - M^2})\left(\frac{dc_t}{d\alpha_t}\right)\frac{1}{i\pi \text{A.R.}_t}} \times$$

$$\left[\alpha_{w_i}\sqrt{1 - M^2} + \frac{C_L}{\pi \text{A.R.}_w}(1 - \sqrt{1 - M^2}) + i_t + \nu - \epsilon_{t_e}\right] \qquad (77)$$

The airplane pitching moment coefficient, C_m is obtained from the relation

$$C_m = C_{m_0} + C_L[(d - d_0)/c] - c_t \eta V \qquad (78)$$

Here, c = mean aerodynamic chord (M.A.C.)
d = distance of airplane center of gravity from leading edge of M.A.C. section
d_0 = distance of aerodynamic center of M.A.C. section from leading edge
V = tail volume coefficient = $S_t l/S_w c$
S_t = horizontal tail surface area
S_w = wing area
l = horizontal distance of tail center of pressure from airplane c.g.
η = tail "efficiency" (measure of reduced velocity at tail)
C_{m_0} = wing pitching moment coefficient with respect to aerodynamic center of M.A.C. section

From Eqs. (77) and (78) the first order effect of compressibility on dC_m/dC_L for a fixed elevator and tab position is

$$\Delta\left(\frac{dC_m}{dC_L}\right) = \eta \frac{V\left(\frac{dC_t}{d\alpha_t}\right)_i}{\left(\frac{dC_L}{d\alpha_w}\right)_i}\left[K\left(\frac{d\epsilon_t}{d\alpha_w}\right)_e - \left(\frac{d\epsilon_t}{d\alpha_w}\right)_i + \right.$$

$$\left.(1 - K\sqrt{1 - M^2}) - \frac{K}{\pi \text{A.R.}_w}\left(\frac{dC_L}{d\alpha_w}\right)_i(1 - \sqrt{1 - M^2})\right] \qquad (79)$$

where

$$K = 1/\left[\sqrt{1-M^2} + (1-\sqrt{1-M^2})\left(\frac{dC_l}{d\alpha_l}\right)_l \frac{1}{\pi \text{A.R.}_t}\right]$$

Since the down-wash at the tail is only slightly reduced by compressibility at a given wing lift coefficient (Fig. 17), while the wing angle of attack is considerably reduced (Eq. (70)), the first order effect of compressibility on the static longitudinal stability is destabilizing. The values of $\Delta(dC_m/dC_L)$ in Table 2 have been calculated for a representative airplane, where $\text{A.R.}_w = 7$, $\text{A.R.}_t = 3.5$, $V = 0.60$, $(d\epsilon_t/d\alpha_w)_t = 0.4$, $(dC_L/d\alpha_w)_t = 4.60$, $(dC_l/d\alpha_t)_t = 3.0$, and $\eta = 0.65$. Increments in dC_m/dC_L of the magnitude shown are of considerable importance in the calculation of maneuver tail loads for airplanes that have marginal stability at low speeds.

TABLE 2

M	$\Delta(dC_m/dC_L)$
0.4	+0.005
0.5	0.010
0.6	0.015
0.7	0.021
0.75	0.027

THREE-DIMENSIONAL WIND-TUNNEL CORRECTIONS FOR SUBSONIC COMPRESSIBLE FLOW

For incompressible flow, wind-tunnel corrections to measurements on wings of finite span have been calculated from the Prandtl wing theory by replacing the physical constraints with a suitable system of "image" vortexes. It has been shown in a previous section that the induced velocity field around a semi-infinite vortex filament lying parallel to the direction of the main flow is unaffected by compressibility to a first approximation in a plane perpendicular to the vortex line through one end of the line. Since the trailing vortexes of the wing "images" are represented as semi-infinite vortex lines parallel to the x-axis, the velocities induced at the lifting line, or wing, by the "images" will be independent of the Mach Number, M. Therefore, the wind-tunnel corrections for the lift distribution can be calculated by the same method used for incompressible flow.

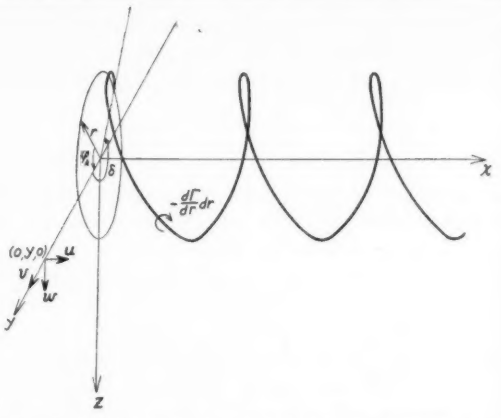

FIG. 18. Helicoidal trailing vortex shed from a propeller blade.

However, from the qualitative discussion of the induced velocity field of the horseshoe vortex, it can be seen that the velocities induced by the wing "images" at points *behind* the wing will be increased by compressibility. A first approximation for the wind-tunnel correction to the down-wash at an airplane tail surface is given by the correction for incompressible flow taken not at the actual value of the nondimensional parameter x/r for the tail location (r = appropriate lateral dimension of wind-tunnel test section) but at the greater value $x/r\sqrt{1-M^2}$.

AERODYNAMIC CHARACTERISTICS OF LIGHTLY LOADED PROPELLERS IN SUBSONIC COMPRESSIBLE FLOW

If an airplane propeller is lightly loaded, so that the induced velocities are everywhere small, the trailing vortexes shed from the propeller blades can be regarded approximately as semi-infinite helices (Fig. 18). Since the flow velocity referred to a fixed coordinate system is only slightly different from the flight velocity U, the approximate Biot-Savart law for subsonic compressible flow (Eqs. (53), (55), and (56)) can be applied to this problem.* The induced velocity components at a point $(0, y, 0)$ on one of the propeller blades are given by the expressions:

$$u(0,y,0) = -\frac{(1-M^2)}{4\pi}\int_{r_0}^{R}\frac{d\Gamma}{dr}\,dr\sum_{k=1}^{B}\int_0^\infty \frac{r^2 - ry\cos\varphi_k\,d\varphi}{[(1-M^2)(r^2+y^2-2ry\cos\varphi_k)+\lambda_0^2R^2\varphi^2]^{3/2}} \tag{80}$$

$$v(0,y,0) = -\frac{(1-M^2)}{4\pi}\int_{r_0}^{R}\frac{d\Gamma}{dr}\,dr\sum_{k=1}^{B}\int_0^\infty \frac{\lambda_0 r(\varphi\cos\varphi_k - \sin\varphi_k)\,d\varphi}{[(1-M^2)(r^2+y^2-2ry\cos\varphi_k)+\lambda_0^2R^2\varphi^2]^{3/2}} \tag{81}$$

$$w(0,y,0) = -\frac{(1-M^2)}{4\pi}\int_{r_0}^{R}\frac{d\Gamma}{dr}\,dr\sum_{k=1}^{B}\int_0^\infty \frac{[y - r(\varphi\sin\varphi_k + \cos\varphi_k)]\,d\varphi}{[(1-M^2)(r^2+y^2-2ry\cos\varphi_k)+\lambda_0^2R^2\varphi]^{3/2}} \tag{82}$$

* After the induced velocities are calculated, the blade angle and other local section characteristics can be determined by using the well-known airfoil relation. However, it should be noted that the section properties must correspond to the Mach Number of the air velocity relative to the blade section, which is quite different from the flight Mach Number M and varies along the blade.

Here, r = radial distance of the point on a propeller blade from which the trailing vortex is shed.
r_0 = radius of propeller hub
φ = parametric angle of helix
$\varphi_k = \varphi + 2\pi[1 - (k/B)], \quad k = 1, 2, 3, \ldots B$
$= \varphi + \delta$
B = number of blades
$\Gamma(r)$ = circulation around blade section
D = propeller diameter $= 2R$
$\lambda_0 = U/\pi nD = J/\pi$
U = flight velocity
n = revolutions per second of propeller

If the nondimensional variables $r' = r/R$, $y' = y/R$ are introduced, the expressions for the induced velocity components become:

$$u(0, y', 0) = -\frac{1}{4\pi R\sqrt{1 - M^2}}\int_{r_0'}^{1}\frac{d\Gamma}{dr'}dr'\sum_{k=1}^{B}\int_0^{\infty}\frac{(r'^2 - r'y'\cos\varphi_k)\,d\varphi}{\{r'^2 + y'^2 - 2r'y'\cos\varphi_k + [\lambda_0^2/(1 - M^2)]\varphi^2\}^{3/2}} \tag{83}$$

$$v(0, y', 0) = -\frac{1}{4\pi R\sqrt{1 - M^2}}\int_{r_0'}^{1}\frac{d\Gamma}{dr'}dr'\sum_{k=1}^{B}\int_0^{\infty}\frac{\lambda_0 r'(\varphi\cos\varphi_k - \sin\varphi_k)\,d\varphi}{\{r'^2 + y'^2 - 2r'y'\cos\varphi_k + [\lambda_0^2/(1 - M^2)]\varphi^2\}^{3/2}} \tag{84}$$

$$w(0, y', 0) = -\frac{1}{4\pi R\sqrt{1 - M^2}}\int_{r_0'}^{1}\frac{d\Gamma}{dr'}dr'\sum_{k=1}^{B}\int_0^{\infty}\frac{[y' - r'(\varphi\sin\varphi_k + \cos\varphi_k)]\,d\varphi}{\{r'^2 + y'^2 - 2r'y'\cos\varphi_k + [\lambda_0^2/(1 - M^2)]\varphi^2\}^{3/2}} \tag{85}$$

By following the suggestion of Konstantinov (reference 8, p. 692) the integral inside the summation sign in Eq. (83) can be rewritten as

$$\int_0^{2\pi}(r'^2 - r'y'\cos\varphi_k)\,d\varphi\sum_{m=0}^{\infty}1/\left[r'^2 + y'^2 - 2r'y'\cos\varphi_k + \frac{\lambda_0^2}{1 - M^2}(\varphi + 2m\pi)^2\right]^{3/2} \tag{86}$$

The first term in the Euler-Maclaurin expansion for the infinite series inside the integral sign in Eq. (86) is given by

$$\int_0^{\infty}dm/\left[r'^2 + y'^2 - 2r'y'\cos\varphi_k + \frac{\lambda_0^2}{1 - M^2}(\varphi + 2m\pi)^2\right]^{3/2} = \frac{\sqrt{1 - M^2}}{2\pi\lambda_0}\left[\frac{1}{(r'^2 + y'^2 - 2r'y'\cos\varphi_k)}\right] -$$
$$\frac{1}{2\pi}\left[\varphi/\left(r'^2 + y'^2 - 2r'y'\cos\varphi_k\right)\left(r'^2 + y'^2 - 2r'y'\cos\varphi_k + \frac{\lambda_0^2}{1 - M^2}\varphi^2\right)^{1/2}\right] \tag{87}$$

The leading term in the integral in Eq. (86) then becomes

$$\frac{\sqrt{1 - M^2}}{2\pi\lambda_0}\int_0^{2\pi}\frac{r'^2 - r'y'\cos(\varphi + \delta)}{r'^2 + y'^2 - 2r'y'\cos(\varphi + \delta)}\,d\varphi = \begin{cases}\sqrt{1 - M^2}/\lambda_0, & r' \geq y' \\ 0, & r' < y'\end{cases} \tag{88}$$

Let the value of the integral of all the remaining terms be denoted by $F_k[r', y', (\lambda_0/\sqrt{1 - M^2})]$. Then by using the condition that $\Gamma(1) = 0$ and Eq. (88), the expression for the axial induced velocity component (Eq. 83) is transformed to

$$u(0, y', 0) = \frac{B\Gamma(y')}{4\pi R\lambda_0} - \frac{1}{4\pi R\sqrt{1 - M^2}}\int_{r_0'}^{1}\frac{d\Gamma}{dr'}dr'\sum_{k=1}^{B}F_k\left(r', y', \frac{\lambda_0}{\sqrt{1 - M^2}}\right) \tag{89}$$

The first term, which is the axial component of induced velocity calculated for an infinite number of blades, is unaffected by compressibility. Physically, this result is a consequence of the assumption that the induced velocities are small; hence, to a first approximation the density variations can be neglected. The calculation of the axial momentum for an infinite number of blades will then be the same for subsonic compressible flow as for incompressible flow, and the expression for the axial component of induced velocity will also be unchanged.

The second term in the expression for $u(0, y', 0)$ represents the correction for a finite number of blades. This correction must be calculated at an advance ratio equal to $\lambda_0/\sqrt{1 - M^2}$ and then increased in the ratio $1:\sqrt{1 - M^2}$. Since the magnitude of the correction for a finite number of blades increases with increasing advance ratio, the first-order effect of compressibility is to increase this correction in a ratio somewhat greater than $1:\sqrt{1 - M^2}$.

(Continued on page 202)

Shock Waves in Aerodynamics

HOWARD W. EMMONS*
Harvard University

SUMMARY

This paper reviews some of the physical aspects of shock waves as they affect the high-velocity performance of airfoils. It is shown that the conventional frictionless, adiabatic, irrotational fluid motion can admit shocks only as an added discontinuity. Real fluids with viscosity and thermal conductivity will admit shocks as a necessary part of the complete solution of high-velocity problems. A brief discussion is given of oblique shock waves and of the necessarily rotational motion in the region behind a shock wave. A few words are included on the subject of the critical Mach Number for airfoils. Finally, combustion, detonation, and condensation waves are mentioned.

INTRODUCTION

THE MODERN DEVELOPMENT of aircraft has been in the direction of high velocity and high altitude. Both of these developments cause the velocity of the plane to approach the velocity of sound in the air through which it moves. Thus there are many new problems for the aerodynamicist to consider. These are, however, not confined to the external parts of the airplane.

In the attempt to reach high altitude, supercharger development has carried velocities inside of the engine to values where compressibility troubles are just as important. Indeed, every improvement in planes or their mode of propulsion introduces further problems, in which the compressibility of the fluids involved is of increasing importance. The development of gas turbines introduces the same difficulties as are already present for the propeller. The new jet propulsion developments involve high velocities in the jets, which brings to aerodynamics the same problems that have been present for years in steam turbine nozzle design.

This list of ways in which compressibility effects arise would not be complete without at least a mention of the difficulties connected with the measurement of the high velocities themselves and the military problem of flow about projectiles.

In all of these problems the understanding of what is occurring proceeds rather smoothly until shock waves arise. The occurrence of shock waves, their cause, their location, their magnitude, their shape are all so poorly understood that little more than guesswork is possible at the present time. Some of the positive information about this "discontinuity" phenomena is reviewed in the following paragraphs.

Received August, 1944.

* Associate Professor of Mechanical Engineering.

SYMBOLS

a = velocity of sound or acceleration along a streamline
a_* = velocity of sound in fluid for state where $M = 1$
c_v = specific heat at constant volume
h = enthalpy
l = distance along a streamline
M = Mach Number
n = distance normal to streamline
p = pressure
q = resultant velocity
r = radius of curvature of a streamline
R = gas constant
s = entropy
t = shock thickness
T = temperature
u = velocity (component normal to a shock wave)
v = velocity (component parallel to a shock wave)
α = Mach angle
β = angle between constant velocity line and streamline in hodograph plane
δ = angle between $M = 1$ line and normal to a surface
γ = isentropic exponent
ω = rate of rotation of fluid element
φ = velocity potential
ψ = stream function
ρ = mass density
θ = oblique shock angle or velocity vector direction

SHOCK WAVES

By way of introducing some concrete ideas about shock waves, consider a frictionless constant area pipe as shown in Fig. 1.

Suppose that a fluid of known properties flows steadily into the pipe through section 1. Under steady conditions what emerges from the pipe at section 2? To answer this question we apply to the fluid between sections 1 and 2 the laws that govern the motion of bodies. First, conservation of matter requires that as much fluid flows out at section 2 as flows in at section 1. This gives

$$\rho_1 u_1 = \rho_2 u_2 \tag{1}$$

The conservation of momentum requires that the forces applied to the section of fluid between 1 and 2 along the axis of the pipe must balance the change in momentum, or

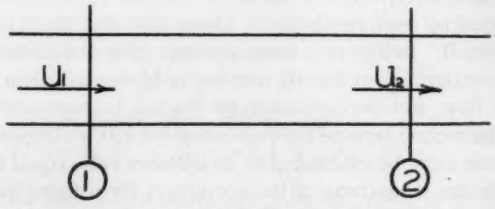

FIG. 1.

$$p_1 + \rho_1 u_1^2 = p_2 + \rho_2 u_2^2 \tag{2}$$

Finally, conservation of energy requires that the energy entering section 1 must pass out through section 2, since there is to be no work done on, or heat transferred to, the fluid between sections 1 and 2. Therefore

$$h_1 + (u_1^2/2) = h_2 + (u_2^2/2) \tag{3}$$

In these Eqs. (1), (2), and (3) we regard all quantities with subscript 1 as known, all quantities with subscript 2 as unknown. Thus, we have as unknowns the pressure, density, enthalpy, and velocity of the fluid at section 2. So far there are not sufficient equations to determine what will leave at section 2. However, the three properties—pressure, density, and enthalpy—are connected as soon as the nature of the flowing substance is known. To be specific, assume that the fluid entering section 1 is a perfect gas for which Eqs. (4) and (5) hold.

$$p = \rho RT \tag{4}$$

$$h_1 - h_2 = c_p(T_1 - T_2) = \left(\frac{\gamma}{\gamma - 1}\right)\left(\frac{p_1}{\rho_1} - \frac{p_2}{\rho_2}\right) \tag{5}$$

It is now possible to solve for conditions at 2.

By eliminating the properties p_2, ρ_2, and T_2, we get the following equation connecting the velocity at 2 with conditions at 1:

$$u_2^2 - \left(\frac{2\gamma}{\gamma + 1}\right)\left(\frac{p_1}{\rho_1 u_1^2} + 1\right)u_1 u_2 + \frac{2\gamma p_1}{(\gamma + 1)\rho_1} + \left(\frac{\gamma - 1}{\gamma + 1}\right)u_1^2 = 0 \tag{6}$$

The first thing to observe in this equation is that it is of second degree in u_2. This means that we have not one possible fluid leaving at 2 but two possible fluids leaving at 2. The solutions of this equation are

$$u_2 = u_1$$

$$u_2 = \left\{[2\gamma/(\gamma + 1)](p_1/p_1 u_1^2) + (\gamma - 1)/(\gamma + 1)\right\}u_1 \tag{7}$$

Naturally, we find that one possible leaving condition is identical to the entering condition. There would be something fundamentally wrong if this were not the case, since it is common experience that what comes out of a pipe is identical to what went in (neglecting friction). The other solution, however, requires some examination. First, if this second solution is real, then there must be inside of the pipe some stationary disturbance—that is, some disturbance that remains between sections 1 and 2 and through which the fluid passes. To see the meaning of this second solution, introduce the speed of sound by

$$a^2 = \gamma p/\rho \tag{8}$$

The second solution becomes

$$u_2 = \left\{[2/(\gamma + 1)](a_1/u_1)^2 + (\gamma - 1)/(\gamma + 1)\right\}u_1 \tag{9}$$

This can be further simplified in the following way. Consider the frictionless, adiabatic flow through a nozzle of varying area. The energy equation for this case is the same as Eq. (3). Introduce into Eq. (3) the speed of sound from Eq. (8).

$$a_1^2/(\gamma - 1) + (u_1^2/2) = a_3^2/(\gamma - 1) + (u_3^2/2) \tag{10}$$

Suppose now that the arbitrary state (3) at some nozzle area is such that the fluid had the same velocity as the speed of sound $u_3 = a_3 = a_*$—that is, such that the Mach Number $M_3 = 1$. Thus

$$a_*^2 = 2a_1^2/(\gamma + 1) + [(\gamma - 1)/(\gamma + 1)]u_1^2 \tag{11}$$

Hence, Eq. (9) becomes

$$u_2 u_1 = a_*^2 \tag{12}$$

This equation states that the velocity of the fluid at section 2, u_2, times the velocity of the fluid at section 1, u_1, is equal to the velocity of sound squared under that condition of the fluid for which $M = 1$. Since the velocity of sound in the fluid varies with the fluid properties, this last specification (that the properties be such that $M = 1$) is an important consideration. This equation was first presented by Prandtl[1] in 1904. Now, to analyze this equation, suppose $u_1 = a_*$—that is, suppose that the fluid enters with a velocity equal to the velocity of sound in the fluid. Then u_2 also equals a_* and the two solutions of Eq. (6) have merged into a single solution. There is no stationary disturbance possible that is consistent with the physical laws and the fluid properties as given by Eqs. (1) through (5). On the other hand, suppose u_1 is greater than a_*—that is, $M_1 > 1$. In this case $u_2 < a_*$ and some kind of a compression process must have occurred inside of the pipe. Finally, if $u_1 < a_*$—that is, $M_1 < 1$—u_2 will be greater than a_* and an expansion disturbance must be occurring between sections 1 and 2. For both of these cases the magnitude of the change in pressure is easily found by eliminating ρ_2 from Eqs. (1) and (2). Thus

$$p_2 - p_1 = \rho_1 u_1(u_2 - u_1) \tag{13}$$

So far, there is no reason why either an expansion or compression might not take place with equal ease. Of course, experience shows that we never are embarrassed by having a fluid leave a short section of pipe at a far higher velocity than that at which it enters, so that physically the expansion disturbance is not observed in spite of the fact that the physical laws of conservation of matter, energy, and momentum have no objections.

The objection to an expansion disturbance arises from the second law of thermodynamics. For a perfect gas

$$ds = c_v(dT/T) - R(d\rho/\rho) \tag{14}$$

By integrating this equation and substituting from Eqs. (1), (2), (3), (11), and (12), we get the following equation for the entropy change:

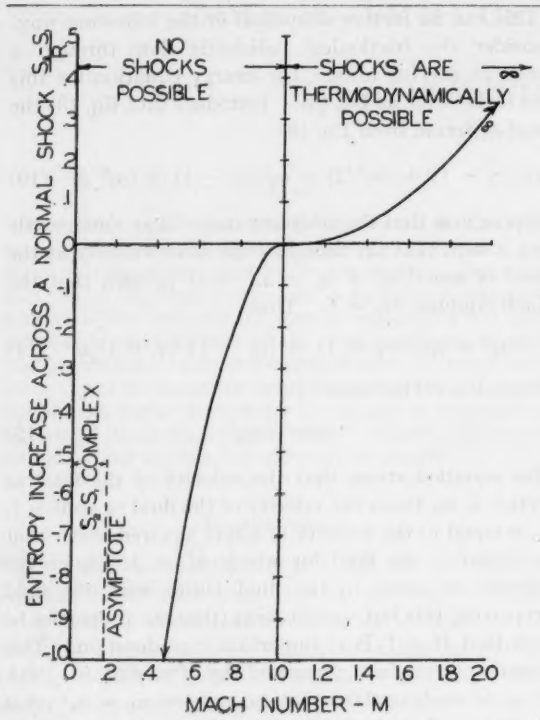

FIG. 2. The entropy increase across a normal shock. By second law of thermodynamics shocks are not possible for a Mach Number less than unity.

$$\frac{s_2 - s_1}{R} = \frac{1}{\gamma - 1}\left\{ln\left[\left(\frac{2\gamma}{\gamma+1}\right)M_1^2 - \left(\frac{\gamma-1}{\gamma+1}\right)\right] + ln\left[\frac{2}{(\gamma+1)M_1^2} + \left(\frac{\gamma-1}{\gamma+1}\right)\right]\right\} \quad (15)$$

From this equation it is obvious that no change of entropy occurs if $M_1 = 1$. By reference to Fig. 2, it is clear that the entropy will increase from section 1 to section 2 only if $M_1 > 1$. Thus, only the case of a compression disturbance can arise in practice, since the occurrence of an expansion disturbance of this type would make a perpetual motion machine possible.

It appears that any stream flowing at supersonic velocity may, if it so chooses, slow down to the appropriate subsonic velocity at any time and continue at this new condition. Thus, so far, there is no reason whatever why any supersonic stream should or should not at any time change its mind as to its properties and velocity.

Since the compression disturbance remains between sections 1 and 2, its velocity must be equal to u_1. Since, as shown above, $u_1 > a_*$, the disturbance must be moving with a velocity higher than the velocity of sound. Notice further by Eq. (12), the greater the disturbance the greater the velocity. These compression disturbances always move at a greater speed than the speed of sound if they introduce a finite disturbance into the stream.

Nature of Shock Waves

Having assured ourselves that the laws of nature permit these finite disturbances to remain stationary in a fluid and having observed such disturbances experimentally, it is natural to ask how thick they are and what process occurs in the fluid during passage through such a disturbance. First, it should be noted that the treatment, so far, gives no information whatever relative to these questions. Section 1 and section 2 might have been separated by 1/1,000,000th of an inch as far as our discussion was concerned. It would make absolutely no difference to our treatment as long as the assumptions that no forces external to the pipe and no heat or work exchange occurred within the fluid and as long as the gas laws (4) and (5) continue to hold. Thus it is necessary, in order to answer the above questions, to find to what extent these assumptions break down. It is only through the failure of these assumptions that a compression disturbance can have any finite thickness. If it were not for such additional considerations, a zero thickness compression shock would be the only physical possibility. This is important since problems in aerodynamics treated by the conventional theory of a frictionless, adiabatic, perfect gas continuum can admit compression shocks only as something extra (and of zero thickness).

The actual physical process that takes place in a compression shock has been considered by a number of workers.[2-8] In each of these references a more or less complete picture of a real fluid has been introduced into the more complete differential equations describing the motion through the disturbance—that is, equations replacing and supplementing Eqs. (1) through (5). The various combinations considered are: (1) an adiabatic continuum with viscosity, thus, friction will control the shock thickness; (2) a frictionless fluid with thermal conductivity, thus, heat conduction will control the shock thickness under those conditions in which heat conduction is adequate to permit a shock (not always the case); (3) a continuum with both

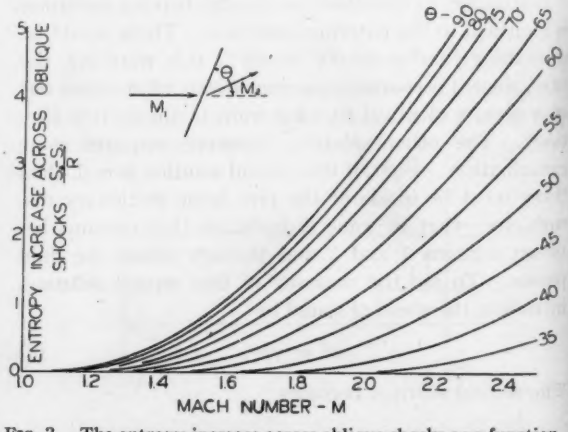

FIG. 3. The entropy increase across oblique shocks as a function of the initial stream Mach Number and the angle of obliquity.

thermal conductivity and viscosity. For details of these treatments see references 1 through 8. They are all in agreement on the following points. The stationary disturbance, the shock wave, is dependent in thickness upon the velocity. For $M = 1$ the thickness becomes infinite. For relatively small velocity changes the thickness becomes small. The following formula is given by Taylor.[8]

$$t(\text{in.}) = 1/80(u_2 - u_1)(\text{ft. per sec.}) \qquad (16)$$

Notice that a change of velocity of 10 ft. per sec. would occur in a thickness of 1/800th of an inch. Shock waves involving greater changes in velocity are thinner, so thin in fact that there is no hope at the present to obtain experimental measurements with which to check the results.

This, however, is hardly necessary. First, it is sure in many cases that the actual dimensions specified by the above theories would probably not be correct. For so thin a layer, often approaching molecular dimensions, the continuum treatment by way of viscosity and thermal conductivity could hardly be correct. A new treatment, based upon kinetic theory of gases, would be indicated. Modern physics, moreover, shows that for many gases even this treatment would be wholly inadequate. The quantum theory has shown the necessity of considering the distribution of energy between the various energy states of the atoms and molecules comprising the gas. It is known that in many gases internal equilibrium could not readjust itself so rapidly as required by a compression shock. What we are saying here is that the properties of the fluid Eqs. (4) and (5) will, in general, not be correct for the fluid within the disturbance if the disturbance is as thin as predicted above. In general, then, we can expect thickness of the order of magnitude of those predicted with, however, no expectation of detailed agreement with any future thickness measurements.

Second, the above discussion of kinetic and quantum effects need not disturb us as aerodynamicists so long as the thickness is of the order of a fraction of an inch, since Eqs. (1) through (5), as used in the original derivation of the shock-wave equations, are entirely correct for sections 1 and 2, provided these sections are placed before and after the disturbance. Thus, we can, in aerodynamics, proceed as if the shocks were real discontinuities. No matter what future internal aspects a shock may develop, it cannot alter the shock equations already developed, provided there is no energy transmitted from the region of the disturbance to other distant regions. It might be interesting to mention here the fact that such energy loss can take place if the shock wave is sufficiently strong. There is some indication that an extremely strong shock wave—arising, for example, in the case of a meteor entering our atmosphere at a Mach Number in the neighborhood of 100—gives rise to such a great disturbance to the air that electrons are torn from the atoms and, on return, radiate energy out of the shock-wave region in all directions. Some of the light that is seen as a meteor streaks across the sky may be evidence of a failure of the formulas used in the first section.

Oblique Shock Waves

So far, we have considered shock waves so placed in the air stream that the direction of the air was unaltered. The shock wave is normal to the incoming and outgoing air velocity. When fluid flows toward a shock wave, it may or may not be normal to that shock wave. Oblique shock waves, oblique to the oncoming velocity, can be considered as normal shock waves to a component of the oncoming velocity. The simplest way to assure ourselves of the correctness of this is to imagine a normal shock and observation of it from a vehicle moving along the shock. Thus, the fluid appears to the moving observer as though it were oblique to the shock (see Fig. 4). It is also evident from Fig. 4 that the velocity of the fluid as viewed by our moving observer will have, after the shock, the same velocity component along the shock as before but a smaller normal component. Thus, in an oblique shock the fluid suffers an abrupt change in direction.

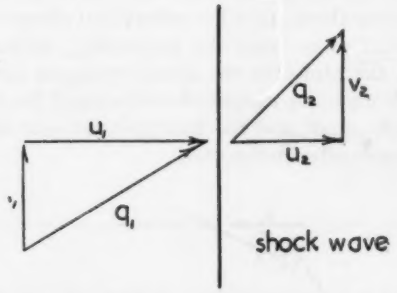

Fig. 4. An oblique shock is a normal shock to a velocity component. The velocity direction changes abruptly.

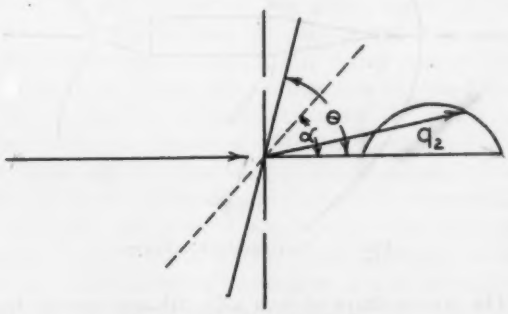

Fig. 5. The shock polar.

If, as in Fig. 5, there is a fixed oncoming velocity and shock waves are considered at various angles, then two effects occur as θ is decreased from 90°. The direction of the stream alters and the magnitude of velocity fol-

lowing the shock alters. As θ is decreased, the component of the entering velocity is decreased and, hence, the jump in normal component of velocity is decreased. This gives rise to velocity vectors terminating on a curve somewhat as in Fig. 5. It should be observed that as the shock-wave angle θ becomes smaller, it finally assumes such a direction that the normal component of velocity is equal to the speed of sound. As we already noticed, there can then be no change in normal component and, hence, no real disturbance at all. This direction is at what is known as the Mach angle $= \sin^{-1} a/u_1$.

Oblique shock waves are to be understood in precisely the same way as normal shock waves, except that a component of the entering velocity is to be used instead of the entering velocity itself.

It is instructive to think about what takes place through the shock wave that attends the motion of a blunt projectile through air. Fig. 6 shows the approximate location and shape of the shock wave that has often been observed at velocities below those at which the wave is attached to the nose. Immediately in front of the projectile the wave is normal to the undisturbed air ahead of the projectile, and, hence, immediately following this shock there is fluid at a small velocity and high pressure moving toward the stagnation point. A little away from the axis of the projectile the shock wave is oblique, and the velocity of the fluid following the shock wave has suffered an abrupt change in direction away from the projectile. At distances far from the projectile the shock wave has turned to the Mach angle, the magnitude of the shock has become vanishingly small, and the fluid proceeds past the projectile essentially undisturbed.

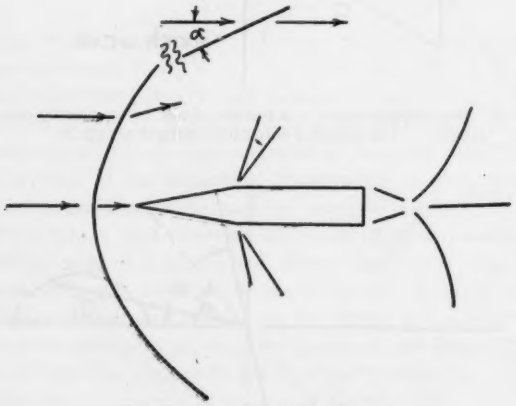

FIG. 6. A projectile headwave.

The precise shape of such a disturbance has not been predicted to date. In fact, one occasionally hears that the fluid in the region behind a shock is turbulent or otherwise disturbed in an unpredictable way. The fluid behind a shock is disturbed in perhaps an undesirable way but not in an unpredictable way.[9–11] Only the case of flow in two dimensions will be considered here. The flow prior to a shock wave—around, let us say, an airfoil—is assumed to be irrotational. It is so assumed because the fluid can always be supposed to have started from uniform conditions at rest and to be frictionless and adiabatic. It now follows by Helmholtz's theorem that the rotation originally zero will remain so. The rotation of fluid elements can be derived in a rather general way from Fig. 7.

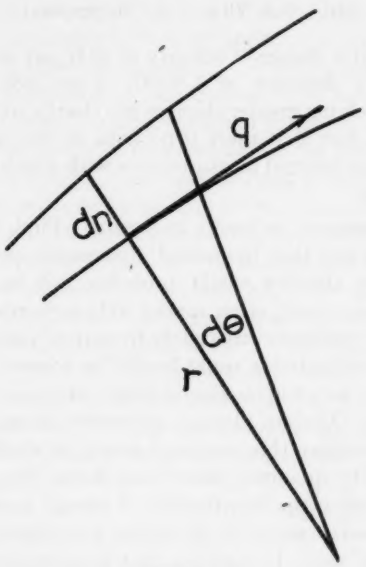

FIG. 7.

By the definition of rotation we get

$$2\omega = -(\partial q/\partial n) - (q/r) \tag{17}$$

Since the fluid can be assumed frictionless in the region behind a shock wave, the acceleration normal to a stream line must be balanced by the corresponding pressure gradient.

$$\partial p/\partial n = \rho q^2/r \tag{18}$$

By eliminating the radius of curvature from these two equations there follows

$$2\omega = -(\partial q/\partial n) - (1/\rho q)(\partial p/\partial n) \tag{19}$$

Introduce the stagnation enthalpy

$$h_0 = h + (q^2/2) \tag{20}$$

and the thermodynamic relation

$$dh = Tds + (dp/\rho) \tag{21}$$

Thus

$$2\omega = (1/q)[T(\partial s/\partial n) - (\partial h_0/\partial n)] \tag{22}$$

This equation gives a relation between the rotation and the rate of change of entropy and stagnation enthalpy normal to the stream lines. This is a local fluid property and is independent of the reason for the existence of the variation in s and h_0. Thus, if for any

reason the entropy or stagnation enthalpy is altered, the rotation will also be altered, unless the changes take place in precisely the amount required to keep the rotation constant. This latter case is of no importance, since it can be satisfied at only one velocity on each stream line. In particular, if a perfect gas flows from rest from a chamber of zero velocity and constant pressure but of nonconstant temperature, the rotation varies along each stream line according to the formula

$$2\omega = (\rho q^2/2)(\partial ln T_0/\partial \psi) \tag{23}$$

The rotation is zero in the zero velocity chamber but does not remain zero thereafter.

As long as there is no transfer of work or heat normal to stream lines, the stagnation enthalpy remains constant. Thus, in most aerodynamic work it follows that h_0 is constant along stream lines. In particular, since it is usually possible to assume that the fluid starts from rest in a uniform temperature and pressure chamber, h_0 is constant everywhere. The corresponding statement for the entropy is derived as follows. Differentiate Eq. (20) along a stream line

$$(\partial h/\partial l) + q(\partial q/\partial l) = 0 \tag{24}$$

Also, the momentum equation

$$(1/\rho)(\partial p/\partial l) + q(\partial q/\partial l) = 0 \tag{25}$$

from which

$$\partial s/\partial l = (1/T)[(\partial h/\partial l) - (1/\rho)(\partial p/\partial l)] = 0 \tag{26}$$

Thus, generally both the entropy and h_0 are constant on streamlines and, considering the source of the stream lines, they are constant everywhere. Through a shock, h_0 remains constant, as is seen by examining Eq. (3). The entropy, however, must change as by Eq. (15) (or its equivalent for oblique shocks obtained by replacing M_1 by $M_1 \sin\theta$; see Fig. 3). Thus, in the region following a shock the rotation will not, in general, be zero but will vary from point to point as required by Eq. (22) and the corresponding entropy changes. It is only when a shock wave of fixed obliquity crosses a stream of uniform direction and velocity that the entropy change will be the same on all stream lines, and, hence, it is only then that the rotation would be zero after the shock. In Fig. 6, for example, there will be continuously distributed rotation through the region following the shock.

Critical Flow About Airfoils

So far, no consideration has been given to the question of when shocks will arise. It has been shown that shocks *can* occur at any time when the fluid has a velocity at any point exceeding the velocity of sound, but nothing has been said about what *will* happen. Unfortunately, nothing too significant can yet be said in a general way about this circumstance. Consider first the familiar case of flow through a Laval nozzle. In such a nozzle with specified entrance conditions, the flow increases as the pressure following the nozzle is decreased. This increase in flow continues until the velocity of the fluid reaches the velocity of sound at the minimum section of the nozzle. No further flow is possible. However, as the pressure is further dropped at the nozzle exit, the fluid flows with increasing velocity through the speed of sound, becoming supersonic in some part of the outlet section of the nozzle. If it continued supersonic to the end of the nozzle, the stream would arrive at too low a pressure to satisfy the exit conditions. Hence, a shock wave forms somewhere in the nozzle so that the pressure of the fluid can agree with that at the nozzle outlet. In this one-dimensional case the shock wave is not a haphazard matter but stands in a predictable location so that the boundary conditions at the nozzle exit can be met. It should be explained here that this discussion considers only flow through a frictionless nozzle and that the "predictable" above may be modified considerably by the friction.

When one considers the two-dimensional flow about an airfoil, it has not yet been possible to discover just where and why shock waves arise. Some thoughts on this matter appear as follows. As the velocity about the airfoil increases, some region will become supersonic as in Fig. 8. That this region is real can be seen from

FIG. 8. Conditions where the $M = 1$ line touches an airfoil surface.

experimental or theoretic pressure distributions along airfoils in which pressures below critical are found. We visualize that something like the magnified portion of Fig. 8 occurs for some speed of the airfoil. A streamline near the surface and the surface of the airfoil form a converging-diverging passage, and under some conditions this passage acts like the Laval nozzle of the one-dimensional theory for which no higher flows are permitted. Hence, shock waves, at first small and near the surface, must appear. That this view is at least reasonable follows by considering the criterion for infinite acceleration described by Ringleb[12] and von Kármán.[13] von Kármán shows that for infinite acceleration a streamline in the hodograph plane must be tangent to one of the characteristics. This idea can be further developed as follows (see Fig. 9):

$$\tan\beta = \frac{1}{q}\left(\frac{\partial q}{\partial \theta}\right)_\psi = \frac{1}{q}\left(\frac{\partial l}{\partial \theta}\right)_\psi \left(\frac{\partial q}{\partial l}\right)_\psi = \frac{ra}{q^2} \tag{27}$$

where r is the radius of curvature of a stream line in the

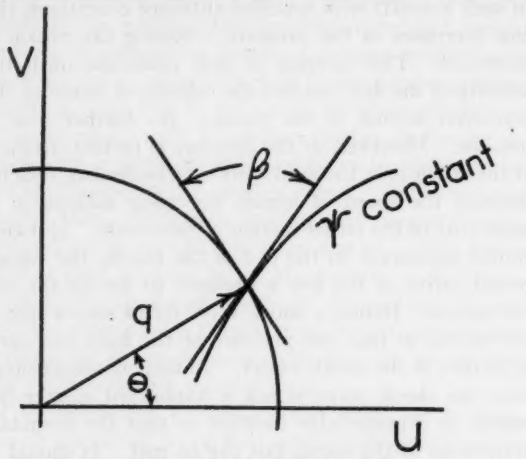

FIG. 9. A stream line in the hodograph plane.

physical plane and a is the acceleration of the fluid along a streamline.

$$a = q(\partial q/\partial l)_\psi \tag{28}$$

The streamline that is the surface of the airfoil has a specified radius of curvature, not zero, at all points. Hence, if there is to be an infinite acceleration, tan β becomes infinite or β becomes 90°. Since von Kármán has already shown that β must equal the Mach angle for infinite acceleration, the Mach angle must be 90° also—that is, $M = 1$ at the point where the infinite acceleration occurs. Further indication of the correctness of this qualitative idea follows from Fig. 8. The angle δ between a normal to the surface and a constant velocity line is

$$\tan \delta = (dl/dn)_q = -(\partial q/\partial n)_\varphi/(\partial q/\partial l)_\psi \tag{29}$$

Using Eq. (19) with the rotation set equal to zero and Eq. (28) for the acceleration,

$$\tan \delta = q^2/ra \tag{30}$$

or comparing this with Eq. (27),

$$\tan \beta \tan \delta = 1 \tag{31}$$

Now for the case under consideration in which the surface of the airfoil is a streamline and is without points for which $r = 0$, an infinite acceleration implies $\delta = 0$—that is, it implies that the constant velocity line is normal to the surface. With these two facts it appears that the limiting flow about an airfoil without shocks occurs when the constant velocity line $M = 1$ becomes normal to the surface at some point. Following this, a shock wave must begin near the surface, much as in a Laval nozzle.

After a shock wave has once started, the whole flow to infinity behind this wave is altered because, of the change in entropy, and, hence, new considerations must arise before the magnitude, location, and shape of a finite shock wave can be discussed.

General Shock Waves

In the preceding discussion the general treatment of the propagation of waves of permanent type was dropped after writing the energy, continuity, and momentum equations for the physical system of Fig. 1. All the remaining treatment has been concerned with a perfect gas.

Many types of shock waves are encountered in various physical phenomena. The most spectacular shock-wave phenomena is that involved in combustion waves as in a burning gas or a Bunsen burner, or detonation waves as in an explosive. These phenomena can be treated with the same three Eqs. (Eqs. (1), (2) and (3)) but with an appropriate specification of properties.

At least one of these more general shock waves is of some concern to aerodynamicists—namely, condensation shocks. In tests in high-speed wind tunnels in which atmospheric air is used, the large fall in temperature causes the air to become supersaturated on moist days. The moisture then "suddenly"[1] condenses in the form of minute droplets. This condensation is accompanied by the change of properties and velocity of the entire stream. In a Schlieren photograph, a condensation shock is undistinguishable from the common shock wave in air. Hence, wind-tunnel photographs must be interpreted with caution. Since the moisture varies from day to day, the condensation shock pattern also varies. This furnishes a method of locating the condensation shocks.

It may be argued that the airfoil or other object being tested will be used in moist air, hence, condensation shocks are desirable in wind-tunnel tests. This is only partly true because moving an airfoil through the atmosphere raises the stagnation temperature of the air relative to the airfoil; therefore, there will be smaller temperature drops and less condensation than in a wind-tunnel test with the same air at the same velocity.

References

[1] Prandtl, L., *Beiträge zur Theorie der Dampfströmung durch Düsen*, Z.V.D.I., s348, 1904.

[2] Ackeret, J., *Gasdynamik*, Handbuch der Physik, Vol. 7, pp. 289–342; Julius Springer, Berlin, 1927.

[3] Hugoniot, H., *Sur la propagation du mouvement dans les corps et specialement dans les gaz parfaits*, Journal de l'École Polytechnique, Vol. 58, p. 80, 1889.

[4] Rankine, W. J. M., *Theory of Shockwaves*, Trans. Roy. Soc., Vol. 160, p. 277, 1870.

[5] Prandtl, L., *Zur Theorie des Verdichtungsstosses*, Zeitschrift für das gesamte Turbinen-Wesen, Vol. 3, p. 241, 1906.

[6] Taylor, G. I., *The Conditions Necessary for Discontinuous Motion in Gases*, Proc. Roy. Soc., Vol. 84, pp. 371–377, 1910.

[7] Rayleigh, J., *Aerial Plane Waves of Finite Amplitude*, Proc. Roy. Soc., Vol. 84, pp. 247–284, 1910; Scientific Papers, Vol. 5, pp. 573–610.

[8] Taylor and Maccoll, *Aerodynamic Theory*, W. F. Durand, Editor, Vol. III, Div. H, p. 218.

[9] Crocco, L., *Eine neue Strömungsfunktion für die Erforschung der Gase mit Rotation*, Z.A.M.M., Vol. 17, pp. 1–7, 1937.

(*Continued on page 216*)

Measurement of Maneuvering Loads in Flight

C. J. BUZZETTI* AND W. L. HOWLAND†
Lockheed Aircraft Corporation

INTRODUCTION

DURING THE PAST 20 years, improvements in aircraft design have, to a large measure, been due to aerodynamic theory and wind-tunnel tests. There has been, however, one major weakness in both design tools and that has been in dealing with dynamic or nonuniform conditions. This is not because these two methods cannot handle dynamic conditions, for quite the reverse is the case. It does mean that serious difficulties and complications are encountered. Spin tunnels have been successful in giving the general behavior of an airplane, but they have produced little quantitative data. Gust tunnels have encountered great difficulties in accurately measuring the dynamic loads and assimilating actual conditions.

Design of large aircraft has been seriously impeded because of a lack of accurate knowledge of basic loads resulting from maneuvers. Many of the design loads for structural components of an airplane are governed by maneuvering loads. Because of this lack of information, the maneuvering loads required by the Civil Aeronautics Authority are based on an arbitrary normal force coefficient for the surface and the maneuvering speed, with the additional specification that the load need not be greater than that which is possible to obtain with a certain applied control force. Interest in dynamic loads has been greatly stimulated in recent years because of service failures, particularly of horizontal surfaces, which have occurred on several types of aircraft. Research work has been carried on by several organizations along both analytical and experimental lines. The analytical work has suffered for lack of sufficient flight data. Most calculations of maneuvering loads required a fundamental assumption of a certain rate of control surface movements. As this paper will show and as was brought out by Beman and Frost,[1] maneuvering loads appear to be a complicated function of not only what the airplane and its control system can do but, in addition, what the pilot will or chooses to do.[2] The experimental work has been handicapped because of the difficulties of making accurate measurements in flight and the absence of adequate instruments or methods. In general, the structural measurements made in flight in the past have been crude. Scratch gauges, deflection photographs, pressure distributions, and transit measurements of deflections have been made. The majority of measurements made during maneuvers have been with accelerometers. None of these methods has satisfactorily given the maneuvering load or stresses on the structure.

With the advent of wire resistance strain gauges, the measurement of maneuvering loads in flight becomes possible and feasible. The technique of making stress measurements in flight has advanced a great deal in the past few years. It is the object of this paper to describe some of the work carried on along this line at Lockheed Aircraft Corporation. Throughout this paper the term "maneuvering stress" is taken to mean that increment in stress which is caused by, or entirely dependent upon, the maneuver being made (maneuvering stress = total stress − balancing stress).

INSTRUMENTATION

Wire resistance-type strain gauges were used to measure boom and fuselage bending moments, wing stresses, stabilizer stresses, accelerations, control forces, control surface hinge moments, and surface positions during the tests to ascertain maneuvering loads.

The general electrical circuit used was a simple Wheatstone bridge, the output of which was recorded directly on an oscillograph without the use of intermediate amplifiers. This was made possible by the use of sensitive galvanometers in the oscillograph and by obtaining maximum power output from the gauges themselves.

A typical installation of the oscillograph and an automatic observer in the nose compartment of a P-38 is shown in Fig. 1. The oscillograph is seen in the lower center; the automatic observer camera is located directly above the oscillograph and is hidden by a

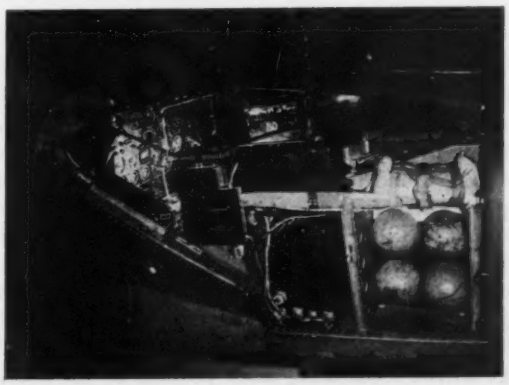

FIG. 1. Picture of test equipment in P-38 nose compartment.

Presented at the Summer Annual Meeting, I.A.S., Los Angeles, July 27-28, 1944.

* Engineer.
† Research Group Engineer.

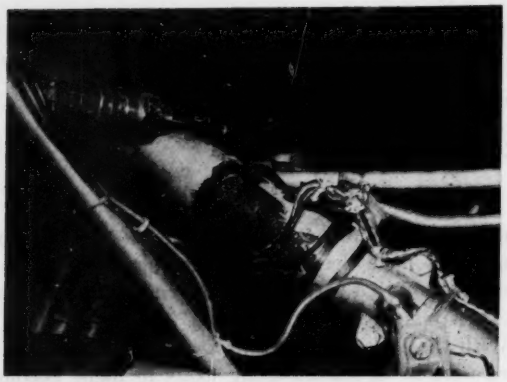

FIG. 2. Strain gauge bridge installation on engine mount member.

battery box. The thin black boxes are junction boxes for strain gauge and testing equipment wires. The remote control for the oscillograph was connected to the automatic observer control switch so that the pilot or flight engineer operated both simultaneously. The power supply to the strain gauges was also connected through the main control switch so that the strain gauges were drawing current only when in actual use. To insure constant voltage to the gauge circuits and thereby greater accuracy, special batteries other than the airplane's were used.

The oscillograph installation in the Constellation was more elaborate. A switching system was used which made it possible to connect to the oscillograph any desired arrangement of 50 or more separate strain gauge bridges. This was to permit the measurement of several different loads during one flight or in rapid sequence. The oscillograph control was designed so that operation of the automatic observer by the flight test engineer did not turn on the oscillograph, but operation of the oscillograph by its operator turned on the automatic observer. Thus, complete aerodynamic and engine information was assured during each operation of the load-recording oscillograph.

ROLL TESTS

One of the common maneuvers performed with a fighter airplane is a roll. Recently, a series of roll tests were conducted on a P-38 to determine the operating characteristic of a hydraulic booster on the aileron control system and to measure the stresses caused in the airplane's structure due to the high rates of roll. Calculations based on the predicted roll performance indicated that the engine mount might become critical under side loads (centrifugal force). Also the wing might be critical as a result of forces caused by large deflections of the aileron at high airplane speeds, the large aileron loads being made possible by the booster system.

In addition to the many quantities that were recorded by the automatic observer camera, eleven items were measured with electrical strain gauge bridges and recorded simultaneously on a Miller oscillograph. The eleven values measured were:

(1) Stresses in four members of the right engine mount and support bay.

(2) Shear stresses in the rear shear beam and in the upper surface of the wing near the main beam (outboard nacelle).

(3) Spanwise bending stresses in the upper surface of the wing at the main beam, just outboard of the nacelle.

(4) Pilot effort in terms of aileron control wheel moment.

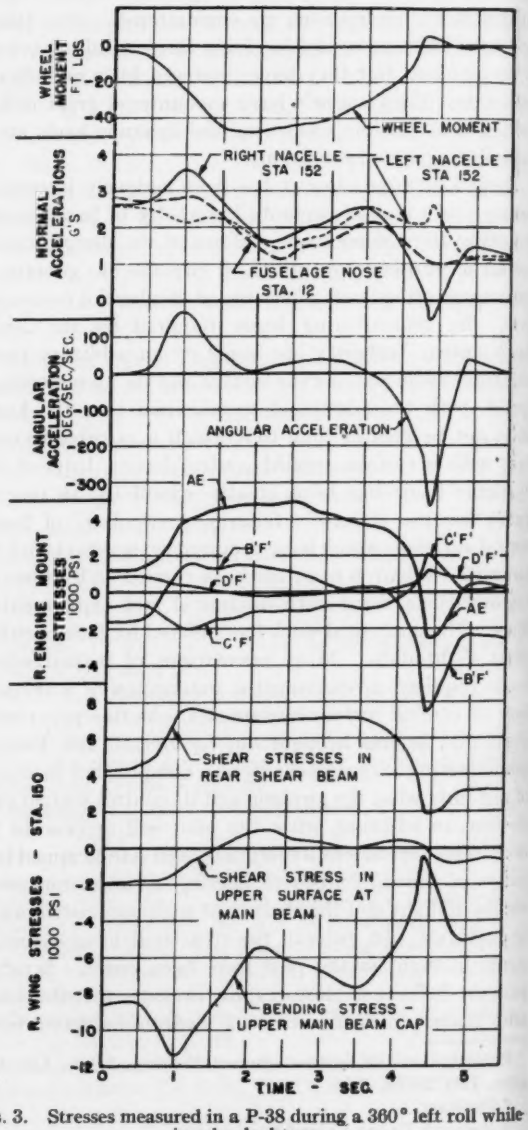

FIG. 3. Stresses measured in a P-38 during a 360° left roll while in a banked turn.

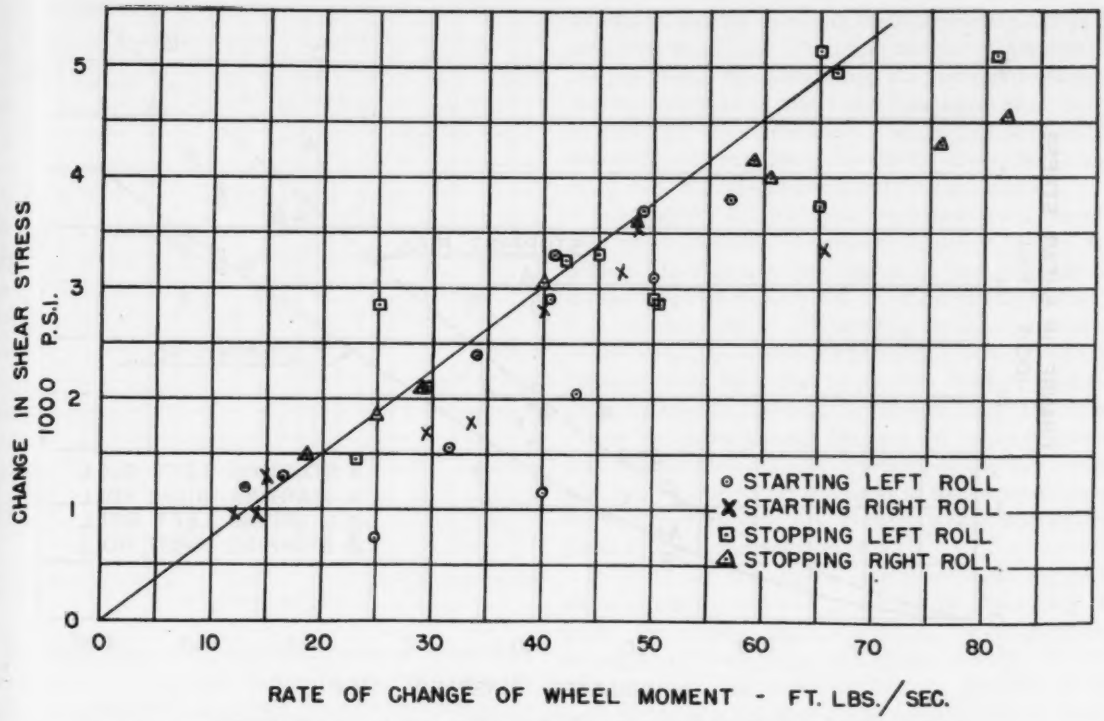

FIG. 4. Maneuvering stresses in P-38 rear shear beam versus rate of change of aileron control force.

(5) Vertical (normal to the spanwise axis) accelerations at each engine mount and at the nose of the airplane.

The method of obtaining the stress measurements was described earlier.

The aileron control loads were measured by means of a strain gauge bridge placed on the spokes of the control wheel so that it only responded to a twisting moment applied to the wheel and was independent of fore and aft loads.

Results of some of the stress measurements made during the roll tests are shown in Figs. 3, 4, 5, and 6. Fig. 3 shows the stresses measured during a 360° left roll while in a banked turn. The top curve in Fig. 3 is the control wheel moment exerted by the pilot. The next three curves are the accelerations measured at the right and left nacelles and at the fuselage nose. Note that all three accelerometers are at about 2.75 *g*'s at the start of the record. This is a result of the steady turn. The next lower curve is the angular acceleration of airplane caused by the aileron movement. This curve was calculated from the normal accelerations in each nacelle and by knowing the distance between them. The lower seven curves are stresses in various members in the airplane.

Engine Mount Stresses

In all maneuvers the engine mount stresses were found to be low. The maximum values recorded in any engine member during any rolling maneuver was +7,200 and −6,500 lbs. per sq.in. To substantiate the low engine mount stress values measured in flight and to obtain the load distribution for different loading conditions, a series of static tests were conducted on the right engine mount. These static tests showed that the mount stresses actually were low and that the cowling and its support structure were evidently taking most of the load. Static tests were made with and without the cowling. Since the cowling was not taken into account in the stress analysis, it means that the engine support is actually over strength. Here is an example where, had it not been for structural flight measurements, needless weight would have been added to the engine support structure.

Rear Shear Beam Stresses

The shear stresses measured in the rear shear beam were high in comparison with the allowable stresses, the maximum value measured being +7,600 lbs. per sq.in. Positive shear stresses are considered to be those resulting from a diving moment on the wing; thus, positive shear in the rear beam indicates an up load on the rear beam.

Because of the interesting nature and magnitude of the rear shear beam stresses during the rolls, the data were carefully investigated. One of the results of the analysis is given in Fig. 4. This figure shows the maneuvering stresses in the rear beam plotted up against rate of change of aileron control force. The points were obtained from a large number of roll tests made

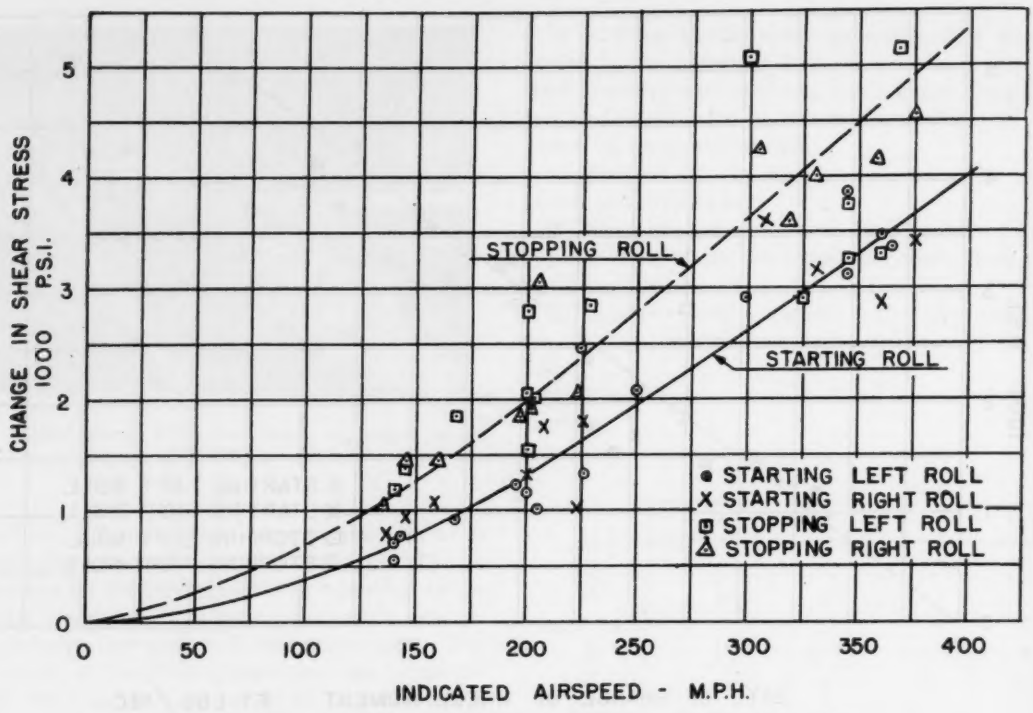

FIG. 5. Maneuvering stresses in P-38 rear shear beam versus speed for rolls.

over the complete speed range, with right and left and starting and stopping rolls. The scatter is admittedly large, but, when it is considered that two different pilots did the testing and that they rolled the ship as hard as they could at each air speed, it is not unreasonable. The line corresponds roughly to the upper limits. However, if the maneuvering stress is divided by the dynamic pressure and plotted against rate of change of wheel moment, no correlation is revealed.

Speed Versus Roll Maneuvering Stresses

In order to investigate the effect of speed on the maneuvering stresses resulting from rolls, Fig. 5 was plotted. This figure shows the maneuvering stress versus indicated air speed. Here a reasonable correlation is found. There appears to be a consistent variation between the maneuvering stress caused in starting the roll compared with stopping it, stopping being higher. This is probably to be expected, since in stopping the roll the force on the aileron helps the pilot return the surface to neutral, whereas it opposed when starting. Then there is also the psychologic effect on the pilot; he feels he is causing more load on the structure when he suddenly deflects the surfaces than when he suddenly returns them to neutral.

After studying Figs. 4 and 5 it is apparent that maneuvering stresses due to rolls are influenced just as much by the rate of application of control movement as by the air speed at which the maneuver was made. This brings out one of the most difficult problems connected with the calculation of maneuvering loads—they are dependent upon the behavior of the pilot. When looking at Figs. 4 and 5 it should be remembered that the balancing stress or nonaccelerated flight stress changes with speed so that the most critical stress (balancing plus maneuvering stress) on the structure will still, in general, be at the highest speed. In this particular case the higher the air speed, the more critical the stress in the rear shear beam, since for a given roll maneuver the balancing stress increases with speed. Likewise, a roll, while in a high speed pull-out or tight turn, will produce large total stresses (see Fig. 3).

Angular Acceleration

One of the quantities of considerable interest in roll tests is angular acceleration. In Fig. 6 a plot of rate of change of aileron control force versus angular acceleration is shown. Here again considering the large number of variables, a good correlation is obtained. From this figure it can be said that the angular acceleration must be governed just as much by the rate of change of control force as by air speed.

PULL-OUTS

In addition to the measurements during roll tests, some measurements of tail load during pull-outs have been made to determine what the maneuvering increment of tail load would be on a P-38 during a pull-out from a dive.

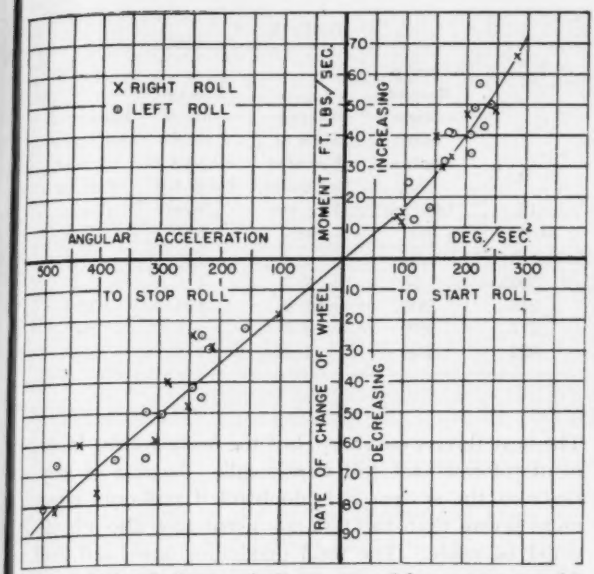

FIG. 6. Rate of change of aileron control force versus angular acceleration for P-38.

The oscillograph and automatic observer installation was identical to that used during the roll tests, but the values measured with the strain gauges were changed to the items listed blow.

(1) Bending moments in both booms at two stations—wheel well station 250 and aft boom Station 330.
(2) Elevator hinge moment.
(3) Elevator stick force.
(4) Elevator angle.
(5) Center of gravity and tail acceleration.

The strain gauges used in measuring the boom loads were calibrated directly in terms of boom moment by loading the stabilizer at a given location.

In order to determine tail air load from measured boom moments it is necessary to correct the boom moments for the effects of acceleration loads on the structure. Corrections for the acceleration loads are made by subtracting the moments due to acceleration from the measured moments. The moments due to acceleration are calculated by multiplying the measured center of gravity acceleration times the calculated dead weight moment for 1g acceleration. When tail acceleration measurements were made, the effects of angular acceleration were included in calculating the moments.

Calculations of tail air load were based on a constant and assumed center-of-pressure location on the stabilizer. In this case the center of pressure was assumed to be at Station 410 or, approximately, the 27 per cent chord point. By knowing the air load moment at two separate stations it was possible to determine the moment about the center of gravity. Tail air load was then obtained by dividing the moment about the center of gravity by the distance between the center of gravity and the assumed center of pressure of the tail. Since this tail air load is proportional to the moment about the center of gravity, it is a direct measure of the airplane-less-tail pitching moments.

In order to check up on instrumentation and technique of making tail load measurements, balancing tail loads for steady flight conditions were measured throughout a wide range of airplane speeds. The results obtained are shown in Fig. 7. Plotted on the same figure is a tail load curve calculated from wind-tunnel data. The two curves compare very well except at the higher speeds. Both the calculated curve and the experimental points are for constant power; thus, the higher speeds had to be obtained by diving the airplane. This may have had some influence on the measured values; however, the discrepancy at the higher speeds is probably due to inaccuracies in the wind-tunnel tests or Mach Number effect.

Load history curves of two pull-outs are shown in Figs. 8 and 9. Fig. 8 represents a relatively easy pull-

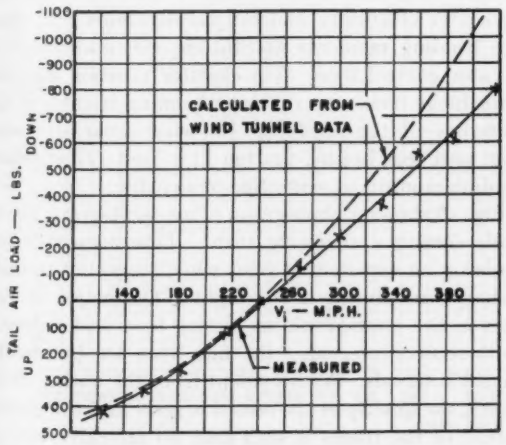

FIG. 7. Balancing tail load measured in flight on a P-38.

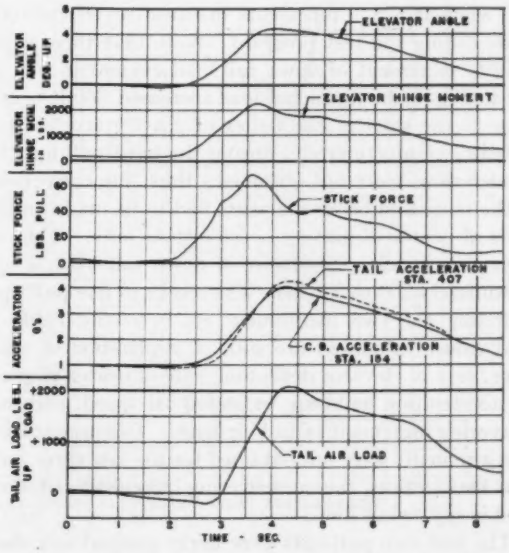

FIG. 8. Stresses measured during a 4g pull-out in a P-38.

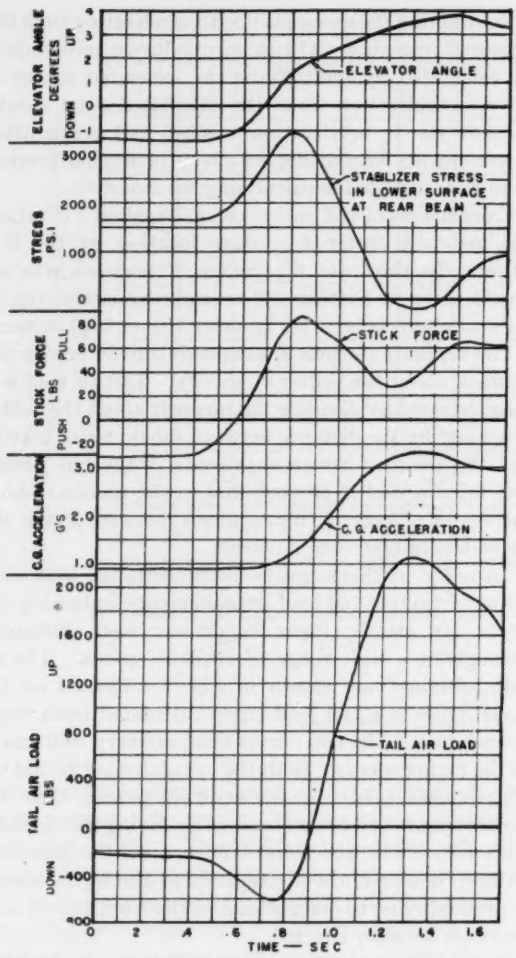

FIG. 9. Stresses measured during a rapid pull-out in a P-38.

out, whereas Fig. 9 represents the most severe pull-out made during the test program. Note that there is no definite increment of down tail load evident in Fig. 8, but in Fig. 9 the down tail load increased 360 lbs. just prior to the start of the center of gravity acceleration increase. Unfortunately, during the hard pull-up, tail accelerations were not obtained; thus, the corrections to the measured boom moments had to be made on the basis of center of gravity accelerations only. This results in a smaller increment of down tail load of approximately 200 to 300 lbs. The results of five pull-ups, including the two mentioned, are given in Table 1. The values tabulated are rate of application of stick force, rate of elevator deflection, rate of center of gravity acceleration build-up, indicated air speed, and maneuvering increment of tail air load. Tail acceleration measurements were not obtained for the last three pull-outs listed; thus, the maneuvering increment of tail air load is somewhat low.

The first two pull-outs were fairly gradual and there was no distinct maneuvering increment of tail air load.

TABLE 1

V_i, M.P.H.	Average Rate of Stick Force Application, Lbs. per Sec.	Average Rate of Elevator Deflection, Deg. per Sec.	Average Rate of C.G. Acceleration Build-Up, g's per Sec.	Maneuvering Increment of Tail Air Load., Lbs.
410	30	1.3	1.1	...
300	45	3.2	1.1	...
246	200	11.0	4.0	320
275	230	9.0	4.5	280
322	330	11.0	9.0	360

The next three were sharp, but the maneuvering increments of tail load still were small. Because of elasticity in the system it is doubtful if pull-outs much more severe than the last one listed (see also Fig. 9) could be made. The total maximum down tail load (maneuvering increment plus balancing) did not exceed 20 per cent of the calculated limit maneuvering load during any of the pull-outs performed. Apparently, the design requirements on maneuvering tail loads are overly conservative for this airplane.

As mentioned in the Introduction, maneuvering loads on the horizontal tail surfaces of large airplanes are currently of particular interest. The addition of special tabs and booster control systems has greatly added to the importance of accurate calculations of maneuvering tail loads. One of the problems that must be answered for large airplane design is whether or not the pilot will recognize the severity of a maneuver that will result from a certain control deflection.

In order to obtain some preliminary information on this general problem, structural loads were measured on the Constellation during some maneuvers. This airplane is a large, fast transport that incorporates the latest developments in control systems and maneuverability. During the test made to determine tail loads, the following items were measured with strain gauges: (1) center of gravity and tail accelerations; (2) fuselage bending moments at Stations 690 and 924; (3) elevator control force; (4) elevator position and elevator hinge moment; (5) wing bending stresses at the centerline of the airplane; (6) wing shear stresses—front and rear beams, Station 118; and (7) stabilizer bending moment at centerline of airplane.

Fig. 10 shows a photograph of an oscillograph record made during a sharp 2g turn. This maneuver was made by an experienced pilot when requested to make a sharp turn during a test flight. The major vertical lines in the photograph are timing lines and represent tenth-second intervals; the fine lines are hundredth-second intervals. As is evident from the nature of the traces, the quality of the record is good and the general spread of the traces is such that no difficulty was encountered in interpreting the record.

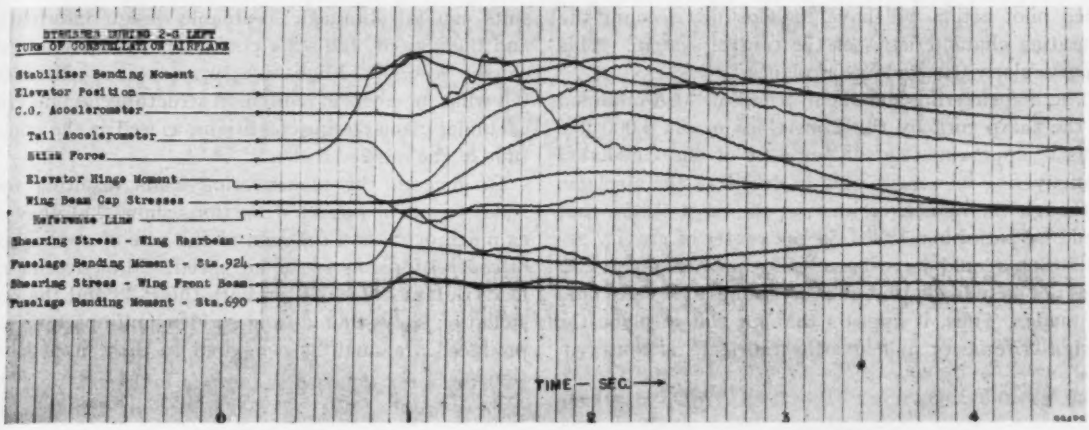

FIG. 10. Oscillograph record of stresses during a 2*g* turn in a Constellation.

Fig. 11 shows a plot of the stresses and loads obtained from the oscillograph record of Fig. 10. The method of calculating tail air load was similar to that described for the P-38 tests. In Fig. 11 the elevator stick force curve is interesting because it shows a rate of application of force of 390 lbs. per second, which slightly exceeds that obtained in the most severe pull-out in the P-38 described previously. Note that there is a lag between the stick force and the elevator hinge moment, whereas in the P-38 pull-outs there was no lag. This small lag is probably due to the operation of the control system, since a certain quantity of oil must flow in the boost system. A reasonable explanation for the greater rate of force application for the Constellation is that during part of the stick force build-up the elevator was not deflecting; thus, the stick deflections were probably small, whereas in the P-38 the elevator deflected almost immediately with application of the stick force, thereby permitting relatively large stick deflections.

From a maneuvering load standpoint the lag or elasticity in a control system is significant because abrupt actions by the pilot are not immediately reflected in the elevator load and position. Thus, any calculations of maneuvering tail loads made on the assumption of spe-

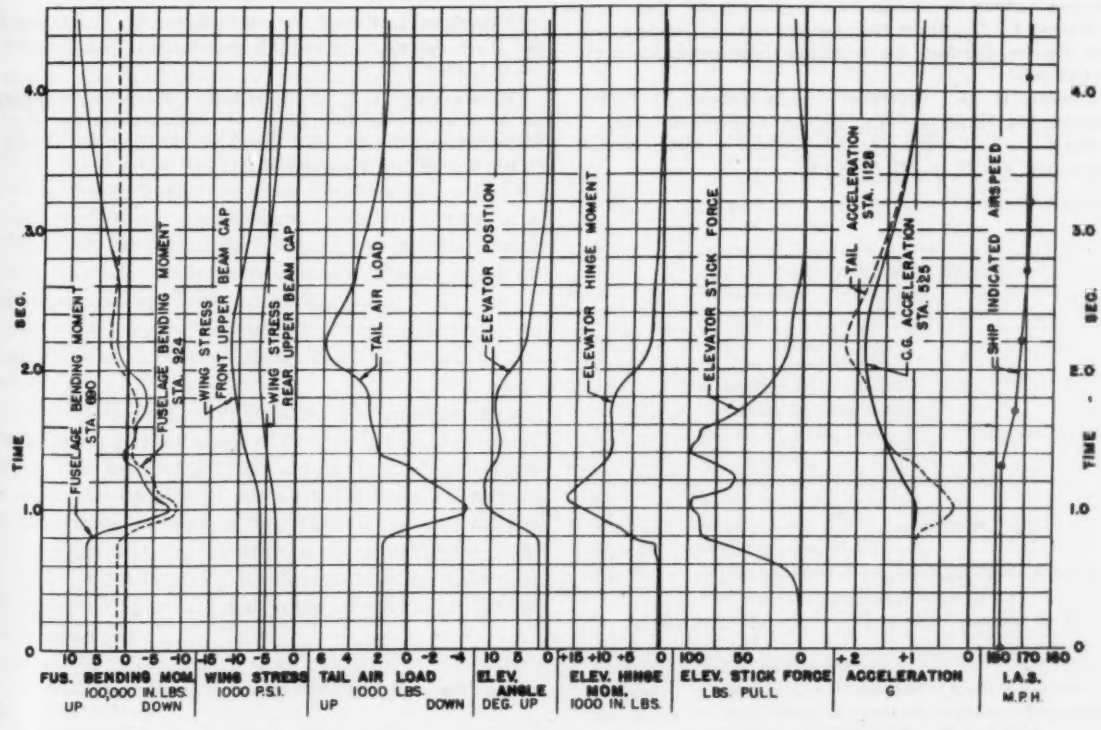
TIME SEC.
FUSELAGE BENDING MOMENT STA 690
FUSELAGE BENDING MOMENT STA. 924
WING STRESS FRONT UPPER BEAM CAP
WING STRESS REAR UPPER BEAM CAP
TAIL AIR LOAD
ELEVATOR POSITION
ELEVATOR HINGE MOMENT
ELEVATOR STICK FORCE
TAIL ACCELERATION STA. 1128
C.G. ACCELERATION STA. 525
SHIP INDICATED AIRSPEED
FUS. BENDING MOM. 100,000 IN. LBS. UP DOWN
WING STRESS 1000 P.S.I.
TAIL AIR LOAD 1000 LBS. UP DOWN
ELEV. ANGLE DEG. UP
ELEV. HINGE MOM. 1000 IN. LBS.
ELEV. STICK FORCE LBS. PULL
ACCELERATION G
I.A.S. M.P.H.

FIG. 11. Maneuvering loads obtained from the oscillograph record shown in Fig. 10—i.e., 2*g* turn in a Constellation.

cified pilot action will have to take into account the operating characteristics of the control system. This is particularly true on large airplanes.

The maneuvering increment of tail air load obtained in the sharp turn by the Constellation was 6,000 lbs. This is approximately 30 per cent of the calculated maneuvering increment used in design of the airplane. Although the maneuver was not the most severe that could be performed based on the center of gravity acceleration (could have been 1.86 times as severe), it does not seem likely that one three times as severe could be made. Thus, it appears that for this airplane the design criteria for maneuvering tail loads is conservative.

Conclusion

From the structural flight test measurements described and many others made at Lockheed Aircraft Corporation, the following conclusions can be drawn: The technique of measuring loads in flight has developed to the point where accurate reproducible results can be obtained. Valuable design information and high speed, full-scale checks on wind-tunnel data can be secured. Flight measurements can definitely tell what members in redundant structures become critical under maneuvering conditions, as well as the magnitude of the applied loads.

In general, the maneuvering loads resulting from sudden control surface deflections show that they are as much or more a function of the rate of applications of control force as of the air speed. Maneuvering tail loads obtained in flight on both the P-38 and the Constellation show that during sudden pull-ups the loads produced are small as compared to those used in design.

References

[1] Beman, W. W., and Frost, C. E., *A New Criterion For Loads in Pitching Maneuvers*, paper presented at the Los Angeles Section, I.A.S., June 15, 1944.

[2] Dickinson, H. B., *Maneuverability and Control Surface Strength Criteria for Large Airplanes*, Journal of the Aeronautical Sciences, Vol. 7, No. 11, September, 1940.

(*Continued from page 187*)

References

[1] Wieselsberger, C., *Über den Einfluss der Windkanalbergrenzung auf den Widerstand insbesondere im Bereiche der kompressiblen Strömung*, Luftfahrtforschung, Vol. 19, pp. 124–128, 1942.

[2] Prandtl, L., *Theorie der Flugzeugtragflügel im zusammendrückbaren Medium*, Jahrbuch der deutschen Luftfahrtforschung, pp. 174–180, 1937.

[3] Küssner, H. G., *Allgemeine Tragflächentheorie*, Luftfahrtforschung, Vol. 17, pp. 370–378, N.A.C.A. T.M. No. 979, 1940.

[4] Husk, D. I., *Compressible Flow Behind a Wing*, Aircraft Engineering, Vol. 14, p. 160, June, 1942.

[5] Glauert, H., *The Elements of Aerofoil and Airscrew Theory* pp. 87–93; Cambridge University Press, Cambridge, England, 1930.

[6] Lamb, H., *Hydrodynamics*, 6th Edition, pp. 208–211; Cambridge University Press, Cambridge, England, 1932.

[7] Silverstein, A., Katzoff, S., and Bullivant, W. K., *Downwash and Wake Behind Plain and Flapped Airfoils*, N.A.C.A. T.R. No. 651, 1939.

[8] Konstantinov, V. A., *Über helikoidale Wirbel in Anwendung zur aerodynamischen Berechnung der Luftschrauben und Windkraftmaschinen*, Compt. rend. (Doklady) Acad. d. Sc. U.S.S.R. (N.S.), Vol. 28, No. 8, pp. 688–693, 1940.

Stress Analysis of Nondevelopable Semimonocoque Structures Considered as Beams of Variable Section

LEON BESKIN*

Consolidated Vultee Aircraft Corporation

Introduction

THE PURPOSE of this paper is to present a rational, although approximate, method of analysis of structures constituted by a shell of elongated shape, reinforced by frames.

Conventionally, beam formulas are applied to such shells and define axial stresses. Shearing stresses are computed, either applying shear distribution formulas for beams—in which case, the shearing forces and torques are corrected by the so-called "shearing components of the axial forces"—or, more accurately, considering shearing forces as equal to the variations of axial loads between consecutive sections, summed along the circumference of the shell. Shear centers are determined in same manner as in cylinders. Stress distributions obtained in that manner do not fulfill the conditions of equilibrium and the conditions of compatibility of deformation.

In the case of elongated closed shells with a small taper, the errors introduced by these approximate methods can be neglected for practical purposes, although the equilibrium of frames, resulting from the shear distribution, may prove unsatisfactory. When the taper of a shell is large, this taper being roughly defined as the difference of average cross dimensions at two sections, divided by their distance, and especially when open shells are considered, the error may be as high as 100 per cent. Such large errors generally result from incorrect distributions in torsion bending which are not in equilibrium with the applied loads.

In view of the inaccurate results obtained by conventional methods, these methods must be revised.

In the following, only conditions of equilibrium will be satisfied, and the study of the conditions of compatibility will be disregarded. More precisely, conventional beam distribution for normal stresses will be used to determine stresses in the shell along the frames. This means that the influence of shear, of the local distribution of loads, and of the flexibility of the frames are disregarded. For that reason the method is considered as approximate.

In many cases, however, the results are not less accurate than for cylindric shells, for which the above-mentioned effects exist, with the exception of the influence of shear, which does not affect normal stresses at great distance of points of load application.

When the differences between a cylindric shell and a noncylindric elongated shell are examined, they can be reduced to three main factors: the taper, defined as indicated previously; the twist, i.e., the effect of the nonsimilar shape of consecutive cross sections; and the curvature of the shell in the direction of its great dimension.

The effect of the taper has been investigated, in relationship with the equilibrium of developable surfaces, in a previous paper by the author,[1] and its physical significance is not examined in this paper. The effect of the curvature is disregarded, because it is assumed to be small in the types of shells under consideration. Thus, the main object of this paper is the study of the effect of the twist and of the combined effects of twist and taper.

Notations

a; a_n	= area; corrected area (Eq. (1)) of a member
a_a	= uncorrected area
a_0	= total area of shell section
δA_m	= elemental double polar area (moment coefficient of an edge)
A_n	= partial double polar area
A_0	= total double polar area (Eq. (42))
B	= bimoment (Eq. (32))
F	= force
g	= twist (Eq. (3))
I_x; I_y	= moments of inertia
I_{xy}	= product of inertia
I_0	= torsion bending constant
L	= length along centerline; distance between frames
M_x; M_y; M_z	= components of a couple on three axes
$\bar{M}_z$	= uncorrected couple (Eq. (44))
M_{tx}; M_{ty}	= torque induced by moments M_x, M_y
M_p; M_q	= components of M_z
N_1; N_2	= normal stress flows; conjugate axial stress flows
N_{12}	= shear flow; conjugate shear flow
n_1; n_2; n_{12}	= projected stress flows corresponding to N_1; N_2; N_{12}
P; P_n	= load in member
P_x; P_y	= components of resultant of loads in members
Q_x; Q_y	= components of resultant of shears along frames
q; q_m; q_0	= cylindric shear flow (Eqs. (14), (45))

Presented at the Summer Annual Meeting, I.A.S., Los Angeles, July 27–28, 1944.

* Structures Engineer, San Diego Division.

s; s_m	= arc along circumference of a frame
V_n	= component of P_n in the plane of a frame
W	= distributed surface load (Eq. (6))
X; Y; Z	= components of a force on three axes
x_1; x_2	= coordinates (Fig. 9)
x, y	= coordinates in the plane of a frame
x_0; y_0	= coordinates of shear center
x_n; y_n	= coordinates of panel points
x_m; y_m	= coordinates of edge middle points
δx_n; δy_n	= projections of distances between panel points
Δx_n; Δy_n	= projections of members
Δx_0; Δy_0	= difference between shear center coordinates at two frames
Δx_c; Δy_c	= difference between centroid coordinates at two frames
α_n	= areas A_n with pole at the centroid
μ_x; μ_y	= constants (Eqs. (35))
ν_n	= moment coefficient of a member
ν_0	= constant (Eq. (27))
σ_n	= projected length of a member
φ	= angle between principal axes at two consecutive frames
Ψ	= angle between member and centerline
ω	= angle between member and frame
Ω	= angle between centerline and shear axis
$(')$; $(")$	= used to distinguish quantities related to a frame or a given system of coordinates from same quantities without index

Assumptions

Semimonocoque structures considered hereafter are defined as follows:

The structure is determined by a series of frames that are defined by plane curves, the planes being parallel or nonparallel. Members connect arbitrarily chosen points on each frame, and the skin is defined by the frame profiles and the members.

The theory developed hereafter is used as basis for graphic methods or for computations by finite elements.

For that reason, axial loads are assumed to be concentrated at the centroids of the finite areas which replace the actual continuous distribution.

The method is an extension to nondevelopable surfaces of a method that is theoretically exact for developable surfaces of infinitely small thickness.[1]

For a developable membrane that is not loaded on the surface, axial stresses along the lines of principal curvature (perpendicular to the generators) are equal to zero. Thus, on such a surface, there are axial stresses along the generators only and shearing stresses along generators and lines of principal curvature.

A somewhat equivalent distribution of stress is assumed to exist in the shells that are examined here.

A centerline is supposed to be defined in the shell. This centerline is the locus of the centroids of the sections perpendicular to it.

The method developed hereafter will be considered as valid for parallel frames with a centerline approximately perpendicular to the frames. If there are frames that form great angles with the planes normal to the centerline, a special study is necessary and the method can be adapted to that special case.

Fundamental Assumptions and Simplifying Approximations

(1) *Normal stresses are directed along the members.* They are defined by the beam distribution theory applied to the section properties calculated in the plane of each frame. For that purpose, actual areas of the member sections can be used (corrected for buckling if necessary). If those areas are variable from frame to frame, average values must be used. These are computed by the following expression:

$$\frac{1}{a} = \frac{1}{L}\int_0^L \frac{dL}{a_a}\frac{1}{\cos^3 \Psi} \tag{1}$$

in which:

a_a	= actual area
a	= average area
L and dL	= total and elemental lengths along the centerline, from one middle point between frames to the following middle point
Ψ	= angle between member and centerline

The correction $\cos^3 \Psi$ takes into consideration the actual length of the member and the fact that the beam distribution gives the components of the stresses along the centerline, rather than the stresses themselves.

(2) *Shearing stresses are defined at the frames as the conjugate shearing stresses corresponding to the direction of the member and the tangent to the frame (Fig. 1).* These stresses actually contain a normal component parallel to the centerline, as shown hereafter.

Let:

N_1, N_2	= conjugate normal flows along the direction D of the frame and the members
N_{12}	= shear flow conjugate to D and the members (angle ω)
N_1', N_2', N_{12}'	= normal and shear flow along the direction perpendicular to the members and the directions of the members

From the equilibrium of the triangle shown Fig. 1 and from assumption 1 ($N_1 = 0$), it is found:

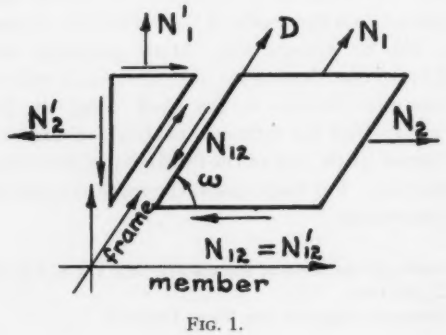

Fig. 1.

$$N_{12}' = N_{12};\ N_2' = N_2 + 2N_{12}\cot\omega \qquad (2)$$

Inside a panel, there are no normal stress flows N_2 (they are assumed to be concentrated at the members).

$$N_2' = 2N_{12}\cot\omega \qquad (2a)$$

This means that additional strains corresponding to the actual axial flows N_2' exist in the structure. These strains are not related in any way to a beam distribution. This seems to indicate that the method used is incorrect. However, for a cylindric beam submitted to a shearing force, conjugate shear flows with inclined sections have the same values as actual shear flows. In this special case, the difference is not in numerical values but in the interpretation of the results. From this comparison it appears reasonable to suppose that the method will generally be acceptable, at least in the case of parallel frames.

Relationship Between the Basic Assumptions and the Membrane Theory

The analysis of monocoque or semimonocoque structures can be approached in two different ways:

(1) In a first manner, taking as a basis the membrane theory, it is possible to set up the differential equations for any given problem and solve it with given edge conditions. The difficulty arises from the consideration of edge conditions. To make the problem statically determined, the edge conditions must fulfill definite requirements. With respect to those requirements, three fundamental conditions may occur:

(a) The edge conditions fulfill the requirements and the membrane problem is statically determined; from the standpoint of membrane theory the solution is absolutely correct.

Nevertheless, it remains to be seen whether local deformations do not necessitate the introduction of bending for an actual shell, which has a finite thickness.

A simple condition of that type is illustrated by a circular cylinder with ribs, submitted to a lateral pressure. In membrane theory the ribs are not deflected, and there appears a discontinuity of the membrane at each rib. Actually, bending occurs in the material of the membrane and produces stresses generally considered as secondary stresses but which may be important, depending on the thickness.

(b) The edge conditions are too numerous as compared with the conditions that lead to a statically determined problem.

The membrane equilibrium cannot exist and, at least locally, bending must be assumed. This will be the case for the cylinder considered under (a), if only a part of the circumference is loaded, or for an open cylinder. The hoop tension, which will not be in equilibrium along the edge generators, will produce local bending and a new equilibrium can be found which will involve local bending.

(c) The edge conditions are not sufficient to define a statically determined structure. This is the general case of structures with numerous frames. If a structure is statically determined when there are end frames only, it becomes redundant with intermediate frames that introduce the possibility of a discontinuity in shear. The problem is far too complex for practical use, and simplifying assumptions must be introduced.

(2) In a second manner, it is possible to start with predetermined types of stress distributions, dictated by the analogy with other types of structures or other shapes of membranes, and adjust the parameters of the stress distribution in order to find an equilibrium. This will apply for the problems of the type (1c), when the general shape of the structure will approximate a beam. Then the redundancy is solved by using a beam distribution for axial loads along the frames.

The fact that this distribution gives only an approximate solution is obvious, and the cases for which the solution is theoretically correct will occur exceptionally—for example, for cylindric shells under constant moment or constant transversal load. When axial load distributions at the frames are defined, either because they are due to given loads or because they are determined approximately by a beam analogy, the structure between two frames, considered as a membrane, generally becomes statically determined.

That fact is known for cylinders and, more generally, for developable surfaces used as monocoque structures. For semimonocoque structures it is necessary to add the condition that the members must be placed along the generators of the membrane.[1]

If that condition is not fulfilled and if the angle between the generators and the members is small, bending occurs in actual structures—although a membrane equilibrium is possible—because of the existence of high differential strains in the membrane equilibrium. Those strains cause local curvature, and redistribution is then made by local bending rather than by inplane stress flows.

Monocoque structures with given normal edge stresses and indeterminate edge shears can also be in statically determined membrane equilibrium, and that result can be considered as general, although many exceptions that frequently occur in practical applications limit the importance of that result.

When the surface is completely of the elliptic type (curvatures in the same direction) or completely of the hyperbolic type (curvatures in opposite directions), the problem is statically determined and equilibrium as a membrane can be found.

On the contrary, when the surface is not completely of one type, there are transition lines or regions along which the surface is developable, and a membrane equilibrium may be impossible, at least locally. That is the case for curved tubes, which are much more flexible than the corresponding straight tubes.

When the surface is open between frames, the edge lines must fulfill definite conditions for surfaces with opposite curvatures: edge lines cannot be generators (or generally asymptotic lines) if they are supposed to be shear absorbing members. If the edge lines coincide with generators, shears along those lines are defined by the surface loads and are generally incompatible with the shears defined by the total shearing force (difference of end loads) along the member; local bending appears in that case.

When a surface with opposite curvatures has a plane of symmetry, members placed along the generators or the asymptotic lines do not intersect the plane of symmetry; the surface must be developable along that plane, and local bending appears in that region.

When a surface of elliptic type is open, there are angles at the corners between the edges in the planes of the frames and the edges connecting the frames. Each of those angles, except for special surface load conditions, is a point of infinite shearing stress of logarithmic type; this causes bending in the region of each corner.

More generally, when curvatures are not distributed in a regular manner along the sections parallel to the frames, there appear high shears in the regions of rapid rate of change of curvature, and the actual stress redistribution is made by bending rather than by inplane stress flows.

The same applies for cutouts, local irregular shapes, and defects due to the material or to the forming process.

The results developed thus far show that a true membrane equilibrium is often impossible to reach and, if found, may lead to high local inplane stresses, even infinite in some conditions.

Moreover, a membrane equilibrium cannot be developed from local considerations only, and integration of local equilibrium in the two-dimensional system represented by the membrane is essential. Thus, except for special shapes—cylinders, cones, general developables, surfaces of revolution, surfaces of translation, surfaces of second degree (ellipsoids, paraboloids, hyperboloids)—it is impossible to solve the equations of equilibrium for membranes by elementary methods.

On the contrary, from elementary considerations, it is possible to find an equilibrium that involves limited local bending, thus leading to the development of a general method valid for semimonocoque structures. The bending involved does not exist when the semimonocoque structure is made of a developable surface with members along the generators. The bending is small if the actual surface is not too skewed between members—i.e., if the torsion of the surface along a member is small.

The equilibrium of each panel limited by two frames and two members can be examined successively, provided the equilibrium of one panel is defined. If the membrane is open, the equilibrium of an end panel can

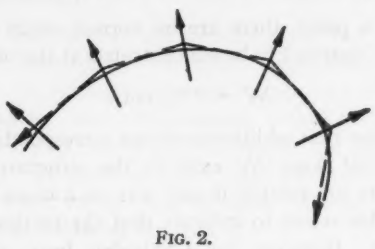

FIG. 2.

be obtained, and by iteration all the panels can be examined. If the membrane is closed, a fictitious cut along a member must be effected, and any actual solution will be obtained by superposition of the solution for the open surface and a unit solution involving shear only along the end frames.

(3) The previous results show that the problem of equilibrium of a semimonocoque structure can be expressed as follows:

Knowing the normal stresses in a membrane at two frames, determine a distribution of shearing stresses which will fulfill the conditions of equilibrium; as the structure is of semimonocoque type, local bending of the skin between members may exist.

Between the frames, members can be curved or straight. If they are curved, local bending due to axial load will exist in the members. That local bending is seldom absorbed by the membrane by hoop effect under concentrated loads for the following reasons:

(a) It causes local bending in the membrane proper (difference between contour and pressure polygon—Fig. 2).

(b) If the membrane is not closed, the thrust of the pressure polygon is not absorbed, and there must exist some bending in the panels that are along the edges.

(c) Because of the variation of the hoop load, secondary shear develops between frames.

For these reasons, it is assumed that members absorb in bending all the effects due to curvature between frames. As the same effect results from the curvature of the membrane in the direction of the members, it is assumed that this is also absorbed by bending of the members.

Equilibrium of an Element of a Semimonocoque Structure Limited to Two Parallel Sections

It is assumed that the members are straight. To the actual curved shape of the frames a polygonal line is

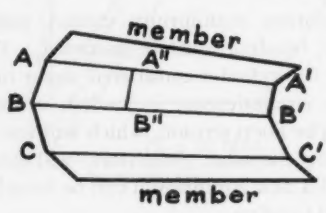

FIG. 3.

substituted, and an element of the membrane is replaced by a surface limited to four straight lines (Fig. 3), the lines AA', BB', CC' being assumed straight as well as the members. Thus, the given surface is replaced by a polyhedron composed of small surfaces limited by 4 straight lines.

For the purpose of analysis, it is assumed that any section parallel to the frames is a straight line, as well as the two sections at the frames. Then the elemental surface is defined as a skew surface defined by two fixed generators (AA', BB') and a moving generator $A''B''$, which remains parallel to a fixed plane (plane of the frames) when it describes the surface.

That surface is a hyperbolic paraboloid, except when the fixed generators are parallel, and in that case it is a plane. When the elemental surfaces are planes, the actual surface with straight members is close to a developable surface.[1]

Equilibrium of Plane Panels

The equilibrium of a tapered panel belonging to a polyhedron is defined when the shearing force along one of its edges is given and when it is assumed that no normal force can act on the edges (see "Assumptions"). Since all loads on the panel are pure shearing forces, there are three unknowns (shearing forces on three sides), and the equilibrium can be obtained by conditions of statics (Fig. 4). Replacing the panel by a latticed structure by adding one of the two diagonals AB' or $A'B$, the equilibrium is obtained as follows:

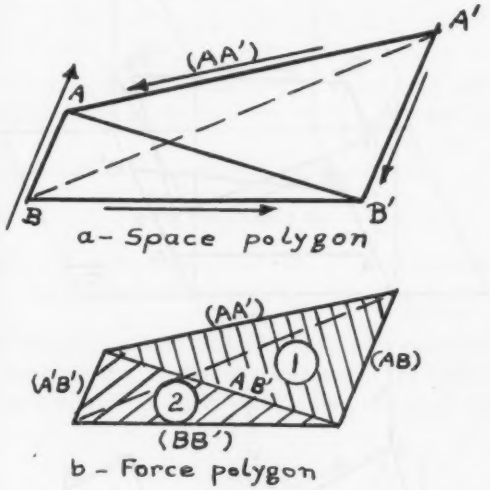

FIG. 4.

In A, forces (AB), (AA'), (AB') must be in equilibrium, which defines the values of (AB') and (AB) (triangle (1)).

In B', forces (AB'), ($A'B'$), (BB') must be in equilibrium, which defines the values of ($A'B'$) and (BB') (triangle (2)). For checking purposes, the diagonal $A'B$ can be used, which defines the two other triangles of the force polygon.

Actually, the space polygon and the force polygon are similar figures but the following must be noted:

The side AB of the space polygon is transmitting a shearing force (AB) which, in the two similar figures, corresponds to A'B': To the small side corresponds the large force, and reciprocally.

That property is the result of the well-known relation in tapered panels: The shear flow is inversely proportional to the square of the length of the side. Since the shearing force is equal to the produce of the shear flow by the length of the side, it appears that the force is inversely proportional to the length of the side. This theorem is valid for the two parallel sides only, while on the nonparallel sides, shearing forces are proportional to the sides.

Depending on the conventions of sign for shear and the sense of the end forces that produce the shear, the force polygon can be placed in two opposite manners, which result one from the other by a rotation of 180° (Fig. 5).

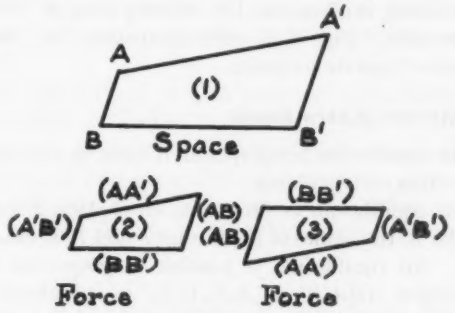

FIG. 5.

The space polygon (1) and the force polygon (2) are homothetic with a positive ratio of homothecy, while the space polygon (1) and the force polygon (3) have a negative ratio of homothecy (opposite to the previous ratio). Shear stresses along the parallel sides AB, $A'B'$ are constant. Shear stresses along the nonparallel sides are variable and follow the distribution for tapered panels.

When the shearing force transmitted between two points along a generator must be determined, the graphic construction is the following (Fig. 6):

The equilibrium of the panel being determined, the load along $A'A''$, for instance, is determined as follows: the line $A''B''$, parallel to AB, $A'B'$ is drawn and the equilibrium of the panel $A'B'A''B''$ is determined in manner similar to the equilibrium of the whole panel. The only difference is that the starting line is ($A'B'$). The two diagonals $A''B'$ and $A'B''$ are drawn and the force along $A''B''$ is determined (passes by $a''b''$).

If the load between two interior points of a generator $A'''A''''$, for instance, must be determined, the construction is repeated between those points, starting from $A''B''$, in the same manner as previously made for the panel $A'B'A''B''$. A final check can be made by

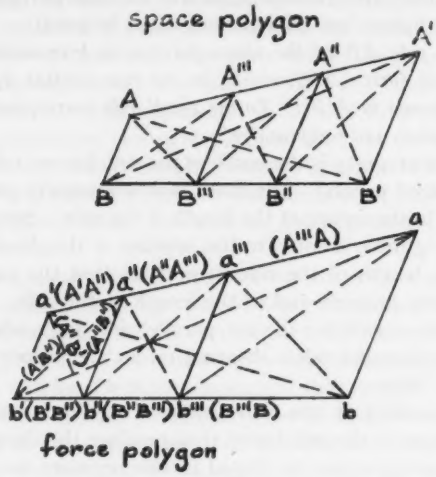

FIG. 6.

determining the load on AB, starting from $A'''B'''$, or reciprocally. Fig. 6 is self-explanatory for the sequence of operations made.

Equilibrium of Skew Panels

The equilibrium being spatial, it must be examined in projection on two planes.

The equilibrium in projection on a plane P perpendicular to the planes of the frames F and F' is examined first. An equilibrium is possible in projection if the projection $ABA'B'$ of $A_0B_0A_0'B_0'$ is considered as a plane-tapered panel.

It is seen that an equilibrium of the shell is possible when the forces along the sides project with the values defined by the projected equilibrium.

If the surface $A_0B_0A_0'B_0'$ is considered as a solid and not as a membrane, forces in equilibrium in the plane of projection are projections of forces in equilibrium in the space. This equilibrium is indeterminate, since the components of the forces perpendicular to P are not known. It becomes more determined if the forces projected along AA' and BB' are, in the space, placed along A_0A_0', B_0B_0'—i.e., they are true shearing forces.

The equilibrium is completed with a second plane of projection parallel to the frames (Fig. 8).

The projection of $A_0B_0A_0'B_0'$ is $ABA'B'$. Let F_1 and F_2 be the forces acting along AA' and BB'. Diagonals are used to determine the loads on the four sides knowing one of the loads.

Load F_1, decomposed in the plane $AA'B'$ into the directions AB' and $A'B'$, gives in A two components: one along AB' and the other F_A parallel to $A'B'$. This is the force that is supposed to be acting along AB and which in projection on P is directed along AB (Fig. 7). But in projection on F this result does not hold, and the force acting along A_0B_0 is parallel to the projection of $A_0'B_0'$.

The force F' on AB' being decomposed in the plane ABB' into F_2 along BB' and F_B' acting on $A'B'$, it appears again that the force acting on $A_0'B_0'$ projects parallelly to AB.

So far there is an equilibrium between F_1, F_2, F_A, F_B'. The operation can be repeated using the other diagonal, and an equilibrium between F_1, F_2, F_A', F_B can be obtained. Both equilibriums thus found are unsymmetric, since the resultant on AB is located at one or the other end of AB. If the total equilibrium is considered as the sum of two halves, each diagonal giving one of the half equilibrium, F_A and F_B are replaced by their half sum F_{AB} placed in the middle of the element AB, and the same is effected on the other side. (On the space polygon, at the four corners, half forces F_{AB}, and F_{AB}' are shown under F_A, F_A', F_B, F_B'.)

It is obvious that the construction thus defined is an extension to nonparallel end lines AB, $A'B'$ of the construction used for parallel end lines. The construction is projective and can be made on any plane of projection, giving the same results. Returning to Fig. 7, it appears that in the space the resultant acting on A_0B_0 is parallel to $A_0'B_0'$ and is located in the middle of A_0B_0. The same holds for the other end.

It appears that the loads along the frames are not pure shearing forces and have components perpendicu-

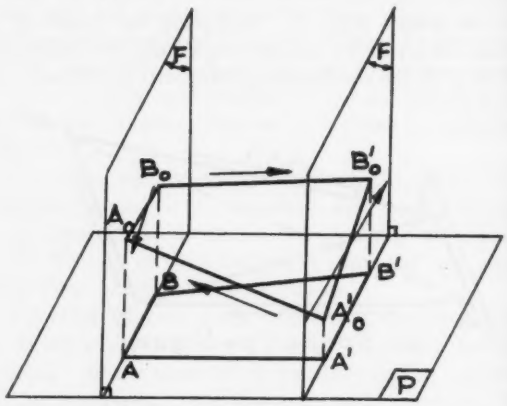

FIG. 7.

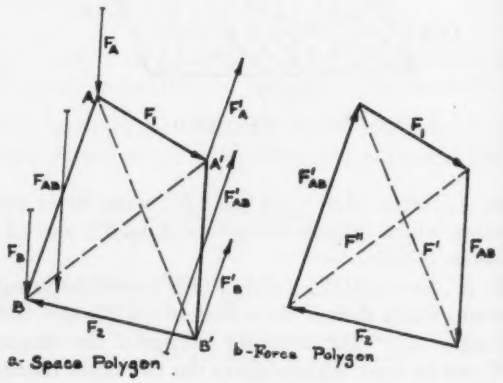

FIG. 8.

lar to the surface of the membrane, which means that bending must exist in the membrane.

As the equilibrium has been established disregarding the fact that the solid $A_0B_0A_0'B_0'$ is a membrane or a thin shell, it is necessary to find the relationship between the membrane theory and the equilibrium thus found and to see what equilibrium, among the various possible equilibriums (for instance, the two equilibriums taken with each of the diagonals, or the mean equilibrium finally chosen), suits the membrane theory the best.

Relationship Between the Infinitesimal Membrane Equilibrium and the General Equilibrium of a Panel

Using coordinates x_1 along one generator, x_2 along one intersection with a frame, and z along the intersection of the frame with a plane parallel to the generators limiting the panel (Fig. 9), the surface is considered to be a hyperbolic paraboloid of the equation

$$z = gx_1x_2 \tag{3}$$

g being determined by the coordinates of B'

$$\bar{z} = g\bar{x}_1\bar{x}_2 \tag{4}$$

All the generators project as lines $x_1 = c$, $x_2 = c'$. The equilibrium of this structure under pure shear (in projection) corresponds to constant shear, since in oblique coordinates the equations of equilibrium,

$$\frac{\partial n_1}{\partial x_1} + \frac{\partial n_{12}}{\partial x_2} = 0; \quad \frac{\partial n_2}{\partial x_2} + \frac{\partial n_{12}}{\partial x_1} = 0 \tag{5}$$

(in which n_1, n_2 are conjugate axial stress flows and n_{12} the shear flow), are satisfied with $n_1 = n_2 = 0$, and $n_{12} = c$.

The equation of equilibrium on the axis z is

$$W + 2n_{12}g = 0 \tag{6}$$

in which W is the surface load for a projected parallelogram having unit sides parallel to the axes of coordinates.

As this surface load W does not actually exist, bending corresponding to that load appears in the thickness of the skin, and the equilibrium is that of a shell under inplane loads and bending without surface applied loads.

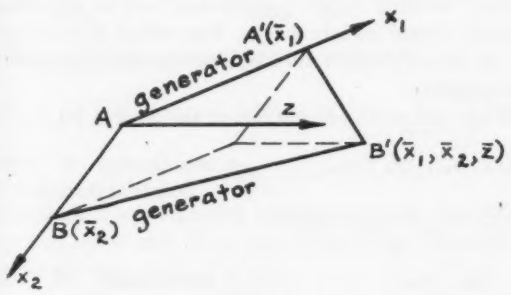

Fig. 9.

Assuming that the length of the members between frames is several times greater than the distance between members, bending corresponding to the fictitious load W appears between members and is transmitted to the frames by bending of the members. At the ends of the members the shearing loads in the direction of the z axis are:

$$F = (1/4)\bar{x}_1\bar{x}_2W = -(1/2)n_{12}g\bar{x}_1\bar{x}_2 = -(1/2)n_{12}\bar{z} \tag{7}$$

That value is precisely the value of the component of the forces F_A, F_A', F_B, F_B' (Fig. 8a) parallel to the z direction (which is the intersection of the plane of the frame with a plane parallel to both generators). Thus, it is justified to divide the loads by halves between both ends. However, if the shell is considered as continuous, the division by halves of the transverse loads (true for a plate on two lines of supports) is not accurate. But the twist g of the surface being small, the loads W it produces are also small, and their actual distribution can be disregarded provided an equilibrium is obtained.

Thus, the method used to determine the equilibrium of the panel as a solid is compatible with a possible distribution of loads in the actual shell considered as supported on four lines of simple supports; those supports transmit exclusively shear loads either in the plane tangent to the shell or perpendicular to the shell.

Summary of the Equilibrium of Skew Panels Between Parallel Frames

The equilibrium of a panel can be obtained by using one of the two following methods of projection:

(a) *Projection on a plane perpendicular to the frames.* That equilibrium is identical to the equilibrium obtained for a plane surface that would coincide with the projection of the actual surface and be submitted to edge loads (shears) equal to the projection of the actual edge loads. Since shear flows are essentially projective, the value of a projected shearing force is obtained by multiplication of a shear flow by the projected length of the edge.

(b) *Projection on a plane parallel to the frames.* That equilibrium differs greatly from the previous equilibrium because the projection of a force acting along one frame is parallel to the edge contained in the other frame. The properties of reciprocity between the loads and the edges on which they act still subsist (this can be seen from the similitude of Figs. 8a and 8b), but the loads do not correspond to pure membrane equilibrium.

The method of research of edge loads acting on given segments of the member cannot be applied on this plane of projection without modification and the first system of projection should be used for this problem.

Determination of Shear Flows in a Semimonocoque Structure Limited to Two Parallel Sections

In a conventional cylindric membrane considered as a beam, shears are defined between two sections when resulting loads at the two sections are known. The solution is simple for open membranes when the transverse loads are applied to the shear center and for closed membranes.

It is somewhat complicated by introduction of torsion bending, when shearing forces do not pass by the shear center of open membranes, and by consideration of deformations for multicelled structures.

For cylindric membranes, shear flows are defined in function of normal stress flows by the differential relation

$$(\partial N_z/\partial z) + (\partial N_{12}/\partial s) = 0 \tag{8}$$

in which s and z are the coordinates along the circumference and the generators. Integrated, Eq. (8) yields

$$N_{12} = \sum_0^n (P - P')/L \tag{9}$$

in which P and P' are the loads in members at the frames; L, the distance between frames; and N_{12}, the shear flow past member of rank n. For noncylindric membranes, Eq. (9) must be modified, but its application is not changed because its general form remains the same.

Expression of Shear Flows in Function of Axial Loads

Considering the equilibrium represented on Figs. 8a and 8b, it appears that the space polygon and the force polygon are similar figures, and

$$F_{AB}'/AB = F_{AB}/A'B' = F_1/AA' = F_2/BB' \tag{10}$$

Considering a succession of panels (Fig. 10) with the same type of equilibrium as that of Fig. 8, with a load applied along BB' and transmitted toward EE', it appears that

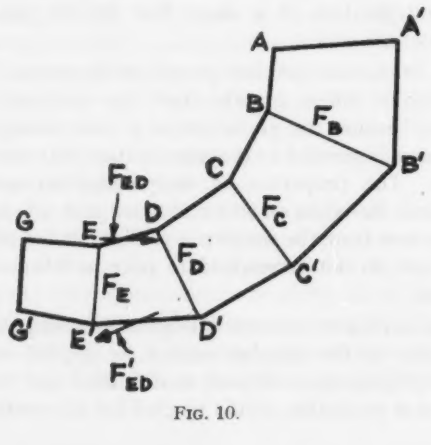

FIG. 10.

$$F_B/BB' = F_C/CC' = F_D/DD' = F'_{ED}/ED = F_{ED}/E'D' \tag{11}$$

Calling P_B and P_B' the axial components of the loads acting at B and B', then

$$F_B/BB' = (P_B - P_B')/L \tag{12}$$

Thus

$$\left.\begin{aligned} N_{ED}' &= F_{ED}'/E'D' = (ED/E'D')[(P_B - P_B')/L] \\ N_{ED} &= F_{ED}/ED = (E'D'/ED)[(P_B - P_B')/L] \end{aligned}\right\} \tag{13}$$

in which N_{ED} and N_{ED}' are the shear flows along the edges ED and $E'D'$. If various loads are applied at the various points A, B, C, A', B', C', equations of type (13) can be added, and the final shear flows can be found. Then, introducing a fictitious "cylindric shear flow" q_m,

$$q_m = \sum_0^m (P_n - P_n')/L \tag{14}$$

and

$$N_{12} = (s'/s)q_m; \quad N_{12}' = (s/s')q_m \tag{15}$$

in which

N_{12}; N_{12}' = shear flows along end frames in the panel m

s, s' = lengths of the edges of the panel m

P_n, P_n' = axial components of loads in the members at the frames

Comparing Eqs. (14) and (15) and Eq. (9), it appears that the differences are:

(a) *Taper effect.* The shear flows at the edges of a panel along frames are inversely proportional to the lengths of the edges.

(b) *Twist effect.* The shear flow at one edge of a panel along a frame is parallel to the opposite edge, and its resultant is acting in the middle of the edge to which it is applied.

Computation of Shears and Resultants at Frames

For any distribution of axial loads, it is necessary to find the value and location of the resultant of shears which is in equilibrium with the axial loads in order to locate the shear center and the distribution of loads in torsion bending (open membranes) or to determine torques (closed membranes). The values of resultants can be directly determined by considerations of general equilibrium.

With axes ox and oy parallel to the frames, let

$(x_n; y_n)$; $(x_n'; y_n')$ = coordinates of panel points at frames F, F'

$\left(x_m = \dfrac{x_n + x_{n+1}}{2}; y_m\right)$;

$(x_m'; y_m')$ = coordinates of edge middle points

$(\delta x_m = x_{n+1} - x_n;\ \delta y_m)$; $(\delta x_m';\ \delta y_m')$ = projections of distances between panel points

$(\Delta x_n = x_n' - x_n;\ \Delta y_n = y_n' - y_n)$ = projections of the members

$(s_m = \sqrt{(\delta x_m)^2 + (\delta y_m)^2};\ s_m')$ = lengths of edges

$(\delta A_m = \delta x_m y_m' - \delta y_m x_m';\ \delta A_m')$ = moment coefficients of the edges

$(A_n = \sum^{n} \delta A_m;\ A_n')$ = total moment coefficients

$(\nu_n = x_n' y_n - y_n' x_n)$ = moment coefficient of a member

$(\nu_0 = \nu_n - A_n' + A_n)$ = constant

$(Q_x;\ Q_y;\ Q_x';\ Q_y')$ = components of the resultant shears at frames

$(P_x;\ P_y;\ Q_x;\ Q_y)$ = components of the resultants of axial loads in members

$(M_q;\ M_p;\ M_q';\ M_p')$ = resulting moments due to forces $(Q_x,\ Q_y)$, $(P_x,\ P_y)$

$(X;\ Y;\ Z;\ M_x;\ M_y;\ M_z)$ = components of the general resultant and resulting moment at frame F

From Eqs. (15), the shearing force along a panel at frame F is

$$N_{12} s_m = s_m' q_m \tag{16}$$

and the components of the resultant of all shearing forces are

$$Q_x = \sum \frac{\delta x_m'}{s_m'} s_m' q_m = \sum q_m \delta x_m';\ Q_y = \sum q_m \delta y_m' \tag{17}$$

The corresponding resulting moment is

$$M_q = \sum q_m \delta x_m' y_m - \sum q_m \delta y_m' x_m = \sum q_m \delta A_m' \tag{18}$$

The three components of the resultant of the axial forces in the members are, at frame F,

$$P_x = \sum \frac{P_n \Delta x_n}{L};\ P_y = \sum \frac{P_n \Delta y_n}{L};\ Z = \sum P_n \tag{19}$$

The corresponding resulting moments are

$$M_p = \frac{1}{L}\{\sum P_n y_n \Delta x_n - \sum P_n x_n \Delta y_n\} = \sum \frac{P_n \nu_n}{L} \tag{20}$$

$$M_x = -\sum P_n y_n;\ M_y = \sum P_n x_n \tag{21}$$

Resultant Z and resulting moments M_x, M_y are defined by Eqs. (19) and (21); the three other elements of reduction are

$$X = Q_x + P_x;\ Y = Q_y + P_y;\ M_z = M_q + M_p \tag{22}$$

Torsion Bending in Semimonocoque Structures

Up to this point, only the six elements of statical reduction of applied loads have been defined. For stress distribution purposes, the elements of reduction are to be taken in respect to the centroid at each frame and in principal coordinates if beam distributions are used.

It is known that those elements of reduction are insufficient to define stresses in open membranes, and consideration of torsion bending is necessary.

As torsion bending is not defined by considerations of statical equilibrium in the space, consideration of the actual shape of the membrane is essential, and the shear center, as well as the torsion bending constant, cannot be determined in a section in the same way as for cylindric membranes, although that correspondence applied for the centroid and the principal axes.

A procedure entirely similar to that used for torsion bending of cylinders[2] can be used in the present problem. Third, Eq. (22) can be written (for both ends of the membrane):

$$\left.\begin{aligned} LM_z &= \sum P_n \nu_n + L\sum q_m \delta A_m' \\ &= \sum P_n' \nu_n + L\sum q_m \delta A_m \end{aligned}\right\} \tag{23}$$

A summation by parts can be applied to terms containing q_m:

$$\left.\begin{aligned} L\sum q_m \delta A_m' &= [L q_m A']_0^F - L\sum A_n' \delta q_m \\ L\sum q_m \delta A_m' &= -\sum A_n'(P_n - P_n') \end{aligned}\right\} \tag{24}$$

(the first summation along the frame gives 0 since there are no shears applied along the outer edges). Substituting in Eq. (23),

$$\left.\begin{aligned} LM_z &= \sum P_n \nu_n - \sum (P_n - P_n') A_n' \\ &= \sum P_n' \nu_n - \sum (P_n - P_n') A_n \end{aligned}\right\} \tag{25}$$

It can be verified that the two values of LM_z are equal, i.e.,

$$\sum P_n(\nu_n - A_n' + A_n) = \sum P_n'(\nu_n - A_n' + A_n) \tag{26}$$

this relation is satisfied if

$$\nu_0 = \nu_n - A_n' + A_n = \text{Const.} \tag{27}$$

since $\sum P_n = \sum P_n' = Z$. Eq. (27) can be replaced by an equation of differences:

$$\delta A_m' - \delta A_m = \delta \nu_n \tag{28}$$

which, by substitution of the definitions, becomes:

$$(\delta x_m' y_m - \delta y_m' x_m) - (\delta x_m y_m' - \delta y_m x_m') = (x_{n+1}' y_{n+1} - y_{n+1}' x_{n+1}) - (x_n' y_n - y_n' x_n) \tag{29}$$

and by substitution of the definitions of δx_m, x_m.... it appears that Eq. (29) is an identity. Then, the two Eqs. (25) can be written as one equation:

$$2LM_z + \sum P_n(A_n' + A_n - \nu_n) = \sum P_n'(A_n' + A_n + \nu_n) \tag{30}$$

Replacing ν_n by its value from Eq. (27), it is found that

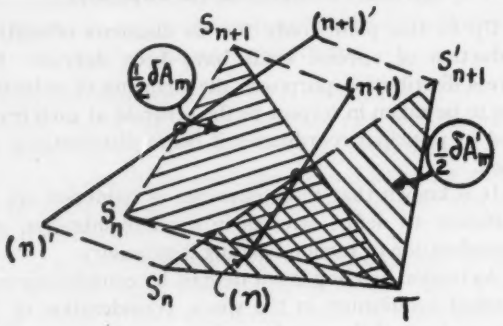

FIG. 11.

$$-\nu_0 Z + LM_z + \sum P_n A_n = \sum P_n' A_n' \qquad (31)$$

This expression is of the same general type as the relation defining bimoments in cylindric membranes,[2] except that the axial force appears in the equation. This shows that an axial force cannot be transmitted without introducing, at least in general, a torsion bending effect in the membrane.

In the same manner as in the case of cylindric membranes, the quantity $\Sigma P_n A_n$ can be considered as a mechanical concept, called bimoment B of the forces P_n in reference to the axis z:[2]

$$B = \sum P_n A_n \qquad (32)$$

Then, Eq. (31) can be written:

$$B' = B + LM_z - \nu_0 Z \qquad (33)$$

The constant ν_0 is equal to ν_n along the generators for which $A_n = A_n' = 0$, which correspond to a neutral line in pure torsion bending.[2]

In the definition of the bimoment, the quantity A_n is the double of the integral of elemental areas δA_m:2 defined as follows (Fig. 11): Drawing, through the middle of the intersection of a panel with the frame F', a line $S_n S_{n+1}$ equal and parallel to the intersection of the panel with the frame F, the area δA_n:2 is equal to the area of the triangle defined by the points S_n, S_{n+1} and T, the latter being the common pole for distances and origins of areas, placed at the origin of coordinates, heretofore arbitrary.

The definition of a bimoment for the present problem is an extension of the definition given for cylindric membranes. When the surface is a cylinder, the line $S_n S_{n+1}$ coincides with the intersection of the frame, and the areas A_n, A_n' are equal, which simplifies the definition of the bimoment. In order to have a complete representation of torsion bending, it is necessary to determine the shear center and a neutral line. The shear center is defined, for cylindric membranes, as the point through which the resultant of transverse loads passes when a beam distribution is used to define the axial loads. This implies that the distribution of areas is identical in each section; otherwise, the shear center changes along the axis of the cylinder. For tapered panels, the definition of the shear center depends on the relative value of the bending moments and the shearing forces, because pure bending produces secondary torque that displaces the shear center. In order to obtain a precise definition of the shear center, it can be stated that the shear center at a frame is defined by transverse loads applied at that frame, without bending moment. This determines two shear centers at two end frames. The line that connects the two shear centers will be called the shear axis and has the following properties (Fig. 12):

(1) A transverse load intersecting the shear axis does not produce torsion bending.

(2) A transverse load passing at a distance d from the shear axis—this distance being measured in a plane parallel to the frames—produces a torque equal to the product of that distance by the value of the load. The first property results from the fact that a load intersecting the shear axis can be decomposed into two parallel loads at the frames, both passing through the shear centers and producing no torsion bending. The second property obviously results from the first.

(3) A bending couple having its axis perpendicular to the shear axis produces no torsion bending.

(4) A bending couple having its axis perpendicular to the direction defined under (3) produces a torque equal to the product of the bending couple by tan Ω (Ω being the angle between the shear axis and the direction perpendicular to the frames). Properties (3) and (4) result from the application of (1) and (2) to loads placed at infinity.

From these properties it results that the knowledge of the shear centers at the end frames defines completely the torsion bending resulting from any transverse load and bending moment applied on an open membrane. The location of the shear center at frame F' is given by

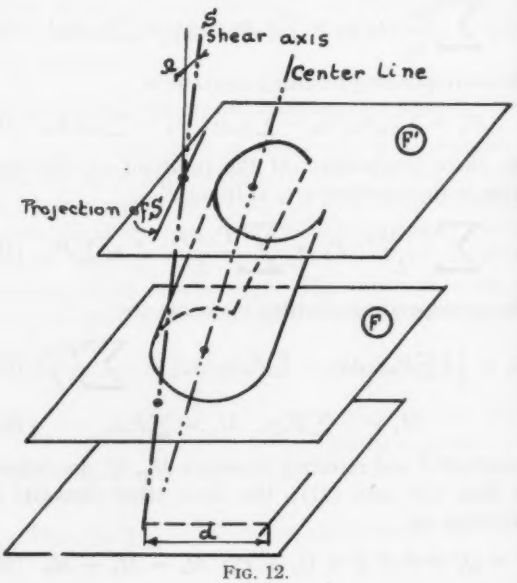

FIG. 12.

means of the section properties at frame F, and reciprocally, since the distribution of shearing stress due to a transverse load applied at F' is function of the distribution of axial stresses at F.

In same manner as for cylindric membranes, using the areas of the type of A_n' and A_n which are called a_n', a_n when the origin of coordinates is at the centroid, the following results are found.[2]

(a) Taking arbitrary directions of axes for the two end frames, the origin of the axes being taken at the centroid of each section, the coordinates of the shear center, at frame F' for instance, are given by the following expressions:

$$\text{Frame } F' \begin{cases} y_0' = (\mu_x I_y - \mu_y I_{xy})/[I_x I_y - (I_{xy})^2] \\ x_0' = -(\mu_y I_x - \mu_x I_{xy})/[I_x I_y - (I_{xy})^2] \end{cases} \quad (34)$$

in which:

$$\left.\begin{aligned} \mu_x &= \sum \alpha_n a_n x_n; \quad \mu_y = \sum \alpha_n a_n y_n \\ \alpha_n &= \sum \delta\alpha_m = \sum (\delta x_m y_m' - \delta y_m x_m') \\ I_x &= \sum a_n (x_n)^2; \; I_{xy} = \sum a_n x_n y_n; \; I_y = \sum a_n (y_n)^2 \end{aligned}\right\} \quad (35)$$

It is to be noted that axes without (′) refer to the centroid of frame F, while the axes noted (′) may be at any point of frame F' but must be parallel to the axes of F. In order to avoid the use of two sets of axes at each section, the axes (′) are taken at the centroid of F'. Then the formulas giving the centroid at F are deduced from Eqs. (34) and (35) by simple permutation of notations. If the principal axes at both frames are parallel, Eqs. (34) can be simplified by using the directions of principal axes as directions of coordinates. Then

$$\text{Frame } F' \begin{cases} y_0' = \sum \alpha_n a_n x_n / I_x \\ x_0' = -\sum \alpha_n a_n y_n / I_y \end{cases} \quad (36)$$

($I_x I_y$ are the principal moments of inertia.) If the principal axes at both frames are not parallel, it is possible to use the same formulas, but two sets of axes must be used at each frame, one set being the principal axes at the frame and the other being parallel to the principal axes at the other frame, with an arbitrary origin. Then, Eqs. (36) are valid, provided: the axes without (′) be the principal axes at frame F; the axes marked (′) be the axes at frame F' parallel to the principal axes at frame F.

In order to define the shear center at frame F with these notations, two other sets of axes must be introduced, defined by the principal directions at frame F'.

For the determination of the torsion bending constants, quantities x_m', y_m', x_m, y_m in areas A_n', A_n will be taken from the shear centers of the respective sections, and the origin vectors of the areas will be defined by

$$\sum A_n' a_n' = 0; \; \sum A_n a_n = 0 \quad (37)$$

The torsion bending constants are

$$I_0' = \sum (A_n')^2 a_n'; \; I_0 = \sum (A_n)^2 a_n \quad (38)$$

It is to be noted that I_0' is to be used for frame F' under torque applied at frame F (or moments in respect to shear center at frame F), and reciprocally. If the areas of the members at both frames are equal, the definition of ν_0 is simplified. Multiplying the first term of Eq. (27) by the area to which it corresponds and summing for all the members:

$$\sum \nu_n a_n - \sum A_n a_n + \sum A_n' a_n = \nu_0 \sum a_n$$

and from Eq. (37)

$$\nu_0 = \sum \nu_n a_n / a_0 \quad (39)$$

which shows that ν_0 is an average value of quantities ν_n. From the coordinates of the shear centers at both frames, the value of the torques related to bending moments can be determined. Calling M_{xx} and M_{xy} the torques due to moments M_x and M_y and introducing the differences between coordinates of shear centers called Δx_0 and Δy_0, the following equations can be written (assuming all quantities are taken with the same directions of coordinates):

$$\left.\begin{aligned} M_{xx} &= M_x \Delta x_0 / L \\ M_{xy} &= -M_y \Delta y_0 / L \end{aligned}\right\} \quad (40)$$

Those relations result from the consideration of a couple formed by two parallel forces placed at the end shear centers. The two components of the couple are a bending couple and a torque, which are obviously in such relation that they satisfy Eqs. (40).

Closed Membranes—Determination of the Origin for Shear

Introducing a fictitious cut along a generator, the membrane becomes open and a stress center is defined which is the shear center of the open membrane. A pure torque is transmitted by pure shear and produces a "cylindric shear flow" q_0, which, from Eq. (14), is constant since there are no loads P.

From Eq. (18), the torque corresponding to q_0 is

$$M_z = q_0 \sum \delta A_m = q_0 A_0 \quad (41)$$

with the two equivalent definitions of A_0

$$A_0 = \sum \delta A_m = \sum \delta A_m' \quad (42)$$

Eqs. (41) and (42) generalize the conventional formulas valid for cylinders only. The torques due to moments with respect to the stress center of the transversal forces, as well as the torques induced by bending moments (Eq. 42), are transmitted by shear flow defined by

$$N_{12}' = \frac{s_m}{s_n'} \frac{M_z}{A_0}; \; N_{12} = \frac{s_m'}{s_m} \frac{M_z}{A_0} \quad (43)$$

General Analysis of Semimonocoque Structures Between Parallel Frames

Closed Monocoque Structure

(a) *Distribution of axial loads determined at both ends.* This case corresponds either to actual applied axial

loads or to beam (or equivalent) distributions that must be defined prior to the present calculation.

Assuming a cut along a generator, shear flows are calculated by Eqs. (14) and (15), and torques are calculated by Eqs. (18) and (22) which, combined, give

$$\bar{M}_z = \sum q_m \delta A_m + \sum P_n' \nu_n / L \tag{44}$$

The difference between the actual torque M_z and torque $\bar{M}_z$ defines the correcting cylindric shear flow q_0:

$$q_0 = -(M_z - \bar{M}_z)/A_0 \tag{45}$$

Thus, the shear distribution is entirely defined.

(b) *Distribution of axial loads determined at one end, beam distribution at the other end.* If it is impossible to separate the loads into unit solutions corresponding to shears, bending moments, torque, and axial load at the frame where beam distribution is used, the procedure is essentially same as in previous subcondition, the first operation being the calculation of load distributions at the end when beam distribution is used:

$$P/a = (Z/a_0) - (M_y x/I_x) + (M_x y/I_y) \tag{46}$$

(a = elemental area, a_0 = total area). If loads at the end where the predetermined distribution exists can be distributed in order to correspond to unit solutions at the other end, unit solutions for complete distributions can be used. There will be six unit solutions, and for each unit solution shear will be defined by expressions of the type of (14), (15) and (45).

(c) *Distribution of loads defined by beam distributions at both ends.* An important difference with cylindric structures is the fact that basic unit solutions at one end do not remain unit solutions at the other end. For that reason, it is necessary to use one end frame as the basic frame for definition of unit solutions. Assuming that the frame chosen is the frame F', at the frame F will be applied: shearing forces, X', Y'; moments, M_x', M_y'; axial force, Z'; and torque, M_z. Those forces will be applied as follows:

All loads X', Y', M_x', M_y' are defined in reference to the principal directions of F'; Z' is applied at the centroid at the frame F'; and the cylindric shear flow q_0 is chosen for all unit solutions in such manner that $M_z = 0$, in reference to a determined axis, i.e.,

$$q_0 = -\bar{M}_z/A_0 \tag{47}$$

The torque M_z is the only element of reduction which is a unit solution for both end frames. The corresponding cylindric shear flow is defined by Eq. (41).

It is to be noted that at frame F, moments M_x', M_y', Z' produce, at least in general, moments M_x, M_y given by:

$$\left.\begin{aligned} M_x &= M_x' \cos\varphi - M_y' \sin\varphi + Z' \Delta y_c \\ M_y &= M_x' \sin\varphi + M_y' \cos\varphi - Z' \Delta x_c \end{aligned}\right\} \tag{48}$$

φ being the angle of the principal axes at frames F' with the axes at F and (Δy_c, Δx_c) being the coordinates of the centroid at F' in respect to the principal axes at F.

Open Monocoque Structure

(a) *Distribution of axial loads determined at both ends.* It is assumed that the condition of equilibrium of bimoments (Eq. (33)) is satisfied. Then, an equilibrium is possible, the procedure is essentially the same as for a closed structure under the same type of loads, and cylindric shear flows are given by Eq. (14). The resulting torque is M_z defined by Eq. (44); it is thus determined by axial forces exclusively, in same manner as transverse loads, as known from torsion bending theory.

(b) *Distribution of axial loads determined at one end, beam distribution at the other end.* The procedure is essentially the same as for a closed structure under the same type of loads, with the difference that Eq. (46) is replaced by

$$\frac{P}{a} = \frac{Z}{a_0} - \frac{M_y x}{I_x} + \frac{M_x y}{I_y} + \frac{BA}{I_0} \tag{49}$$

in which B is the bimoment defined by Eq. (32) and the torsion bending constant is defined by one of Eqs. (38). There are six unit solutions as for a closed membrane, with the difference that the unit solution under torque with pure shear is replaced by a unit solution with torsion bending.

(c) *Distribution of loads defined by beam distributions at both ends.* The general procedure is also the same as for a closed structure, with the substitution of the solution with bimoment to the solution with pure shear. At frame F are applied unit shearing forces X', Y' and torque M_z, bicouple B, moments M_x', M_y', and axial force Z'. Those forces will be applied as follows:

Transverse forces X', Y' at the shear center at frame F.

Torque M_z, at frame F (resulting bimoment at F').

Bicouple B, at any frame, since it is conservative in the absence of other loading.

Moments M_x', M_y' at frame F. These moments produce secondary torques M_{zx}' and M_{zy}' given by Eqs. (40). These torques can be separated from the moments, or their load distribution (bimoment, shear) can be superposed to that of the moments, thus reducing those applied moments to pure bending without secondary torque. With that method axial loads are defined, at frame F:

$$P/a = (M_x y/I_y) - (M_y x/I_x) \tag{50}$$

(M_x, M_y given by Eqs. (48) in function of each unit solution M_x', M_y' taken separately); at frame F':

$$\frac{P'}{a'} = M_x'\left(\frac{y'}{I_y'} - \frac{\Delta x_0' A'}{I_0'}\right) + M_y'\left(-\frac{x'}{I_x'} - \frac{\Delta y_0' A'}{I_0'}\right) \tag{51}$$

Load Z' at frame F'. This load causes secondary moments and bimoment, the latter given by Eq. (33):

$$B' = \nu_0 Z' \tag{52}$$

In same manner as for moments, the bicouple can be

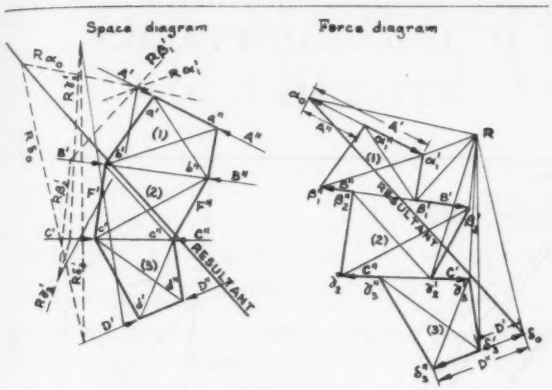

FIG. 13.

incorporated into, or calculated separately from, the axial load distribution. The axial loads are defined at frame F:

$$P/a = Z'[(y\Delta y_c/I_y) + (x\Delta x_c/I_x) + (1/a_0)] \quad (53)$$

at frame F' (bicouple being added):

$$P'/a' = Z'[(1/a_0') - (\nu_0 A'/I_0')] \quad (54)$$

GRAPHIC METHODS

Graphic methods can be used to determine values of shears, locations of shear centers, and locations of resulting transverse forces and bicouples when axial end forces are given.

A plane of projection must be chosen for a graphic analysis. Two types of projection can be used.

Projection on a Plane Perpendicular to the Frames

The frames appear as parallel lines and the effect of twist is hidden. As was indicated previously, the analysis of a plane panel or of a skew panel is the same in this mode of projection, and there is no difference between developable and nondevelopable surfaces.

The reader will find in reference 1 the corresponding graphic analysis, which can be considered as a special case of the following method of projection.

Projection on a Plane Parallel to the Frames

The method is derived from Fig. 8 and makes use of the components of the end loads parallel to the frames. σ_n being the length of the projection of a member on the frames, the corresponding projections V_n of the loads are, at the two frames:

$$V_n = P_n(\sigma_n/L); \quad V_n' = P_n'(\sigma_n/L) \quad (55)$$

It is to be noted that under given shearing forces, L is eliminated from the expressions, since under an X load, for instance (applied at frame F'):

$$V_n = \frac{\sigma_n}{L}(L)\left(\frac{a_n x_n}{I_x}\right) = (\sigma_n)\left(\frac{a_n x_n}{I_x}\right); \quad V_n' = 0 \quad (56)$$

Knowing the loads V_n/X and V_n', force diagrams can be determined (Fig. 13).

Loads at the ends of $a'a''$, called $\vec{A}'$, $\vec{A}''$, are drawn end to end. Their sum is $\alpha_1''\alpha_1'$. The equilibrium of panel (1) is determined by drawing, through α_1'' and α_1', parallels to the sides and diagonals corresponding to a'', a' of panel (1) and closing with a parallel ($\beta_1'\beta_1''$) to the side $b'b''$. The inversion of correspondence between a', α_1'' and a'', α_1' must be noted. The load along $b'b''$ in panel (1) is $\beta_1''\beta_1'$. Adding forces $\vec{B}'$ and $\vec{B}''$, it appears that the load along $b'b''$ in panel (2) is $\beta_2''\beta_2'$.

From $\beta_2''\beta_2'$ panel (2) can be analyzed in same manner as panel (1) and the procedure can be repeated for each panel.

The projections of the loads in members and the shearing forces along frame F' are the following:

Member Load	$a'a''$ $\alpha_0\alpha_1'$	$b'b''$ $\beta_1'\beta_2'$	$c'c''$ $\gamma_2'\gamma_3'$	$d'd''$ $\delta_3'\delta_0$
Side Shearing force	$a'b'$ $\alpha_1'\beta_1'$	$b'c'$ $\beta_2'\gamma_2'$	$c'd'$ $\gamma_3'\delta_3'$	

Dividing the shearing forces by the lengths of the sides, the shear flows along the frame are determined.

For the graphic analysis, it must be noted that the directions of the loads are such that in the completed figure, the sequence is, for instance, $\vec{D}''$, $\vec{C}''$, $\vec{B}''$, $\vec{A}''$, $\vec{A}'$, $\vec{B}'$, $\vec{C}'$, $\vec{D}'$, which shows that two opposite forces $\vec{B}'$, $\vec{B}''$, for instance, are measured in same direction along their line of support $\beta_1''\beta_1'$.

It results that compression forces are measured in one direction, while tension forces are measured in opposite direction. Those directions are not parallel from generator to generator and must be considered as going from one frame to another. Thus, on Fig. 13, starting from the top, compression forces are drawn from F' toward F'' and tension forces are drawn from F'' toward F'.

Once the force polygon is completed, the value of $\alpha_0\delta_0$, resultant of the shears acting along the frames, is determined. Its location is determined by a classic construction of addition of forces. Starting with an arbitrary pole R, place the force corresponding to the first ray $R\alpha_0$ at the intersection of A' and $\alpha_1'\beta_1'$ in the space diagram. As known, the force $\alpha_1'\beta_1'$ acting on a $a'b'$ is parallel to a $a''b''$ and passes through the middle of $a'b'$. Ray $R\alpha_1'$ is useless. A parallel to ray $R\beta_1'$, originating at the intersection of $\vec{A}'$ and the parallels to $\alpha_1'\beta_1'$ and $R\alpha_0$, is drawn until it meets B'. From that point, a parallel to ray $R\beta_1'$ is drawn to the intersection to a parallel to $\beta_2'\gamma_2'$ drawn through the middle of $b'c'$. The construction is repeated until the last line parallel to the ray $R\delta_0$ is drawn. The parallels to $R\alpha_0$ and $R\delta_0$ intersect in a point through which the resultant $\alpha_0\delta_0$ is drawn. This locates the resultant in position. A check can be made repeating the same operation at the other frame.

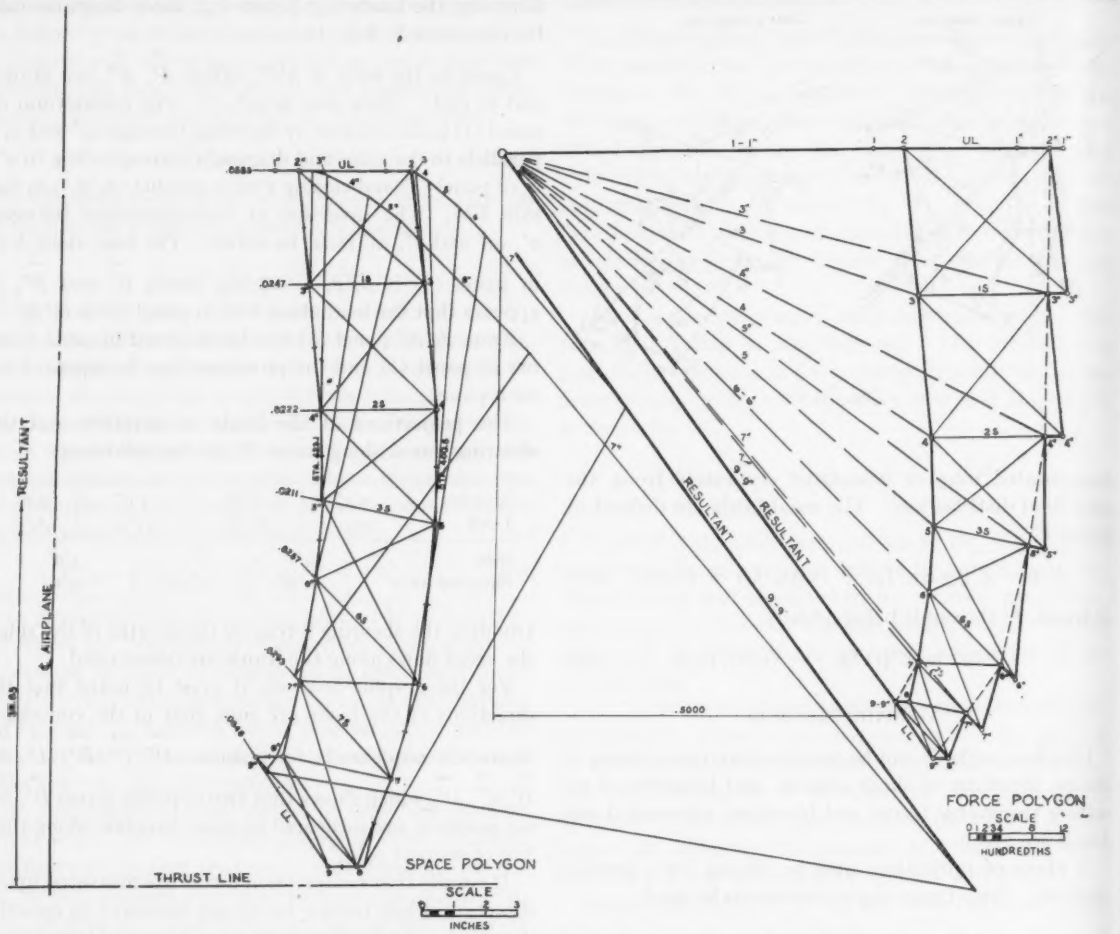

FIG. 14. Shear flow distribution under unit Y load. Station 400.5 to station 423.1.

Combining various unit solutions, shear centers or stress centers can be determined by intersection of two such resultants. (It is unnecessary to use principal axes.) Then, arms and areas can be measured for the calculation of moment coefficients for torsion bending, and the torsion bending constant may be determined. In case of closed profile, a cut is always made in order to start the calculation, and a unit solution is made under pure shear transmission. If on Fig. 13 the force placed on $a'a''$ is equal to $a'a''$ at a certain scale, the space polygon for shear transmission becomes the force polygon. From that force polygon and an arbitrary pole the resulting couple can be determined: When determining the resultant there will be a first and a last line, both parallel to $R\alpha_1'$; $R\alpha_1'$ multiplied by the distance between the two lines, will give the torque corresponding to the unit shearing force $a'a''$. Then, by proportion, shear flows corresponding to the unit torque will be found.

REFERENCES

[1] Beskin, L., *Theory of Membranes in Shape of Developable Surfaces*, Journal of Applied Physics, p. 547, July, 1944.

[2] Beskin, L., *Stress Analysis of Open Membranes*, Journal of the Aeronautical Sciences, Vol. 11, No. 4, p. 343, October, 1944.

(*Continued from page 194*)

[10] Friedricks, K. O., *Fluid Dynamics* (mimeographed notes); Advanced Instruction and Research in Mechanics, Brown University, 1941.

[11] Vaszonyi, A., *On Two-Dimensional Rotational Gas Flows*, abstract of paper No. 88, Bull. Amer. Math. Soc., Vol. 50, No. 3, p. 188, 1944.

[12] Ringleb, F., *Exakte Lösungen der Differentialgleichungen einer adiabatischen Gasströmung*, Z.A.M.M., Vol. 20, pp. 185–198, 1940.

[13] von Kármán, Th., *Compressibility Effects in Aerodynamics*, Journal of the Aeronautical Sciences, Vol. 8, No. 9, pp. 337–356, 1941.

Determination of the Axis of Rotation of a Skewed Axis Landing Gear

J. J. JERGER*

Curtiss-Wright Corporation

Introduction

In the design of landing gears it is often necessary to find an axis of rotation which will accurately locate the wheel in certain desired retracted and extended positions, with no motion other than that of rotation about the axis.

Several methods have been formulated for the solution of this problem. References 1 and 2 are such methods. Experience has shown that these solutions are cumbersome, partly because of the excellent visualization of space geometry required of the person seeking an answer and partly because of the large drawing-board area sometimes needed.

It is believed that the equations presented here afford a simplified aid for solving this problem quickly and accurately. The method has been used for actual design work by several landing-gear designers who have found that a complete solution can be made in as little as $1^1/_2$ hours, including all layout work. Calculations were made in about 30 min.

This method is employed to determine accurately the axis of rotation after reasonably satisfactory positions have been selected for the extended and retracted positions of the landing wheel. The procedure usually followed is to establish the tread and extended position and then to rotate the wheel about three axes through some point within the wing, thus placing the wheel approximately within the desired stowage space. Some adjustment may be made in order to reach a satisfactory compromise with other parts of the airplane.

The coordinates of points D and E of Fig. 1 may then be measured on the layout or computed from the two known wheel positions. After this has been done, there remains the problem of accurately locating the axis of rotation. The purpose of this paper is to present a set of equations that will solve this one problem

In the event that the axis of rotation does not fall sufficiently within the wing to house completely the pivot bearing, it is necessary to adjust the wheel position and to solve for a new axis.

When no adjustments are required to the wheel position, it is usually the case that the axis of rotation will pass through the point that was selected for the three initial rotations placing the wheel in its retracted position.

In this case one additional point fixes the axis. This point can be computed, using Eqs. (VI), (VII), and (VIII) and assigning one arbitrary value to the parameter "O." The value usually chosen is zero, because of its convenience.

Simple formulas that determine the direction and position of the axis of rotation are given. These equations may be used directly and without a great deal of study, requiring only knowledge of the three sets of coordinates which locate the landing wheel in both the retracted and extended positions. Following an explanation of the equations and the symbols employed, an example is carried out in detail to illustrate the method.

A complete draft of the derivation is included as an appendix for those who are interested in the mathematical phase of the solution. The mathematics of the appendix, while essential in producing the required equations, is in no way necessary to their solution. The formidable appearance of the working equations is misleading, as shown by the numerical example which serves to illustrate the simplicity of the operations involved. It will be noted that many of the terms in the formulas are repetitions, thereby reducing labor.

Symbols (See Fig. 1)

X, Y, Z = coordinates of a point on the desired axis of rotation. "O" is the origin.

x_1, y_1, z_1 = coordinates (with "O" as origin) of the point "A," which is located in the axis of the wheel. The length $\overline{OA}$ may be arbitrarily selected but should not be unreasonably small (i.e., approaching zero).

x_2, y_2, z_2 = coordinates (with "A" as origin) of the midpoint of the line $\overline{AB}$, where "B" is the position that "A"

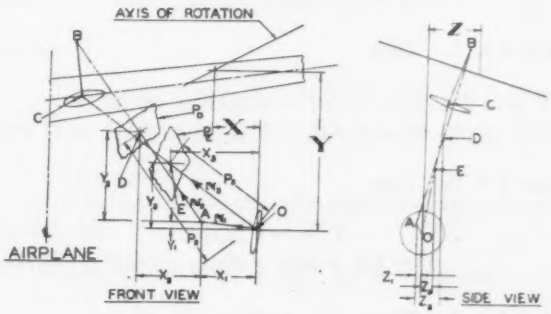

Fig. 1

Received August 18, 1944.

* Power Plant Staff Engineer, Airplane Division.

assumes when the wheel is in the retracted position.

x_3, y_3, z_3 = coordinates (with "O" as origin) of the midpoint of the line $\overline{OC}$ where "C" is the position that the wheel center "O" assumes when the wheel is in the retracted position.

$n_2^2, q_2, q_3,$ λ, λ_1 = constants used to determine the axis of rotation. These constants are determined by means of Eqs. (I) to (V) inclusive.

θ = a parameter that may arbitrarily be assigned any value. For each assigned value of θ, there is a corresponding point on the axis of rotation.

Sign conventions have been taken as follows:

X = direction positive to the left.
Y = direction positive upward.
Z = direction positive away from the reader—i.e., toward the paper.

Working Equations

$$n_2^2 = x_2^2 + y_2^2 + z_2^2 \tag{I}$$

$$q_2 = x_2^2 + y_2^2 + z_2^2 + x_1x_2 + y_1y_2 + z_1z_2 \tag{II}$$

$$q_3 = x_3^2 + y_3^2 + z_3^2 \tag{III}$$

$$\lambda = \frac{q_2q_3 - q_3(x_2x_3 + y_2y_3 + z_2z_3)}{n_2^2q_3 - (x_2x_3 + y_2y_3 + z_2z_3)^2} \tag{IV}$$

$$\lambda_1 = \frac{n_2^2q_3 - q_2(x_2x_3 + y_2y_3 + z_2z_3)}{n_2^2q_3 - (x_2x_3 + y_2y_3 + z_2z_3)^2} \tag{V}$$

$$X = \lambda x_2 + \lambda_1 x_3 + \theta(y_2z_3 - z_2y_3) \tag{VI}$$

$$Y = \lambda y_2 + \lambda_1 y_3 + \theta(z_2x_3 - x_2z_3) \tag{VII}$$

$$Z = \lambda z_2 + \lambda_1 z_3 + \theta(x_2y_3 - y_2x_3) \tag{VIII}$$

The known values of coordinates (x_1, y_1, z_1), (x_2, y_2, z_2), and (x_3, y_3, z_3) when substituted into Eqs. (I), (II), and (III) give values of n_2^2, q_2, and q_3. The values of n_2^2, q_2, and q_3, together with the required known values of (x_2, y_2, z_2) and (x_3, y_3, z_3) when substituted into Eqs. (IV) and (V), result in numerical values of λ and λ_1. Substitution of the numerical values of λ and λ_1 and the known values of (x_2, y_2, z_2) and (x_3, y_3, z_3), as required in Eqs. (VI), (VII), and (VIII), results in numerical values for $(X, Y, \text{and } Z)$, the coordinates of a point on the axis of rotation. As previously mentioned, numerical values of θ are assigned arbitrarily.

The following detailed example will clarify the procedure (these dimensions are taken from an actual case):

Given:

$x_1 = 10$ in. $\quad x_2 = 18.87$ in. $\quad x_3 = 23.43$ in.
$y_1 = 0$ in. $\quad y_2 = 27.63$ in. $\quad y_3 = 22.65$ in.
$z_1 = 0$ in. $\quad z_2 = 7.53$ in. $\quad z_3 = 7.53$ in.

From Eq. (I):

$$n_2^2 = (18.87)^2 + (27.63)^2 + (7.53)^2 = 1{,}176.1938$$

From Eq. (II):

$$q_2 = 1{,}176.05 + 10 \times 18.87 + 0 \times 27.63 + 0 \times 7.53 = 1{,}364.8838$$

From Eq. (III):

$$q_3 = (23.43)^2 + (22.65)^2 + (7.53)^2 = 1{,}118.6874$$

From Eq. (IV):

$$\lambda = \frac{1{,}364.8838 \times 1{,}118.6874 - 1{,}118.6874\,(18.87 \times 23.43 + 27.63 \times 22.65 + 7.53 \times 7.53)}{1{,}176.1938 \times 1{,}118.6874 - (18.87 \times 23.43 + 27.63 \times 22.65 + 7.53 \times 7.53)^2} = 5.2727$$

From Eq. (V):

$$\lambda_1 = (1{,}315{,}723 - 1{,}364.8838 \times 1{,}124.6436)/50{,}970 = -4.3008$$

Substituting in Eqs. (VI), (VII), and (VIII):

$$X = \lambda x_2 + \lambda_1 x_3 + \theta(y_2z_3 - z_2y_3) \tag{VIa}$$

Let $\theta = 1$. Then

$$X = +5.2727 \times 18.87 - 4.3008 \times 23.43 + 27.63 \times 7.537 - 7.53 \times 22.65 = +36.277$$

Let $\theta = 0$. Then

$$X = -1.2719$$

$$Y = \lambda y_2 + \lambda_1 y_3 + \theta(z_2x_3 - x_2z_3) \tag{VIIa}$$

Let $\theta = 1$. Then

$$Y = +5.2727 \times 27.63 - 4.3008 \times 22.65 + 7.53 \times 23.43 - 18.87 \times 7.53 = +82.6084$$

Let $\theta = 0$. Then

$$Y = +48.2716$$

$$Z = \lambda z_2 + \lambda_1 z_3 + \theta(x_2y_3 - y_2x_3) \tag{VIIIa}$$

Let $\theta = 1$. Then

$$Z = 5.2727 \times 7.53 - 4.3008 \times 7.53 + 18.87 \times 22.65 - 27.63 \times 23.43 = -212.6476$$

Let $\theta = 0$. Then

$$Z = +7.3184$$

The numerical example has been carried out with the aid of a computing machine. Accuracy of the computation is essential, since a slight error in the position of the axis of rotation creates an appreciable error in landing wheel position.

Appendix

The working equations were derived with the use of simple vector analysis. For those not familiar with the subject, references 3 and 4 are given.

Notation

P_D is a plane perpendicular to the line $\overline{AB}$ and passing through its midpoint D.

P_E is a plane perpendicular to the line $\overline{OC}$ and passing through its midpoint E.

Let the lines $\overline{OA}$, $\overline{AD}$, and $\overline{OE}$ be represented as the vectors N_1, N_2, and N_3, respectively.

p_2 = perpendicular distance from point "O" to plane P_D.

p_3 = perpendicular distance from point "O" to plane P_E.

The axis of rotation is determined by the intersection of the two planes P_D and P_E.[2]

The purpose of the following mathematics is to develop the working equations that determine this line of intersection:

Let r be the position vector from an origin "O" to any point within a given plane.

The plane is then defined by the equation $r \cdot N = q = pn$,[3] where N is any vector normal to the plane, n is the module or magnitude of vector N, p is the perpendicular distance from origin "O" to the plane, and $r \cdot N$ is the scalar product of the vectors r and N.

The equation of the plane P_D may therefore be written:

$$r \cdot N_2 = q_2 = p_2 n_2 \tag{1}$$

where n_2 is the magnitude or length of vector N_2.

Also, the equation of the plane P_E may be written:

$$r \cdot N_3 = q_3 = p_3 n_3 \tag{2}$$

where n_3 is the magnitude or length of vector N_3.

$$N_1 = x_1 i + y_1 j + z_1 k$$

$$N_2 = x_2 i + y_2 j + z_2 k$$

$$N_3 = x_3 i + y_3 j + z_3 k \tag{3}$$

where i, j, and k are mutually perpendicular unit vectors in the direction of the coordinate axes.

$$n_2^2 = x_2^2 + y_2^2 + z_2^2 \tag{4}$$

$$n_3 = \sqrt{x_3^2 + y_3^2 + z_3^2} = p_3 \tag{5}$$

The scalar product $a \cdot b$ of two vectors a and b is defined as the product $ab \cos \theta$, where a and b are the magnitudes of vectors a and b, respectively, and θ is the angle between the vectors.[4]

Referring to Fig. 2, it can be seen that the product $a \cdot b$ may be looked upon as the product of the length of either vector with the length of the projection of the other vector upon it—i.e., $a \cdot b = a(b \cos \theta)$ where $(b \cos \theta)$ is the projection of vector b upon vector a. Also $a \cdot b = b(a \cos \theta)$ where $(a \cos \theta)$ is the projection of vector a upon vector b.

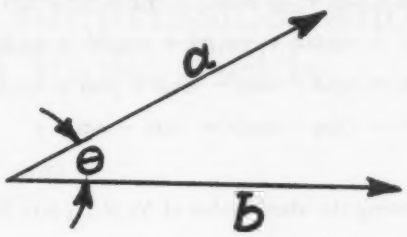

FIG. 2.

Referring to Fig. 1, p_2 = length of vector N_2 plus the projection of vector N_1 upon vector N_2:

$$p_2 = n_2 + \hat{N}_2 \cdot N_1 \tag{6}$$

where $\hat{N}_2$ is unit vector in the direction of vector N_2:

$$N_2 = \hat{N}_2 / n_2$$

$$p_2 = n_2 + (N_2 \cdot N_1 / n_2)$$

$$p_2 = n_2 + \frac{(x_2 i + y_2 j + z_2 k) \cdot (x_1 i + y_1 j + z_1 k)}{\sqrt{x_2^2 + y_2^2 + z_2^2}}$$

$$p_2 = \sqrt{x_2^2 + y_2^2 + z_2^2} + (x_1 x_2 + y_1 y_2 + z_1 z_2) / \sqrt{x_2^2 + y_2^2 + z_2^2}$$

$$p_2 = \frac{x_2^2 + y_2^2 + z_2^2 + x_1 x_2 + y_1 y_2 + z_1 z_2}{\sqrt{x_2^2 + y_2^2 + z_2^2}} \tag{7}$$

$$q_2 = p_2 n_2 = x_2^2 + y_2^2 + z_2^2 + x_1 x_2 + y_1 y_2 + z_1 z_2 \tag{8}$$

And from Eq. (5) it can be seen that

$$q_3 = p_3 n_3 = x_3^2 + y_3^2 + z_3^2 \tag{9}$$

In reference 3, the vector equation of the line of intersection of two planes whose vector equations are

$$r \cdot N_2 = q_2 \tag{1a}$$

$$r \cdot N_3 = q_3 \tag{2a}$$

is given as

$$r = \lambda N_2 + \lambda_1 N_3 + \theta N_2 \times N_3 \tag{10}$$

where

$$\lambda = (q_2 n_3^2 - q_3 N_2 \cdot N_3) / [n_2^2 n_3^2 - (N_2 \cdot N_3)^2] \tag{11}$$

$$\lambda_1 = [n_2^2 q_3 - q_2 (N_2 \cdot N_3)] / [n_2^2 n_3^2 - (N_2 \cdot N_3)^2] \tag{12}$$

θ is a parameter.

$N_2 \times N_3$ is the cross or vector product of the vectors N_2 and N_3.

$$N_2 \cdot N_3 = (x_2 i + y_2 j + z_2 k) \cdot (x_3 i + y_3 j + z_3 k)$$

$$N_2 \cdot N_3 = x_2 x_3 + y_2 y_3 + z_2 z_3$$

$$N_2 \times N_3 = (x_2i + y_2j + z_2k) \times (x_3i + y_3j + z_3k) =$$
$$x_2y_3ixj + x_2z_3ixk + y_2x_3jxi + y_2z_3jxk + z_2x_3kxi +$$
$$z_2y_3kxj = x_2y_3k - x_2z_3j - y_2x_3k + y_2z_3i + z_2x_3j - z_2y_3i$$
$$N_2 \times N_3 = (y_2z_3 - z_2y_3)i + (z_2x_3 - x_2z_3)j + (x_2y_3 - y_2x_3)k$$

Substituting the above value of $N_2 \times N_3$ into Eq. (10)

$$r = \lambda N_2 + \lambda_1 N_3 + \theta[(y_2z_3 - z_2y_3)i + (z_2x_3 - x_2z_3)j + (x_2y_3 - y_2x_3)k] \quad (13)$$

Substituting the above value of $N_2 \cdot N_3$ into Eqs. (11) and (12),

$$\lambda = \frac{q_2n_3^2 - q_3(x_2x_3 + y_2y_3 + z_2z_3)}{n_2^2n_3^2 - (x_2x_3 + y_2y_3 + z_2z_3)^2} \quad (14)$$

$$\lambda_1 = \frac{n_2^2q_3 - q_2(x_2x_3 + y_2y_3 + z_2z_3)}{n_2^2n_3^2 - (x_2x_3 + y_2y_3 + z_2z_3)^2} \quad (15)$$

but from Eqs. (5) and (9) $q_3 = n_3^2$ and

$$\lambda = \frac{q_2q_3 - q_3(x_2x_3 + y_2y_3 + z_2z_3)}{n_2^2q_3 - (x_2x_3 + y_2y_3 + z_2z_3)^2} \quad (16)$$

$$\lambda_1 = \frac{n_2^2q_3 - q_2(x_2x_3 + y_2y_3 + z_2z_3)}{q_3n_2^2 - (x_2x_3 + y_2y_3 + z_2z_3)^2} \quad (17)$$

Substituting values of N_2 and N_3 into Eq. (13),

$$r = \lambda(x_2i + y_2j + z_2k) + \lambda_1(x_3i + y_3j + z_3k) + \theta[(y_2z_3 - z_2y_3)i + (z_2x_3 - x_2z_3)j + (x_2y_3 - y_2x_3)k] \quad (18)$$

Expanding Eq. (18) and collecting terms, it is found that

$$r = Xi + Yj + Zk \quad (19)$$

where

$$X = +\lambda x_2 + \lambda_1 x_3 + \theta(y_2z_3 - z_2y_3)$$
$$Y = +\lambda y_2 + \lambda_1 y_3 + \theta(z_2x_3 - x_2z_3)$$
$$Z = +\lambda z_2 + \lambda_1 z_3 + \theta(x_2y_3 - y_2x_3)$$

Eq. (19) determines the desired axis of rotation in terms of the given dimensions, specifying the location of a point on the axis for each assigned value of the parameter θ.

Collecting Eqs. (4), (8), (9), (16), (17), and (19) and employing Roman numerals for identification, we have the required working Eqs. (I) to (VIII), inclusive.

References

[1] Oldendorph, O. F., *General Solution of the "Skewed Axis" Landing Gear*, Aero Digest, Vol. 36, No. 2, p. 101, February, 1940.

[2] Spaeth, Herman E., *Finding an Axis of Rotation for a Retractable Landing Gear*, Aero Digest, Vol. 37, No. 2, p. 68, August, 1940.

[3] Weatherburn, C. E., *Elementary Vector Analysis;* G. Bell & Sons, Ltd., London, 1928.

[4] Coffin, Joseph G., *Vector Analysis;* John Wiley & Sons, New York, 1911.

Letters to the Editor

Dear Sir:

The values of γ, the ratio of the specific heats, for dry air are given incorrectly on page 227 of the article titled "The Thermodynamics of Air at High Velocities," by Neil P. Bailey, which appeared in the July, 1944, issue of the JOURNAL OF THE AERONAUTICAL SCIENCES.

The correct values of γ for dry air as given by Heck[1] are:

°F.	γ
80	1.400
140	1.398
240	1.395
440	1.386
490	1.383
740	1.368

The writer recommends that a γ value of 1.400 be used as a standard for all airflow computations within a temperature range of at least −360° to +240°F. Keenan and Kaye[2] list the value of γ as 1.400 from −360° to about +80°F., and from 80° to 240°F. the γ value may be taken as 1.40. Also a γ value of 1.400 corresponds to the measured speed of sound under standard conditions. The same value of γ is also obtained from the kinetic theory of gases. For a perfect diatomic gas molecule with 5 degrees of freedom (3 in translation and 2 in rotation) the value of γ will be seven-fifths or 1.400. For a real diatomic gas this value of γ will be decreased by any vibrational energy within the molecule. However, for a moderate range of temperature dry air should be expected to behave as a perfect diatomic gas, since dry air is composed mainly of nitrogen and oxygen molecules whose vibrational energy will be negligible at ordinary temperatures.

References

[1] Heck, R. C. H., *The New Specific Heats*, Mechanical Engineering, Vol. 63, No. 2, February, 1941, pp. 126–135.

[2] Keenan, Joseph H., and Kaye, Joseph, *A Table of Thermodynamic Properties of Air*, Journal of Applied Mechanics, Vol. 10, No. 3, September, 1943, pp. A-123, A-130.

EDMUND V. LAITONE
Aeronautical Engineer
Theoretical Aerodynamics Section, N.A.C.A.

Dear Sir:

While careful checks from Heck's Gas Tables for *dry* air yield values from 1.397 to 1.398, the effects of the moisture normally present make 1.395 a better value. This value has been accepted by the General Electric Company and several other manufacturers of superchargers.

NEIL P. BAILEY
Head, Mechanical Engineering Dept.
Rensselaer Polytechnic Institute

Equivalent Circuits of Compressible and Incompressible Fluid Flow Fields

GABRIEL KRON*

General Electric Company

SYNOPSIS

Equivalent circuits are developed to represent the following partial differential equations of mathematical physics

(1) Div $\bar{p}\cdot\nu = Q$; curl $\nu = \Gamma$

(2) Div a grad $\phi = b = b_1\frac{\partial^2\phi}{\partial t^2} + b_2\frac{\partial\phi}{\partial t} + b_3\phi + b_4$

(3) Curl c curl $\bar{\psi} = d = d_1\cdot\frac{\partial^2\bar{\psi}}{\partial t^2} + d_2\cdot\frac{\partial\bar{\psi}}{\partial t} + d_3\cdot\bar{\psi} + d_4$

under transient, sinusoidal, or steady-state conditions, thereby allowing their solution either by a network analyzer or by numerical and analytic circuit methods. In fluid dynamics these equations represent the steady potential flow of a *compressible* fluid when expressed in the hodograph plane or the general nonviscous flow of an *incompressible* fluid when expressed in the physical plane or space. (In representing the flow of a compressible fluid in the *physical* space, the networks have variable units, since the equations are nonlinear.)

The same equations and networks may be considered to represent *static* electromagnetic fields in current-carrying regions or in regions with stationary charges or poles. The second equation may also represent the conduction of heat (or diffusion) in a nonisotropic medium, or it may represent the general wave equation.

All networks are expressed in curvilinear orthogonal coordinates to simplify the networks in case of curvilinear boundaries and to express three-dimensional problems with axial or other symmetry by means of a two-dimensional network. The coefficients $\bar{p}$, a, and c are not scalars but elements of diagonal matrices, allowing special types of nonisotropic properties in the fields. All coefficients may be constants or functions of the independent space variables, thereby allowing nonhomogeneous fields. The fields may contain multiply connected regions, and a method showing how to represent Riemann-surfaces by equivalent circuits is given.

Most transient and steady-state equivalent circuits require only resistances, inductances, and capacitors, while some transient networks also require ideal transformers. The blocks into which space is divided may have arbitrary lengths in different directions. General nonisotropic fields and nonorthogonal reference frames require an extension of the present equivalent circuits.

Numerical methods of solving the equivalent circuits are given in another publication.[8] In general the circuits may be used to check the consistency and accuracy of the results arrived at by other methods, approximate or exact. The unbalanced currents at the junctions (easily calculated) give a *quantitative* measure of the deviations from the correct answer.

THE METHOD OF ATTACK

THE PHILOSOPHY underlying the representation of physical phenomena by models (equivalent circuits) has been given in three other publications[1, 3, 6] presenting equivalent circuits for the electromagnetic field, for the elastic field, and for oscillating dynamic systems. It is suggested that for visualization the equivalent circuits of an ordinary or partial differential equation should not be assumed to represent the condition at selected discrete points of the field. Instead, the network quantities should be considered to represent line, surface, and volume integrals of field quantities related to infinitesimal blocks into which space is divided.

The conventional equations of Vector Analysis (used in the body of the paper) expressing the condition of a field at a point are changed to the needed tensorial form in the Appendix.

TYPES OF FLOW CONSIDERED

Assuming the nonviscous flow of a fluid as an illustrative example, let its velocity vector be ν. Four special cases will be considered:

(a) The flow is *general*—that is, both sources and vortices exist

$$\text{div } \bar{p}\cdot\nu = Q \qquad \text{curl } \nu = \Gamma$$

No potential functions can be introduced.

(b) The flow is *irrotational*—that is, sources exist but no vortexes

$$\text{div } \bar{p}\cdot\nu = Q \qquad \text{curl } \nu = 0$$

There exists a scalar potential ϕ (velocity potential)

$$\nu = \text{grad } \phi$$

so that the above two relations may also be expressed as

$$\text{div } \bar{p} \text{ grad } \phi = Q \qquad \text{curl grad } \phi = 0$$

(c) The flow is *solenoidal*—that is, vortexes exist but no sources

$$\text{curl } \nu = \Gamma \qquad \text{div } \bar{p}\cdot\nu = \bar{0}$$

There exists a vector potential $\bar{\psi}$ (stream function)

$$\bar{p}\cdot\nu = \text{curl } \bar{\psi}$$

so that the above two relations become

$$\text{curl } \bar{p}^{-1} \text{ curl } \bar{\psi} = \Gamma \qquad \text{div curl } \bar{\psi} = \bar{0}$$

(d) The flow is a *potential flow*—that is, neither sources, nor vortexes exist

$$\text{div } \bar{p}\cdot\nu = 0 \qquad \text{curl } \nu = 0$$

Received June 3, 1944. To have been presented at the I.A.S. Thirteenth Annual Meeting, which was canceled to cooperate with a Government appeal (January, 1945) to refrain from holding conventions and meetings.

* Consulting Engineer.

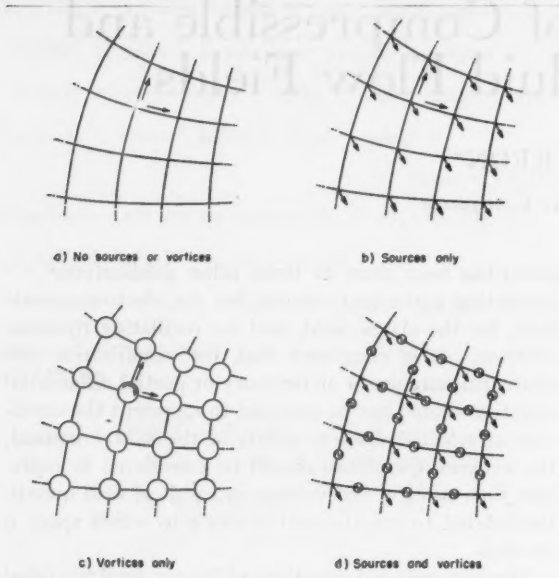

FIG. 1. Schematic representation of *two-dimensional* fluid flow.

There exist both a scalar potential ϕ and a vector potential $\bar{\psi}$

$$\boldsymbol{v} = \text{grad } \phi \qquad \bar{\rho}\cdot\boldsymbol{v} = \text{curl } \bar{\psi}$$

so that the above two relations become

$$\text{div } \bar{\rho} \text{ grad } \phi = 0 \qquad \text{curl grad } \phi = 0$$
$$\text{curl } \bar{\rho}^{-1} \text{ curl } \bar{\psi} = 0 \qquad \text{div curl } \bar{\psi} = 0$$

The relation between the two potentials is

$$\bar{\rho} \text{ grad } \phi = \text{curl } \bar{\psi}$$

SCHEMATIC EQUIVALENT CIRCUITS

Before presenting the equivalent circuits in detail, a schematic representation of the four types of models will be considered: first a two-dimensional, then a three-dimensional model.

Let a two-dimensional flow of fluid particles be simulated by electric charges flowing through a net of conductors. Then $\bar{\rho}\cdot\boldsymbol{v}$, the time rate of flow of fluid, is represented by the current $i = dq/dt$ in the conductors. Corresponding to the four types of flow assumed, four types of equivalent circuits will be constructed:

(a) The *potential* flow of a fluid (in a region having no sources or vortexes) can be represented by a net of current-carrying conductors (Fig. 1a), where, in general:

(1) The current i in the conductors represents the time rate of flow of fluid $\bar{\rho}\cdot\boldsymbol{v}$.
(2) The admittance of the conductors y represents the density of fluid $\bar{\rho}$.
(3) The differences of potential e between junctions represent the velocity of the fluid particles $\boldsymbol{v}$.

(b) The presence of sources in an *irrotational* flow may be represented (Fig. 1b) by currents entering the junctions. Then:

(4) The junction currents represent the source strengths Q.
(5) The absolute potential of the junctions represents the scalar potential ϕ.

(c) The presence of vortexes in a *solenoidal* flow may be represented (Fig. 1c) by circular conductors formed at the junctions. Then:

(6) The voltage drops in the circular conductors represent the vorticity $\bar{\Gamma}$.
(7) The circulating currents represent the vector potential $\bar{\psi}$.

(d) When both sources and vortexes are present the vortexes are no longer represented by a flow in circular conductors but by generators (Fig. 1d). Then:

(8) The junction currents represent the source strength Q.
(9) The generator voltages represent the vorticity $\bar{\Gamma}$.

In this fourth case neither the scalar potential ϕ nor the vector potential $\bar{\psi}$ exist.

In all four networks Kirchhoff's first law—that is, the summation of the voltages around the meshes—corresponds to the equation

$$\text{curl } \boldsymbol{v} = \bar{\Gamma}$$

and Kirchhoff's second law—that is, the summation of currents entering a junction—corresponds to

$$\text{div } \bar{\rho}\cdot\boldsymbol{v} = Q$$

A *three-dimensional* flow is represented by a set of analogous three-dimensional networks shown schemati-

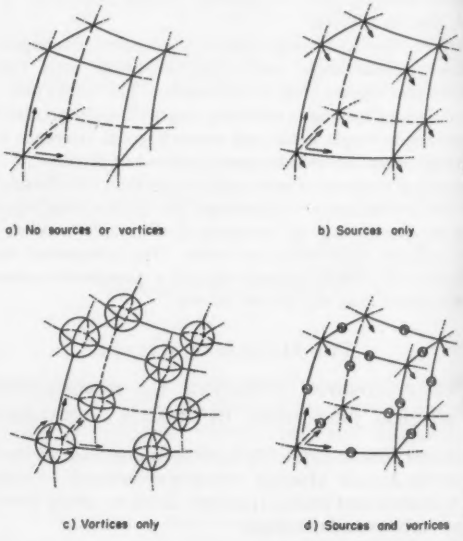

FIG. 2. Schematic representation of *three-dimensional* fluid f

cally in Fig. 2. In Fig. 2c there exist now three sets of circular currents, representing the three components of the vector potential $\bar{\psi}$.

It should be noted that the same networks are used whether the concepts of potentials are introduced or not. The introduction of potentials simply identifies in a network not only $\boldsymbol{v}$ and $\bar{\rho}\cdot\boldsymbol{v}$ but also ϕ or $\bar{\psi}$. However, for analytic purposes either the velocity or the potential equations are sufficient.

In case of the $\bar{\psi}$ networks, each has a dual network of the same form but in which the role of the voltages and currents, impedances and admittances are interchanged.

In presenting next the detailed equivalent circuits, at first the three-dimensional circuits will be developed valid for all curvilinear orthogonal reference frames and afterward the two- and one-dimensional ones.

Equivalent Circuits of the Potential Flow

The three-dimensional networks for ϕ and $\bar{\psi}$ for a potential flow are shown in Figs. 3 and 4. (The $\bar{\psi}$ network has also a dual.) In both networks:

(1) The differences of potential between junctions represent the *line-integral* of $\boldsymbol{v}$.

(2) The admittances $\boldsymbol{a}$ or $\boldsymbol{c}$ represent the specific conductance of a unit cube of fluid. (If the components of $\boldsymbol{a}$ or $\boldsymbol{c}$ assume both plus and minus values, the positive and negative resistors are to be replaced by inductors and capacitors.)

(3) The currents represent the *surface integral* of the fluid entering the block through one of the planes in 1 sec.

The ψ-networks include ideal transformers ($L = M = \infty$) connected across the diagonals of the circular meshes—two transformers in each plane of the cubes—to make the two diagonally opposite currents equal. If so desired, every other sphere of circular coils may be left out, but less points of space are thereby identified.

It should be noted that, if a certain point in space is a singular point, it is possible to add a source Q there in the form of a junction current and to add a vortex Γ in the form of a set of equal generators arranged along a line from the singular point to the boundary, as shown in Figs. 10 and 11-3. In any closed mesh not surrounding the singular point, the voltages still add up to curl $\boldsymbol{v} = 0$.

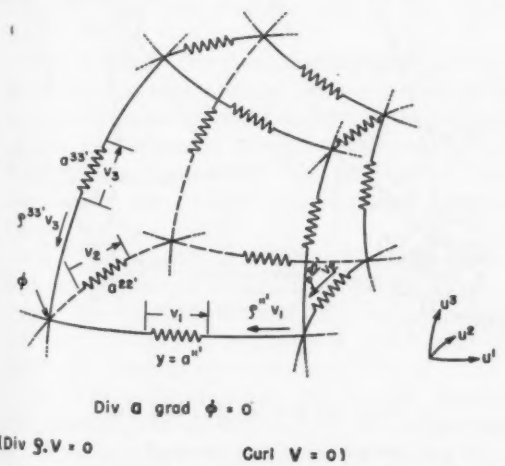

Fig. 3. Potential flow, three-dimensional, ϕ-network.

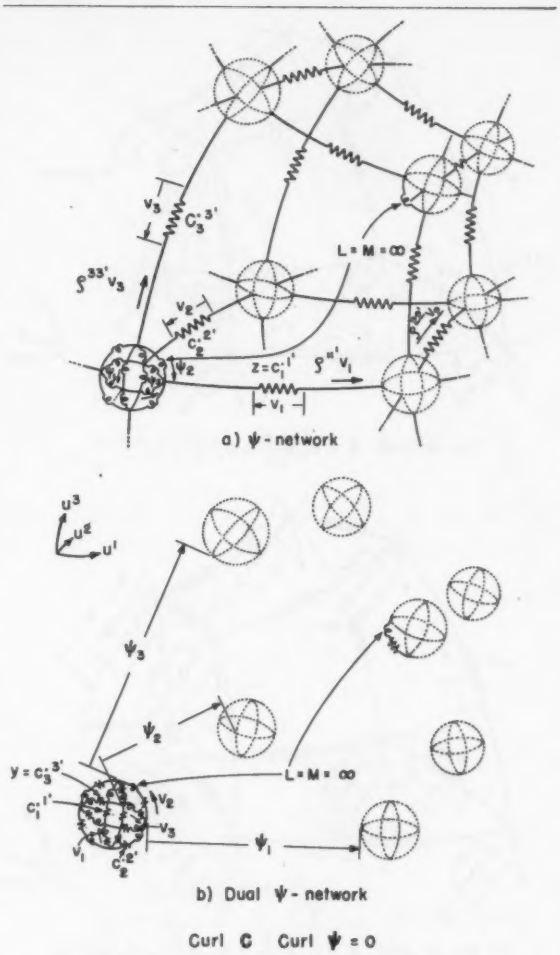

Fig. 4. Potential flow, three-dimensional, ψ-networks.

Equivalent Circuits of the Irrotational Flow

The three-dimensional equivalent circuits for ϕ are shown in Fig. 5, being an extension of the basic network of Fig. 3. Two cases have to be distinguished:

(1) The right-hand side of the equation does not contain $b_1(\partial^2\phi/\partial t^2)$—that is, div $\boldsymbol{a}$ grad $\phi = b_2(\partial\phi/\partial t) + b_3\phi + b_4$. Then the admittances $\boldsymbol{a}$ and b_3 are represented by resistances, $b_2\partial/\partial t$ by capacitors, and b_4 by impressed currents as shown in Fig. 5a.

(2) The right-hand side of the equation does contain $b_1\partial^2\phi/\partial t^2$. In that case, first divide the equation by $p = \partial/\partial t$ so that

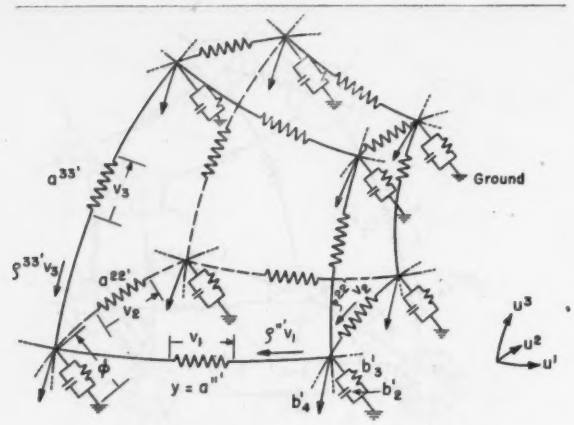

a) Div $\mathbf{a}$ grad $\phi = b_2 \dfrac{\partial \phi}{\partial t} + b_3 \phi + b_4$

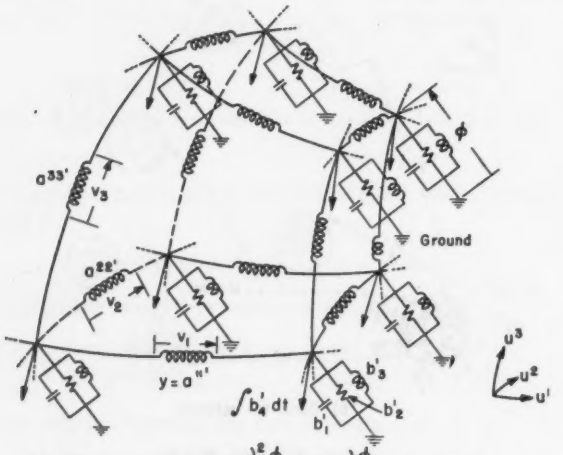

b) Div $\mathbf{a}$ grad $\phi = b_1 \dfrac{\partial^2 \phi}{\partial t^2} + b_2 \dfrac{\partial \phi}{\partial t} + b_3 \phi + b_4$

(Div $\rho \mathbf{v} = Q$ Curl $\mathbf{v} = 0$)

FIG. 5. Irrotational flow, three-dimensional.

$$\text{div } \frac{\boldsymbol{a}}{p} \text{ grad } \phi = b_1 \left(\frac{\partial \phi}{\partial t}\right) + b_2 \phi + \left(\frac{b_3}{p}\right) \phi + \left(\frac{b_4}{p}\right)$$

Then in Fig. 5b the admittances $\boldsymbol{a}/p$ and b_3/p are represented by inductances, b_2 by resistances, $b_1 \partial/\partial t$ by capacitances, and the impressed currents at the junctions represent

$$b_4/p = b_4 dt$$

In Fig. 5a the physical interpretation of the network quantities is the same as in the potential flow network of Fig. 3. In addition, the presence of sources introduces the ground currents representing the *volume integral* of the quantity of fluid entering or leaving a block in 1 sec.

The above networks assume that all coefficients $\boldsymbol{a}$ and b in the equations are positive and real. Special circuits may be developed for cases where some of the coefficients assume also negative or imaginary values.

Electromagnetic, Heat, and Other Analogues

The given three-dimensional networks may represent any one of the following phenomena.

(1) The irrotational flow of an *incompressible* fluid. Then all the admittances $\boldsymbol{a}$ are functions of only the space coordinates.

(2) The irrotational flow of a *compressible* fluid in the physical space. Now, however, all the admittances $\boldsymbol{a}$ are functions of the currents and voltages. That is, the network is nonlinear, and it has to be solved numerically by a cut-and-try procedure.

(3) Electrostatic flux distribution due to stationary charges. In that case:

$$\bar{p} = \bar{\epsilon} \qquad \boldsymbol{v} = \boldsymbol{E} \qquad \bar{p} \cdot \boldsymbol{v} = \boldsymbol{D} \qquad Q = \rho$$

(4) Magnetic flux distribution due to magnetic poles. In that case:

$$\bar{p} = \bar{\mu} \qquad \boldsymbol{v} = \boldsymbol{H} \qquad \bar{p} \cdot \boldsymbol{v} = \boldsymbol{B} \qquad Q = m$$

(5) Conduction of heat.

(6) Diffusion.

(7) Propagation of sound waves.

There are also special problems in elasticity (for instance, in torsion), in hydrodynamics (in bearing lubrication), and in several other branches of physics in which some form of the above wave equations occurs.

Equivalent Circuits of the Solenoidal Flow

The three-dimensional equivalent circuits for $\bar{\psi}$ are shown in Figs. 6 and 7 (and their duals in Fig. 8), both being extensions of the basic network of Fig. 3. Here also two cases have to be distinguished.

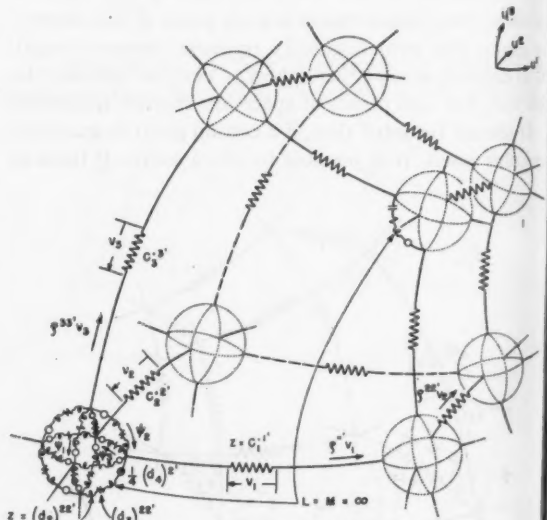

a) Curl $\mathbf{C}$ curl $\bar{\psi} = d_2 \dfrac{\partial \bar{\psi}}{\partial t} + d_3 \cdot \bar{\psi} + d_4$

Div $\rho \mathbf{v} = 0$ Curl $\mathbf{V} = \Gamma$

FIG. 6. Solenoidal flow, three-dimensional (no $\partial^2\psi/\partial t^2$).

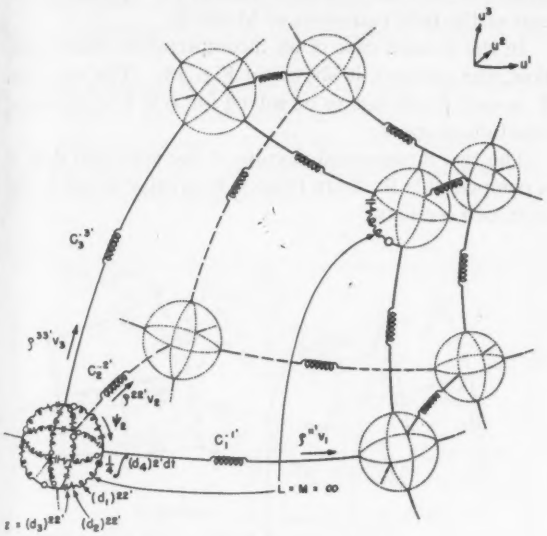

b) Curl $\mathbf{C}$ Curl $\bar{\psi} = \boldsymbol{d}_1 \cdot \frac{\partial^2 \bar{\psi}}{\partial t^2} + \boldsymbol{d}_2 \cdot \frac{\partial \bar{\psi}}{\partial t} + \boldsymbol{d}_3 \cdot \bar{\psi} + \boldsymbol{d}_4$

FIG. 7. Solenoidal flow, three-dimensional (with $\partial^2\bar{\psi}/\partial t^2$).

(1) The right-hand side of the equation does not contain $\boldsymbol{d}_1 \cdot (\partial^2\bar{\psi}/\partial t^2)$. That is,

$$\text{curl } \boldsymbol{c} \text{ curl } \bar{\psi} = \boldsymbol{d}_2 \cdot \frac{\partial \bar{\psi}}{\partial t} + \boldsymbol{d}_3 \cdot \bar{\psi} + \boldsymbol{d}_4$$

Then in Fig. 6 the impedances $\boldsymbol{c}$ and $\boldsymbol{d}_3$ are represented by resistances, $\boldsymbol{d}_2$ by inductors, and $\boldsymbol{d}_4$ by impressed voltages.

(2) The right-hand side of the equation does contain $\boldsymbol{d}_1 \cdot (\partial^2\bar{\psi}/\partial t^2)$. In that case again the equation is divided by $p = \partial/\partial t$, so that

$$\text{curl } \frac{\boldsymbol{c}}{p} \text{ curl } \bar{\psi} = \boldsymbol{d}_1 \cdot \frac{\partial \bar{\psi}}{\partial t} + \boldsymbol{d}_2 \cdot \bar{\psi} + \frac{\boldsymbol{d}_3}{p} \cdot \bar{\psi} + \frac{\boldsymbol{d}_4}{p}$$

Then in Fig. 7 the representation of Fig. 5b is followed.

In Figs. 6 and 7 the physical interpretation is the same as in Fig. 3, except now the junction potentials do not correspond to any physical entity and the admittances of the net represent specific resistances instead of conductances. However, the presence of vortexes introduces the following additional interpretations:

(1) The currents in the circular conductors represent the *line-integral* of $\psi_{(1)}$—namely, $\psi_{(1)}h_1$.

(2) The impedances $\boldsymbol{d}$ of the circular conductors represent the specific resistance of a unit cube of the fluid to the various types of circulations.

(3) The voltages across the circular impedances represent the circulation—namely, the *surface-integral* of the various types of vorticities on the face of a unit cube.

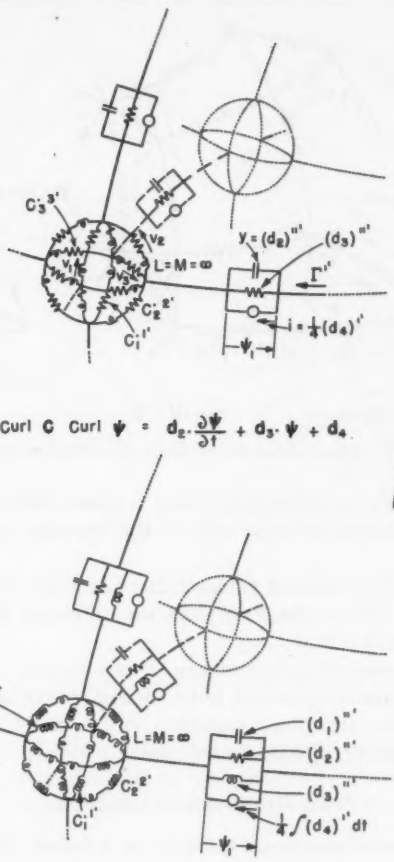

a) Curl $\mathbf{C}$ Curl $\bar{\psi} = \boldsymbol{d}_2 \cdot \frac{\partial \bar{\psi}}{\partial t} + \boldsymbol{d}_3 \cdot \bar{\psi} + \boldsymbol{d}_4$

b) Curl $\mathbf{C}$ Curl $\bar{\psi} = \boldsymbol{d}_1 \cdot \frac{\partial^2 \bar{\psi}}{\partial t^2} + \boldsymbol{d}_2 \cdot \frac{\partial \bar{\psi}}{\partial t} + \boldsymbol{d}_3 \cdot \bar{\psi} + \boldsymbol{d}_4$

FIG. 8. Dual networks of Figs. 6 and 7.

Besides hydrodynamics, there are other branches of physics in which the vector wave equation appears. For instance, if $\bar{\psi}$ represents the electromagnetic vector potential, then curl $\bar{\psi} = \boldsymbol{B}$ and the solenoidal network represents the magnetic flux distribution $\boldsymbol{B}$ in a current-carrying region (see Fig. 19).

EQUIVALENT CIRCUITS OF THE GENERAL FLOW

When the vortex strengths are known functions of space, the equivalent circuit representing the equations

$$\text{div } \bar{\rho} \cdot \boldsymbol{v} = Q \qquad \text{curl } \boldsymbol{v} = \Gamma$$

is given in Fig. 9. It is the same as the basic network of Fig. 3, with the source strength added as a junction current and the vortex strength as a generator at every point of space.

It should be expressly noted that the vector $\boldsymbol{E}$ formed by the generators does not represent the known vector Γ. The magnitudes $\boldsymbol{E}$ of the generators are unknown, and they are to be found first from the equation

$$\Gamma = \text{curl } \boldsymbol{E}$$

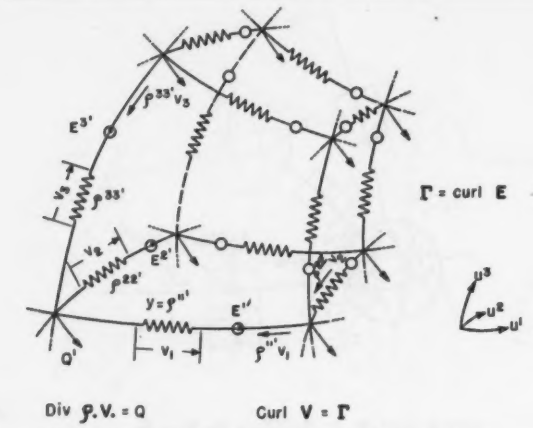

FIG. 9. General nonviscous flow, three-dimensional.

If Γ has components only along one direction u^3, then:

(1) Generators exist only in the branches along u^2 (or u^1).

(2) The generator values E increase along u^1 (or u^2) by Γ, so that in the u^1-u^2 plane the difference between the two E's is Γ.

The same type of arrangement may be repeated if Γ has all three components, but each component is a function of the other two variables only. In the general case, however, $\boldsymbol{E}$ must be calculated.

TWO-DIMENSIONAL CIRCUITS

The two-dimensional circuits for ϕ follow automatically from Figs. 3 and 5 by simply leaving out the coils along u^2 as shown in Figs. 10 and 12. In case of the $\bar{\psi}$-networks, the original three-dimensional networks (Figs. 4 and 6–8) split into two independent networks, one containing ψ_1 and ψ_3 (and v_2), the other containing the remaining ψ_2 (and v_1 and v_3) Figs. 11 and 13–14.

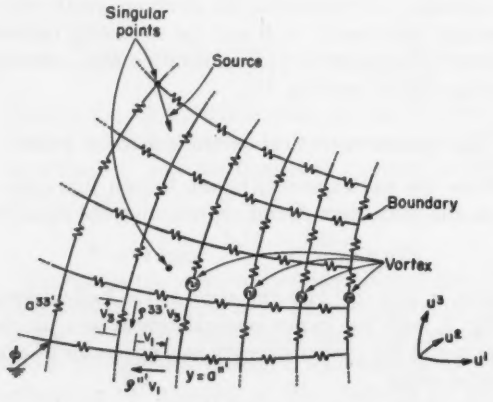

FIG. 10. Potential flow, two-dimensional, ϕ-network (sources and vortexes at singular points).

This split-up is analogous to that in the equivalent circuit of the field equations of Maxwell.

In the general case of an incompressible, nonviscous flow, the network is shown in Fig. 15. The equation $\Gamma = \text{curl } \boldsymbol{E}$ still has to be solved for $\boldsymbol{E}$ if Γ is a general function of space.

The two-dimensional circuits of the potential flow of a compressible fluid are treated in greater detail in the next two sections.

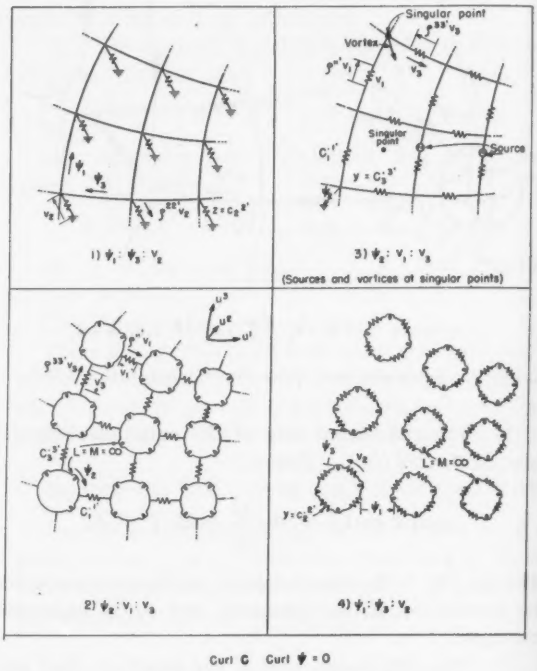

FIG. 11. Potential flow, two-dimensional, ψ-networks.

CIRCUIT OF THE COMPRESSIBLE POTENTIAL FLOW IN THE HODOGRAPH PLANE

If the two-dimensional potential flow of a compressible fluid in the physical plane is considered, the equivalent circuits for ϕ and $\bar{\psi}$ are given in Figs. 10 and 11. However, the value of ρ and thereby the network impedances are not constants, but functions of the unknown ϕ and ψ and the network may be solved only by a cut-and-try procedure.

It is well known that by introducing new variables the nonlinear partial differential equations may be changed to linear equations in some cases. For instance, if the radial velocity w and the angle θ are assumed as independent variables, the value of $\bar{\rho}$ becomes

$$\rho_{(1)} = \frac{\rho}{\rho_0}\left[\frac{1}{1-(w^2/c^2)}\right] \quad \text{and} \quad \rho_{(2)} = \frac{\rho}{\rho_0}$$

Hence, the networks of Figs. 10 and 11-3 for ϕ and ψ still have linear impedances in hodograph coordinates as shown in Fig. 16.

Here again, sources and vortexes may be assumed only at singular points in the manner of Figs. 10 and 11-3.

In the subsonic region the networks only have inductors, while in the supersonic region they contain both inductors and capacitors. Hence, for a study in the subsonic region, pure resistance networks and d.c. voltages and currents may be used.

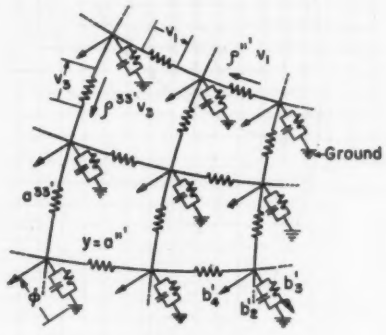

a) Div a grad $\phi = b_2 \frac{\partial \phi}{\partial t} + b_3 \phi + b_4$

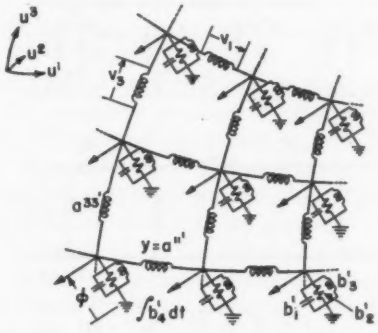

b) Div a grad $\phi = b_1 \frac{\partial^2 \phi}{\partial t^2} + b_2 \frac{\partial \phi}{\partial t} + b_3 \phi + b_4$

(Div ρ.V = 0 Curl V = 0)

FIG. 12. Irrotational flow, two-dimensional.

REPRESENTATION OF MULTIPLE-VALUED FUNCTIONS

In the representation of the fluid flow in the hodograph plane, more than one portion of the physical plane may occupy the same region in the hodograph plane. As a consequence for a given w and θ, two values of ϕ or ψ appear. By assuming the standard equivalent circuits to cover two Riemann sheets joined together at a singular point, the resultant network is shown in Fig. 17, where actual junctions are represented by the heavier dots. It should be noted that the singular point separates lines that are joined to the boundaries in different manner.

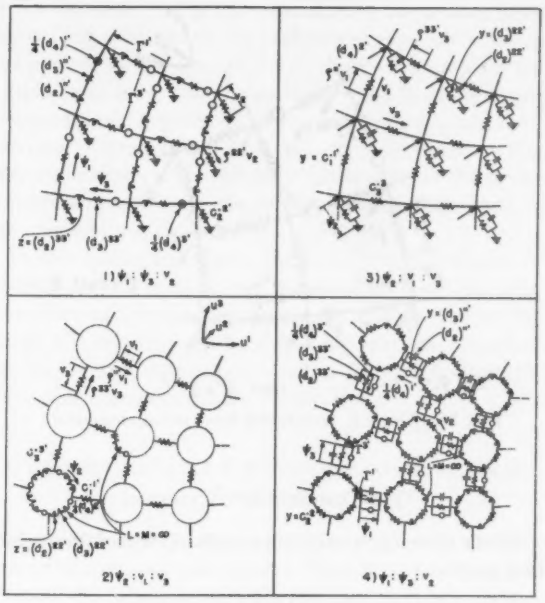

a) Curl C Curl $\psi = d_2 \cdot \frac{\partial^2 \psi}{\partial t^2} + d_3 \cdot \psi + d_4$

(Div ρ.V = 0 Curl V = Γ)

FIG. 13. Solenoidal flow, two-dimensional (no $\partial^2\psi/\partial t^2$).

It is interesting that on the network there are no traces of a branch cut, in conformity with the fact that the particular location of a branch cut has no physical significance.

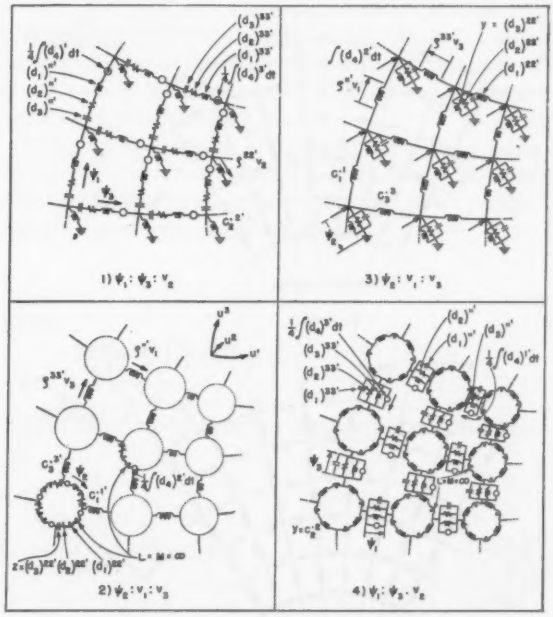

b) Curl C Curl $\psi = d_1 \cdot \frac{\partial^2 \psi}{\partial t^2} + d_2 \cdot \frac{\partial \psi}{\partial t} + d_3 \cdot \psi + d_4$

(Div ρ.V = 0 Curl V = Γ)

FIG. 14. Solenoidal flow, two-dimensional (with $\partial^2\psi/\partial t^2$).

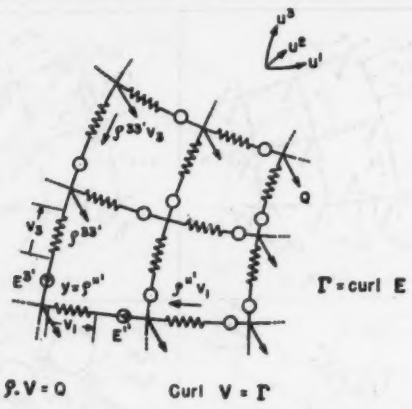

FIG. 15. General, nonviscous flow, two-dimensional.

ONE-DIMENSIONAL CIRCUITS

In one dimension only one standard form of flow equation exists.

$$\left(\frac{\partial}{\partial u^1}\right) a'\left(\frac{\partial}{\partial u^1}\right)\theta = b_1'\left(\frac{\partial^2\theta}{\partial t^2}\right) + b_2'\left(\frac{\partial\theta}{\partial t}\right) + b_3' + b_4'$$

where θ may represent either ϕ or $\bar{\psi}$. Although some of the ψ-networks of Fig. 18 originally contain ideal transformers, in one dimension they may be left out. The ideal transformers play the same role here as in the field equations of Maxwell.

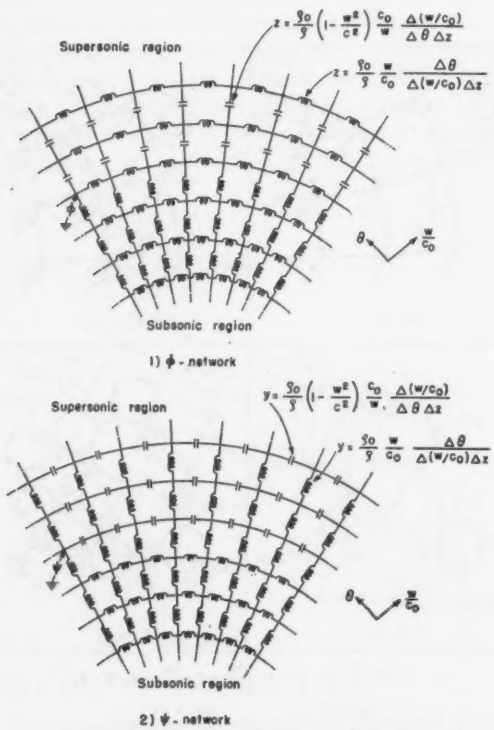

FIG. 16. Compressible, potential flow in the hodograph plane.

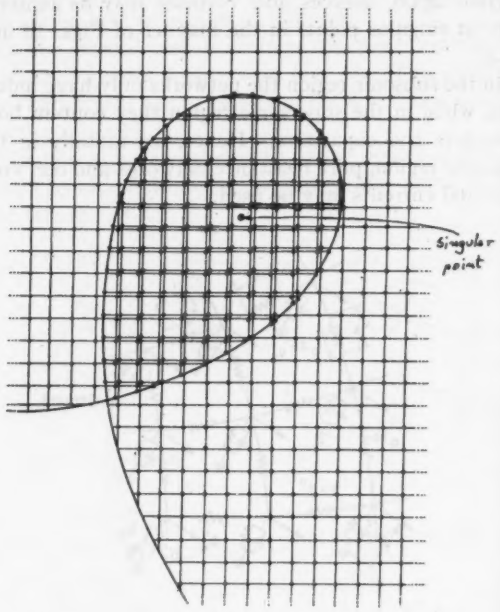

FIG. 17. Equivalent circuit representation of multiply connected regions.

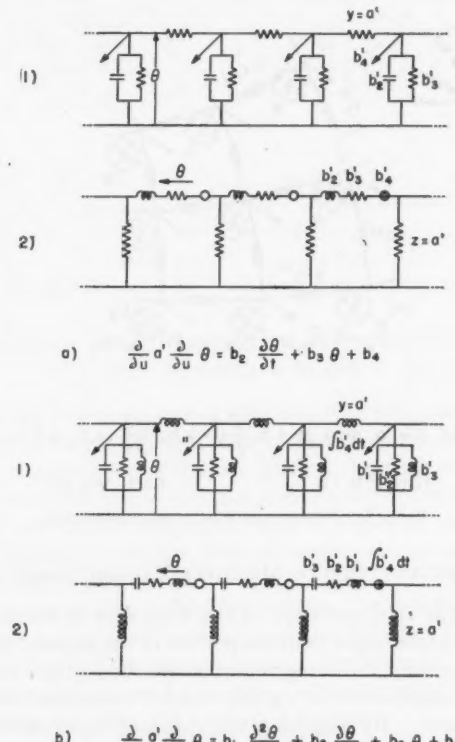

FIG. 18. One-dimensional flow.

BOUNDARY CONDITIONS

In many problems the boundary conditions are the *known* values of ϕ or $\bar{\psi}$ around the entire boundary. In

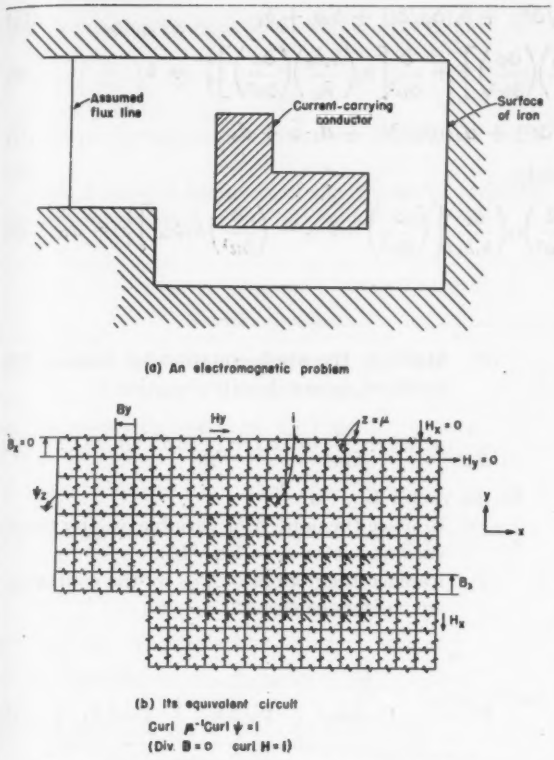

FIG. 19. Boundary conditions in a solenoidal flow.

such cases generators with known voltages are impressed at all the boundary junctions to the ground. These voltages may be equal everywhere around the boundary or only at some places. Where ϕ (and in two-dimensional problems, ψ) is known to be zero, the corresponding junctions are shorted to the ground.

In some problems the line currents ($\boldsymbol{a}$ grad ϕ or $\boldsymbol{c}$ curl ψ) may be known; in case they are zero, the corresponding branches in the circuit are open-circuited. In other problems the line voltages (grad ϕ or curl $\vec{\psi}$) may be known; in case they are zero, the corresponding branches are short-circuited.

For instance, for a current-carrying electromagnetic field of Fig. 19a, the circuit is shown in Fig. 19b. Along the surface of the iron H_x or H_y (line currents) are assumed to be zero, and the corresponding lines are open; along a known flux line B_x or B_y (line voltages) are zero, and the corresponding lines are short-circuited. The current flowing perpendicularly to the sheet of the paper is represented in the network by currents impressed at the corresponding junctions.

In the hodograph plane the boundary conditions in general are not known, and the solution corresponding to a given problem in the physical plane may be established only by a reasoned cut-and-try process. Further studies on the equivalent circuits for the hodograph plane will appear in future publications.

A Check on the Self-Consistency of Approximate Methods

The solution of the networks by numerical methods is treated in another publication.[8] Here it may be pointed out that the networks may also be used to check the accuracy and self-consistency of results arrived at by other methods, approximate or exact. Both linear and nonlinear networks may equally serve such purposes.

The check consists of assuming the absolute potentials at every junction to represent a known field distribution. Then all currents flowing between the junctions may be calculated (or the currents may be assumed to be known and the junction potentials calculated).

Now if the assumed potentials are correct, then the sum of the currents entering each junction is zero. If, however, the assumed potentials are only approximate, an unbalanced current is left over at every junction. *The magnitude of the unbalanced currents is a measure of the deviation of the approximate results from the correct ones at every point in space.*

Guided by the known unbalanced currents, a guess may be made at a more correct field distribution. The newly calculated unbalanced currents offer further clues for a continued approximation.

Appendix

Conventional Form of the Equations

In orthogonal curvilinear coordinates, and in the special nonisotropic medium under consideration, the equations—for which equivalent circuits are to be established—are:

$$1.\quad \text{Div } \bar{\rho}\cdot\boldsymbol{v} = Q \tag{1}$$

$$\frac{1}{h_1h_2h_3}\left[\frac{\partial}{\partial u^1}(\rho_1 v_{(1)}h_2h_3) + \frac{\partial}{\partial u^2}(\rho_2 v_{(2)}h_3h_1) + \frac{\partial}{\partial u^3}(\rho_3 v_{(3)}h_1h_2)\right] = Q \tag{2}$$

$$\text{Curl } \boldsymbol{v} = \Gamma \tag{3}$$

$$(1/h_2h_3)[(\partial/\partial u^3)h_2v_{(2)} - (\partial/\partial u^2)h_3v_{(3)}] = \Gamma_{(1)} \tag{4}$$

and two similar equations

$$2.\ \text{Div}\ \boldsymbol{a}\ \text{grad}\ \phi = b = b_1(\partial^2\phi/\partial t^2) + b_2(\partial\phi/\partial t) + b_3\phi + b_4 \tag{5}$$

$$\frac{1}{h_1h_2h_3}\left\{\frac{\partial}{\partial u^1}\left[a_1\left(\frac{h_2h_3}{h_1}\right)\left(\frac{\partial\phi}{\partial u^1}\right)\right] + \frac{\partial}{\partial u^2}\left[a_2\left(\frac{h_3h_1}{h_2}\right)\left(\frac{\partial\phi}{\partial u^2}\right)\right] + \frac{\partial}{\partial u^3}\left[a_3\left(\frac{h_1h_2}{h_3}\right)\left(\frac{\partial\phi}{\partial u^3}\right)\right]\right\} = b \tag{6}$$

$$3.\ \text{Curl}\ \boldsymbol{c}\ \text{curl}\ \bar{\psi} = \boldsymbol{d} = \boldsymbol{d}_1\cdot(\partial^2\bar{\psi}/\partial t^2) + \boldsymbol{d}_2\cdot(\partial\bar{\psi}/\partial t) + \boldsymbol{d}_3\cdot\bar{\phi} + \boldsymbol{d}_4 \tag{7}$$

where $\boldsymbol{d}_1$, $\boldsymbol{d}_2$ and $\boldsymbol{d}_3$ are matrices with diagonal elements only

$$\frac{1}{h_2h_3}\left\{\left(\frac{\partial}{\partial u^2}\right)c_3\left(\frac{h_3}{h_1h_2}\right)\left[\left(\frac{\partial}{\partial u^1}\right)h_2\psi_{(2)} - \left(\frac{\partial}{\partial u^2}\right)h_1\psi_{(1)}\right] - \left(\frac{\partial}{\partial u^3}\right)c_2\left(\frac{h_2}{h_1h_3}\right)\left[\left(\frac{\partial}{\partial u^3}\right)h_1\psi_{(1)} - \left(\frac{\partial}{\partial u^1}\right)h_3\psi_{(3)}\right]\right\} = d_{(1)} \tag{8}$$

and two analogous equations.

The variables u^α and the metrical coefficients h are given in Table 1 for the three most common orthogonal frames. Their values in other frames (such as elliptic, spheroidal, etc., frames) are given in books on applied mathematics.

TABLE 1

	u^1	u^2	u^3	h_1	h_2	h_3
Cartesian	x	y	z	1	1	1
Cylindric	r	θ	z	1	r	1
Spherical	r	θ	ϕ	1	r	$r\sin\theta$

The following should be noted:

(1) The variables ψ; the matrices $\boldsymbol{a}$, $\boldsymbol{c}$; and the applied forces b, $\boldsymbol{d}$, etc., are not tensors (ϕ happens to be a tensor).

(2) The equations themselves are not tensor equations—that is, they cannot be transformed, as they stand, to, say, nonorthogonal reference frames, nor can they be represented by a physical model.

Only in the special case of Cartesian coordinates, when the metrical coefficients h are unity, do the equations reduce to a tensor equation.

Tensor-Density Form of the Equations

The conventional equations may be changed to the needed tensor-density form by the following steps:

(a) In the *scalar* Eq. (2):

(1) Replace the nontensor scalar Q by the tensor-density Q' as

$$Q' = Qh_1h_2h_3 \tag{9}$$

(2) Replace the nontensor variables $v_{(\alpha)}$ by the covariant vector v_α

α	1	2	3
$v_\alpha =$	$v_{(1)}h_1$	$v_{(2)}h_2$	$v_{(3)}h_3$

(10)

(3) Replace the nontensor $\rho_{(\alpha)}$ by the tensor-densities $\rho^{\alpha\beta'}$.

$$\rho^{11'} = \rho_{(1)}\left(\frac{h_2h_3}{h_1}\right),\ \rho^{22'} = \rho_{(2)}\left(\frac{h_1h_3}{h_2}\right),\ \rho^{33'} = \rho_{(3)}\left(\frac{h_1h_2}{h_3}\right) \tag{11}$$

(4) Multiply the whole equation by $h_1h_2h_3$. The resultant tensor-density equation is

$$\frac{\partial}{\partial u^1}(\rho^{11'}v_1) + \frac{\partial}{\partial u^2}(\rho^{22'}v_2) + \frac{\partial}{\partial u^3}(\rho^{33'}v_3) = Q' \tag{12}$$

In the vector Eq. (4):

(1) Replace the nontensor variables $v_{(\alpha)}$ by the covariant vector v_α of Eq. (10).

(2) Replace the nontensor $\Gamma_{(\alpha)}$ by the contravariant vector-density $\Gamma^{\alpha'}$ as

α			
$\Gamma^{\alpha'} =$	$\Gamma_{(1)}h_2h_3$	$\Gamma_{(2)}h_1h_3$	$\Gamma_{(3)}h_1h_2$

(13)

(3) The first equation is divided by h_1, the second by h_2, and the third by h_3.

(4) All three equations are multiplied by $h_1h_2h_3$.

The resultant tensor-density equation is

$$(\partial v_2/\partial u^2) - (\partial v_3/\partial u^2) = \Gamma^{1'} \tag{14}$$

and two analogous equations.

(b) In the scalar Eq. (6) the previous steps 1, 3, and 4 under (a) for the scalar equation are repeated, giving

$$\left(\frac{\partial}{\partial u^1}\right)a^{11'}\left(\frac{\partial\phi}{\partial u^1}\right) + \left(\frac{\partial}{\partial u^2}\right)a^{22'}\left(\frac{\partial\phi}{\partial u^2}\right) + \left(\frac{\partial}{\partial u^3}\right)a^{33'}\left(\frac{\partial\phi}{\partial u^3}\right) = b' \tag{15}$$

(c) In the vector Eq. 8 the previous steps under (a) for the vector equation are repeated with an additional step.

(5) Replace the matrices $\boldsymbol{d}_1$, $\boldsymbol{d}_2$, and $\boldsymbol{d}_3$ by the tensor-densities $(d_1)^{\alpha\beta'}$, $(d_2)^{\alpha\beta'}$, and $(d_3)^{\alpha\beta'}$ as

$$(d_1)^{11'} = (d_1)_{(1)}\left(\frac{h_2h_3}{h_1}\right),\quad (d_1)^{22'} = (d_1)_{(2)}\left(\frac{h_1h_3}{h_2}\right),\quad (d_1)^{33'} = (d_1)_{(3)}\left(\frac{h_1h_2}{h_3}\right) \tag{16}$$

Similar formulas apply to the components of $(d_2)^{\alpha\beta'}$ and $(d_3)^{\alpha\beta'}$.

The resultant tensor-density equations are

$$\left(\frac{\partial}{\partial u^2}\right)c_3^3\left(\frac{\partial\psi_2}{\partial u^1} - \frac{\partial\psi_1}{\partial u^2}\right) - \left(\frac{\partial}{\partial u^3}\right)c_2^2\left(\frac{\partial\psi_1}{\partial u^3} - \frac{\partial\psi_3}{\partial u^1}\right) = d^{1'} \tag{17}$$

and two analogous equations, where

$$c_1^{1} = c_1\left(\frac{h_1}{h_2h_3}\right), \quad c_2^{2} = c_2\left(\frac{h_2}{h_1h_3}\right), \quad c_3^{3} = c_3\left(\frac{h_3}{h_1h_2}\right) \tag{18}$$

and where the primed quantities represent tensor-densities.

Table 2 shows a summary of the constants, including the arbitrary widths of the blocks Δu^1, Δu^2, Δu^3.

TABLE 2

Network Constants

(1) Let Q, b_1, b_2, b_3, and b_4 be denoted by A. Then

$$A' = Ah_1h_2h_3\Delta u^1\Delta u^2\Delta u^3$$

(2) Let v and ψ be denoted by B. Then

$$B_1 = B_{(1)}h_1\Delta u^1, \quad B_2 = B_{(2)}h_2\Delta u^2, \quad B_3 = B_{(3)}h_3\Delta u^3$$

(3) Let c be denoted by c. Then

$$c_1^{1'} = c_{(1)}\left(\frac{h_1}{h_2h_3}\right)\left(\frac{\Delta u^1}{\Delta u^2\Delta u^3}\right), \quad c_2^{2'} = c_{(2)}\left(\frac{h_2}{h_1h_3}\right)\left(\frac{\Delta u^2}{\Delta u^1\Delta u^3}\right),$$

$$c_3^{3} = c_{(1)}\left(\frac{h_3}{h_1h_2}\right)\left(\frac{\Delta u^3}{\Delta u^1\Delta u^2}\right)$$

(4) Let Γ and d_4 be denoted by D then

$$D^{1'} = D_{(1)}h_2h_3\Delta u^2\Delta u^3, \; D^{2'} = D_{(2)}h_1h_3\Delta u^1\Delta u^3, \; D^{3'} = D_{(3)}h_1h_2\Delta u^1\Delta u^2$$

(5) Let a, ρ, d_1, d_2, and d_3 be denoted by F. Then

$$F^{11'} = F_{(1)}\left(\frac{h_2h_3}{h_1}\right)\left(\frac{\Delta u^2\Delta u^3}{\Delta u^1}\right), \quad F^{22'} = F_{(2)}\left(\frac{h_1h_3}{h_2}\right)\left(\frac{\Delta u^1\Delta u^3}{\Delta u^2}\right),$$

$$F^{33'} = F_{(3)}\left(\frac{h_1h_2}{h_3}\right)\left(\frac{\Delta u^1\Delta u^2}{\Delta u^3}\right)$$

ACKNOWLEDGMENT

The writer wishes to acknowledge his indebtedness to D. R. Shoults for suggesting, and to S. B. Crary for encouraging, the use of equivalent circuits for the study of compressible fluid flow; also to H. Kraft and C. Dibble, of the Turbine Engineering Department, and to G. K. Carter and C. Concordia, of the Central Station Divisions for numerous discussions.

REFERENCES

[1] Kron, G., *Equivalent Circuit of the Field Equations of Maxwell—I*, Proc. I.R.E., Vol. 32, pp. 289–299, May, 1944.

[2] Concordia, C., Kron, G., Ridgway, W., and Whinnery, W. R., *A-C Network Analyzer Studies of Electromagnetic Cavity Resonators*, Proc. I.R.E., Vol. 32, pp. 360–367, June, 1944.

[3] Kron, G., *Equivalent Circuits of the Elastic Field*, Journal of Applied Mechanics, pp. A-149–161, September, 1944.

[4] Carter, G. K., *Numerical and Network Analyzer Solution of the Equivalent Circuits for the Elastic Field*, Journal of Applied Mechanics, pp. A-162–167, September, 1944.

[5] Paschkis and Baker, *A Method for Determining Unsteady-State Heat Transfer by Means of an Electrical Model*, A.S.M.E. Transactions, Vol. 64, No. 1, pp. 105–112, January, 1942.

[6] Kron, G., *Equivalent Circuits for Oscillating Systems and the Riemann-Christoffel Curvature Tensor*, A.I.E.E. Transactions, Vol. 62, pp. 27–35, 1943.

[7] Bers and Gelbart, *On a Class of Differential Equations in Mechanics of Continua*, Quarterly of Applied Mathematics, Vol. I, No. 2, p. 168, July, 1943.

[8] Kron, G., *Numerical Solution of Ordinary and Partial Differential Equations by Means of Equivalent Circuits;* scheduled to appear in the March, 1945, issue of the Journal of Applied Physics.

[9] Kron, G., *Electric Circuit Models of the Schrödinger Equation*, Physical Revue, Vol. 67, No. 1 and 2, p. 39, January, 1945.

Numerical and Network-Analyzer Tests of an Equivalent Circuit for Compressible Fluid Flow

G. K. CARTER* AND G. KRON†

General Electric Company

FOREWORD

Of the circuits described in the companion paper, "Equivalent Circuits of Compressible and Incompressible Fluid Flow Fields" (page 221, this issue), one was chosen for further study and testing. Because of recent interest in that field, the one selected for this purpose was the network representing the flow function ψ in the hodograph plane for compressible, potential flow. The equivalent circuit for this function is pictured in Fig. 1. The circuit was first tested by calculating the current balance at several junction points of the network, using a distribution of ψ values calculated from analytic solutions of the original differential equation. This procedure having shown the validity of the equivalent circuit, the network was set up on the a.c. network analyzer[1] and was used to solve a whole field from given boundary conditions; the solution so obtained matches the differential analyzer solution of the same field[2] and thus shows the feasibility of solving such field problems with present network-analyzer equipment.

NUMERICAL CHECKS

IT HAS BEEN SHOWN[2] that the flow function ψ in the hodograph plane for compressible potential flow is described by

$$w^2\left(\frac{\partial^2\psi}{\partial w^2}\right)+w\left(1+\frac{w^2}{c^2}\right)\frac{\partial\psi}{\partial w}+\left(1-\frac{w^2}{c^2}\right)\left(\frac{\partial^2\psi}{\partial\theta^2}\right)=0 \quad (1)$$

where (w, θ) are polar components of fluid velocity and c is local sound velocity, a function of w. By linear combination of elementary solutions of Eq. (1), for a fluid having $c_p/c_v = 1.4$, a possible solution can be shown to be

$$\psi = M\theta + N\left\{\left(1-\frac{w^2}{5c_0^2}\right)^{1/2}+\frac{1}{3}\left(1-\frac{w^2}{5c_0^2}\right)^{3/2}+\frac{1}{5}\left(1-\frac{w^2}{5c_0^2}\right)^{5/2}+\ln\left[1-\left(1-\frac{w^2}{5c_0^2}\right)^{1/2}\right]-\frac{1}{2}\ln\left(\frac{w^2}{5c_0^2}\right)\right\}+P\frac{c_0\sin\theta}{w}+Q \quad (2)$$

where M, N, P, Q are arbitrary constants and c_0 is the velocity of sound in the stationary fluid.

For the numerical checks of the equivalent circuit, Eq. (2) was used, with $M = N = P = 1$ and $Q = 0$. The mesh size selected was $\Delta\theta = \Delta(w/c_0) = 0.1$, and the current balances were calculated at the points $(w/c_0 = 0.5, \theta = 1.1)$, $(w/c_0 = 0.9, \theta = 1.1)$, and $(w/c_0 = 1.3, \theta = 1.1)$, being, respectively, below, near, and above local sound velocity $(w/c_0 = 0.9129)$. The calculated currents are listed in Table 1. The current-balance test gives confirmation of the correctness of the equivalent circuit and at the same time shows that useful accuracy may be attainable with only moderately small subdivisions of the field.

TABLE 1

CURRENT BALANCE, USING ANALYTIC SOLUTION OF FIELD

Point	Current Away	Current Into
$w/c_0 = 0.5$	0.3342	0.3044
$\theta = 1.1$	0.0906	0.1220
	0.4248	0.4264
$w/c_0 = 0.9$	0.00897	0.00840
$\theta = 1.1$	0.05454	0.05524
	0.06351	0.06364
$w/c_0 = 1.3$	0.4402	0.4632
$\theta = 1.1$	0.1051	0.0820
	0.5453	0.5452

NETWORK-ANALYZER TEST

The alternating-current network analyzer[1] consists of a set of adjustable resistance, inductance, and capacitance units, each connected to a pair of flexible cords and plugs. Connections between units to form any desired network are made by inserting the plugs in adjacent jacks in a jack panel. As many units as desired can be connected to a common point. Alternating-current electric power is supplied by a motor-generator set to individual generator units so that several different voltages, independently adjustable, can be inserted into different parts of the network. A centrally located set of measuring instruments can be connected to any unit or circuit by means of a set of key switches.

In the circuit shown in Fig. 1, which was the one tested on the network analyzer, it is seen that in the region above local sound velocity it is necessary to use both negative and positive admittances. Since it is impractical to simulate a large number of negative-resistance units, the network was made up of positive and negative reactance units—i.e., of inductors and capacitors. Fields were then measured corresponding to chosen boundary values of ψ, impressed by the a.c. generator units.

One example of the field solutions obtained on the network analyzer is given in Table 2. This particular

Received June 3, 1944. To have been presented at the I.A.S. Thirteenth Annual Meeting, which was canceled to cooperate with a Government appeal (January, 1945) to refrain from holding conventions and meetings.

* Analytical Division, Central Station Engineering Divisions.
† Consulting Engineer.

TABLE 2

Field Solution Obtained on A.C. Network Analyzer. Impressed Voltages (Values of ψ) Underscored. Readings from Differential Analyzer Solution in Parentheses

w/c_0 ⟶ / θ ↓	0.4	0.5	0.6	0.7	0.8	0.9	1.0	1.1	1.2	1.3	1.4
2.7					116.9	111.8	107.3	105	102.9	100.5	
					(117.5)	(112.2)	(107.7)	(105.5)	(102.8)	(100.3)	
2.4		134.6	124.6	116.9	111.2	107	102.6	99.6	97.0	95.0	93.6
		(135)	(125.2)	(117.5)	(112)	(107)	(103)	(100.5)	(97.5)	(95.5)	(93.6)
2.1	139.0	126	117.9	109.5	104.1	100	96.1	93.5	91.2	89.0	87.2
	(139.2)	(125.5)	(116.8)	(109.5)	(104.7)	(99.8)	(96.2)	(93.5)	(91.3)	(89.5)	(87.5)
1.8	124.6	113.5	106.1	98.8	93.6	90.2	86.4	84	81.7	80	78.3
	(125.8)	(114.7)	(105.2)	(99)	(95)	(90.3)	(87.5)	(84.5)	(82.5)	(80.8)	(79.0)
1.5	109.5	99.9	92.7	86	81.5	78	75	72.9	70.9	69.6	68.5
	(109.7)	(99.8)	(91.7)	(86.5)	(83)	(79)	(76)	(73.7)	(71.7)	(70.4)	(68.8)
1.2	91.6	83	77.6	72.1	68.9	66	63.8	62.2	60.1	58.7	57.0
	(91.5)	(82.5)	(76.5)	(71.5)	(68.5)	(65)	(62.7)	(61)	(59.3)	(58.2)	(57.0)
0.9	70.1	64	59.3	55	51.9	49.4	47	45.7	44.7	44	43.7
	(70.6)	(63.3)	(59)	(55.5)	(52.5)	(50)	(48.5)	(47)	(45.5)	(44.7)	(43.7)
0.6	48.2	43.9	40.8	38	36.1	34.8	33.7	32.7	31.5	30.5	
	(48.2)	(44)	(40.6)	(37.4)	(36)	(34.3)	(33.2)	(32)	(31.3)	(30.5)	
0.3	25.2	22.8	21	19.4	18.1	17.3	16.7	16.2	16.0		
	(25.3)	(23)	(21)	(19.4)	(18.5)	(17.8)	(17.2)	(16.8)	(16.0)		
0		0	0	0	0	0	0	0			

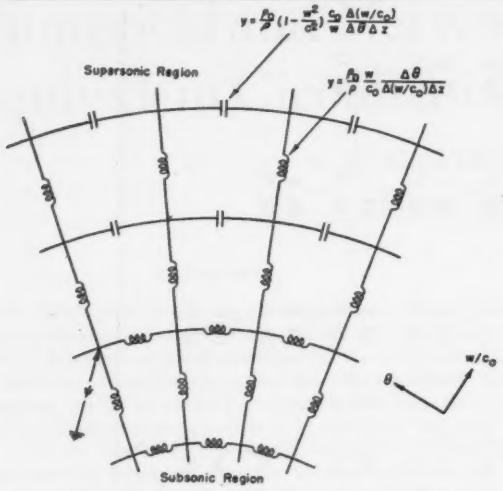

FIG. 1. Equivalent circuit for compressible, potential flow in hodograph coordinates.

example was chosen to represent a field previously solved on the differential analyzer; the differential analyzer solution, reproduced from reference 2, is shown in Fig. 2. Table 2 gives in parentheses readings taken from the differential analyzer solution at the points corresponding to the junction points in the network; they therefore give an indication of the accuracy of the network solution. It is notable that the network solution is exceedingly good for supersonic, as well as subsonic, regions, and this with the extremely large increment $\Delta\theta = 0.3$ rad. It should be observed that part of the difference between the two solutions is attributable to slight discrepancies in the boundary conditions, and some additional difference must be ascribed to possible error in reading coordinates from the differential analyzer curves.

CONCLUSION

The correctness of the equivalent circuit for compressible flow in hodograph coordinates is demonstrated by calculation of current balance in the network using known analytic solutions. The practical usefulness of

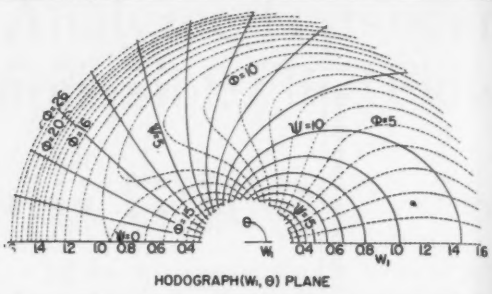

FIG. 2. Differential analyzer solution of a compressible flow field, used for testing the a.c. network analyzer solution.

the circuit in solving field problems is shown by actual solution of such a problem on the a.c. network analyzer and comparison of this solution with the corresponding one obtained on the differential analyzer.

In comparison with either analytic or differential analyzer methods, however, the equivalent circuit gives the possibility of a much greater variety of solutions. This is a result of offering a field solution directly for any specified boundary conditions, instead of having to resort to separation of variables, or series solutions, or other analytic devices.

One simplification of the circuit solution comes about when the field of interest lies entirely below local sound velocity. In such a case all network elements have like sign and may therefore be represented by ordinary resistor units; the power supply may then be either d.c. or a.c. A further possibility with the equivalent circuit in any case is that of either solving or improving a solution by hand, using some method of relaxation[4] of the calculated residual junction currents.

REFERENCES

[1] Kuehni, H. P., and Lorraine, R. G., *A New A-C Network Analyzer*, A.I.E.E. Transactions, Vol. 57, p. 67, 1938.

[2] Kraft, H., and Dibble, C. G., *Some Two-Dimensional Adiabatic Compressible Flow Patterns*, Journal of the Aeronautical Sciences, Vol. 11, p. 283, October, 1944.

[3] Ringleb, F., *Exakte Lösungen der Differentialgleichungen einer adiabatischen Gasströmung*, ZAMM, Vol. 20, p. 185, 1940.

[4] Southwell, R. V., *Relaxation Methods in Engineering Science*, Oxford University Press, London, 1940.

Stresses in a Ring Loaded Normal to Its Plane

E. R. WALTERS*

Consolidated Vultee Aircraft Corporation

SUMMARY

General equations are developed for the internal forces in a closed plane ring or frame loaded perpendicular to its plane. The equilibrium condition is determined in the ordinary manner by minimizing the strain energy with respect to bending, torsion, and shear at an imaginary cut. Parameters required for numerical solution of problems may indicate a method similar to the "column analogy" for rings loaded in their plane.

Formulas and charts are given in the Appendix for a circular ring of constant cross section with a point load and reaction distributed as the axial stress in a cylinder. The internal forces are given immediately by coefficients read from the charts. Any set of point loads may be built up by superposition of single loads, and the distributed reaction disappears if the applied loads are self-equilibrating.

INTRODUCTION

THE FOLLOWING THEORY is concerned with a plane elastic ring of arbitrary plan form and cross section. The principal axes of all sections are parallel and perpendicular to the ring plane so that transverse bending is not coupled with bending in the plane. It is loaded by forces perpendicular to its plane and moments which may be represented, according to the right-hand screw rule, by vectors in the plane. Since all forces are considered loads they must form a self-equilibrating system.

The resultant traction on any cross section consists of a shear perpendicular to the plane and a moment defined by a vector in the plane. The moment vector may be resolved into components normal and parallel to the ring axis, and these components are, respectively, bending moment and torsional moment.

THEORY

This analysis assumes linear elasticity and large enough ratio of radius of curvature to section size to approximate linear distribution of bending stress across the section and allow the neglect of direct shear energy in relation to bending and torsion energy. The method is generally similar to that of reference 1.

In general, a closed ring is three times indeterminate, but by cutting in one place it is rendered determinate. The forces in the complete ring will be those in the cut ring plus those due to the unknown forces at the cut. The strain-energy expression is set up in terms of the unknowns and the statically determinate ring. Partial derivatives with respect to each of the unknowns are set equal to zero, thus defining the condition for minimum strain energy, which is the equilibrium state. Three equations in three unknowns result; their solution is given in determinates whose factors are explicit functions of the ring dimension and loads. By Castigliano's theorem it is seen that the above process simply requires the deformations at the cut to be consistent.

If the ring consists of more than one closed member, more than one cut is necessary to remove the redundancy, and the above process yields a number of equations equal to the number of redundants.

Received August 28, 1944.

* Stress Analyst, San Diego Development Engineering Department.

NOTATION

V_0, M_0, T_0	= shear, bending moment, and torque in the ring due to the applied loads on the structure as rendered statically determinate by an imaginary cut
X_v, X_m, X_t	= shear, bending moment, and torque at the cut to be determined to make the strain energy a minimum
V, M, T	= total shear, bending moment, and torque at any point
$M_m = \partial M/\partial X_m$	= bending moment due to unit bending moment at cut
$T_m = \partial T/\partial X_m$	= torque due to unit bending moment at cut
$M_t = \partial M/\partial X_t$	= bending moment due to unit torque at cut
$T_t = \partial T/\partial X_t$	= torque due to unit torque at cut
$M_v = \partial M/\partial X_v$	= bending moment due to unit shear at cut
$T_v = \partial T/\partial X_v$	= torque due to unit shear at cut
U	= total internal strain energy
EI	= flexural rigidity (E = Young's modulus)
GJ	= torsional rigidity (G = shear modulus)
k	= constant of proportionality for shear strain, depending on the section
R	= radius of curvature of the member centroid
s	= coordinate along member centroidal axis

STRAIN ENERGY

The strain energy (U) in a member subject to shear, bending, and torsion is

$$U = \int \left(\frac{kV^2}{2AG} + \frac{M^2}{2EI} + \frac{T^2}{2GJ} \right) ds \qquad (1)$$

The total shear, bending moment, and torque at any point are found by superimposing the forces due to the unknowns at the cut on those of the statically determinate ring.

$$\left.\begin{aligned} V &= V_0 + \sum_j (V_{vj}X_{vj} + V_{mj}X_{mj} + V_{tj}X_{tj}) \\ M &= M_0 + \sum_j (M_{vj}X_{vj} + M_{mj}X_{mj} + M_{tj}X_{tj}) \\ T &= T_0 + \sum_j (T_{vj}X_{vj} + T_{mj}X_{mj} + T_{tj}X_{tj}) \end{aligned}\right\} \qquad (2)$$

The $\sum$ and subscript j indicate the summation over all members and cuts if the ring is braced to require j cuts to make it statically determinate.

Equilibrium Condition

Taking partial derivatives with respect to each of the unknowns and equating to 0 for the energy to be a minimum:

$$\left.\begin{aligned}
\frac{\partial U}{\partial X_{vj}} &= \sum_j \int \left[\left(\frac{kV}{AG}\right)V_{vj} + \left(\frac{M}{EI}\right)M_{vj} + \left(\frac{T}{GJ}\right)T_{vj}\right] ds = 0 \\
\frac{\partial U}{\partial X_{mj}} &= \sum_j \int \left[\left(\frac{kV}{AG}\right)V_{mj} + \left(\frac{M}{EI}\right)M_{mj} + \left(\frac{T}{GJ}\right)T_{mj}\right] ds = 0 \\
\frac{\partial U}{\partial X_{tj}} &= \sum_j \int \left[\left(\frac{kV}{AG}\right)V_{tj} + \left(\frac{M}{EI}\right)M_{tj} + \left(\frac{T}{GJ}\right)T_{tj}\right] ds = 0
\end{aligned}\right\} \quad (3)$$

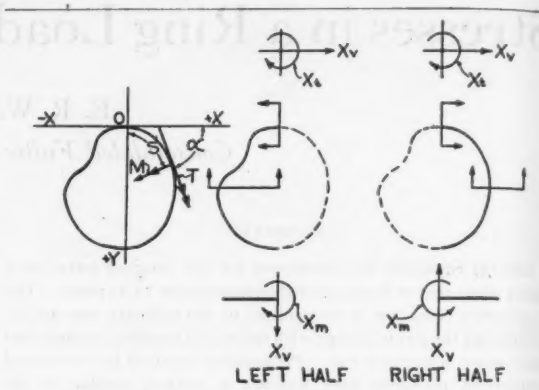

Fig. 1. Direction of axes and positive forces.

Omitting the terms due to shear and assuming only one cut necessary to remove the redundancy set the derivatives equal 0, Eqs. (3) become

$$\left.\begin{aligned}
\frac{\partial U}{\partial X_v} &= \int \left[\left(\frac{M}{EI}\right)M_v + \left(\frac{T}{GJ}\right)T_v\right] ds = 0 \\
\frac{\partial U}{\partial X_m} &= \int \left[\left(\frac{M}{EI}\right)M_m + \left(\frac{T}{GJ}\right)T_m\right] ds = 0 \\
\frac{\partial U}{\partial X_t} &= \int \left[\left(\frac{M}{EI}\right)M_t + \left(\frac{T}{GJ}\right)T_t\right] ds = 0
\end{aligned}\right\} \quad (3a)$$

Substituting Eqs. (2), the actual bending and torsion moments, in Eqs. (3a) and noting that the X's are not functions of the variable s and so may be removed from the integral gives Eqs. (3b) below.

$$\left.\begin{aligned}
0 = \frac{\partial U}{\partial X_v} &= X_v \int \left(\frac{M_v^2}{EI}\right) ds + X_m \int \left(\frac{M_m M_v}{EI}\right) ds + X_t \int \left(\frac{M_t M_v}{EI}\right) ds + X_v \int \left(\frac{T_v^2}{GJ}\right) ds + \\
&\quad X_m \int \left(\frac{T_m T_v}{GJ}\right) ds + X_t \int \left(\frac{T_t T_v}{GJ}\right) ds + \int \left(\frac{M_0 M_v}{EI}\right) ds + \int \left(\frac{T_0 T_v}{GJ}\right) ds \\
0 = \frac{\partial U}{\partial X_m} &= X_v \int \left(\frac{M_v M_m}{EI}\right) ds + X_m \int \left(\frac{M_m^2}{EI}\right) ds + X_t \int \left(\frac{M_t M_m}{EI}\right) ds + X_v \int \left(\frac{T_v T_m}{GJ}\right) ds + \\
&\quad X_m \int \left(\frac{T_m^2}{GJ}\right) ds + X_t \int \left(\frac{T_t T_m}{GJ}\right) ds + \int \left(\frac{M_0 M_m}{EI}\right) ds + \int \left(\frac{T_0 T_m}{GJ}\right) ds \\
0 = \frac{\partial U}{\partial X_t} &= X_v \int \left(\frac{M_v M_t}{EI}\right) ds + X_m \int \left(\frac{M_m M_t}{EI}\right) ds + X_t \int \left(\frac{M_t^2}{EI}\right) ds + X_v \int \left(\frac{T_v T_t}{GJ}\right) ds + \\
&\quad X_m \int \left(\frac{T_m T_t}{GJ}\right) ds + X_t \int \left(\frac{T_t^2}{GJ}\right) ds + \int \left(\frac{M_0 M_t}{EI}\right) ds + \int \left(\frac{T_0 T_t}{GJ}\right) ds
\end{aligned}\right\} \quad (3b)$$

If the terms due to shear strain had been retained, there would be four more terms in each of Eqs. (3b), which makes one additional term in each of Eqs. (4). However, all except those of A_{11} and D_1 contain either V_m or V_t and so are zero (see Eqs. (7)). The additional term for A_{11} is

$$\int (kV_v^2/AG)\, ds = \int (k/AG)\, ds$$

and for D_1 is

$$\int (kV_0 V_v/AG)\, ds = \int (kV_0/AG)\, ds$$

as may be easily verified.

For convenience let

$$\left.\begin{aligned}
A_{11} &= \int (M_v^2/EI)\, ds + \int (T_v^2/GJ)\, ds \\
A_{12} &= \int (M_m M_v/EI)\, ds + \int (T_m T_v/GJ)\, ds = A_{21} \\
A_{13} &= \int (M_t M_v/EI)\, ds + \int (T_t T_v/GJ)\, ds = A_{31} \\
A_{22} &= \int (M_m^2/EI)\, ds + \int (T_m^2/GJ)\, ds \\
A_{23} &= \int (M_t M_m/EI)\, ds + \int (T_t T_m/GJ)\, ds = A_{32} \\
A_{33} &= \int (M_t^2/EI)\, ds + \int (T_t^2/GJ)\, ds \\
D_1 &= \int (M_0 M_v/EI)\, ds + \int (T_0 T_v/GJ)\, ds \\
D_2 &= \int (M_0 M_m/EI)\, ds + \int (T_0 T_m/GJ)\, ds \\
D_3 &= \int (M_0 M_t/EI)\, ds + \int (T_0 T_t/GJ)\, ds
\end{aligned}\right\} \quad (4)$$

Then, using the notation of Eqs. (4), Eqs. (3) become

$$\left.\begin{aligned} A_{11}X_v + A_{12}X_m + A_{13}X_t &= -D_1 \\ A_{21}X_v + A_{22}X_m + A_{23}X_t &= -D_2 \\ A_{31}X_v + A_{32}X_m + A_{33}X_t &= -D_3 \end{aligned}\right\} \quad (5)$$

Solution of Equations

Solution of Eqs. (5) for X_v, X_m, and X_t may be written in the determinant form as below where

$$\left.\begin{aligned} |A| &= \begin{vmatrix} A_{11} & A_{12} & A_{13} \\ A_{21} & A_{22} & A_{23} \\ A_{31} & A_{32} & A_{33} \end{vmatrix} \\ X_v &= \frac{\begin{vmatrix} D_1 & A_{12} & A_{13} \\ D_2 & A_{22} & A_{23} \\ D_3 & A_{32} & A_{33} \end{vmatrix}}{|A|} \\ X_m &= \frac{\begin{vmatrix} A_{11} & D_1 & A_{13} \\ A_{21} & D_2 & A_{23} \\ A_{31} & D_3 & A_{33} \end{vmatrix}}{|A|} \\ X_t &= \frac{\begin{vmatrix} A_{11} & A_{12} & D_1 \\ A_{21} & A_{22} & D_2 \\ A_{31} & A_{32} & D_3 \end{vmatrix}}{|A|} \end{aligned}\right\} \quad (6)$$

Axes and Sign Convention

Although the solution as given by Eqs. (6) does not require axes, the following convention will be used for solving problems (see Fig. 1): a positive coordinate, s, clockwise along the ring centroidal axis from the cut, fixing the positive tangent, a positive normal directed inward, x and y axis along the tangent and normal at the cut, and a positive clockwise angle α included between positive x and plus tangent.

Positive bending and torsional moments are those applied by material or forces on the negative side to the positive material, when these moments are represented by vectors in the plus directions of tangent and normal. Positive lateral loads are directed upward from plane of paper and positive shear is that produced by positive lateral loads acting on the negative material.

Now having established a coordinate system the internal forces at any section due to the unknowns at the cut are given by Eqs. (7).

$$\left.\begin{aligned} M_m &= \cos\alpha & T_m &= \sin\alpha \\ M_t &= -\sin\alpha & T_t &= \cos\alpha \\ M_v &= -x\cos\alpha - y\sin\alpha \\ T_v &= -x\sin\alpha + y\cos\alpha \\ V_v &= 1 & V_m &= V_t = 0 \end{aligned}\right\} \quad (7)$$

Ring Symmetric About One Axis

If the ring is symmetric about an axis in its plane, the calculations are simplified by taking this as the y axis as in Fig. 2. Then it is seen that terms involving $\sin\alpha$ change from + to − at $\alpha = \pi$ (i.e., at the lower centerline) and being integrated over equal positive and negative ranges give zero. The same applies to terms involving x but not, of course, to those having a product $x\sin\alpha$. The same results are obtained by considering the right and left halves of the ring separately and adding the integrals for both halves, with due regard to sign.

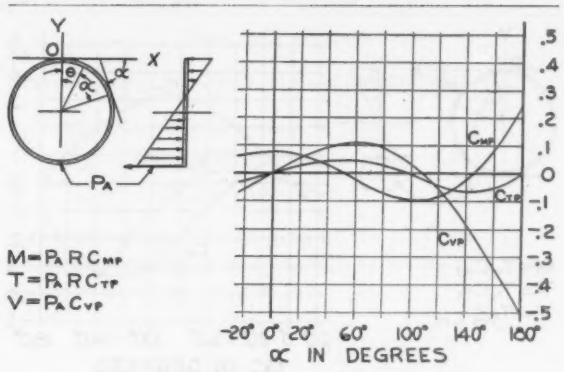

FIG. 2. Ring loaded by normal force P_A.

Denoting the right and left halves by the subscripts r and l,

$$\left.\begin{aligned} M_{ml} &= M_{mr} & T_{tl} &= T_{tr} \\ T_{ml} &= -T_{mr} & M_{vl} &= -M_{vr} \\ M_{tl} &= -M_{tr} & T_{vl} &= T_{vr} \end{aligned}\right\} \quad (8)$$

Noting the parameters affected

$$\left.\begin{aligned} A_{12} &= 0 & A_{13} &= 2A_{13r} \\ A_{22} &= 2A_{22r} & A_{23} &= 0 \\ A_{33} &= 2A_{33r} \end{aligned}\right\} \quad (8a)$$

Then Eqs. (5) become

$$\left.\begin{aligned} A_{11}X_v + A_{13}X_t &= -D_1 \\ A_{22}X_m &= -D_2 \\ A_{31}X_v + A_{33}X_t &= -D_3 \end{aligned}\right\} \quad (9)$$

And the solutions are

$$\left.\begin{aligned} X_v &= (A_{33}D_1 - A_{13}D_3)/(A_{13}^2 - A_{11}A_{13}) \\ X_m &= -D_2/A_{22} \\ X_t &= (A_{11}D_3 - A_{13}D_1)/(A_{13}^2 - A_{11}A_{13}) \end{aligned}\right\} \quad (10)$$

Ring and Load Symmetric About One Axis

As before, let the axis of symmetry be the y axis. Then, in addition to Eqs. (8a) concerning only the ring, the following equations regarding the load will hold:

$$\left.\begin{aligned} M_{0l} &= M_{0r} & T_{0l} &= -T_{0r} \\ D_1 &= 0 & D_2 &= 2D_{2r} & D_3 &= 0 \end{aligned}\right\} \quad (11)$$

so from Eqs. (9) $X_v = X_t = 0$ and

$$X_m = -D_2/A_{22} \quad (11a)$$

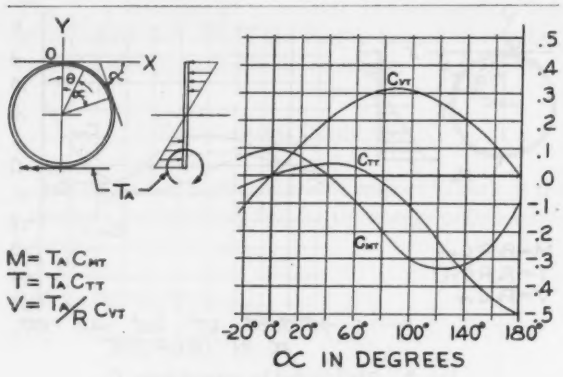

FIG. 3. Ring loaded by torque T_A.

APPLICATIONS TO PROBLEMS

V_0, M_0, and T_0 due to point forces and moments are readily calculated, but distributed loads can be expressed analytically for only the simplest cases; consequently, their contributions must be evaluated numerically. If W is a distributed load intensity, the moments M_x and M_y, parallel to the x and y axes, which it imposes at point $s_1 = (x_1, y_1)$ are:

$$M_{x_1} = \int_0^{s_1} W(y_1 - y)\, ds \qquad M_{y_1} = \int_0^{s_1} W(x - x_1)\, ds \quad (12)$$

M_x and M_y due to point forces and moments must be added to expressions above.

Then

$$\left.\begin{aligned} M_0 &= M_y \cos\alpha - M_x \sin\alpha \\ T_0 &= M_y \sin\alpha + M_x \cos\alpha \end{aligned}\right\} \quad (12a)$$

Having M_0, T_0, and V_0, the necessary parameters of Eqs. (4) are evaluated, and substitution in Eq. (6) (or Eq. (10) if there is an axis of symmetry) gives the forces at the cut. Then the forces in the complete ring are obtained by superposing those at the cut by means of Eqs. (2) and (7). In general, M_x, M_y, and the integrals of Eqs. (4) will have to be evaluated by numerical methods, but this should present no particular difficulty.

CONCLUSION

The general Eqs. (6) give the internal forces for a ring of any arbitrary plan form and loading. In most cases the ring will be symmetric about an axis so that the simpler Eqs. (10) can be used. If the load is also symmetric about the same axis, the shear and torque are zero at the cut and the bending moment is determined by Eqs. (11a). Except for simple ring shapes and loading, M_0, T_0, V_0, and the parameters of Eqs. (4) will have to be evaluated by numerical methods, but tabular forms can be arranged for the calculations and no particular difficulty should be encountered. If Eqs. (10) are applicable, nine parameters of Eqs. (4) are required, while only two parameters are necessary if Eqs. (11) can be used.

Eqs. (V) of the Appendix give the forces in a circular ring for a point force, moment, or torque with the reaction distributed as the stress in a cylindric shell. Any arbitrary system of concentrated loads may be built up by superposing the internal forces due to each load. As pointed out before, the distributed reactions cancel if the applied loads are in equilibrium. Thus, in combination with reference 2 for loads in the plane, a convenient method of analysis is provided for engine mount rings, monocoque frames, and similar structural members. Eqs. (V) have been plotted in Figs. 2, 3, and 4.

APPENDIX—EXAMPLES

A circular ring of uniform cross section is loaded by a single point force, moment, or torque. The reaction is normal to the ring plane and distributed to the periphery with linear variation along a diameter—i.e., the classic stress distribution in a cylindric shell subject to the applied loads. If a balanced set of loads is applied, the distributed reaction disappears, there being no resultant stress in the supporting shell. The reaction provided by an actual cylinder will depart from that assumed by an amount depending on the relative stiffness of ring and cylinder. However, if the ring is not attached to a shell, the reaction is only a convenient reference so ring deflections do not affect the result.

The problem of a circular ring is especially simple and useful in that the location of the load point depends only on an arbitrary reference; thus, a single set of formulas or charts can be used to build up any conceivable loading by superposition of a number of simple loads. These examples were suggested by G. G. Green* and both he and C. D. Mills† have calculated the formulas given in this Appendix without reference to the general equations.

In the calculations that follow the imaginary cut is at $\theta = 0$, and the applied load is at $\theta = \pi$. To avoid the

* Chief Structures Engineer, C.V.A.C., San Diego Division.
† Stress Analyst, C.V.A.C., San Diego Division.

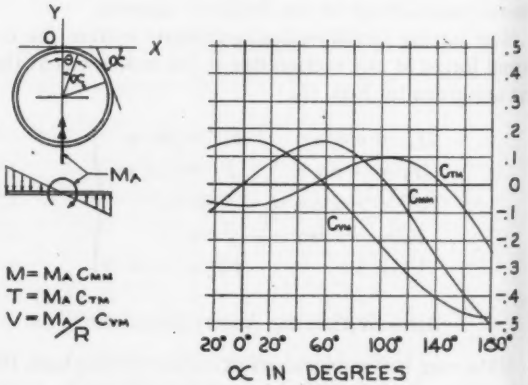

FIG. 4. Ring loaded by moment M_A.

discontinuity at $\theta = \pi$, the parameters of Eqs. (10) are evaluated from $-\pi$ to $+\pi$. Eqs. (V)—the formulas for bending moment, torque, and shear—are plotted as coefficients in Figs. 2, 3, and 4. It should be noted that the internal forces for an applied torque have been plotted for a round tube assuming $E = 2.6G$ so that the factor $(3EI - GJ)/(EI + GJ) = 1.262$.

1—Circular Ring and Single Load P_A (Fig. 2)

$$W = (-P_A/\pi R)(1/2 - \cos\theta)$$

M_0, T_0, and V_0 at a point determined by α are $M_{0\alpha}$, $T_{0\alpha}$, and $V_{0\alpha}$ as below.

$$\left.\begin{aligned} M_{0\alpha} &= -\int_0^\alpha WR^2 \sin(\alpha - \theta)\, d\theta \\ T_{0\alpha} &= -\int_0^\alpha WR^2[1 - \cos(\alpha - \theta)]\, d\theta \\ V_{0\alpha} &= \int_0^\alpha WR\, d\theta \end{aligned}\right\} \quad \text{(I)}$$

Substituting W and integrating

$$\left.\begin{aligned} M_{0\alpha} &= (P_AR/2\pi)(1 - \cos\alpha - \alpha\sin\alpha) \\ T_{0\alpha} &= (P_AR/2\pi)(\alpha - 2\sin\alpha + \alpha\cos\alpha) \\ V_{0\alpha} &= (P_A/2\pi)(2\sin\alpha - \alpha) \end{aligned}\right\} \quad \text{(Ia)}$$

Evaluation of parameters

$$D_2 = 2D_{2r} = 2\int_0^\pi \frac{M_0M_m}{EI}\,ds + 2\int_0^\pi \frac{T_0T_m}{GJ}\,ds$$

$$D_2 = (-P_AR^2/4)[(1/EI) + (1/GJ)]$$

$$A_{22} = 2A_{22r} = 2\int_0^\pi \frac{M_m^2}{EI}\,ds + 2\int_0^\pi \frac{T_m^2}{GJ}\,ds$$

$$A_{22} = \pi R[(1/EI) + (1/GJ)]$$

$$X_m = -D_2/A_{22} = P_AR/4 \quad \text{(II)}$$

As noted before $X_v = X_t = 0$

Now having the forces at the cut the forces at any point are readily obtained from statics (see Eqs. (2)).

2—Circular Ring and Single Torque T_A (Fig. 3.)

$$W = T_A/\pi R^2 \cos\theta$$

Substituting W in Eqs. (I) and integrating

$$\left.\begin{aligned} M_{0\alpha} &= (-T_A/2\pi)\,\alpha\sin\alpha \\ T_{0\alpha} &= (-T_A/2\pi)(\sin\alpha - \alpha\cos\alpha) \\ V_{0\alpha} &= (T_A/\pi R)\sin\alpha \end{aligned}\right\} \quad \text{(Ib)}$$

$$D_2 = 2D_{2r} = 2\int_0^\pi \frac{M_0M_m}{EI}\,ds + 2\int_0^\pi \frac{T_0T_m}{GJ}\,ds$$

$$D_2 = (T_AR/4)[(1/EI) - (3/GJ)]$$

NOTE: A_{22} is the same as for Example 1.

$$X_m = \frac{-D_2}{A_{22}} = \frac{-T_A}{4\pi}\left[\frac{GJ - 3EI}{GJ + EI}\right] \quad \text{(III)}$$

3—Circular Ring and Single Moment M_A (Fig. 4)

$$W = (M_A/\pi R^2)\sin\theta$$

Substituting W in Eqs. (I) and integrating

$$\left.\begin{aligned} M_{0\alpha} &= (-M_A/2\pi)(\sin\alpha - \alpha\cos\alpha) \\ T_{0\alpha} &= (M_A/2\pi)(2\cos\alpha + \alpha\sin\alpha - 2) \\ V_{0\alpha} &= (-M_A/\pi R)(\cos\alpha - 1) \end{aligned}\right\} \quad \text{(Ic)}$$

Because of the discontinuity at the load point ($\alpha = \pi$) consider the right and left halves of the ring separately.

$$M_{0l} = -M_{0r} \qquad T_{0l} = T_{0r}$$
$$M_{ml} = M_{mr} \qquad T_{ml} = -T_{mr}$$

$$D_2 = \int_{-\pi}^{\pi}\left(\frac{M_0M_m}{EI}\right)ds + \int_{-\pi}^{\pi}\left(\frac{T_0T_m}{GJ}\right)ds = 0$$

so by Eq. (11a) $X_m = 0$

$$M_{vl} = -M_{vr} = R\sin\alpha$$
$$T_{vl} = T_{vr} = R(\cos\alpha - 1)$$

Now evaluating D_1 and D_3,

$$D_1 = 2D_{1r} = 2\int_0^\pi \left(\frac{M_0M_v}{EI}\right)ds + 2\int_0^\pi \left(\frac{T_0T_v}{GJ}\right)ds$$

$$D_1 = (M_AR^2/4)[(3/EI) + (7/GJ)]$$

$$D_3 = 2D_{3r} = 2\int_0^\pi \left(\frac{M_0M_t}{EI}\right)ds + 2\int_0^\pi \left(\frac{T_0T_t}{GJ}\right)ds$$

$$D_3 = (M_A3R/4)[(1/EI) + (1/GJ)]$$

Evaluating A_{11}, A_{13}, and A_{33},

$$A_{11} = 2A_{11r} = 2\int_0^\pi \left(\frac{M_v^2}{EI}\right)ds + 2\int_0^\pi \left(\frac{T_v^2}{GJ}\right)ds$$

$$A_{11} = \pi R^3[(1/EI) + (3/GJ)]$$

$$A_{13} = 2A_{13r} = 2\int_0^\pi \left(\frac{M_tM_v}{EI}\right)ds + 2\int_0^\pi \left(\frac{T_tT_v}{GJ}\right)ds$$

$$A_{13} = \pi R^2[(1/EI) + (1/GJ)]$$

$$A_{33} = 2A_{33r} = 2\int_0^\pi \left(\frac{M_t^2}{EI}\right)ds + 2\int_0^\pi \left(\frac{T_t^2}{GJ}\right)ds$$

$$A_{33} = \pi R[(1/EI) + (1/GJ)]$$

Substituting the parameters in Eqs. (10),

$$X_v = \frac{A_{33}D_1 - A_{13}D_3}{A_{13}^2 - A_{11}A_{33}} = \frac{-M_A}{2\pi R}$$

$$X_t = \frac{A_{11}D_3 - A_{13}D_1}{A_{13}^2 - A_{11}A_{33}} = \frac{-M_A}{4\pi}$$

Adding the forces due to the unknowns to those in the statically determinate ring and combining the results of all three examples give Eqs. (V) below for the total forces in the ring. These equations are valid from $-\pi < \alpha < \pi$

$$
\left.\begin{aligned}
M &= \frac{P_A R}{4\pi}(2 - \cos\alpha - 2\alpha\sin\alpha) + \\
&\quad \frac{T_A}{4\pi}\left[\left(\frac{3EI - GJ}{EI + GJ}\right)\cos\alpha - 2\alpha\sin\alpha\right] + \\
&\quad \frac{M_A}{4\pi}(\sin\alpha + 2\alpha\cos\alpha) \\
T &= \frac{P_A R}{4\pi}(2\alpha - 3\sin\alpha + 2\alpha\cos\alpha) + \frac{T_A}{4\pi}\times \\
&\left[\left(\frac{3EI - GJ}{EI + GJ}\right)\sin\alpha - 2\sin\alpha + 2\alpha\cos\alpha\right] + \\
&\quad \frac{M_A}{4\pi}(\cos\alpha + 2\alpha\sin\alpha - 2) \\
V &= \frac{P_A}{2\pi}(2\sin\alpha - \alpha) + \\
&\quad \frac{T_A}{\pi R}\sin\alpha - \frac{M_A}{2\pi R}(2\cos\alpha - 1)
\end{aligned}\right\} \quad (V)
$$

The formulas above have been plotted in Figs. 2, 3, and 4. It should be noted that Fig. 3 applies only to round tube sections.

References

[1] Lundquist, Eugene E., and Burke, Walter F., *General Equations for the Stress Analysis of Rings*, N.A.C.A. T.R. No. 509, 1934.

[2] Wise, Joseph A., *Analysis of Circular Rings for Monocoque Fuselages*, Journal of the Aeronautical Sciences, Vol. 6, No. 11, pp. 460–463, September, 1939.

Letter to the Editor

Dear Sir:

Professor Eryk Kosko, in his paper on "A Simplified Analysis of Hollow Beams with Longitudinal Webs Subjected to Torsional Loads" (JOURNAL OF THE AERONAUTICAL SCIENCES, Vol. 12, No. 1, page 103, January, 1945), has shown how the number of equations that must be solved simultaneously in such analyses can be decreased. His method appears to be technically sound though there may be some question as to the actual amount of laborsaving it provides. In his paper, however, he makes certain statements that must be challenged.

Throughout the paper he contends that the "standard" method involves the simultaneous solution of $n + 1$ equations, where n is the number of cells into which the shell may be subdivided. He obtains this result by adding to the equation of equilibrium an expression for the angle of twist per unit length in terms of the properties of each cell. In practice, the deformation equations that enter the simultaneous solution are made up by equating these expressions for angle of twist, $n - 1$ independent equations being obtained in that manner. Thus the true number of equations to be solved simultaneously is n, not $n + 1$. After these equations have been solved a separate computation is made for the angle of twist, if that is desired, in much the same manner as that employed in the paper. Therefore, the standard method does not call for the use of $n + 1$ equations any more than that of the paper calls for n.

The author is also in error in his statement that "a simple tube under torsional load can be considered as a statically determinate structure." It is not statically determinate and cannot be treated as one if correct results are desired. Furthermore, the author, in spite of his statement, does not so treat it. What the author does is to use for his included or base structure a statically indeterminate structure for which the stresses and deformations can be easily computed. As a general procedure, this device is not new. It was described as early as 1926[1] and was probably not new even then. The specific application to shells is probably new. The practice of claiming that a structure is statically determinate simply because a simple procedure can be devised for its analysis is entirely too common, and its occurrence should arouse protest.

The writer's third criticism of the paper is that the author refers to the Maxwell-Mohr method of writing equations of continuity as if it were a less respectable substitute for a more fundamental method of minimum strain energy or "least work." This is putting the cart before the horse. Castigliano developed the method of least work by showing that the deflections required in the continuity equations could be obtained by differentiation of the strain energy of the loaded structure[2] and that, if the net deflections of the points of application of the redundants were all zero, then the strain energy of the structure would be the minimum consistent with equilibrium. The Maxwell-Mohr method is therefore the more fundamental, as well as the more widely applicable, of the two, and there is no reason for apologizing for its use. Furthermore, it has the advantage that the computer can more easily visualize the physical relations expressed by his equations.

References

[1] Parcel, J. I., and Maney, G. A., *Statically Indeterminate Stresses*, p. 149; John Wiley and Sons, Inc., New York, 1926.

[2] Andrews, E. S., *Elastic Stresses in Structures*; Scott, Greenwood and Son, London, 1919.

ALFRED S. NILES
Professor, Aeronautical Engineering
Stanford University

The Thermodynamics of the Laminar Boundary Layer of a Heated Body in a High-Speed Gas Flow Field

ARTHUR N. TIFFORD*

Lockheed Aircraft Corporation

SUMMARY

The thermal boundary-layer equations for a two-dimensional shockless gas flow are treated in a manner similar to Falkner and Skan's general solution of the velocity boundary-layer equations. When the local velocity outside the boundary layer increases as a power of the distance along the surface, a particularly simple solution for the temperature field exists. A rather general differential equation defining the effect of the generation of heat by friction and shockless compressibility in the boundary-layer results. Some numerical integrations of this equation are presented, and it is found that the effect of the internal heat generation on the rate of heat transfer depends on the pressure gradient along the surface, as well as on the Prandtl Number of the gas when the latter differs from unity. In the absence of this internal heat generation, the difference between the gas stagnation temperature and the surface temperature is shown to be the temperature difference causing the flow of heat. The effect of the internal heat is only that of a correction factor on the stagnation temperature as the effective gas temperature. When the Prandtl Number of the gas is unity, no correction is required.

An exact solution for the heat transfer from a body of arbitrary shape, obtainable through Taylor series expansions along the surface, is outlined. The tables required for its general application remain to be computed from the derived linear differential equations. Until these tables are completed, a first approximation may be based on solutions for velocity fields of the type: $u_1 = cx^m$. It is shown that these solutions indicate an analogy exists between the *momentum loss* in the boundary layer and the rate of heat transfer despite the presence of a pressure gradient. This finding is at variance with the common belief that skin friction and heat transfer are analogous quantities. The latter is true only in the absence of a pressure gradient. The analogy is applied to the calculation of the variation of the local heat transfer coefficient over the front half of a circular cylinder, and good agreement with experimental data is shown.

INTRODUCTION

THIS PAPER is the second† of a series being prepared by the author investigating the flow of heat through laminar boundary layers in incompressible and compressible fluids. The results of these investigations should prove useful in many diverse applications. A few that come to mind immediately are the deicing of aircraft; the performance of hot wires and thermocouples; and the aerodynamic heating of aircraft surfaces. The latter will become more and more important as the speed of air travel increases and is already today a serious problem in high-speed wind tunnels.

Earlier work on the thermal behavior of laminar boundary layers has had to do, for the most part, with the performance of a flat plate as a thermometer, as well as a heat transfer surface when aligned with the free stream. The original paper[2] on the subject was written by Pohlhausen in 1921. His assumptions of constant fluid properties have been refined and the results extended in later papers by Busemann,[3] von Kármán and Tsien,[4] Emmons and Brainerd,[5,6] and Eckert and Drewitz.[7] Eckert and Drewitz have also recently published[8] the solution for the heat transfer from a wedge to an incompressible fluid. This solution has been expanded upon and the effect of the frictional generation of heat in the boundary layer has been analyzed in the first paper[1] of this series. In the present paper, the effect of the compressibility of gases is included in a general treatment of the rate of heat transfer through a laminar boundary layer subject to a pressure gradient.

SYMBOLS

c, c_1, c_2,	=	constants
c_p	=	specific heat of gas at constant pressure, B.t.u. per lb. per °F.
D	=	diameter of circular cylinder, ft.
f	=	$q/(u_1 x v)^{1/2}$
$\bar{f}$	=	$\sqrt{[(m+1)/2]}\, f$
g	=	acceleration of gravity, ft. per sec.^{2}
h	=	heat transfer coefficient, °F., B.t.u. per sec. per sq.ft. per °F.
h_e	=	heat transfer coefficient based on effective temperature difference, B.t.u. per sec. per sq.ft per °F.
i	=	constant
J	=	mechanical equivalent of heat, 778 ft.lbs. per B.t.u.
k	=	thermal conductivity of gas (usually at surface), B.t.u. per sec. per sq.ft. per °F./ft.
m	=	exponent
M	=	$\rho u_1^2 \delta^{**}$, momentum loss in boundary layer, lbs. per ft.
p	=	static pressure, lbs. per sq.ft.
p_1	=	local static pressure, lbs. per sq.ft.
q	=	stream function of flow in the boundary layer
T	=	gas temperature, °F.
T_1	=	local temperature of gas in free stream, °F.
T_s	=	stagnation temperature of gas, °F.
T_w	=	constant temperature of surface, °F.

Presented at the Summer Annual Meeting, I.A.S., Los Angeles, July 27–28, 1944.

* Engineer.

† The first paper[1] was presented at the A.S.M.E. Aviation Meeting in Los Angeles on June 5, 1944.

u = gas velocity along surface, ft. per sec.
u_1 = local gas velocity outside the boundary layer, ft. per sec.
v = gas velocity perpendicular to surface, ft. per sec.
x = distance along surface measured from stagnation point, ft.
X = function of ξ
y = distance perpendicular to surface, ft.
Y = function of η
exp. = exponential function
α = constant
β = $2m/(m + 1)$, pressure gradient parameter
δ^* = $\int_0^\infty [1 - (u/u_1)]dy$, displacement thickness of boundary layer, ft.
δ^{**} = $\int_0^\infty (u/u_1)[1 - (u/u_1)]dy$, momentum thickness of boundary layer, ft.
η = $(u_1/x\nu)^{1/2}y$, nondimensional boundary layer coordinate
$\bar{\eta}$ = $\sqrt{[(m + 1)/2]}\,\eta$, generalized nondimensional boundary layer coordinate
θ = $(T - T_w)/(T_1 - T_w)$, temperature field function
μ = absolute viscosity of gas (usually at surface), slugs per sec.-ft.
ν = kinematic viscosity of gas (usually at surface), sq.ft. per sec.
ξ = $(T_1 - T_w)/(u_1^2/gc_pJ)$, parameter providing measure of temperature equivalent of local kinetic energy of gas just outside boundary layer
ρ = density of gas (usually at surface), slugs per cu.ft.
ρ_1 = local density of gas in free stream, slugs per cu.ft.
σ = $gc_p\mu/k$, Prandtl Number of gas
τ_0 = $\mu(\partial u/\partial y)_{y=0}$, surface shearing stress, lbs. per sq.ft.
ϕ = nondimensional temperature field function
χ = $(x/u_1)(du_1/dx)$
χ_0' = $(d\chi/dx)_{x=0}$
ψ = nondimensional temperature field function
$\bar{\psi}$ = $\psi + 1/2$

Analysis

The general differential equations governing the motion and energy exchange of a compressible fluid include terms describing the effect on the structure of the velocity and temperature boundary layers of the expansion and compression of the fluid in the boundary layers. At low speeds these terms may naturally be neglected. At the higher speeds of modern flight, however, the justification for their neglect is not at all obvious. Fortunately, information is available from which general conclusions concerning their significance may be drawn.

Three effects are produced by the compression and expansion of the fluid in the two boundary layers: (1) a viscous stress resisting the change in volume of the fluid, (2) a change in the fluid's temperature or enthalpy, and (3) a change in the magnitude of the fluid's physical properties, particularly its density. The first effect, the viscous stress, is negligible as compared with the other stresses occurring in the boundary layer. The second, the change in enthalpy of the fluid, is of the same order of magnitude as the frictional generation of heat in the boundary layer and must therefore be considered when, as in this paper, the frictional heat is regarded as significant. With regard to the third effect, the change in magnitude of the fluid's properties, Eckert and Drewitz[7] have shown that, in the case of a compressible fluid flowing along a flat plate, the surface shearing stress and the rate of heat transfer derived neglecting the change of fluid properties in the boundary layer (i.e., assuming the fluid properties at the surface exist throughout the boundary layer), agrees within 3 per cent with their values derived with these changes considered, when the Mach Number of the flow is less than 2 and the Prandtl Number of the fluid is not very different from 1. It may be expected that similarly, in the general case of flow over a surface of arbitrary shape, the effect of the variation of the physical properties of the fluid in the thermal and velocity boundary layers is negligible (except in the neighborhood of a shock wave) if the *local* Mach Number of the external flow is somewhat below 2 and if the fluid's Prandtl Number is close to 1. Since the Prandtl Numbers of most gases are between 0.6 and 2, this conclusion is generally applicable to gas flows.

In view of the foregoing analysis, the general boundary layer equations for a steady-state two-dimensional gas flow at local Mach Numbers below about 2 reduce to Eqs. (1), (2), and (3) when terms of relatively small order of magnitude are neglected.

The equation of continuity:

$$(\partial u/\partial x) + (\partial v/\partial y) = 0 \tag{1}$$

The Navier-Stokes equations of motion:

$$u\left(\frac{\partial u}{\partial x}\right) + v\left(\frac{\partial u}{\partial y}\right) = -\left(\frac{1}{\rho}\right)\left(\frac{\partial p}{\partial x}\right) + \nu\,\frac{\partial^2 u}{\partial y^2} \tag{2}$$

$$0 = \partial p/\partial y \tag{2a}$$

The equation of energy:

$$gc_pJ\left[u\left(\frac{\partial T}{\partial x}\right) + v\left(\frac{\partial T}{\partial y}\right)\right] = Jk\left(\frac{\partial^2 T}{\partial y^2}\right) + \mu\left(\frac{\partial u}{\partial y}\right)^2 + u\left(\frac{\partial p}{\partial x}\right) \tag{3}$$

Since, as Eq. (2a) indicates, the pressure gradient across the boundary layer is generally negligible, the pressure gradient along the surface, $\partial p/\partial x$, is the same in the boundary layer as at its outer edge. Applying Bernoulli's equation, $\int(dp/\rho) + (u^2/2) = \text{constant}$, there, the pressure gradient along the surface is obtained as Eq. (4):

$$\partial p/\partial x = dp_1/dx = -\rho u_1(du_1/dx) \tag{4}$$

Falkner and Skan[9] have shown that Eqs. (1), (2), and (4) can be combined and expressed without loss of generality by Eq. (5):

$$x\left[\left(\frac{\partial f}{\partial \eta}\right)\left(\frac{\partial^2 f}{\partial \eta\,\partial x}\right) - \left(\frac{\partial^2 f}{\partial \eta^2}\right)\left(\frac{\partial f}{\partial x}\right)\right] + \chi\left(\frac{\partial f}{\partial \eta}\right)^2 - \left(\frac{\chi + 1}{2}\right) f\left(\frac{\partial^2 f}{\partial \eta^2}\right) - \frac{\partial^3 f}{\partial \eta^3} - \chi = 0 \tag{5}$$

with the boundary conditions: $\eta = 0, f = \partial f/\partial\eta = 0$ and $\eta \to \infty$, $\partial f/\partial\eta = 1$, by changing the variables as follows:

$$\begin{aligned} \chi &= (x/u_1)(du_1/dx) \\ \eta &= (u_1/xv)^{1/2}y \\ f &= q/(u_1xv)^{1/2} \\ u &= \partial q/\partial y = u_1(\partial f/\partial\eta) \\ v &= -\partial q/\partial x \end{aligned}$$

In a somewhat similar manner the equation of energy, Eq. (3), may be combined with Eqs. (1) and (4) and, through a transformation of variables, expressed as Eq. (6):

$$-\chi\left(\frac{\partial f}{\partial\eta}\right)\theta - \chi\xi(1+2\xi)\left(\frac{\partial f}{\partial\eta}\right)\left(\frac{\partial\theta}{\partial\xi}\right) + \chi\xi(1+2\xi)\times \left(\frac{\partial f}{\partial\xi}\right)\left(\frac{\partial\theta}{\partial\eta}\right) - \left(\frac{\chi+1}{2}\right)\xi f\left(\frac{\partial\theta}{\partial\eta}\right) - \left(\frac{\xi}{\sigma}\right)\left(\frac{\partial^2\theta}{\partial\eta^2}\right) = \left(\frac{\partial^2 f}{\partial\eta^2}\right)^2 - \chi\left(\frac{\partial f}{\partial\eta}\right) \quad (6)$$

with the boundary conditions: $\eta = 0, \theta = f = 0$ and $\eta \to \infty$, $\theta = 1$, where the new variables are:

$$\begin{aligned} \theta &= (T - T_w)/(T_1 - T_w) \\ \xi &= (T_1 - T_w)/(u_1^2/gc_pJ) \\ \sigma &= gc_p\mu/k \end{aligned}$$

Eq. (6) states that the shape of the temperature field in the boundary layer—i.e., the functional relation between θ and η, ξ—depends, in general, on the Prandtl Number of the gas, σ; on the temperature rise equivalent of the local kinetic energy of the gas just outside the boundary layer, $1/\xi$; on the local pressure gradient, χ; and on the shape of the velocity field in the boundary layer, f, $\partial f/\partial\xi$, $\partial f/\partial\eta$, and $\partial^2 f/\partial\eta^2$.

The Velocity and Temperature Fields in the Boundary Layer When $u_1 = cx^m$

It is known from potential flow theory that the local velocity outside the boundary layer increases as a power function of the distance from the leading edge when an incompressible fluid flows over a wedge. It is also known that, no matter what the shape of the body, the local velocity near the leading edge may always be expressed as $u_1 = cx^m$, where m is a constant determined by the central angle of the wedge formed by tangent planes on either side of the leading edge—i.e., m = central angle/2π − central angle. Similarly, in a compressible fluid flow, a "power law" variation of local velocity will be found along the surface of a body related to the wedge through the "apparent thickening effects" of compressibility (see Fig. 1) and will also be found close to the leading edge of any body, since the flow behaves there as essentially incompressible. This power law variation of local velocity is of especial interest because it leads to relatively simple particular solutions of the velocity and thermal boundary-layer equations.

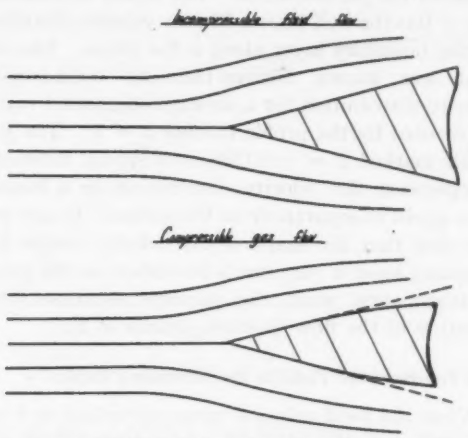

Fig. 1. Flow fields in which local velocity varies according to power law: $u_1 = cx^m$.

The Velocity Field in the Boundary Layer

When the local velocity varies according to a power law, the parameter, χ, reduces to the constant exponent, m. As Falkner and Skan[9] have already shown for incompressible fluids, the shape of the velocity field in the boundary layer is then the same at all points of the surface (for which $u_1 = cx^m$) and is determined solely by m. The general velocity boundary-layer equation, Eq. (5), simplifies for this case to Eq. (7), which has been carefully integrated with the aid of a differential analyzer by Hartree.[10]

$$(d^3\bar{f}/d\bar{\eta}^3) + \bar{f}\,(d^2\bar{f}/d\bar{\eta}^2) = \beta[(d\bar{f}/d\bar{\eta})^2 - 1] \quad (7)$$

with the boundary conditions: $\bar{\eta} = 0, \bar{f} = d\bar{f}/d\bar{\eta} = 0$ and $\bar{\eta} \to \infty$, $d\bar{f}/d\bar{\eta} = 1$, where

$$\begin{aligned} \beta &= 2m/(m+1) \\ \bar{\eta} &= \sqrt{[(m+1)/2]}\,\eta = \sqrt{[(m+1)/2]}\,(u_1/xv)^{1/2}y \\ \bar{f} &= \sqrt{[(m+1)/2]}\,f \\ u &= u_1(d\bar{f}/d\bar{\eta}) \end{aligned}$$

Fig. 2 shows the derived velocity profiles for various

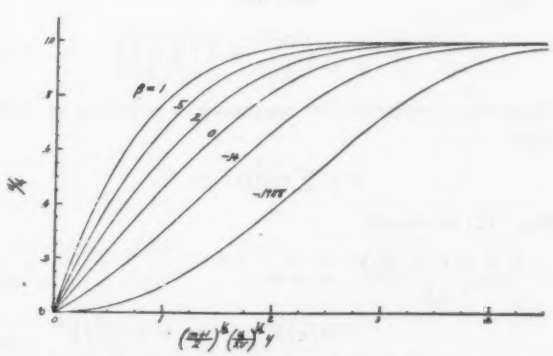

Fig. 2. Velocity profiles in the boundary layer.

values of the parameter, β. The profile corresponding to $\beta = 0$ is the well-known Blasius velocity distribution for the boundary layer along a flat plate. The somewhat less known Blasius-Heimenz boundary-layer velocity distribution for a forward stagnation region is represented by the profile labeled $\beta = 1$. The lowest profile marked $\beta = -0.1988$ is of special interest, for it represents the velocity distribution in a boundary layer about to separate from the surface. In any event, it is seen that the shape of the velocity profile in the boundary layer is very much dependent on the pressure gradient, even when the pressure decreases in the direction of the flow (positive values of β).

The Temperature Field in the Boundary Layer

When the local velocity varies according to a power law, the equation for the temperature field in the boundary layer, Eq. (6), is also simplified and may be expressed as Eq. (8), in which f is no longer a function of ξ.

$$-m\frac{df}{d\eta}\theta - m\xi(1+2\xi)\left(\frac{df}{d\eta}\right)\left(\frac{\partial\theta}{\partial\xi}\right) - \left(\frac{m+1}{2}\right)\xi f\left(\frac{\partial\theta}{\partial\eta}\right) - \left(\frac{\xi}{\sigma}\right)\left(\frac{\partial^2\theta}{\partial\eta^2}\right) = \left(\frac{d^2f}{d\eta^2}\right)^2 - m\left(\frac{df}{d\eta}\right) \quad (8)$$

By assuming a solution of the form

$$\theta = \phi(\eta, \xi) + \psi(\eta)/\xi \quad (9)$$

a partial separation of variables is effected.

$$-2m\left(\frac{df}{d\eta}\right)\psi + \left(\frac{m+1}{2}\right) f\left(\frac{d\psi}{d\eta}\right) + \left(\frac{1}{\sigma}\right)\left(\frac{d^2\psi}{d\eta^2}\right) + \left(\frac{d^2f}{d\eta^2}\right)^2 - m\left(\frac{df}{d\eta}\right) = i = -\left[m\left(\frac{df}{d\eta}\right)\phi + m\xi(1+2\xi) \times \left(\frac{df}{d\eta}\right)\left(\frac{\partial\phi}{\partial\xi}\right) + \left(\frac{m+1}{2}\right)\xi f\left(\frac{\partial\phi}{\partial\eta}\right) + \left(\frac{\xi}{\sigma}\right)\left(\frac{\partial^2\phi}{\partial\eta^2}\right)\right] \quad (10)$$

where i is a constant. The boundary conditions at the outer edge of the boundary layer require the constant, i, to be zero. Thus, the homogeneous equation, Eq. (11), is obtained for the function, ϕ.

$$m\left(\frac{df}{d\eta}\right)\phi + m\xi(1+2\xi)\left(\frac{df}{d\eta}\right)\left(\frac{\partial\phi}{\partial\xi}\right) + \left(\frac{m+1}{2}\right)\xi f\left(\frac{\partial\phi}{\partial\eta}\right) + \left(\frac{\xi}{\sigma}\right)\left(\frac{\partial^2\phi}{\partial\eta^2}\right) = 0 \quad (11)$$

Separating variables by assuming a solution of the type:

$$\phi = \sum cX(\xi)Y(\eta)$$

Eq. (12) is found.

$$-\frac{X + \xi(1+2\xi)X'}{\xi X} = \alpha = \frac{(1/\sigma)Y'' + [(m+1)/2]fY'}{mf'Y} \quad (12)$$

where the primes indicate total derivatives and α is a constant. From the left-hand side of this equation, the solution, $X = (1 + 2\xi^{1-(\alpha/2)})/\xi$ is readily established; while from the right-hand side, it is found that in order to satisfy the boundary conditions at the outer edge of the boundary layer—i.e., $Y''(\infty) = 0$ and $Y(\infty) \neq 0$ in general—the constant, α, must be zero. It follows that the X function is $(1 + 2\xi)/\xi$ or simply $2(T_s - T_w)/(T_1 - T_w)$. Therefore, not only the shape of the velocity field in the boundary layer but also the shape of the temperature field due to the ϕ term—the term neglecting the effect of the internal generation of heat—is the same for all points of the surface for which the local velocity varies according to a power law, $u_1 = cx^m$.

After transformation of the right-hand side of Eq. (12) to the $\bar{\eta}$ coordinate, the equation for the Y function becomes

$$(d^2Y/d\bar{\eta}^2) + \sigma\bar{f}(dY/d\bar{\eta}) = 0 \quad (13)$$

The general solution of Eq. (13) is

$$Y = c_1\int_0^{\bar{\eta}}\exp.\,(-\sigma\int_0^{\bar{\eta}}\bar{f}\,d\bar{\eta})d\bar{\eta} + c_2$$

and therefore the complete expression for ϕ is

$$\phi = \frac{T_s - T_w}{T_1 - T_w}[c_1\int_0^{\bar{\eta}}\exp.(-\sigma\int_0^{\bar{\eta}}\bar{f}\,d\bar{\eta})d\bar{\eta} + c_2]$$

The arbitrary constants, c_1 and c_2, may be evaluated by referring back to Eq. (9) and substituting the boundary conditions given with Eq. (6). Thus, at $\eta = 0$,

$$\theta = 0 = \left(\frac{T_s - T_w}{T_1 - T_w}\right)c_1\cdot 0 + c_2 + \frac{\psi(0)}{\xi}$$

Therefore the constant, c_2, is zero and one of the boundary conditions for the function, ψ, is: $\eta = 0$, $\psi = 0$. At $\eta \to \infty$,

$$\theta = 1 = \frac{T_s - T_w}{T_1 - T_w}[c_1\int_0^{\infty}\exp.\,(-\sigma\int_0^{\bar{\eta}}\bar{f}\,d\bar{\eta})d\bar{\eta}] + \frac{\psi(\infty)}{\xi}$$

It follows that

$$c_1 = 1/\int_0^{\infty}\exp.\,(-\sigma\int_0^{\bar{\eta}}\bar{f}\,d\bar{\eta})d\bar{\eta}$$

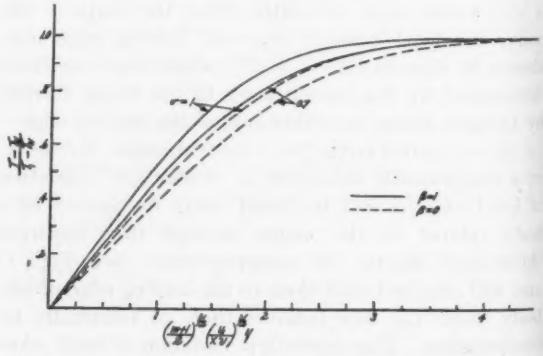

FIG. 3. Temperature profiles in the boundary layer.

and that another boundary condition for ψ is:

$$\eta \to \infty, \quad \psi = -1/2$$

The ϕ term now simplifies to

$$\phi = \frac{T_s - T_w}{T_1 - T_w}\left[\frac{\int_0^{\bar{\eta}} \exp.\ (-\sigma \int_0^{\bar{\eta}} \bar{f}\, d\bar{\eta})d\bar{\eta}}{\int_0^{\infty} \exp.\ (-\sigma \int_0^{\bar{\eta}} \bar{f}\, d\bar{\eta})d\bar{\eta}}\right] \tag{14}$$

The fraction in the bracket describes the shape of the temperature profile in the boundary layer when the generation of heat by friction and compressibility is negligible. Fig. 3 shows such profiles for Prandtl Numbers of 0.7 and 1 when $\beta = 0$, as on a flat plate, and when $\beta = 1$, as in a forward stagnation region. It is seen that the pressure gradient, represented by β, has the same relative effect on the temperature distribution in the boundary layer, independent of the Prandtl Number. In Fig. 4 is shown the effect of various pressure gradients when the Prandtl Number is 0.7. A comparison of these curves with the velocity profiles of Fig. 2 reveals that the effect of a pressure gradient on the temperature profile is much smaller than its effect on the velocity profile.

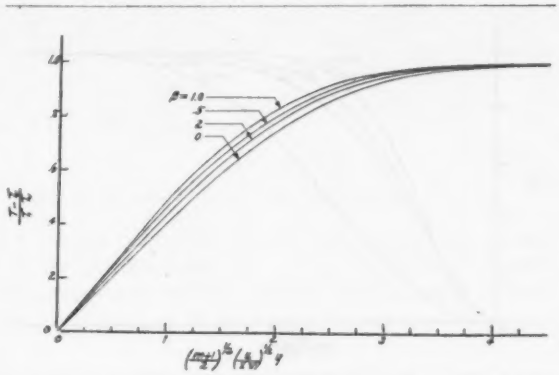

FIG. 4. Temperature profiles in the boundary layer at $\sigma = 0.7$.

The local rate of heat transfer per unit surface may be obtained from Eqs. (9) and (14) as

$$k\left(\frac{\partial T}{\partial y}\right)_{y=0} = k\left(\frac{\partial \theta}{\partial y}\right)_{y=0}(T_1 - T_w) = k\frac{\sqrt{\frac{m+1}{2}}\left(\frac{u_1}{xv}\right)^{1/2}\left[T_s + 2\int_0^{\infty} \exp.\left(-\sigma\int_0^{\bar{\eta}} \bar{f}d\bar{\eta}\right)d\bar{\eta}\left(\frac{d\psi}{d\bar{\eta}}\right)_{\bar{\eta}=0}\frac{u_1^2}{2gc_pJ} - T_w\right]}{\int_0^{\infty} \exp.\ (-\sigma\int_0^{\bar{\eta}} \bar{f}\, d\bar{\eta})d\bar{\eta}} \tag{15}$$

It is seen that the only effect of the function, ψ, accounting for the generation of heat inside the boundary layer is a change in the effective temperature difference causing the heat flow. In the hypothetic case where the internal generation of heat is negligible—i.e., hypothetic because a significant variation in local temperatures due to compressibility outside the boundary layer implies a significant magnitude for the internal heat generation—this temperature difference is simply the difference between the stagnation temperature of the gas and the temperature of the surface. The internal generation of heat because of its distortion of the temperature field near the surface requires a correction to the stagnation temperature in general in order to obtain the true effective gas temperature

A local Nusselt Number based on the difference between the effective gas temperature and the temperature of the surface may be found from Eq. (15) as:

$$\frac{h_x x}{k} = \frac{1}{\int_0^{\infty} \exp.\ (-\sigma\int_0^{\bar{\eta}} \bar{f}\, d\bar{\eta})d\bar{\eta}}\sqrt{\frac{m+1}{2}}\left(\frac{u_1 x}{v}\right)^{1/2} \tag{16}$$

Just as in the case of incompressible fluids,[1] the local Nusselt Number increases as the square root of the local Reynolds Number, $u_1 x/v$. The magnitude of the infinite integral in Eq. (16) depends mainly on the Prandtl Number, σ, and to a small extent on the exponent, m. Table 1 lists its value for Prandtl Numbers from 0.6 to 1.1 for a flat plate ($m = 0$) and for a forward stagnation region ($m = 1$).

Returning now to the evaluation of the function, ψ, the total differential Eq. (17) is obtained from the left-hand side of Eq. (10) after a transformation to the $\bar{\eta}$ coordinate.

TABLE 1

The Effect of the Prandtl Number on the Nusselt Number. The Value of $[1/\int_0^{\infty} \exp.(-\sigma\int_0^{\bar{\eta}} \bar{f}\, d\bar{\eta})d\bar{\eta})]$ for Several Prandtl Numbers

σ	Flat Plate	Forward Stagnation Region
0.6	0.390	0.466
0.7	0.413	0.495
0.8	0.434	0.521
0.9	0.452	0.546
1.0	0.469	0.570
1.1	0.485	0.592

$$\left(\frac{1}{\sigma}\right)\left(\frac{d^2\psi}{d\bar{\eta}^2}\right) + f\left(\frac{d\psi}{d\bar{\eta}}\right) - 2\beta\left(\frac{df}{d\bar{\eta}}\right)\psi = -\left(\frac{d^2 f}{d\bar{\eta}^2}\right)^2 + \beta\left(\frac{df}{d\bar{\eta}}\right) \tag{17}$$

with the boundary conditions

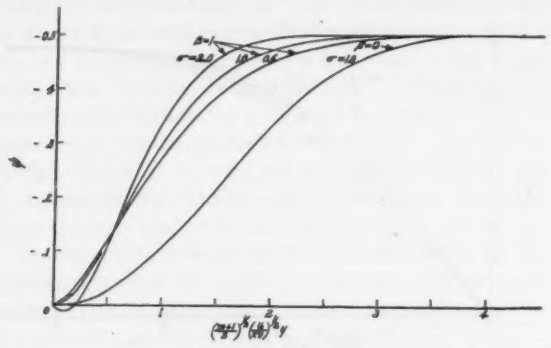

FIG. 5. Temperature field due to generation of heat in boundary layer

$$\bar{\eta} = 0, \quad \bar{\psi} = 0$$
$$\bar{\eta} \to \infty, \quad \bar{\psi} = -1/2$$

Eq. (17) has been numerically integrated by an adaptation of the Milne method for several Prandtl Numbers when the local velocity increases linearly along the surface ($\beta = 1$). Fig. 5 compares these results with an evaluation of ψ for flow along a flat plate when the Prandtl Number is unity. It is seen that the pressure gradient markedly affects the distortion of the temperature field caused by the generation of heat inside the boundary layer. It is also seen that the initial slope of the ψ profile, $(d\psi/d\bar{\eta})_{\bar{\eta}=0}$, is governed mainly by the Prandtl Number of the gas. When the Prandtl Number is unity, the initial slope is zero, or, in other words, when $\sigma = 1$, the temperature field near the surface is unaffected by the internal generation of heat. Therefore, the effective gas temperature is the same as if there were no generation of heat in the boundary layer—namely, the stagnation temperature of the gas. This result also follows directly from Eq. (15), since, as is well known, when $\sigma = 1$, the surface of an insulated body acquires the stagnation temperature of the gas.

The difference between the effective gas temperature and the stagnation temperature is given as a function of the Prandtl Number in Table 2 for flow along a flat plate and in a forward stagnation region. As Eckert and Drewitz have shown,[7] the effective gas temperature for a flat plate is the same as the temperature indicated by a plate thermometer. Therefore, Pohlhausen's square root law[2] takes care of the Prandtl Number effect in this case. When a pressure gradient exists, however, the square root law no longer applies. Thus, in Table 2, when $\beta = 1$, the difference between the effective and stagnation gas temperature is much greater at a given Prandtl Number than in flow along a flat plate (except, of course, when $\sigma = 1$). In fact

TABLE 2

The Temperature Correction, $(T_e - T_s)/(u_1^2/2gc_pJ)$, as a Function of the Prandtl Number and the Pressure Gradient

	Flat Plate		Forward Stagnation Region
σ	$\beta = 0$	$\sigma^{1/3} - 1$	$\beta = 1$
0.6	−0.230	−0.225	−0.395
0.8	−0.105	−0.105	−0.181
1.0	0	0	0
2.0	.....	+0.414	+0.681

no simple power law adequately describes the effect of the Prandtl Number on the effective gas temperature when $\beta = 1$.

Before leaving the subject of the effect of the internal generation of heat on the thermal performance of the boundary layer, it should be observed that the total differential Eq. (17) for ψ is of fundamental importance. For by changing the dependent variable from ψ to $\psi + 1/2 = \bar{\psi}$, Eq. (18) is obtained, and Eq. (18) is identical with the equation obtained for incompressible fluid flow,[1] with that obtained for compressible flow over insulated surfaces,[8] and with that similarly obtainable for incompressible flow over insulated surfaces.

$$\left(\frac{1}{\sigma}\right)\left(\frac{d^2\bar{\psi}}{d\bar{\eta}^2}\right) + f\left(\frac{d\bar{\psi}}{d\bar{\eta}}\right) - 2\beta\left(\frac{df}{d\bar{\eta}}\right)\bar{\psi} = -\left(\frac{d^2f}{d\bar{\eta}^2}\right)^2 \quad (18)$$

Only the boundary conditions differ for these several cases. They are, in the order of mention:

(1) Compressible flow with heat transfer—

$$\bar{\eta} = 0, \bar{\psi} = +1/2; \quad \bar{\eta} \to \infty, \bar{\psi} = 0$$

(2) Incompressible flow with heat transfer—

$$\bar{\eta} = 0, \bar{\psi} = 0; \quad \bar{\eta} \to \infty, \bar{\psi} = 0$$

(3) Compressible flow over insulated surface—

$$\bar{\eta} = 0, d\bar{\psi}/d\bar{\eta} = 0; \quad \bar{\eta} \to \infty, \bar{\psi} = 0$$

(4) Incompressible flow over insulated surface—

$$\bar{\eta} = 0, d\bar{\psi}/d\bar{\eta} = 0; \quad \bar{\eta} \to \infty, \bar{\psi} = 0$$

Furthermore, the solutions for these cases serve as good approximations to the solutions for surfaces of arbitrary shape when the local value of β at any point on the surfaces is evaluated as $2x/(x + 1)$. This follows from Falkner and Skan's finding[9] that a similar handling of the general velocity boundary layer equations resulted in fairly good approximations to the velocity profiles in the boundary layer of bodies of arbitrary shape.

THE VELOCITY AND TEMPERATURE FIELDS IN THE BOUNDARY LAYER OF BODIES OF ARBITRARY SHAPE

As Falkner has shown, for incompressible fluids,[11] an exact general solution for the velocity field in the boundary layer of any body may be obtained through Taylor series expansions with η constant:

$$f = (f)_{x=0} + x\left(\frac{\partial f}{\partial x}\right)_{x=0} + \frac{x^2}{2!}\left(\frac{\partial^2 f}{\partial x^2}\right)_{x=0} + \cdots$$

$$\frac{u}{u_1} = \frac{\partial f}{\partial \eta} = \left(\frac{\partial f}{\partial \eta}\right)_{x=0} + x\left(\frac{\partial^2 f}{\partial \eta\, \partial x}\right)_{x=0} + \frac{x^2}{2!}\left(\frac{\partial^3 f}{\partial \eta\, \partial x^2}\right)_{x=0} + \cdots$$

$$\frac{\tau_0}{\rho u_1^2}\left(\frac{u_1 x}{\nu}\right)^{1/2} = \left(\frac{\partial^2 f}{\partial \eta^2}\right)_{\eta=0} = \left(\frac{\partial^2 f}{\partial \eta^2}\right)_{\eta=0,\, x=0} + x\left(\frac{\partial^3 f}{\partial \eta^2\, \partial x}\right)_{\eta=0,\, x=0} + \frac{x^2}{2!}\left(\frac{\partial^4 f}{\partial \eta^2\, \partial x^2}\right)_{\eta=0,\, x=0} + \cdots \quad (19)$$

Since the local velocity always varies as a power law near a leading edge, the values of $(f)_{x=0}$, $(\partial f/\partial \eta)_{x=0}$, and $(\partial^2 f/\partial \eta^2)_{\eta=0,\, x=0}$ are determined by the solution described in the preceding section. These values depend only on the shape of the body near the leading edge. The remaining terms of Eq. (19) may be evaluated by successive differentiations of Eq. (5) with respect to x, substituting $x = 0$ into each of the derived equations.

In a similar manner the somewhat more involved general solution for the thermal boundary layer of any body may be expressed as Taylor series expansions involving the sum of two series with η constant:

$$\theta = \phi + \frac{\psi}{\xi} = (\phi)_{x=0} + x\left(\frac{\partial \phi}{\partial x}\right)_{x=0} + \frac{x^2}{2!}\left(\frac{\partial^2 \phi}{\partial x^2}\right)_{x=0} + \cdots + \frac{1}{\xi}\left[(\psi)_{x=0} + x\left(\frac{\partial \psi}{\partial x}\right)_{x=0} + \frac{x^2}{2!}\left(\frac{\partial^2 \psi}{\partial x^2}\right)_{x=0} + \cdots\right]$$

$$\frac{\sigma k (\partial T/\partial y)_{y=0}}{(T_1 - T_w) g \rho u_1 c_p}\left(\frac{u_1 x}{\nu}\right)^{1/2} = \left(\frac{\partial \theta}{\partial \eta}\right)_{\eta=0} = \left(\frac{\partial \phi}{\partial \eta}\right)_{\eta=0,\, x=0} + x\left(\frac{\partial^2 \phi}{\partial \eta\, \partial x}\right)_{\eta=0,\, x=0} + \frac{x^2}{2!}\left(\frac{\partial^3 \phi}{\partial \eta\, \partial x^2}\right)_{\eta=0,\, x=0} + \cdots +$$

$$\frac{1}{\xi}\left[\left(\frac{\partial \psi}{\partial \eta}\right)_{\eta=0,\, x=0} + x\left(\frac{\partial^2 \psi}{\partial \eta\, \partial x}\right)_{\eta=0,\, x=0} + \frac{x^2}{2!}\left(\frac{\partial^3 \psi}{\partial \eta\, \partial x^2}\right)_{\eta=0,\, x=0} + \cdots\right] \quad (20)$$

Because of the power-law variation of the local velocity near a leading edge, the values of $(\phi)_{x=0}$, $(\psi)_{x=0}$, $(\partial \phi/\partial \eta)_{\eta=0,\, x=0}$, and $(\partial \psi/\partial \eta)_{\eta=0,\, x=0}$ are those found in the preceding section and are determined solely by the shape of the body near the leading edge.

To evaluate $(\partial \phi/\partial x)_{x=0}$, $(\partial^2 \phi/\partial \eta\, \partial x)_{\eta=0,\, x=0}$, $(\partial \psi/\partial x)_{x=0}$, and $(\partial^2 \psi/\partial \eta\, \partial x)_{\eta=0,\, x=0}$, substitute $\theta = \phi + \psi/\xi$ into the general thermal boundary-layer Eq. (6) and differentiate with respect to x. Putting $x = 0$ into the resulting equation, several terms drop out and Eq. (21) is obtained.

$$\frac{\chi}{x}(1 + 2\xi)\left\{\left(\frac{\chi + 1}{2}\right) f\left(\frac{\partial \phi}{\partial \eta}\right) + \left(\frac{1}{\sigma}\right)\left(\frac{\partial^2 \phi}{\partial \eta^2}\right)\right\} + \xi\left\{(1 - 2\chi)\left[\left(\frac{\partial f}{\partial \eta}\right)\left(\frac{\partial \phi}{\partial x}\right) - \left(\frac{\partial f}{\partial x}\right)\left(\frac{\partial \phi}{\partial \eta}\right)\right] - \left(\frac{\chi'}{2}\right) f\left(\frac{\partial \phi}{\partial \eta}\right) -$$

$$\left(\frac{\chi + 1}{2}\right)\left[\left(\frac{\partial f}{\partial x}\right)\left(\frac{\partial \phi}{\partial \eta}\right) + f\left(\frac{\partial^2 \phi}{\partial \eta\, \partial x}\right)\right] - \left(\frac{1}{\sigma}\right)\left(\frac{\partial^3 \phi}{\partial \eta^2\, \partial x}\right)\right\} - \chi\left[2\left(\frac{\partial f}{\partial \eta}\right)\left(\frac{\partial \phi}{\partial x}\right) - \left(\frac{\partial f}{\partial x}\right)\left(\frac{\partial \phi}{\partial \eta}\right) + \left(\frac{\partial^2 f}{\partial \eta\, \partial x}\right)\phi\right] -$$

$$\chi'\left(\frac{\partial f}{\partial \eta}\right)\phi + \chi'\left[2\left(\frac{\partial f}{\partial \eta}\right)\psi - \left(\frac{f}{2}\right)\left(\frac{\partial \psi}{\partial \eta}\right)\right] + 2\chi\left[\left(\frac{\partial^2 f}{\partial \eta\, \partial x}\right)\psi + \left(\frac{\partial f}{\partial \eta}\right)\left(\frac{\partial \psi}{\partial x}\right)\right] - \left(\frac{\chi + 1}{2}\right)\left[\left(\frac{\partial f}{\partial x}\right)\left(\frac{\partial \psi}{\partial \eta}\right) +$$

$$f\left(\frac{\partial^2 \psi}{\partial \eta\, \partial x}\right)\right] + \left(\frac{\partial f}{\partial \eta}\right)\left(\frac{\partial \psi}{\partial x}\right) - \left(\frac{\partial f}{\partial x}\right)\left(\frac{\partial \psi}{\partial \eta}\right) - \left(\frac{1}{\sigma}\right)\left(\frac{\partial^3 \psi}{\partial \eta^2\, \partial x}\right) = 2\left(\frac{\partial^2 f}{\partial \eta^2}\right)\left(\frac{\partial^3 f}{\partial \eta^2\, \partial x}\right) - \chi\left(\frac{\partial^2 f}{\partial \eta\, \partial x}\right) - \chi'\left(\frac{\partial f}{\partial \eta}\right) \quad (21)$$

where χ' represents $d\chi/dx$. In order to avoid infinities, the sum of terms in each of the braces must be zero when $x = 0$. The first brace yields the relation,

$$[(m + 1)/2] f(\partial \phi/\partial \eta) + (1/\sigma)(\partial^2 \phi/\partial \eta^2) = 0$$

which has been shown to apply at a leading edge. The second brace yields Eq. (22):

$$(1 - 2m)\left[\left(\frac{\partial f}{\partial \eta}\right)\left(\frac{\partial \phi}{\partial x}\right) - \left(\frac{\partial f}{\partial x}\right)\left(\frac{\partial \phi}{\partial \eta}\right)\right] - \left(\frac{m + 1}{2}\right)\left[\left(\frac{\partial f}{\partial x}\right)\left(\frac{\partial \phi}{\partial \eta}\right) + f\left(\frac{\partial^2 \phi}{\partial \eta\, \partial x}\right)\right] - \left(\frac{\chi_0'}{2}\right) f\left(\frac{\partial \phi}{\partial \eta}\right) - \left(\frac{1}{\sigma}\right)\left(\frac{\partial^3 \phi}{\partial \eta^2\, \partial x}\right) = 0 \quad (22)$$

In this equation the values of f, $\partial f/\partial \eta$, and $\partial \phi/\partial \eta$ are known from the solutions of the velocity and thermal boundary-layer equations for a leading edge, and the value of $\partial f/\partial x$ is known from Falkner's general solution[11] of the velocity boundary-layer equations. Therefore, the equation can be numerically integrated with respect to η and the values of $\partial \phi/\partial x$ and $\partial^2 \phi/\partial \eta \partial x$ found. (The boundary conditions are: $\eta = 0$, $\partial \phi/\partial x = 0$; $\eta \to \infty$, $\partial^2 \phi/\partial \eta \partial x = 0$.) This procedure is analogous to the general treatment of the velocity boundary-layer equations.

A simpler, more direct method of finding the values of $(\partial \phi/\partial x)_{x=0}$ and $(\partial^2 \phi/\partial \eta\, \partial x)_{x=0}$, as well as the values of $(\partial^2 \phi/\partial x^2)_{x=0}$ and $(\partial^3 \phi/\partial \eta\, \partial x^2)_{x=0}$, results from an evaluation of the indeterminate groups of terms of Eq. (21) through the application of L'Hospital's rule. Thus,

$$\left\{\frac{\chi}{x}(1+2\xi)\left[\left(\frac{\chi+1}{2}\right)f\left(\frac{\partial\phi}{\partial\eta}\right)+\left(\frac{1}{\sigma}\right)\left(\frac{\partial^2\phi}{\partial\eta^2}\right)\right]\right\}_{x=0}=\frac{0}{0}=$$

$$\left(\frac{\chi(T_s-T_w)\left\{\left(\frac{\chi+1}{2}\right)\left[\left(\frac{\partial f}{\partial x}\right)\left(\frac{\partial\phi}{\partial\eta}\right)+f\left(\frac{\partial^2\phi}{\partial\eta\,\partial x}\right)\right]+\left(\frac{\chi'}{2}\right)f\left(\frac{\partial\phi}{\partial\eta}\right)+\left(\frac{1}{\sigma}\right)\left(\frac{\partial^3\phi}{\partial\eta^2\,\partial x}\right)\right\}}{(1+2\chi)(u_1^2/2gc_pJ)}\right)_{x=0} \tag{23}$$

Since the denominator of Eq. (23) is still zero, the numerator must also be zero, and therefore Eq. (24) is established.

$$[(m+1)/2][(\partial f/\partial x)(\partial\phi/\partial\eta)+f(\partial^2\phi/\partial\eta\,\partial x)]+(\chi'_0/2)f(\partial\phi/\partial\eta)+(1/\sigma)(\partial^3\phi/\partial\eta^2\,\partial x)=0 \tag{24}$$

A comparison of Eq. (24) with Eq. (22) shows that when $x = 0$,

$$(\partial f/\partial\eta)(\partial\phi/\partial x)-(\partial f/\partial x)(\partial\phi/\partial\eta)=0 \text{ or } (\partial\phi/\partial x)_{x=0}=\{(\partial f/\partial x)[(\partial\phi/\partial\eta)/(\partial f/\partial\eta)]\}_{x=0} \tag{25}$$

It follows that

$$\left(\frac{\partial^2\phi}{\partial\eta\,\partial x}\right)_{x=0}=\left[\left(\frac{\partial^2 f}{\partial\eta\,\partial x}\right)\frac{(\partial\phi/\partial\eta)}{(\partial f/\partial\eta)}+\left(\frac{\partial f}{\partial x}\right)\frac{(\partial^2\phi/\partial\eta^2)}{(\partial f/\partial\eta)}-\left(\frac{\partial f}{\partial x}\right)\frac{(\partial\phi/\partial\eta)(\partial^2 f/\partial\eta^2)}{(\partial f/\partial\eta)^2}\right]_{x=0} \tag{26}$$

All the terms on the right-hand side of Eqs. (25) and (26) are known, and therefore the values of $(\partial\phi/\partial x)_{x=0}$ and $(\partial^2\phi/\partial\eta\,\partial x)_{x=0}$ can be computed directly. Higher derivatives with respect to η may be similarly found.

To evaluate $(\partial^2\phi/\partial x^2)_{x=0}$ and $(\partial^3\phi/\partial\eta\,\partial x^2)_{x=0}$, apply L'Hospital's rule again to Eq. (23) as well as to Eq. (27).

$$\left(\frac{T_1-T_w}{u_1^2/gc_pJ}\left\{(1-2\chi)\left[\left(\frac{\partial f}{\partial\eta}\right)\left(\frac{\partial\phi}{\partial x}\right)-\left(\frac{\partial f}{\partial x}\right)\left(\frac{\partial\phi}{\partial\eta}\right)\right]-\left(\frac{\chi+1}{2}\right)\left[\left(\frac{\partial f}{\partial x}\right)\left(\frac{\partial\phi}{\partial\eta}\right)+f\left(\frac{\partial^2\phi}{\partial\eta\,\partial x}\right)\right]-\right.\right.$$

$$\left.\left.\left(\frac{\chi'}{2}\right)f\left(\frac{\partial\phi}{\partial\eta}\right)-\left(\frac{1}{\sigma}\right)\left(\frac{\partial^3\phi}{\partial\eta^2\,\partial x}\right)\right\}\right)_{x=0}=\frac{0}{0} \tag{27}$$

The denominators of the resulting ratios are zero. Therefore, the numerators and their difference, Eq. (28), are also zero.

$$(1-2m)\frac{\partial}{\partial x}\left[\left(\frac{\partial f}{\partial\eta}\right)\left(\frac{\partial\phi}{\partial x}\right)-\left(\frac{\partial f}{\partial x}\right)\left(\frac{\partial\phi}{\partial\eta}\right)\right]-2\chi_0'\left[\left(\frac{\partial f}{\partial\eta}\right)\left(\frac{\partial\phi}{\partial x}\right)-\left(\frac{\partial f}{\partial x}\right)\left(\frac{\partial\phi}{\partial\eta}\right)\right]=0 \tag{28}$$

or

$$\left(\frac{\partial^2\phi}{\partial x^2}\right)_{x=0}=\left[\left(\frac{\partial^2 f}{\partial x^2}\right)\frac{(\partial\phi/\partial\eta)}{(\partial f/\partial\eta)}+\left(\frac{\partial f}{\partial x}\right)\frac{(\partial^2\phi/\partial\eta\partial x)}{(\partial f/\partial\eta)}-\left(\frac{\partial f}{\partial x}\right)\frac{(\partial\phi/\partial\eta)(\partial^2 f/\partial\eta\partial x)}{(\partial f/\partial\eta)^2}\right]_{x=0}+$$

$$\frac{2\chi_0'}{1-2m}\left[\left(\frac{\partial\phi}{\partial x}\right)-\left(\frac{\partial f}{\partial x}\right)\frac{(\partial\phi/\partial\eta)}{(\partial f/\partial\eta)}\right]_{x=0} \tag{28a}$$

All the terms on the right-hand side of Eq. (28a) are known and so $\partial^2\phi/\partial x^2$ may be computed. The derivative, $\partial^3\phi/\partial\eta\,\partial x^2$, and all higher derivatives with respect to η may be obtained by successive differentiations of Eq. (28a).

Another application of L'Hospital's rule to Eqs. (23) and (27) results in denominators which are not zero. The resultant ratios may be substituted back into Eq. (21), and $(\partial\psi/\partial x)_{x=0}$ and $(\partial\psi/\partial\eta\,\partial x)_{x=0}$ can be found by numerical integration. The derivative, $\partial^5\phi/\partial\eta^2\,\partial x^3$, occurring in the revised version of Eq. (21), is evaluated by a second differentiation with respect to x of the general thermal boundary-layer Eq. (6). In a similar manner, the values of higher derivatives with respect to x of both ϕ and ψ are obtained by successive differentiations of Eq. (6).

It has been meant only to outline here the method whereby an exact general solution to the thermal boundary-layer equations may be obtained. The details of its derivation, as well as its application, will be the subject of a later paper. For the present, we will be concerned with a first approximation to the general solution, which has broad implications and is rather convenient to use.

First Approximation to General Solution of Thermal Boundary Layer Equations

The similarity of form of the velocity boundary-layer Eqs. (7) and (13) for Y or $(T-T_w)/(T_s-T_w)$ (neglecting for the time being the generation of heat in the boundary layer) suggests that some similarity must exist between their solutions. That this is so may be shown by changing the dependent variable of Eq. (7) from $\bar{f}$ to the velocity ratio, u/u_1, thus obtaining Eq. (29):

$$[d^2(u/u_1)/d\bar{\eta}^2]+\bar{f}[d(u/u_1)/d\bar{\eta}]=\beta[(d\bar{f}/d\bar{\eta})^2-1] \tag{29}$$

with the boundary conditions $\bar{\eta} = 0$, $u/u_1 = 0$ and $\bar{\eta} \to \infty$, $u/u_1 = 1$, where the remaining functions, $\bar{f}$ and $d\bar{f}/d\bar{\eta}$, are regarded as known functions. The complete solution, Eq. (30), is found by the application of the method of "the variation of constants" to the solution of the related homogeneous equation.

$$\frac{u}{u_1} = \frac{\int_0^{\bar{\eta}} \exp.\,(-\int_0^{\bar{\eta}} \bar{f}\, d\bar{\eta})d\bar{\eta}}{\int_0^{\infty} \exp.\,(-\int_0^{\bar{\eta}} \bar{f}\, d\bar{\eta})d\bar{\eta}} - \beta \int_0^{\infty} \left\{ \exp.\left(-\int_0^{\bar{\eta}} \bar{f}\, d\bar{\eta}\right) \int_0^{\bar{\eta}} \left[\left(\frac{d\bar{f}}{d\bar{\eta}}\right)^2 - 1 \right] \times \right.$$
$$\left. \exp.\left(+\int_0^{\bar{\eta}} \bar{f}\, d\bar{\eta}\right) d\bar{\eta} \right\} d\bar{\eta} \left[\frac{\int_0^{\bar{\eta}} \exp.\,(-\int_0^{\bar{\eta}} \bar{f}\, d\bar{\eta})d\bar{\eta}}{\int^{\infty} \exp.\,(-\int_0^{\bar{\eta}} \bar{f}\, d\bar{\eta})d\bar{\eta}} \right] +$$
$$\beta \int_0^{\bar{\eta}} \left\{ \exp.\left(-\int_0^{\bar{\eta}} \bar{f}\, d\bar{\eta}\right) \int_0^{\bar{\eta}} \left[\left(\frac{d\bar{f}}{d\bar{\eta}}\right)^2 - 1 \right] \exp.\left(+\int_0^{\bar{\eta}} \bar{f}\, d\bar{\eta}\right) d\bar{\eta} \right\} d\bar{\eta} \quad (30)$$

The portion of the velocity profile given by the first term of Eq. (30) is seen to be identical with the "effective" temperature profile in the boundary layer, Eq. (14), when the Prandtl Number is unity. The remaining terms describe the deviation of the velocity field from the temperature field caused by the prevailing pressure gradient. In flow along a flat plate, the pressure gradient, or β, is zero and these disturbing terms disappear. This is the only case in which the velocity field and the "effective" temperature field in the boundary layer are the same.

The surface shearing stress, τ_0, is obtained from the velocity profile, Eq. (30), as:

$$\frac{\tau_0}{u_1} = \mu \left[\frac{d(u/u_1)}{dy}\right]_{y=0} = \mu \sqrt{\frac{m+1}{2}} \left(\frac{u_1}{xv}\right)^{1/2} \left(\frac{1}{\int_0^{\infty} \exp.\,(-\int_0^{\bar{\eta}} \bar{f}\, d\bar{\eta})d\bar{\eta}} - \right.$$
$$\left. \beta \frac{\int_0^{\infty} \left\{ \exp.\,(-\int_0^{\bar{\eta}} \bar{f}\, d\bar{\eta}) \int_0^{\bar{\eta}} [(d\bar{f}/d\bar{\eta})^2 - 1] \exp.\,(+\int_0^{\bar{\eta}} \bar{f}\, d\bar{\eta}) d\bar{\eta} \right\} d\bar{\eta}}{\int_0^{\infty} \exp.\,(-\int_0^{\bar{\eta}} \bar{f}\, d\bar{\eta})d\bar{\eta}} \right) \quad (31)$$

But the shearing stress at any surface has been defined by the momentum equation of the boundary layer as the sum of two stresses: one due to the gradient of the "momentum loss" in the boundary layer, and the other due to the unbalance of stress caused by the local pressure gradient acting on the displacement thickness of the boundary layer.

$$\tau_0/u_1 = (1/u_1)(dM/dx) - (1/u_1)(dp/dx)\delta^*$$

or

$$\tau_0/u_1 = (1/u_1)[d(\rho u_1^2 \delta^{**})/dx] + \rho_1 (du_1/dx)\delta^* \quad (32)$$

where M is the "momentum loss" of the boundary layer, δ^* is the displacement thickness of the boundary layer, and δ^{**} is the momentum thickness of the boundary layer.

Since the first term of Eq. (31) does not involve a pressure gradient, or β, directly, it must correspond to the "momentum loss" gradient term of the momentum Eq. (32). Furthermore, a comparison of this term with Eq. (15) for the thermal boundary-layer equations shows that, when the Prandtl Number of a gas is unity, the momentum loss and heat transfer are simply related.

$$h_e/c_p g = (1/u_1)(dM/dx)$$

or, in dimensionless form,

$$h_e/\rho u_1 c_p g = (1/\rho u_1^2)(dM/dx) \quad (33)$$

This result might have been anticipated by assuming the mechanisms of momentum loss and heat transfer to be similar. Its independent derivation establishes the analogy between the two phenomena.

The question now arises as to how the Prandtl Number affects the analogy. An evaluation of the effect has been obtained in the first paper[1] of this series from

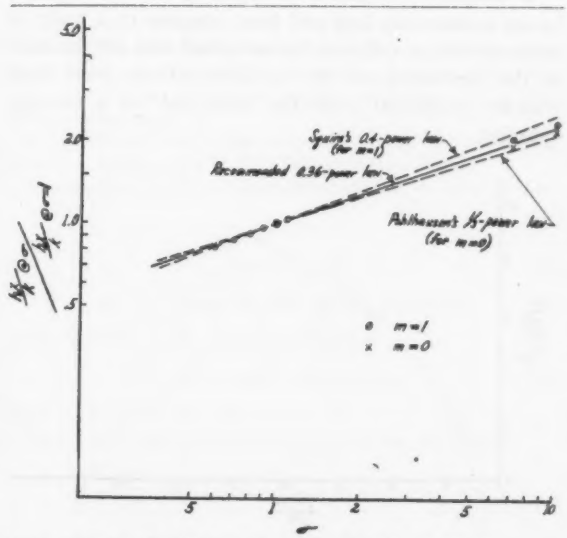

FIG. 6. Effect of Prandtl Number on Nusselt Number.

TABLE 3

Comparison of $(h_e/\rho u_1 c_p g)(u_1 x/\nu)^{1/2}$ Evaluation by Analogy Method, Eq. (34), with Values Obtained from Eq. (16) for Several Wedge Angles When $\sigma = 0.7$

Central Angle of Wedge	m	β	$\left(\frac{1}{\rho u_1^2}\right)\left(\frac{dM}{dx}\right)\sigma^{-0.64}\left(\frac{u_1 x}{\nu}\right)^{1/2}$	$\left(\frac{h_e}{\rho u_1 c_p g}\right)\left(\frac{u_1 x}{\nu}\right)^{1/2}$ from Eq. (16)	Difference, %
0°	0	0	0.417	0.417	0
36	0.111	0.2	0.459	0.473	−3.0
90	0.333	0.5	0.539	0.544	−0.9
180	1.000	1.0	0.734	0.709	+3.4

a reconsideration of the dependence on the Prandtl Number of the heat transfer from a flat plate and from a forward stagnation region. Fig. 6 compares the recommended 0.36-power law with the Pohlhausen[2] 1/3- and the Squire[12] 0.4-power laws. It is seen that the 0.36-power law is the best average representation of the variation of the Nusselt Number with the Prandtl Number.

In order to obtain the heat transfer number, $h_e/\rho u_1 c_p g$, of Eq. (33) from the Nusselt Number, $h_e x/k$, the latter is divided by the product of the Reynold's Number, $u_1 x/\nu$, and the Prandtl Number, $g c_p \mu/k$. It follows that the heat transfer number varies according to the -0.64 power of the Prandtl Number. Therefore the analogy between momentum loss and heat transfer may be generalized as Eq. (34).

$$h_e/\rho u_1 c_p g = (1/\rho u_1^2)(dM/dx)\sigma^{-0.64} \qquad (34)$$

Table 3 compares, for several wedge angles, the value of $(h_e/\rho u_1 c_p g)(u_1 x/\nu)^{1/2}$ as calculated from Eq. (34) with the value obtained from Eq. (16) when $\sigma = 0.7$. The agreement is within better than 3.5 per cent.

Heat Transfer from the Front Half of a Circular Cylinder

A convenient method of applying the analogy between momentum loss and heat transfer to a body of arbitrary shape will now be described and will be used in the derivation of the variation of the local heat transfer coefficient over the front half of a circular cylinder.

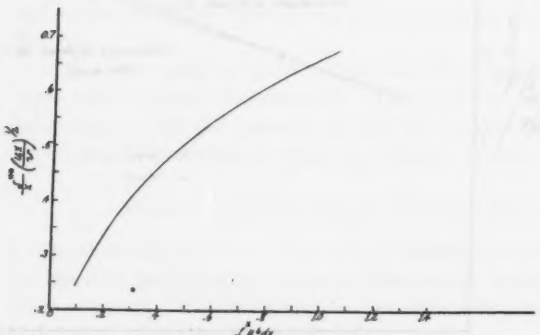

FIG. 7. Curve for determining momentum thickness of boundary layer.

The analogy's usefulness depends on how readily the gradient of the momentum loss, dM/dx or $d(\rho u_1^2 \delta^{**})/dx$, may be evaluated. The variation along the surface of the local velocity, u_1, is, of course, known from the measured pressure distribution about the body. The momentum thickness of the boundary layer, δ^{**}, remains to be found. But Falkner[13] has already shown that δ^{**} is determined by the value of the integral, $(1/u_1^6 x)\int_0^x u_1^6 dx$, through the relation plotted in Fig. 7. Therefore, δ^{**} is easily evaluated. The product, $\rho u_1^2 \delta^{**}$, is next plotted against x. The slope of the resultant curve enables the local heat transfer coefficients to be calculated from Eq. (34).

Fig. 8 compares the curve of local heat transfer coefficients calculated in this manner for air flowing over the front half of a circular cylinder with some averaged data obtained by Schmidt and Wenner.[14] The agreement is fairly good.

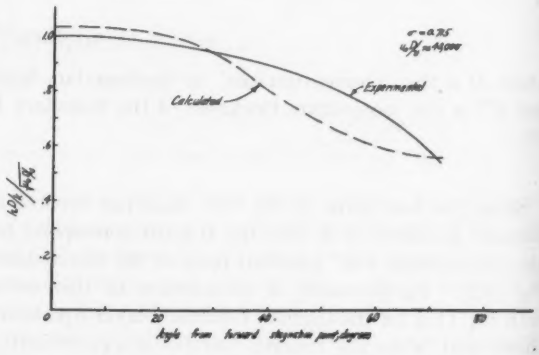

FIG. 8. Heat transfer coefficients for front half of circular cylinder.

CONCLUSIONS

It may be concluded from the foregoing that the same degree of refinement that has been reached in the analysis of laminar velocity boundary layers can be attained in the treatment of laminar thermal boundary layers.

The basic thermodynamics of the compressible flow of a gas requires the stagnation temperature to be the effective gas temperature causing heat flow *in the absence of heat generation* by friction and compressibility in the boundary layer. The presence of internal

heat generation requires a correction factor, dependent on the local pressure gradient, as well as on the Prandtl Number of the gas, to be applied to the stagnation temperature to obtain the effective gas temperature. When the Prandtl Number is unity, no correction is required no matter what the pressure gradient.

As a first approximation, an analogy exists between the *momentum loss* in the boundary layer and the rate of heat transfer despite the presence of a pressure gradient. Accordingly, the common belief that skin friction and heat transfer are analogous quantities is incorrect except when the local pressure gradient is zero.

References

[1] Tifford, A. N., *The Extension of the Analogy Between Momentum and Heat Transfer to Flow Fields Involving Pressure Gradients in Incompressible Fluids; and Some Remarks on the Frictional Generation of Heat in the Boundary Layer*, presented at the A.S.M.E. Aviation Meeting, June 5, 1944.

[2] Pohlhausen, E., *Der Wärmeustausch zwischen festen Körpern und Flüssigkeiten mit kleiner Reibung und kleiner Wärmeleitung*, Z.f.a.M.M., Vol. 1, No. 2, pp. 115–121, 1921.

[3] Busemann, A., *Gas-strömung mit laminaren Grenzschicht entlang einer Platte*, Z.f.a.M.M., Vol. 15, No. 1, p. 23, 1935.

[4] von Kármán, Th., and Tsien, H. S., *Boundary Layer in Compressible Fluids*, Journal of the Aeronautical Sciences, Vol. 5, No. 6, pp. 227–232, April, 1938.

[5] Emmons, H. W., and Brainerd, J. G., *Temperature Effects in a Laminar Compressible-Fluid Boundary Layer Along a Flat Plate*, Journal of Applied Mechanics, Vol. 8, No. 3, pp. 105–110, September, 1941.

[6] Brainerd, J. G., and Emmons, H. W., *Effect of Variable Viscosity on Boundary Layers, With a Discussion of Drag Measurements*, Journal of Applied Mechanics, Vol. 9, No. 1, pp. 1–6, March, 1942.

[7] Eckert, E., and Drewitz, O., *The Heat Transfer to a Plate in Flow at High Speed*, Forschung a. d. Gebiete d. Ingenieurwesens, Vol. 11, No. 3, pp. 116–122, May-June, 1940; also N.A.C.A. T.M. No. 1045, May, 1943.

[8] Eckert, E., and Drewitz, O., *Calculation of the Temperature Field in the Laminar Boundary Layer of an Unheated Body in a High-Speed Flow*, Luftfahrtforschung, Vol. 19, No. 6, pp. 189–196, June, 1942; also British Air Ministry R.T.P. Translation No. 1594.

[9] Falkner, V. M., and Skan, S. W., *Some Approximate Solutions of the Boundary Layer Equations*, British Air Ministry, R. & M. 1314, April, 1930.

[10] Hartree, D. R., *On an Equation Occurring in Falkner and Skan's Approximate Treatment of the Equations of the Boundary Layer*, Proceedings of the Cambridge Philosophical Society, Vol. 33, Part 2, pp. 223–239, April, 1937.

[11] Falkner, V. M., *A Further Investigation of Solutions of the Boundary Layer Equations*, British Air Ministry, R. & M. 1884, November, 1937.

[12] Goldstein, S., *Modern Developments in Fluid Dynamics*, Vol. 2, pp. 631, 632; Oxford University Press, 1938.

[13] Falkner, V. M., *Simplified Calculation of the Laminar Boundary Layer*, British Air Ministry, R. & M. 1895, July, 1941.

[14] Schmidt, E., and Wenner, K., *Heat Transfer Over the Circumference of a Heated Cylinder in Transverse Flow*, Forschung a.d. Gebiete d. Ingenieurwesens, Vol. 12, No. 2, pp. 65–73, March-April, 1941; also N.A.C.A. T.M. No. 1050, October, 1943.

Letters to the Editor

Dear Sir:

In my paper entitled "Buckling Loads of Beams or Plates on Continuous Supports" which appeared in the October, 1944, issue of the JOURNAL OF THE AERONAUTICAL SCIENCES, it has been called to my attention that the condition given by Eq. (33) holds only for one point along the line $x = c$. Consequently, the conclusions drawn just following Eq. (33) and in the examples given in the right-hand column of page 402 are unwarranted. The characteristic equations given in the examples yield the buckling loads for a rectangular plate simply supported around the edges and further restrained from deflecting at the single point (c, y_1) or (x_1, d), respectively.

EDWARD SAIBEL
Associate Professor of Mechanics
Carnegie Institute of Technology

Dear Sir:

In his paper, "A Note on Bending Beyond the Proportional Limit" (JOURNAL OF THE AERONAUTICAL SCIENCES, Vol. 12, No. 1, p. 21, January, 1945), M. Yachter has presented a new solution to the problem of plastic bending. The author's use of a "modified stress-strain" curve makes his solution unnecessarily complicated; the strain energy will be a minimum when the stress distribution is such that S/E_T^* varies linearly across the depth of the cross section. (E_T^* is the tangent modulus of the original stress-strain curve.)

In the following proof of the linearity of S/E_T^* all symbols used have the same meaning as that defined by the author.

It is required to find the stress distribution $S = S(z)$ such that:

$$\int S\,dA = P \tag{1}$$

$$\int Sz\,dA = M \tag{2}$$

$$W = \int \text{energy} = \int A_e\,dA \text{ is a minimum} \tag{3}$$

By the principles of the calculus of variations,

$$\delta W + \lambda_3 \delta P + \lambda_4 \delta M = 0 \tag{4}$$

where λ_3 and λ_4 are constants.

Since S is the only independent variable, Eq. (4) becomes

$$\int \left[\left(\frac{dA_e}{dS} \right) \delta S\,dA + \lambda_3 \delta S\,dA + \lambda_4 \delta S z\,dA \right] = 0$$

(Continued on page 252)

Factoring $\delta S\, dA$ gives

$$\int [(dA_c/dS) + \lambda_3 + \lambda_4 z]\delta S\, dA = 0 \qquad (5)$$

Since δS is arbitrary, Eq. (5) requires that

$$(dA_c/dS) + \lambda_3 + \lambda_4 z = 0 \qquad (6)$$

but

$$dA_c/dS = (dA_c/de)(de/dS)$$

and examination of Fig. 1 indicates that

$$dA_c/de = S \text{ and } de/dS = 1/E_T^*$$

therefore

$$dA_c/dS = S/E_T^* \qquad (7)$$

Substituting Eq. (7) into Eq. (6) gives the result

$$S/E_T^* = -(\lambda_3 + \lambda_4 z) \qquad (8)$$

Since λ_3 and λ_4 are constants Eq. (8) states that S/E_T^* varies linearly across the depth of the cross section.

The use of Eq. (8) instead of the author's Eq. (11) will give results that are identical to those obtained by the author. However, the amount of calculation required will be considerably less than that required by the author's procedure, since it is unnecessary to determine the "modified stress-strain" curve, E_s, E_T, and $\phi(S)$.

Beskin[1] has pointed out that the assumption of a rectangular stress distribution based on a stress equal to the ultimate stress gives predicted ultimate moments that are in better agreement with the test results of Cozzone[2] than the moments predicted from the assumption of linear strain distribution. For materials such as X-4130 steel, or 14ST aluminum alloy, whose tangent modulus approaches zero at the ultimate strength, the ratio S/E_T^* approaches infinity, and the corresponding stress distribution approaches uniformity from the neutral axis to the extreme fiber. This justifies theoretically Beskin's assumption noted above, and the better check of Cozzone's test results using this assumption provides experimental verification of the author's theory.

REFERENCES

[1] Beskin, L., *Letter to the Editor*, Journal of the Aeronautical Sciences, Vol. 12, No. 1, p. 122, January, 1945.

[2] Cozzone, F. P., *Bending Strength in the Plastic Range*, Journal of the Aeronautical Sciences, Vol. 10, No. 5, p. 137, May, 1943.

JACOB KAROL
Head, Stress Analysis Unit
LENARD A. GORAN
Structures Engineer
Curtiss-Wright Corporation, Airplane Division

Periodicals Wanted for Foreign Libraries

A committee of the American Library Association is collecting scientific and technical journals for eventual shipment to foreign libraries and institutions unable to get them now because of the war. The Committee is eager to acquire the JOURNAL OF THE AERONAUTICAL SCIENCES, and only through your gifts can copies be obtained. The Committee will provide storage space if necessary. If you wish to help by donating your periodicals, please write to Dorothy J. Comins, Executive Assistant, Committee on Aid to Libraries in War Areas, Library of Congress Annex, Study 251, Washington 25, D.C.